

Fall 2020

Fermi-Unsmearing in Single Charged Pion Electroproduction Cross-Section Measurements for the Neutron and Proton in Deuterium

Gary Hollis

Follow this and additional works at: <https://scholarcommons.sc.edu/etd>



Part of the [Physics Commons](#)

Recommended Citation

Hollis, G.(2020). *Fermi-Unsmearing in Single Charged Pion Electroproduction Cross-Section Measurements for the Neutron and Proton in Deuterium*. (Doctoral dissertation). Retrieved from <https://scholarcommons.sc.edu/etd/6124>

This Open Access Dissertation is brought to you by Scholar Commons. It has been accepted for inclusion in Theses and Dissertations by an authorized administrator of Scholar Commons. For more information, please contact dillarda@mailbox.sc.edu.

FERMI-UNSMEARING IN SINGLE CHARGED PION ELECTROPRODUCTION
CROSS-SECTION MEASUREMENTS FOR THE NEUTRON AND PROTON IN
DEUTERIUM

by

Gary Hollis

Bachelor of Science
University of South Carolina, 2007

Submitted in Partial Fulfillment of the Requirements

For the Degree of Doctor of Philosophy in

Physics

College of Arts and Sciences

University of South Carolina

2020

Accepted by:

Ralf Gothe, Major Professor

Steffen Strauch, Committee Member

Fred Myhrer, Committee Member

Kijun Park, Committee Member

Cheryl L. Addy, Vice Provost and Dean of the Graduate School

© Copyright by Gary Hollis, 2020
All Rights Reserved.

ACKNOWLEDGEMENTS

I thank God for the many opportunities I have had in this life, but especially for the opportunity to study physics with the mentorship of Ralf Gothe who encouraged and patiently allowed me to explore many rabbit holes and return with knowledge and experiences that I would have never received otherwise. I thank my committee members Ralf Gothe, Steffen Strauch, Fred Myhrer, and Kijun Park for spending their time reviewing my dissertation and offering constructive criticism and encouragement so as to develop this work into a meaningful contribution to science.

I thank Ralf Gothe, Evan Phelps, Arjun Trivedi, and Ye Tian for their critical assistance to this work as well as their many sincere, enlightening conversations which have shaped me not just as a researcher but as a person. I also thank my colleagues, in alphabetical order, Gleb Fedotov, Chris McLauchlin, Krishna Neupane, Evan Phelps, Iuliia Skorodumina, Ye Tian, Arjun Trivedi, and Nick Tyler.

I thank the CLAS collaboration and the National Science Foundation, without which this work would not have been possible.

Last but certainly not least, I thank my parents who have supported me in innumerable ways with constant, continual love and encouragement in both word and deed, giving me a sure foundation on which to build a good life which includes accomplishing this doctorate.

ABSTRACT

Electron scattering cross-sections for two different reaction channels, $e^- + p \rightarrow e^- + n + \pi^+$ and $e^- + n \rightarrow e^- + p + \pi^-$ using an unpolarized deuterium target, were extracted from Jefferson Lab experiment E1E data with a beam energy of 2.039 GeV, providing a (W, Q^2) coverage of $1.1 \text{ GeV} < W < 1.9 \text{ GeV}$ and $0.4 \text{ GeV}^2 < Q^2 < 1.0 \text{ GeV}^2$. Although there has already been an analysis of this same data set for the second reaction channel listed above [1], more of the cross-section domain has been covered in this analysis due to applying a new technique called Fermi-unsmearing. Fermi-smearing is a distortion in a cross-section measurement which occurs whenever the target is erroneously assumed to be at rest but is in fact a bound nucleon as part of a larger nucleus (and thus is in Fermi-motion). Fermi-unsmearing is a Monte Carlo method presented in this work for generating a correction factor that removes the Fermi-smearing effect from an existing cross-section measurement that suffers from Fermi-smearing. Using Fermi-unsmearing can have the advantage of significantly larger statistical sample sizes given the same data set due to allowing less strict final data selection criteria, as occurs in a Fermi-unsmearred analysis of the $e^- + n \rightarrow e^- + p + \pi^-$ channel in contrast to a fully-exclusive analysis of the same channel. The same Fermi-unsmearing method is applied to the first channel after having established the efficacy of the method using the second channel.

TABLE OF CONTENTS

ACKNOWLEDGEMENTS	iii
ABSTRACT	iv
LIST OF TABLES	viii
LIST OF FIGURES	ix
CHAPTER 1: INTRODUCTION	1
1.1 Motivation for Research	1
1.2 Reaction Channels of Interest	7
1.3 Mathematical Foundations and Notation	10
1.4 Experimental Apparatus	16
1.5 Computing Tools	17
CHAPTER 2: DATA SELECTION.	21
2.1 Run Selection	22
2.2 Electron Identification	24
2.3 Hadron Identification	30
2.4 Fiducial Cuts	36
2.5 Exclusivity Cuts and Background Subtraction	48
2.6 Binning	58
CHAPTER 3: DATA CORRECTIONS	62
3.1 Bin-Centering	62
3.2 Kinematic Corrections	64
3.3 Acceptance Corrections	69

3.4	Radiative-Effects Corrections	71
3.5	Normalization	72
3.6	Empty-Target Subtraction	73
CHAPTER 4: FERMI-UNSMEARING		82
4.1	Γ_ν and ϵ Variation	91
CHAPTER 5: CROSS-SECTIONS		95
5.1	π^- Cross-Sections	96
5.2	π^+ Cross-Sections	103
5.3	Structure Functions	109
5.4	Non-Negative Cosine Series Fits	110
5.5	Systematic Uncertainty Estimation	121
CHAPTER 6: DEPENDENCY ORIENTED PROGRAMMING		124
6.1	A Simple Example	127
6.2	Having and Eating Cake: DOP + ROOT + C++	133
6.3	Advanced Usage	137
6.4	Directions For Future Development	140
CHAPTER 7: SUMMARY AND CONCLUSIONS		143
BIBLIOGRAPHY		145
APPENDIX A: Δt SHIFTS		149
A.1	Proton Δt Shifts	149
A.2	π^- Δt Shifts	168
A.3	π^+ Δt Shifts	190
APPENDIX B: FIDUCIAL CUTS		210
B.4	Electron	210
B.5	π^- Fiducial Cuts	211
B.6	π^+ Fiducial Cuts	212
B.7	Proton Fiducial Cuts	214

APPENDIX C: ANALYSIS CUT AND CORRECTION

SUMMARY	215
-------------------	-----

LIST OF TABLES

Table 2.1: EC UVW cuts..	38
Table 2.2: $(W, Q^2, \cos(\theta^*), \phi^*)$ binnings.	59
Table 5.1: Systematic uncertainty components..	123
Table A.1: Experiment Δt shifts for proton.	149
Table A.2: Simulation Δt shifts for proton..	159
Table A.3: Experiment Δt shifts for π^-	168
Table A.4: Simulation Δt shifts for π^-	179
Table A.5: Experiment Δt shifts for π^+	190
Table A.6: Simulation Δt shifts for π^+	200
Table B.1: $\theta_{\min}(p) = a + \frac{b}{p+c}$ minimum electron θ cut parameters.	210
Table B.2: Electron θ - ϕ low fiducial cut parameters..	210
Table B.3: Electron θ - ϕ high fiducial cut parameters.	211
Table B.4: π^- $\theta_{\min}(p) = a + \frac{b}{p+c}$ cut parameters.	211
Table B.5: π^- θ - ϕ low cut parameters.	211
Table B.6: π^- θ - ϕ high cut parameters.	212
Table B.7: π^+ $\theta_{\min}(p) = a + \frac{b}{p+c}$ cut parameters.	212
Table B.8: π^+ θ - ϕ low cut parameters.	212
Table B.9: π^+ θ - ϕ high cut parameters.	213
Table B.10: Proton θ_{\min} value.	214
Table B.11: Proton θ - ϕ low cut.	214
Table B.12: Proton θ - ϕ high cut.	214
Table C.1: Analysis cuts.	215
Table C.2: Analysis corrections.	215

LIST OF FIGURES

Figure 1.2: Demonstration of the Fermi-smearing effect on the center of mass energy W (defined later) for experiment yields from two different analyses of the reaction channel $e^- + n \rightarrow e^- + p + \pi^-$, one Fermi-smearred and one fully exclusive.	8
Figure 1.3: Illustration of angles and momentum vectors for particles involved in a single pion electroproduction reaction in the center of momentum frame. The same labels for particle momenta are used as specified earlier.	9
Figure 1.4: CLAS design schematic.	14
Figure 1.5: CLAS as it used to be situated in Hall B.	17
Figure 1.6: CLAS12 design schematic.	18
Figure 1.7: FTOF12 installation picture during CLAS12 upgrade.	19
Figure 2.1: Binned event rates and scatter plot of event rate versus file index along with $\pm 3\sigma$ cut lines.	20
Figure 2.2: Sampling fraction f_s versus momentum distribution.	23
Figure 2.3: Slice of sampling fraction f_s versus momentum distribution along with Gaussian fit and $3-\sigma$ boundaries.	24
Figure 2.4: Sampling fraction f_s versus momentum distribution along with $3-\sigma$ boundaries and their linear fits.	25
Figure 2.5: N_γ distribution for a selected PMT along with modified Poisson distribution fit to the signal region.	26
Figure 2.6: θ_{CC} angle, SC plane, CC plane, and CC projective plane diagram.	27
Figure 2.7: Single CC counter θ_{CC} distribution with Gaussian fit and asymmetrical cut lines.	28
Figure 2.8: θ_{CC} distribution and cut boundaries for Sector 1 of the CC.	30

Figure 2.9: Δt versus momentum histograms for positive (top) and negative (bottom) particle tracks from E1E data with all selection criteria other than hadron identification applied in the final data set for the $\pi^- + p$ channel analysis.	31
Figure 2.10: Example of a useful Δt distribution for a single SC paddle along with sum-of-Gaussian fit and $\pm 3\sigma$ boundaries.	33
Figure 2.11: Example of a bad SC paddle Δt distribution.	34
Figure 2.12: Example of calculated Δt shifts for protons in $\pi^- + p$ analysis. Here the arithmetic negative of the shifts are plotted as they are the peak positions detected in the Δt distributions, which is more convenient for visualizing and understanding the shifts in relation to the selection bounds. Note that not all paddles have sufficient data for determining shifts and are left as-is, such as paddles 1-8.	35
Figure 2.13: Example of repaired Δt	36
Figure 2.14: Particle ID cuts for π^- , π^+ , and proton candidate particles along with repaired Δt versus momentum histograms having all other cuts applied.	37
Figure 2.15: EC U cuts plotted along with U histograms for all sectors.	39
Figure 2.16: EC V cuts plotted along with V histograms for all sectors.	40
Figure 2.17: EC W cuts plotted along with W histograms for all sectors.	41
Figure 2.18: Electron (θ, ϕ) experiment data histogram for select sector and momentum in (0.8, 1) GeV/c range. Note that a relative ϕ is used, so that each sector has a relative ϕ range of $(-30^\circ, 30^\circ)$	42
Figure 2.19: Electron momentum- θ experiment data histogram with θ_{\min} boundaries and fit function for a selected sector.	42
Figure 2.20: ϕ slice and trapezoid fit for momentum in (0.8, 1) GeV/c range and θ in $(29.25^\circ, 31.05^\circ)$ range for Sector 1 experiment data.	43
Figure 2.21: Comparison of electron fiducial cuts for experiment and simulation data for selected bins.	44
Figure 2.22: θ_{\min} determination for π^- and π^+ particles for experiment and simulation.	45

Figure 2.23: π^- and π^+ (θ, ϕ) histograms and fiducial cuts for experiment and simulation for Sector 1, momentum in (0.4, 0.6) GeV/c.	46
Figure 2.24: Proton θ versus momentum histograms for Sector 1 along with determined θ_{\min} cut for experiment and simulation.	47
Figure 2.25: Example proton fiducial cuts for experiment and simulation, Sector 1, and momentum in (0.47, 0.82) GeV/c. Note that in some bins the θ_{\min} cut is redundant, as in the case of this bin.	47
Figure 2.26: Squared missing mass distribution for the $\pi^- + p$ analysis integrated over full (W, Q^2) domain along with exclusivity cut and the same distribution for events with two pions reconstructed, showing no significant double-pion contamination within the cut range.	50
Figure 2.27: Squared missing mass distribution for the π^- analysis integrated over full (W, Q^2) domain along with the exclusivity cut showing noticeable double-pion contamination within the cut range.	51
Figure 2.28: Squared missing mass distribution for the π^+ analysis integrated over full (W, Q^2) domain along with the exclusivity cut showing noticeable double-pion contamination within the cut range.	52
Figure 2.29: Example of background determination for the π^- analysis.	54
Figure 2.30: Example of background determination for the π^+ analysis.	55
Figure 2.31: Example of squared missing mass cut determination for both experiment yields and simulation in the π^- analysis for a single ($W, Q^2, \cos(\theta^*)$) bin. Background ratio is set at 5%.	56
Figure 2.32: Example of squared missing mass cut determination for both experiment yields and simulation in the π^+ analysis for a single ($W, Q^2, \cos(\theta^*)$) bin. Background ratio is set at 5%.	56
Figure 2.33: Comparison between simulated data with the 200 MeV spectator momentum cut and full simulation yields for the $\pi^- + p$ analysis.	58
Figure 2.34: Factor by which the signal can be reshaped to account for missing Fermi-smearing after applying a 200 MeV missing spectator momentum cut.	59

Figure 2.35: Comparison of squared missing mass distributions for Fermi-smearred yields, Fermi-smearred quasifree yields, and the adjusted-smearing signal distribution obtained from the background-subtracted π^- analysis. Since the signal shape matches the Fermi-smearred quasifree distribution after being adjusted for reduced Fermi-smearing due to the spectator momentum cut, all noticeable final state interactions have been removed via the background subtraction method.	60
Figure 2.36: π^+ final (W, Q^2) yields with binning superimposed.	60
Figure 2.37: π^- final (W, Q^2) yields with binning superimposed.	61
Figure 2.38: $\pi^- + p$ final (W, Q^2) yields with binning superimposed.	61
Figure 3.1: Bin-centering correction factor for selected bins for the $e^- + n \rightarrow e^- + p + \pi^-$ reaction channel.	63
Figure 3.2: Bin-centering correction factor for selected bins for the $e^- + p \rightarrow e^- + n + \pi^+$ reaction channel.	64
Figure 3.3: Example $\delta\theta_e$ distribution and fit for Sector 1, θ_e and ϕ_e	66
Figure 3.4: $\delta\theta_e$ versus. θ_e and ϕ_e with fits for Sector 1 and various θ_e or ϕ_e selections.	67
Figure 3.5: $g(\theta_e, \phi_e, s)$ fits versus θ and ϕ for Sector 1.	68
Figure 3.6: Comparison of the squared missing spectator mass with no kinematic corrections, just electron kinematic corrections, and both electron corrections and proton energy loss corrections applied for subset of $\pi^- + p$ analysis measured data.	69
Figure 3.7: π^+ analysis acceptance for selected bins along with binned acceptance values. $W = 1.25$ GeV, $Q^2 = 0.5$ GeV ² /c ² , $\cos(\theta^*) = 0.1$	75
Figure 3.8: π^- analysis acceptance for selected bins along with binned acceptance values. $W = 1.25$ GeV, $Q^2 = 0.5$ GeV ² /c ² , $\cos(\theta^*) = 0.1$	76
Figure 3.9: $\pi^- + p$ analysis acceptance for selected bins along with binned acceptance values. $W = 1.25$ GeV, $Q^2 = 0.5$ GeV ² /c ² , $\cos(\theta^*) = 0.1$	77
Figure 3.10: Comparison of electron vertex (x, y) distributions for experiment and simulation.	78

Figure 3.11: $e^- + n \rightarrow e^- + p + \pi^-$ channel radiative-effects correction for $W = 1.25$ GeV, $Q^2 = 0.5$ GeV ² , $\cos \theta^* = 0.1$ bin.	79
Figure 3.12: $e^- + p \rightarrow e^- + n + \pi^+$ channel radiative-effects correction for $W = 1.25$ GeV, $Q^2 = 0.5$ GeV ² , $\cos \theta^* = 0.1$ bin.	79
Figure 3.13: Comparison between filled-target and empty-target vertex z-coordinate distributions for the $\pi^- + p$ analysis. Note that the empty-target vertex data is shifted by -1.5 mm for full coincidence with filled-target data.	80
Figure 3.14: Comparison between filled-target and empty-target vertex z-coordinate distributions for the $\pi^- + p$ analysis, zoomed into the film target range. Note that the empty-target vertex data is shifted by -1.5 mm for full coincidence with filled-target data.	81
Figure 4.1: Flowchart of the needed Monte Carlo event generator modifications to include Fermi-motion of the target nucleon. Here a tilde denotes quantities being in the target-at-rest frame.	84
Figure 4.2: Comparison of missing spectator momentum between experiment and reconstructed simulation for the $\pi^- + p$ analysis using the CD-Bonn momentum distribution to generate Fermi-motion in the target. As can be seen, there is close agreement between experiment and reconstructed simulation below 200 MeV, at which point final state interactions become significant.	85
Figure 4.3: Comparison of target mass assumptions via resulting W distributions. The first treatment is the nucleon on-mass shell, the second is the nucleon rest mass plus the (negative) binding energy, and the third treatment is assigning exactly half of the virtuality $V = m_d - (m_t + K_t + m_s + K_s)$ to each nucleon, where m_s and K_s are the mass and kinetic energy of the spectator particle, respectively.	87
Figure 4.4: Plot of $\chi^2(a, b)$ along with the intuitive compromise, showing a trough of optimal treatments in the simple model and the compromise lying in the trough.	90
Figure 4.5: Fermi-unsmearing correction factor for π^- and π^+ analyses for $W = 1.25$ GeV, $Q^2 = 0.5$ GeV ² , $\cos \theta^* = 0.1$ bin along with binned values of the correction factor.	91

Figure 4.6: Comparison between π^- and $\pi^- + p$ cross-section estimates in select bins. $\pi^- + p$ results are taken from [1]. As illustrated here, the Fermi-unsmeared cross-sections are generally in agreement with the results from [1] with additional coverage of the cross-section. Note that the error bars are a combination of statistical and systematic uncertainties which are developed in Section 5.5.	92
Figure 4.7: Examples of Γ_ν variation per event in comparison with the principle value from the kinematic bin.	93
Figure 4.8: Examples of ϵ variation per event in comparison with the principle value from the kinematic bin.	94
Figure 5.1: Comparison between MAID2000, π^- , and $\pi^- + p$ cross-sections for selected bins, with combined statistical and systematic uncertainties for each point.	96
Figure 5.2: Comparison between MAID2000, π^- , and $\pi^- + p$ cross-sections for selected bins, with combined statistical and systematic uncertainties for each point.	97
Figure 5.3: Comparison between MAID2000, π^- , and $\pi^- + p$ cross-sections for selected bins, with combined statistical and systematic uncertainties for each point.	98
Figure 5.4: Comparison between MAID2000, π^- , and $\pi^- + p$ cross-sections for selected bins, with combined statistical and systematic uncertainties for each point.	99
Figure 5.5: Comparison between MAID2000, π^- , and $\pi^- + p$ cross-sections for selected bins, with combined statistical and systematic uncertainties for each point.	100
Figure 5.6: Comparison between MAID2000, π^- , and $\pi^- + p$ cross-sections for selected bins, with combined statistical and systematic uncertainties for each point.	101
Figure 5.7: Comparison between MAID2000, π^- , and $\pi^- + p$ cross-sections for selected bins, with combined statistical and systematic uncertainties for each point.	102
Figure 5.8: Comparison between π^+ cross-section and MAID2000 for selected bins, with combined statistical and systematic uncertainties for each point.	103
Figure 5.9: Comparison between π^+ cross-section and MAID2000 for selected bins, with combined statistical and systematic uncertainties for each point.	104

Figure 5.10: Comparison between π^+ cross-section and MAID2000 for selected bins, with combined statistical and systematic uncertainties for each point.	105
Figure 5.11: Comparison between π^+ cross-section and MAID2000 for selected bins, with combined statistical and systematic uncertainties for each point.	106
Figure 5.12: Comparison between π^+ cross-section and MAID2000 for selected bins, with combined statistical and systematic uncertainties for each point.	107
Figure 5.13: Comparison between π^+ cross-section and MAID2000 for selected bins, with combined statistical and systematic uncertainties for each point.	108
Figure 5.14: Comparison between π^+ cross-section and MAID2000 for selected bins, with combined statistical and systematic uncertainties for each point.	109
Figure 5.15: $\pi^- \sigma_T + \epsilon\sigma_L$ Legendre fits for selected (W, Q^2) bins for both ordinary and non-negative cosine fits. As can be seen, occasionally there is a difference between ordinary and constrained non-negative fit results.	111
Figure 5.16: $\pi^- \sigma_{LT}$ Legendre fits for selected (W, Q^2) bins for both ordinary and non-negative cosine fits. As can be seen, occasionally there is a difference between ordinary and constrained non-negative fit results.	112
Figure 5.17: $\pi^- \sigma_{TT}$ Legendre fits for selected (W, Q^2) bins for both ordinary and non-negative cosine fits. As can be seen, occasionally there is a difference between ordinary and constrained non-negative fit results.	113
Figure 5.18: $\pi^+ \sigma_T + \epsilon\sigma_L$ Legendre fits for selected (W, Q^2) bins for both ordinary and non-negative cosine fits. As can be seen, occasionally there is a difference between ordinary and constrained non-negative fit results.	114
Figure 5.19: $\pi^+ \sigma_{LT}$ Legendre fits for selected (W, Q^2) bins for both ordinary and non-negative cosine fits. As can be seen, occasionally there is a difference between ordinary and constrained non-negative fit results.	115
Figure 5.20: $\pi^+ \sigma_{TT}$ Legendre fits for selected (W, Q^2) bins for both ordinary and non-negative cosine fits. As can be seen, occasionally there is a difference between ordinary and constrained non-negative fit results.	116

Figure 5.21: Example of ordinary least-squares fitting of cross-section data using a cosine series along with a non-negative constrained fit.	117
Figure 6.1: Target graph for simple example.	136

CHAPTER 1

INTRODUCTION

Scattering experiments have been part of nuclear and particle physics experimental methodology for decades and for a good reason: They provide a large amount of data which is directly useful for calculating a variety of meaningful quantities, including scattering cross-sections. As the science progresses, a positive feedback loop between experimental design and theoretical knowledge has been spiraling forward in time, with each new measurement leading to improved theoretical understanding, which enables improvements to future experiments. In the context of the standard model, the strong nuclear interaction's fundamental quantum field theory, quantum chromodynamics (QCD), poses a distinct challenge in comparison to the electroweak interaction due to the presence of a non-perturbative regime. Without presently being able to rigorously calculate QCD's description of nature wherever it is desired, research of the strong force proceeds via attempting a combination of reaction models, Dyson-Schwinger equations (DSEs), and numerical approaches such as lattice QCD (LQCD), all of which are tested or aided by empirical data.

This work presents fully-differential cross-sections for two electroproduction reaction channels along with a method for extracting more cross-section data from existing collected particle accelerator data: Fermi-unsmearing.

1.1 MOTIVATION FOR RESEARCH

Physics as a domain of knowledge has been carried a long way on the shoulders of many giants. Newton's paradigm of the universe made of objects and forces acting on those objects led to a more detailed understanding, which included the fields giving

rise to forces and their intricate mathematical structure through the work of Faraday and Maxwell. Einstein's utilization of Lorentz's transformation of the Maxwell equations so as to produce the special theory of relativity would both further generalize into the geometric approach of the general theory of relativity as well as constrain the theory birthed by Planck, Pauli, Heisenberg, de Broglie, Born, Schrödinger, and Dirac, quantum mechanics. Quantum mechanics was carried forward into the beginnings of quantum electrodynamics (QED) by Dirac, and with the contributions of Jordan, Wigner, and Fermi, it became clear that field phenomena could explain particles themselves in addition to interactions between them. Ingenious mathematical techniques of renormalization developed by Stueckelberg, Schwinger, Dyson, Feynman, and Tomonaga with refined formalization by Bogoliubov and Shirkov would sweep the minefield of infinities that was encountered in promoting quantum mechanics to a relativistic field theory. In the parallel trajectory of experimental physics, Pierre and Marie Curie, Becquerel, Rutherford, Chadwick, Thompson, Geiger, and Marsden demonstrated that the nuclei of atoms are in fact made of protons and neutrons. This trajectory of discovering smaller building blocks of matter continued with the advent of bubble chambers, particle accelerators, and the consequent discovery of a zoo of particles arranged in an ordered structure that, in addition to the revelation through deep-inelastic scattering experiments at Stanford that protons are composed of smaller point-like objects, set the stage for the parton models of Bjorken, Paschos, and Feynman, which then gave way to the theory of quarks and their color charge developed Gell-Mann, Zweig, Greenberg, Han, and Nambu, manifesting as a Yang-Mills theory of the strong nuclear force mediated by the octet of gluons, quantum chromodynamics.

In an analogous way as to how the electron energy level spectra in atoms is due to the quantum nature of the electromagnetic interaction described by QED, the zoo of particles is due to a similar spectrum of excited energy levels due to the quantum

nature of the strong nuclear force, at least insofar as QCD has been verified against empirical data. This is not to suggest that QCD is somehow characteristically devoid of verification, as decades of experiments have confirmed many features predicted by QCD. For a broad survey of such tests as well as a thorough primer on QCD generally, see [2]. To briefly summarize the current state of QCD, the QCD Lagrangian is hoped to fully encode all of the structure of the strong interaction in its formula,

$$\mathcal{L} = \bar{\psi}_q^j (i\gamma^\mu) (D_\mu)_{jk} \psi_q^k - m_q \bar{\psi}_q^j \psi_{qj} - \frac{1}{4} F_{\mu\nu}^a F^{a\mu\nu}, \quad (1.1)$$

where ψ_q^j is the quark field with threefold color index j , γ^μ are the Dirac matrices, m_q are the (bare) quark masses, $F_{\mu\nu}^a$ is the gluon field strength tensor with eightfold adjoint color index a , and D_μ is the covariant derivative

$$(D_\mu)_{jk} = \delta_{jk} \partial_\mu - i g_s t_{jk}^a A_\mu^a,$$

where g_s is the scaled strong coupling such that

$$g_s^2 = 4\pi\alpha_s,$$

A_μ^a is the gluon field with eightfold adjoint color index a , and

$$t_{jk}^a = \frac{1}{2} \lambda_{jk}^a,$$

λ^a being the eight Gell-Mann matrices of SU(3) [3]. The gluon field strength tensor $F_{\mu\nu}^a$ is directly related to the gluon field A_μ^a via

$$F_{\mu\nu}^a = \partial_\mu A_\nu^a - \partial_\nu A_\mu^a + g_s f^{abc} A_\mu^b A_\nu^c$$

with $[A, B] = AB - BA$ denoting commutation and f^{abc} being the structure constants of the SU(3) color group, so that

$$f^{123} = 1,$$

$$f^{147} = f^{246} = f^{257} = f^{345} = \frac{1}{2},$$

$$f^{156} = f^{367} = -\frac{1}{2},$$

and

$$f^{458} = f^{678} = \frac{\sqrt{3}}{2},$$

with f^{abc} being fully antisymmetric in all indices and all other $f^{abc} = 0$. Two key features are known to be encoded in this Lagrangian, asymptotic freedom and dynamical chiral symmetry breaking, with quark confinement being a conjectured, but not yet proven, third property of QCD.

The asymptotic freedom of QCD is due to the strong coupling α_s being a function of Q^2 . For perturbative QCD,

$$\alpha_s(Q^2) = \frac{1}{b_0 \log \frac{Q^2}{\Lambda^2}}, \quad (1.2)$$

where

$$\Lambda \approx 200 \text{ MeV} \quad (1.3)$$

is the cut-off known as the Landau pole and b_0 is the 1-loop coefficient [4] [3]. As a consequence, the running coupling effectively decreases as Q^2 increases, which is the origin of the term “asymptotic freedom” since quarks can be considered free in the limit of $Q^2 \rightarrow \infty$. As can be seen, the coupling diverges as $Q^2 \rightarrow \Lambda^2$, signaling the limit of what can be known through perturbative QCD and the need for alternative methodologies described shortly.

Dynamical chiral symmetry breaking is a specific form of spontaneous symmetry breaking present in QCD. It leads to the generation of mass in bound nucleon states, to the degree that the bare quark masses account for only about 1% of the proton mass as an example. As a consequence of this dynamical chiral symmetry breaking, the vast majority of the observed mass of atomic matter is due to this spontaneous symmetry breaking in QCD [5].

The conjectured feature of QCD, quark confinement, is something indirectly observed empirically through the lack of any observations of free quarks in nature despite not being derived directly from QCD. There are intuitive reasons to believe that it should derive from QCD, such as the functional form of the running coupling $\alpha_s(Q^2)$, but so far a rigorous proof of quark confinement remains to be discovered. If quark confinement is indeed a real feature of QCD, then one of the chief implications for research of QCD is that only bound quark states are available for study. This adds complexity to the study of the strong interaction which is not present in the study of other fundamental interactions since their fundamental particles can be isolated and studied separately from each other, with electrons as an example from the electromagnetic interaction. Due to asymptotic freedom, it is possible through deep-inelastic scattering to study quarks with increased isolation, but in doing so the permitted Q^2 domain is reduced to an extremity. In order to understand the strong interaction anywhere away from the $Q^2 \rightarrow \infty$ asymptote, the growing complexity of bound quark states is unavoidable.

In parallel to the complication caused by confinement, there is the problem of the non-perturbative regime of QCD. As stated previously, QCD poses distinct challenges beyond QED in that the coupling for QCD can cause perturbation theory to fail through divergent sums [3], which divides QCD into perturbative and non-perturbative regimes. Perturbative QCD has been examined and tested in detail and to great precision, especially through experiments at CERN such as the Large

Electron-Positron Collider (LEP). In contrast, non-perturbative QCD can only be explored at present through one of three approaches,

- Lattice QCD [6],
- Dyson-Schwinger Equations [7], or
- Models with effective degrees of freedom, such as constituent quark models [8], MIT-bag models [9], and Nambu-Jona-Lasinio (NJL) models [10].

Lattice QCD is a numerical approach to QCD computation, proceeding by placing spacetime onto a finite, discrete grid and essentially transforming infinite computations into finite approximations that can in principle be made accurate to arbitrary precision given a small enough spacetime grid spacing a . The limiting factor for LQCD is computing power, the demand for which increases dramatically as the grid spacing is reduced and as the various mass parameters supplied to LQCD are brought closer to their true values.

Dyson-Schwinger equations are infinite coupled integral equations, a famous example being the Bethe-Salpeter equation. DSEs provide a method for examining continuous QCD, a complement to the discrete analysis possible with LQCD, with the caveat that some model assumptions must be made in posing the DSEs. For a useful summary of DSE research methodology and recent results, see [7], [11], and [12].

In contrast to the above two methods of examining QCD, it is possible to explore QCD through the use of models having effective degrees of freedom. These models can provide methods to test non-perturbative QCD through a kind of effective limit of QCD; for example, the constituent quark model can be seen as a limit of non-perturbative QCD where the fully dressed quark behavior dominates [8]. In this approach, good agreement between model and data suggests that the QCD feature selected by the model is a dominant component of the strong interaction in the selected domain.

Due to the previously mentioned difficulties in studying QCD, especially in the non-perturbative regime, the choice of observations by which to test and examine QCD is limited, but asymmetries and scattering cross-sections are measurements which can be obtained for the purpose of further analyses, such as the extraction of N-N* transition form factors, which provide a unique opportunity to test the Q^2 dependence of the strong interaction in colorless three-quark systems along a continuous domain from low Q^2 (non-perturbative QCD) to high Q^2 (perturbative QCD). As noted by [1], the available cross-section data from which the N-N* transition form factors can be extracted for single-pion electroproduction off the bound neutron in deuterium is sparse. Stated briefly, as this work applies the new method of Fermi-unsmearing, more of the $e^- + n \rightarrow e^- + p + \pi^-$ cross-section has been extracted, and additionally the bound proton in deuterium's reaction $e^- + p \rightarrow e^- + n + \pi^+$ can be extracted without Fermi-smearing due to applying Fermi-unsmearing to that analysis as well.

1.2 REACTION CHANNELS OF INTEREST

The principle reaction channel of interest is $e^- + p \rightarrow e^- + n + \pi^+$ where the proton is bound in a deuterium atom. Being bound in deuterium, the proton is in a constant state of motion called Fermi-motion as exemplified in Figure 1.1, and because of the low efficiency of detecting neutrons in the CLAS detector (described later), it is not possible to directly detect and reconstruct trajectories of neutrons in the final state of the reaction with sufficient statistics for cross-section extraction. One way this could be addressed is through a compromise. If the target nucleon is assumed to be at rest, then the cross-section can be measured, but now suffers from the effect known as Fermi-smearing. Figure 1.2 shows an example of Fermi-smearing for the sister channel of the principle channel, $e^- + n \rightarrow e^- + p + \pi^-$ for the neutron in deuterium, which is the other reaction channel of interest for this work. For brevity, these channels will often be referred to by just their pion, i.e. the π^- channel and the

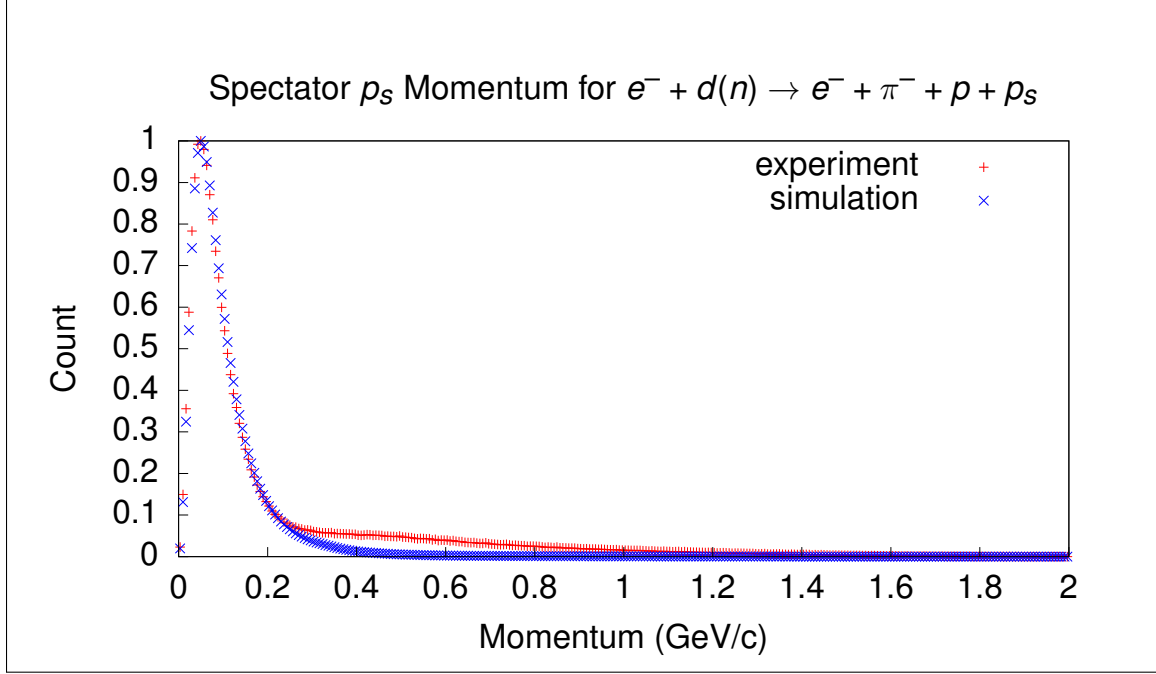


Figure 1.1: Example of missing spectator momentum for $e^- + d \rightarrow e^- + \pi^- + p + p_s$ reaction channel, which for quasifree reactions is the distribution of the spectator nucleon momentum in Fermi-motion with additional final state interactions distorting the high-momentum tail of the distribution if the quasifree reaction cannot be isolated as shown in [1].

π^+ channel. For the π^- reaction channel, all of the final state particles are charged, and the CLAS detector has high enough coverage and efficiencies that a substantial amount of the cross-section can be measured via an analysis that uses reconstructed tracks for all but the leftover nucleon from the deuteron, which is referred to here as an exclusive analysis. The final state baryon can optionally be ignored when analyzing data for this sister channel, which allows not only a detailed examination of the effects of Fermi-smearing on the cross-section, but also allows testing of methods for removing this effect. As will be shown later, ignoring the final state baryon and using Fermi-unsmearing results in equivalent cross-section measurements wherever the all-particles-detected analysis produces a result, and in addition extends the domain of the measured cross-section to previously unmeasured regions, so that it is a direct improvement in measurement technique.

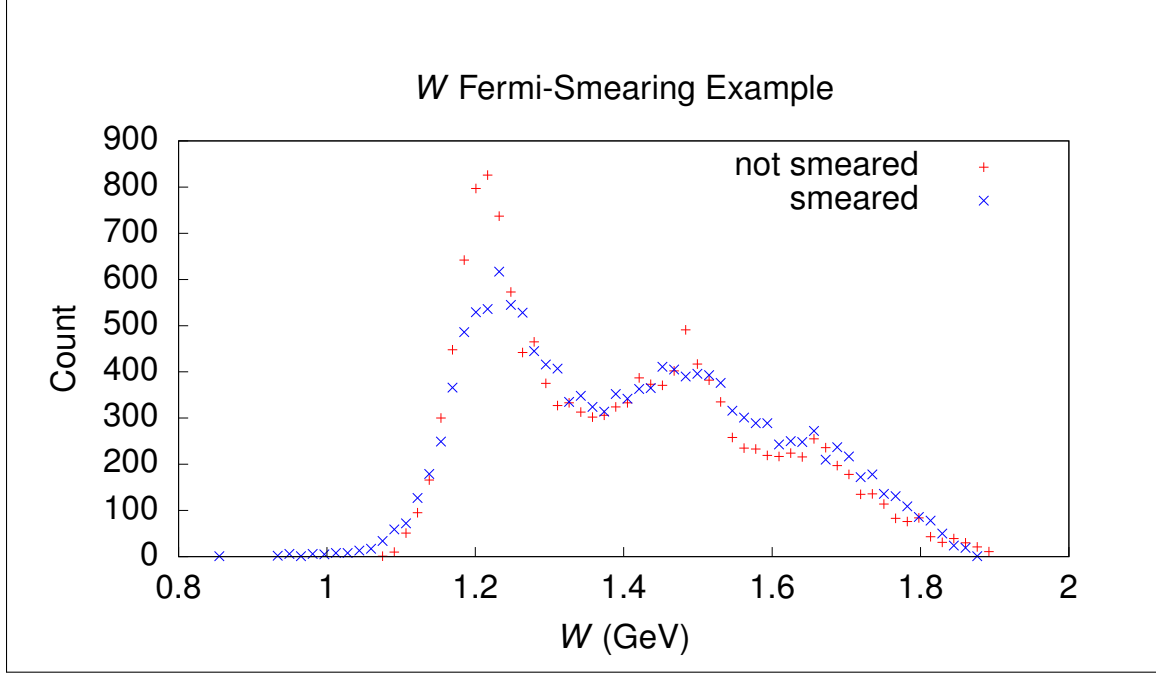


Figure 1.2: Demonstration of the Fermi-smearing effect on the center of mass energy W (defined later) for experiment yields from two different analyses of the reaction channel $e^- + n \rightarrow e^- + p + \pi^-$, one Fermi-smeared and one fully exclusive.

As there are three analyses being considered in parallel, abbreviations are beneficial. Using parentheses to denote particles that are not reconstructed, the abbreviations for the three different analyses are

- π^+ for the $e^- + p \rightarrow e^- + (n) + \pi^+$ analysis,
- π^- for the $e^- + n \rightarrow e^- + (p) + \pi^-$ analysis, and
- $\pi^- + p$ for the $e^- + n \rightarrow e^- + p + \pi^-$ analysis.

These abbreviations are used in multiple places in this work without redundant definition. Here the parentheses denote particles whose tracks are not reconstructed or at least not used for calculations. Note that when comparing cross-section results, the $\pi^- + p$ analysis refers to the results from [1], although some histograms and diagnostic plots have been generated from a new $\pi^- + p$ analysis in this work, whereas the π^+

and π^- analyses yield new cross-section results which also demonstrate the viability of the Fermi-unsmeared method developed later.

1.3 MATHEMATICAL FOUNDATIONS AND NOTATION

Lorentz vectors, also referred to as four-vectors due to the number of dimensions of relativistic spacetime, are a fundamental mathematical tool to better understand scattering events and for extracting useful information from them. The conservation of energy and momentum demands that the energy-momentum Lorentz vector of the initial state of a reaction must be the same as that of the final state. For the principle reaction channel of interest, the conservation of energy and momentum constraint can be expressed by

$$e_\mu + n_\mu = e'_\mu + p_\mu + \pi_\mu^-, \quad (1.4)$$

using the long-standing convention of subscripts representing covariant vector components and superscripts for contravariant components. Minkowski inner products are

$$x^\mu y_\mu.$$

For the special case of the squared Minkowski norm $x^\mu x_\mu$, this can also be denoted by

$$x^2$$

with the Minkowski norm given by

$$|x| = \sqrt{x^\mu x_\mu}.$$

The energy component of a Lorentz vector is by convention made to be the zeroth component, and the three momentum/spatial components are denoted as vector by

placing an arrow marking over the variable name as in

$$\vec{x}.$$

For brevity, units are chosen such that the speed of light $c = 1$, so that a particle with energy E and momentum vector \vec{p} would have a covariant energy-momentum Lorentz vector of

$$p_\mu = (E, -\vec{p}) = (E, -p_x, -p_y, -p_z).$$

Inner products between momentum/spatial vectors are denoted with the \cdot notation:

$$\vec{x} \cdot \vec{y},$$

and similarly their squared Euclidean norm and the norm itself can be written as

$$\vec{x}^2$$

and

$$|\vec{x}|.$$

Whenever the reference frame is not specified or denoted, it should be assumed to be in the laboratory at rest frame. However, for clarity, it may also be denoted with the \diamond symbol, such as

$$x_\mu^\diamond,$$

so that the momentum/spatial vector in the lab frame would be written as

$$\vec{x}^\diamond.$$

Lorentz vectors in the center of momentum (COM) reference frame can be denoted by adding a * marker like so:

$$x_{\mu}^*$$

or

$$\vec{x}^*.$$

For reasons that will be clear later, another convention is needed to denote the reference frame where the target is at rest, which is not necessarily the same as the laboratory rest frame. This is denoted by the \oplus symbol, leading to

$$x_{\mu}^{\oplus}$$

or

$$\vec{x}^{\oplus}.$$

Considering the degrees of freedom for the two reaction channels of interest, if the target and beam Lorentz vectors are both known, then there are 3 unknown Lorentz vectors in the final state, each with 3 unknown components since the masses are fixed. The energy-momentum conservation constraint places 4 constraints on these 9 degrees, and due to the fact that neither the target nor beam are polarized in the data used in this work, each reaction is physically equivalent to any rotation of the same reaction around the beam axis, and therefore one of the remaining degrees of freedom is irrelevant, which leaves exactly 4 degrees of freedom for these channels. In this work, the 4 variables chosen are W , Q^2 , $\cos(\theta^*)$, and ϕ^* , all of which are defined below.

Since the two channels are so similar and have the same degrees of freedom, the following channel-agnostic Lorentz vector notation is introduced:

- e_μ denotes the beam electron,
- e'_μ denotes the scattered electron,
- t_μ denotes the target (either a proton or neutron),
- b_μ denotes the final state baryon (either a neutron or proton), and
- π_μ denotes the final state pion (either a π^+ or π^-).

The degrees of freedom are then defined as:

$$W = |q_\mu + t_\mu| = |b_\mu + \pi_\mu|, \quad (1.5)$$

$$Q^2 = -q^2, \quad (1.6)$$

$$\cos(\theta^*) = \frac{\vec{\pi}^* \cdot \hat{z}}{|\vec{\pi}^*|}, \quad (1.7)$$

and

$$\phi^* = \tan^{-1}(\hat{y} \cdot \vec{b}^*, \hat{x} \cdot \vec{b}^*), \quad (1.8)$$

where

$$q_\mu = e_\mu - e'_\mu, \quad (1.9)$$

$$\hat{z} = \frac{\vec{q}^*}{|\vec{q}^*|},$$

$$\hat{y} = \frac{\vec{e}^* \times \vec{e}'^*}{|\vec{e}^* \times \vec{e}'^*|},$$

and

$$\hat{x} = \hat{y} \times \hat{z},$$

where $\tan^{-1}(y, x)$ returns the polar coordinate angle given the x and y Cartesian coordinates of a point. The relationships between these angles and momentum vectors are illustrated in Figure 1.3.

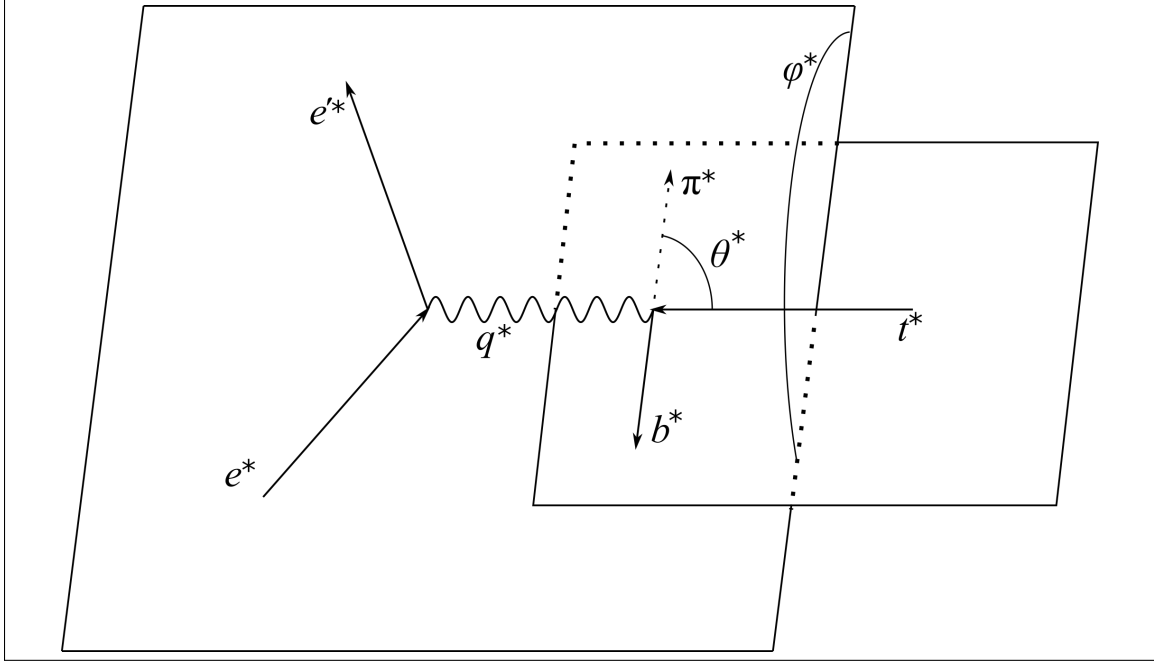


Figure 1.3: Illustration of angles and momentum vectors for particles involved in a single pion electroproduction reaction in the center of momentum frame. The same labels for particle momenta are used as specified earlier.

Once histograms have been gathered for data set of choice parametrized by the four degrees of freedom, they are used to calculate estimates of the scattering cross-sections,

$$\frac{d^4\sigma}{dW dQ^2 d\Omega^*} = L^{-1} \frac{N(W, Q^2, \cos(\theta^*), \phi^*)}{\Delta W \Delta Q^2 \Delta \cos(\theta^*) \Delta \phi^*}, \quad (1.10)$$

where $N(W, Q^2, \cos(\theta^*), \phi^*)$ is the true number of observed events within a given $(W, Q^2, \cos(\theta^*), \phi^*)$ bin, $\Delta W \Delta Q^2 \Delta \cos(\theta^*) \Delta \phi^*$ is the 4-D bin volume, and L is the luminosity given by

$$L = N_e \rho l, \quad (1.11)$$

where N_e is the number of incident electrons, ρ is the number concentration (not mass concentration) of target particles within the CLAS target, and l is the length of the CLAS target. As will be made clear in the subsequent chapters, there are many selection criteria to apply and effects to correct in the raw histograms calculated from

experiment data sets, so that the cross-section can be expressed as

$$\frac{d^4\sigma}{dWdQ^2d\Omega^*} = F(W, Q^2, \cos(\theta^*), \phi^*) L^{-1} \frac{\tilde{N}(W, Q^2, \cos(\theta^*), \phi^*)}{\Delta W \Delta Q^2 \Delta \cos(\theta^*) \Delta \phi^*}, \quad (1.12)$$

where $F(W, Q^2, \cos(\theta^*), \phi^*)$ encapsulates all correction factors applied to measured yields and $\tilde{N}(W, Q^2, \cos(\theta^*), \phi^*)$ is the raw measured yield for a given bin.

Using the results of the single photon approximation as summarized in [13], these estimated scattering cross-sections can be separated into leptonic and hadronic components:

$$\frac{d^4\sigma}{dWdQ^2d\Omega^*} = \Gamma_\nu \frac{d^2\sigma_\nu}{d\Omega^*}(W, Q^2), \quad (1.13)$$

where

$$\Gamma_\nu = \frac{\alpha}{4\pi Q^2} \frac{W}{E^{\oplus 2} M_t^2} \frac{W^2 - M_t^2}{1 - \epsilon}, \quad (1.14)$$

$$\epsilon = \left(1 + 2 \left(1 + \frac{\nu^{\oplus 2}}{Q^2} \right) \tan^2 \left(\frac{\theta_e^\oplus}{2} \right) \right)^{-1}, \quad (1.15)$$

$$E^\oplus = e_0^\oplus,$$

$$\nu^\oplus = q_0^\oplus,$$

and

$$\theta_e^\oplus = \cos^{-1} \left(\frac{\vec{e}'^\oplus \cdot \vec{e}^\oplus}{|\vec{e}'^\oplus| |\vec{e}^\oplus|} \right),$$

where M_t is the target rest mass and $d\Omega^* = d\cos(\theta^*)d\phi^*$. The hadronic cross-section can be further expanded as in [13],

$$\frac{d^2\sigma_\nu}{d\Omega_\pi^*} = \sigma_T + \epsilon\sigma_L + \epsilon\sigma_{TT} \cos(2\phi_\pi^*) + \sqrt{2\epsilon(1+\epsilon)}\sigma_{LT} \cos(\phi_\pi^*), \quad (1.16)$$

where σ_T , σ_L , σ_{TT} , and σ_{LT} are the structure functions dependent on W , Q^2 , and θ_π^* for an unpolarized electron beam. Due to the fact that the beam energy in the target-at-rest frame fluctuates around the experiment beam energy, the structure functions

are extracted by taking values of these terms averaged over the experimentally observed target-at-rest frame beam energy. As shown in Chapter 4, for many bins the average value does not differ significantly from the principle value, but for a select few bins there is a substantial difference, and in general the mean ϵ values for experiment yields are higher than the principle values.

1.4 EXPERIMENTAL APPARATUS

The Thomas Jefferson National Laboratory is the home of CEBAF, the Continuous Electron Beam Accelerator Facility, and currently operates with four halls which can each accept beam activity from CEBAF named A, B, C, and D. Hall B housed CLAS [14], the CEBAF Large Acceptance Spectrometer, which was used to collect the source data for this work and was designed to support the old maximum beam energy of 6 GeV, and now houses CLAS12, the upgraded CLAS detector to support a 12 GeV maximum beam energy of CEBAF. As part of my own service work with the laboratory while researching the contents of this thesis, I participated in building and assessing the performance of FTOF12, the time of flight system for CLAS12. Figures 1.4 through 1.7 show the CLAS design schematic, the CLAS detector as it used to be situated in Hall B, the CLAS12 design schematic, and the FTOF12 situated in Hall B before the rest of the detector components were installed.

CLAS is made of various subsystems which detect and measure particle attributes so that scattering cross-sections can be measured for a variety of reactions over large domains of their dependent variables. The research in this work is concerned with electron scattering experiments so the subsystems concerned with photon scattering are not addressed directly. As described thoroughly in [14], these CLAS subsystems are:

- SC or Time of Flight [15],
- DC or Drift Chambers [16],

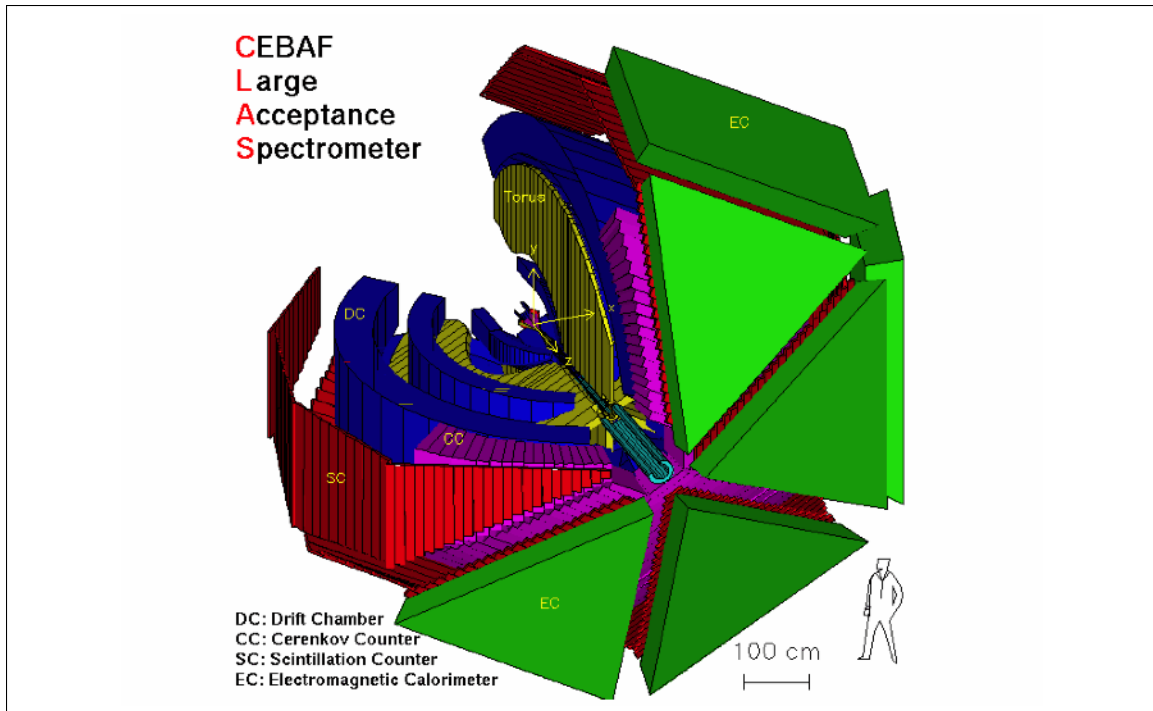


Figure 1.4: CLAS design schematic.

- CC or Cherenkov Counters [17], and
- EC or Electromagnetic Calorimeter [18].

DC provides both a measurement of particle momentum and flight path length, and given that knowledge SC can be used to estimate particle velocity. CC provides a good distinction between electrons and other particles such as pions, and EC provides another mechanism for distinction between electrons and other particles like pions through measuring the electromagnetic shower energy deposited by particles passing through the EC.

1.5 COMPUTING TOOLS

Thomas Jefferson National Laboratory has a computing cluster of thousands of nodes with petabytes of hard drive and magnetic tape storage accessible to them along with software libraries designed to process data collected from each of the beam destination halls. The raw data collected by the data acquisition systems in Hall B are first

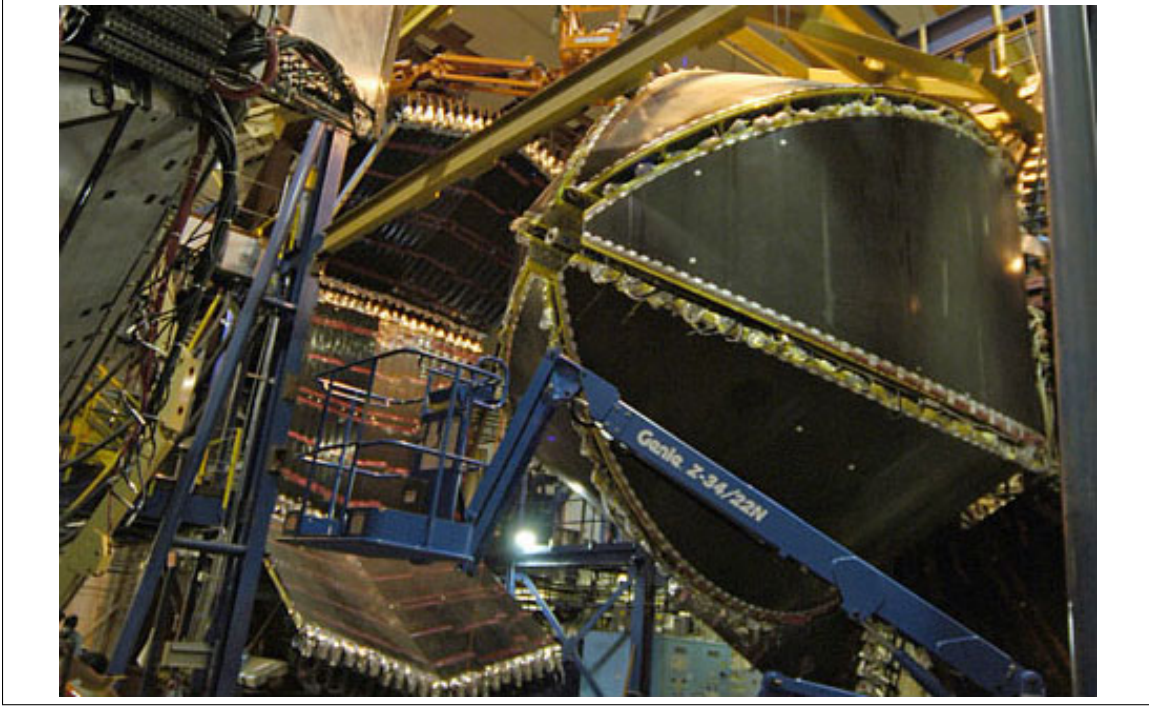


Figure 1.5: CLAS as it used to be situated in Hall B.

processed by the so-called cooking software that infers particle trajectories, deposited energies, and other physically meaningful information from the raw hardware signals. Once data has been cooked, the physically meaningful information is usually analyzed by C++ programs utilizing CERN's ROOT physics data analysis library [19] that are executed on the computing cluster. For my case, I developed a Common Lisp software library that generates C++ programs for the sake of more efficient use of both programming time and program execution time named cl-ana [20]. The end result is a software library that mixes Lisp and C++ code generated based on a set of defined computation goals or targets that are computed on-demand when they need to be updated, similar to how GNU Make or a spreadsheet program will recompute targets or cells automatically. These generated programs are compiled and submitted to the computing cluster and managed so that failed jobs are repaired and resubmitted automatically, along with result downloading automation.

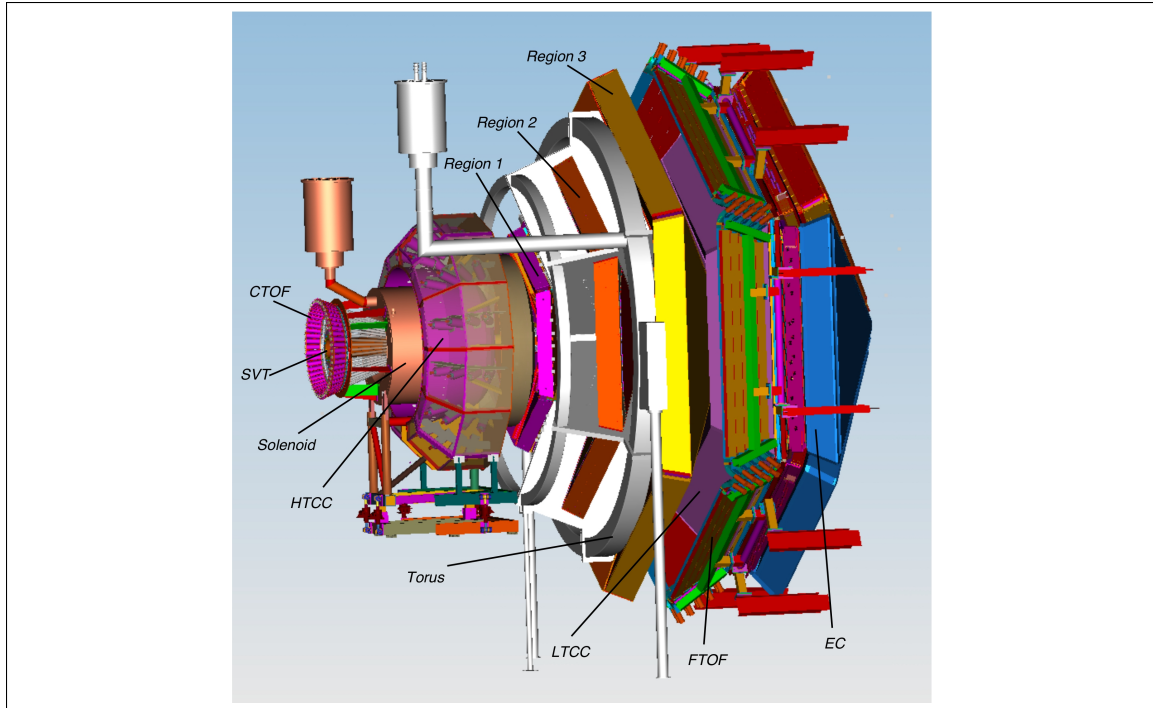


Figure 1.6: CLAS12 design schematic.

Monte Carlo simulations are needed to calculate the acceptance correction factors for each set of selected experiment data. To this end, GEANT [21] supplies the post-reaction physics simulation foundation, given models of the CLAS detector available on the JLAB computing cluster. The `gsim.bat` program is already available through the JLAB SVN repository and allows the user to select an experiment by an identifier, so that `gsim.bat` selects the appropriate parameters to GEANT from MySQL databases. The `gpp` program, also in the JLAB SVN repository, applies effects to simulated event data that are not handled by GEANT through `gsim.bat`. To compute the Fermi-unsmearing factors, the single-pion event generation programs `aao` and `aao_rad`, already available in the JLAB SVN repository, were combined and modified in a new program called `onepigen` [22] to allow both Fermi-motion and radiative effects to be enabled or disabled through input parameters. Being a derivative of the `aao` and `aao_rad` programs, `onepigen` supports the MAID98, MAID2000, and

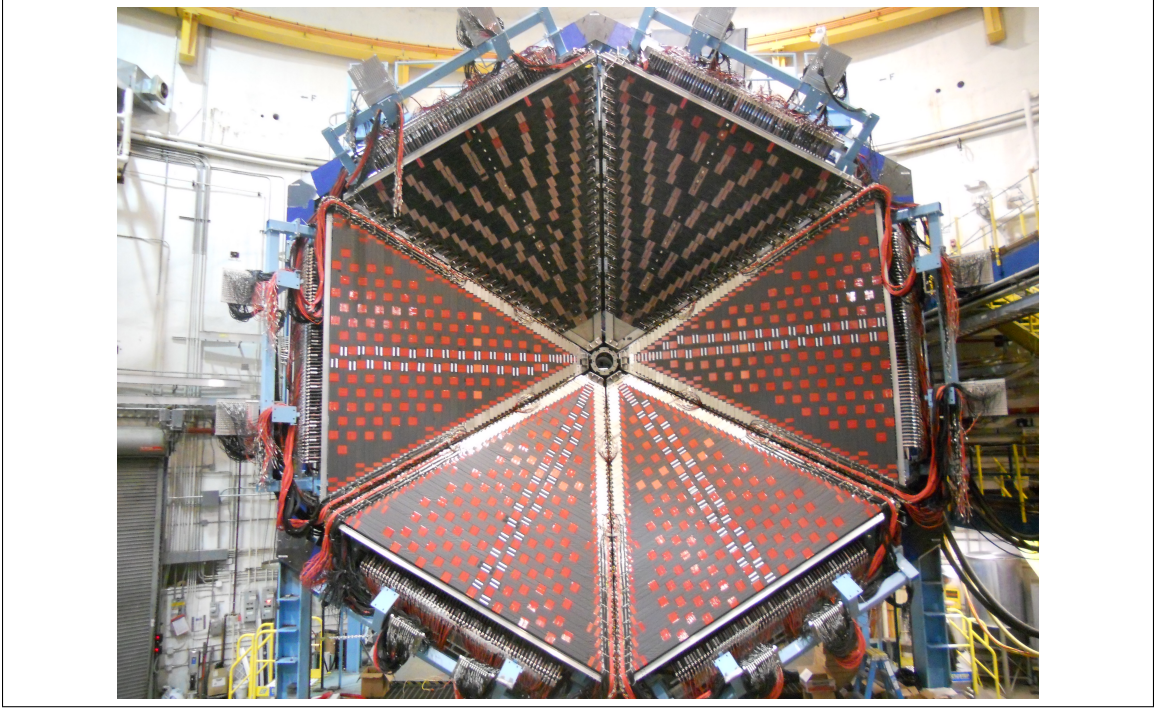


Figure 1.7: FTOF12 installation picture during CLAS12 upgrade.

MAID2003 cross-section models [23], with a separate version that supports MAID2007 also available.

CHAPTER 2

DATA SELECTION

The overarching goal for selecting data is to maximize signal while minimizing background. Of course, this is not a definite process so long as there isn't an explicit figure of merit which encompasses every possible kind of signal and error along with every possible background and their potential errors in measurement, and at present this is infeasible to say the least. The best that can be done is to make use of heuristics which are based on sound principles. In this case, one sound principle provides a framework for regulating data selection criteria: Avoid redundant criteria. To tell whether a criterion is redundant, it suffices to apply that criterion in the context of already established criteria and to observe the effects of that added criterion on the final computation goals, such as the cross-section estimate. So long as that criterion does not significantly improve the estimate at a reasonable cost in terms of overall uncertainty, the criterion is redundant and can be ignored without negatively affecting the estimate. Note that even if one selection criterion is determined to be redundant in the context of a single analysis, this does not generalize to other analyses, as each data set is peculiar and different criteria may be useful for different data sets and goals.

This chapter describes the collection of different techniques used to select final data sets used to estimate scattering cross-sections for the reaction channels analyzed, both for experiment data and for Monte Carlo simulations. Wherever there is a necessary difference between the treatment of experiment and simulated data, the difference and rationale for that difference are explained or referenced. Since the same reaction channel can be analyzed differently depending on what final state particles

are reconstructed, not all techniques are applied to all cross-section estimates. For reference, Appendix B.7.2 summarizes which techniques and selection criteria are used for each treatment of each set of data used in this work.

2.1 RUN SELECTION

Throughout the course of data acquisition via the CLAS detector, various conditions of the experiment can fluctuate. Most of the quality control has been guaranteed by engineers and technicians at JLAB through maintaining the beam and experiment hall equipment, but there remains fluctuations of beam current and detector operation within a given run period. As the data for each run are broken into smaller files, the approach taken in this analysis is to identify files which have insignificant fluctuations for extracting cross-section estimates. The run-level version of this has been called the golden run list, and so this file-based method is here referred to as the golden file list.

The test for whether a file belongs in the golden run list is having a normal event rate, where “normal” is defined by demanding a more or less Gaussian distribution of event rates and selecting files with event rates within $\pm 3\sigma$ of the mean observed event rate. The event rate is defined as

$$r_{\text{event}} = \frac{N_{\text{events}}}{Q_{\text{Faraday}}}, \quad (2.1)$$

where N_{events} is the number of reconstructed events present in the file and Q_{Faraday} is the integrated Faraday cup charge, a measure of the amount of beam delivered to Hall B during the time that the file’s data was observed. Figure 2.1 shows both the binned event rates and a scatter plot of event rate versus file index along with $\pm 3\sigma$ cut lines depicting which files are included in or excluded from the golden file list. The same golden file list is used for both the π^- and π^+ analyses as well as for determining the luminosity as per Equation 1.11.

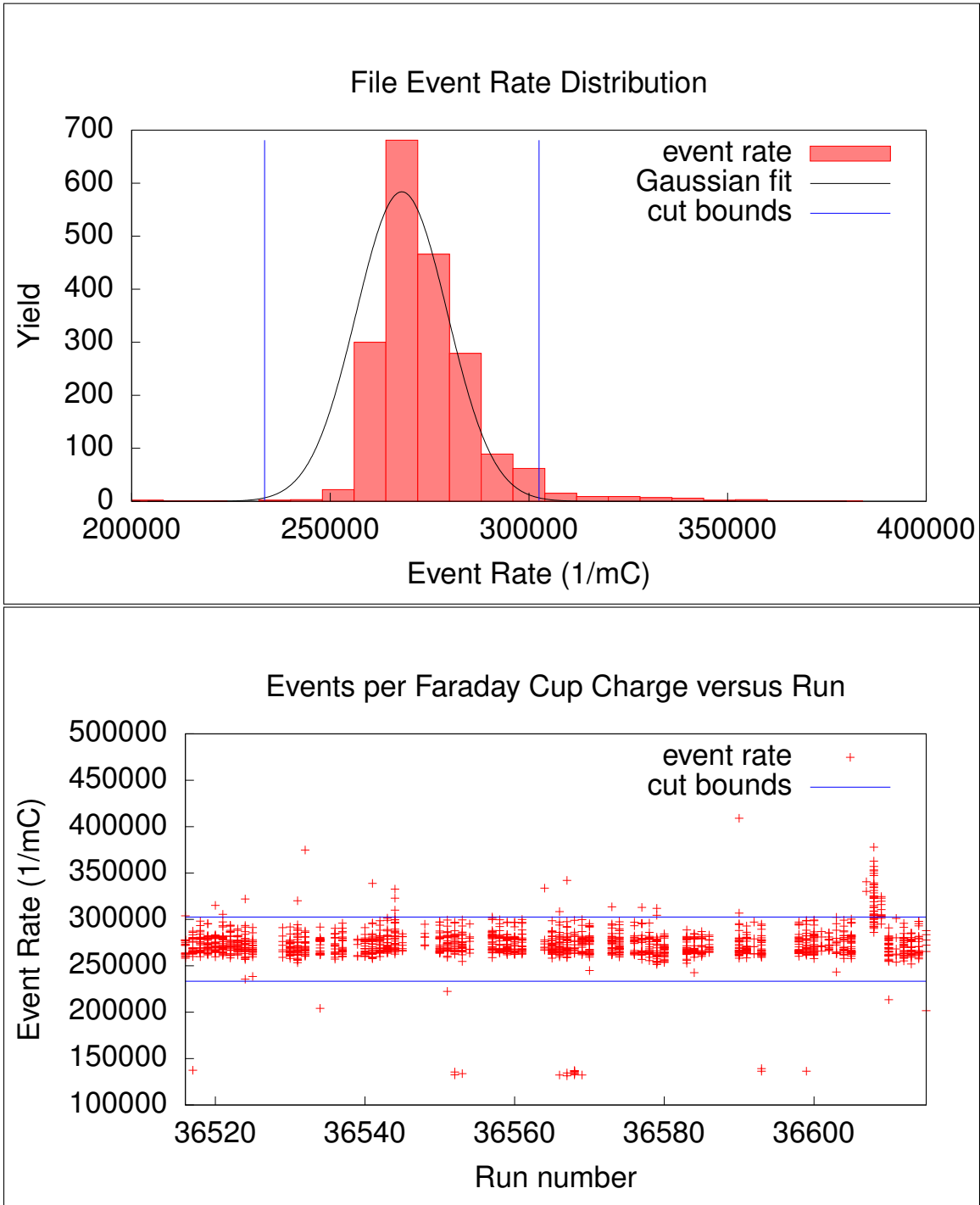


Figure 2.1: Binned event rates and scatter plot of event rate versus file index along with $\pm 3\sigma$ cut lines.

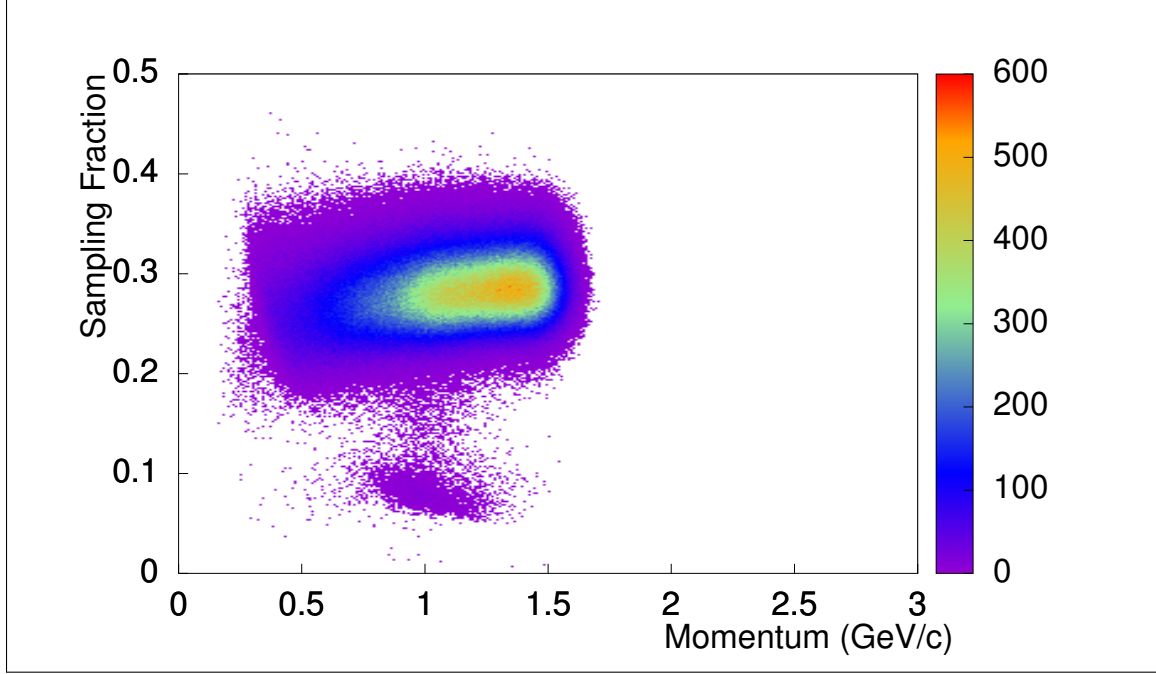


Figure 2.2: Sampling fraction f_s versus momentum distribution.

2.2 ELECTRON IDENTIFICATION

To ensure that the data used for analysis contains quality measurements of the final-state electron, a combination of selection criteria (or “cuts” for brevity) based primarily on the EC and CC are useful. The electromagnetic calorimeter in CLAS is a sampling calorimeter, and as such the appropriate metric for determining how much energy was deposited by a particle into the calorimeter is the sampling fraction,

$$f_s = E_{\text{tot}}/E'_K, \quad (2.2)$$

where E_{tot} is the sum of the deposited energy into the inner and outer sections of the calorimeter and E'_K is the kinetic energy of the scattered electron as determined using the drift chamber information and the knowledge of the magnetic field. Figure 2.2 shows the example 2-D histogram binning sampling fraction along with momentum for negatively charged particles in a sample of data where all other final selection

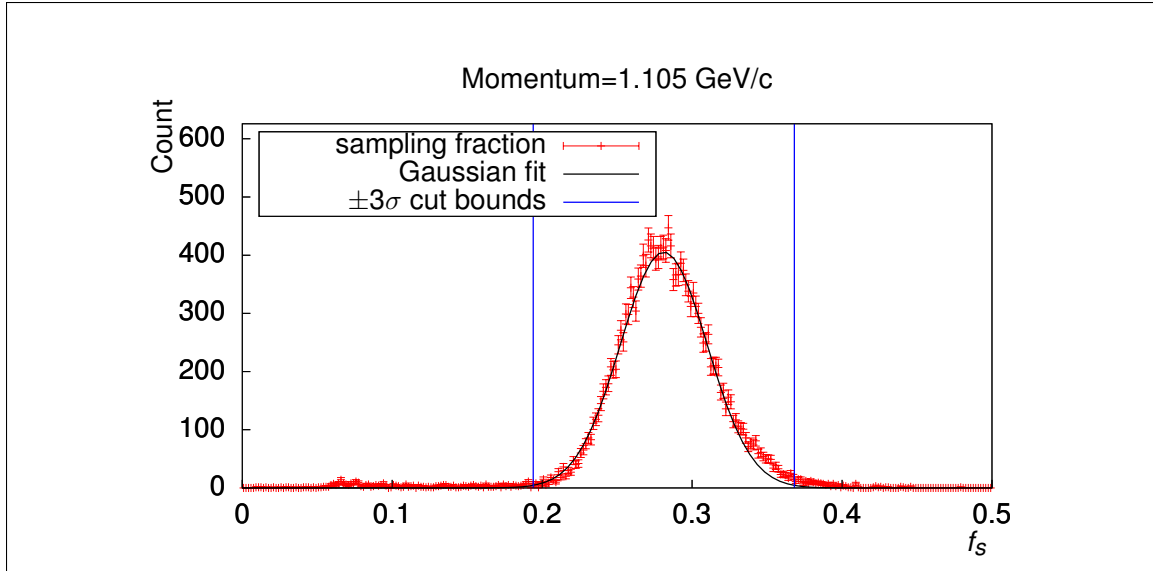


Figure 2.3: Slice of sampling fraction f_s versus momentum distribution along with Gaussian fit and $3\text{-}\sigma$ boundaries.

criteria are enabled. As is visible, the sampling fraction has a stable value in the vicinity of 0.3, and due to the nature of sampling calorimeters, this value designates complete energy absorption from the electron by the calorimeter. Figure 2.3 shows a slice of the 2-D histogram along with a Gaussian fit and $3\text{-}\sigma$ boundary lines. Figure 2.4 finally shows the collection of these for different momenta superimposed on the 2-D histogram along with a linear fit that is used to apply the sampling fraction selection criterion. As there is a clear separation between signal and background, this selection criterion is worth applying in its own right.

The Cherenkov detector can be used to further isolate good electron signals by selecting for sufficiently high velocity. The difference in particle velocity manifests as a difference between no or low photo-electron production and high photo-electron production in the photomultiplier tubes (PMTs) collecting the Cherenkov effect when charged particles pass through it. Particles moving slower than the speed of light in the threshold-Cherenkov detector should in principle produce no photo-electrons, while those moving faster than the speed of light of the Cherenkov detector medium will produce photo-electrons according to a modified Poisson distribution, as is shown

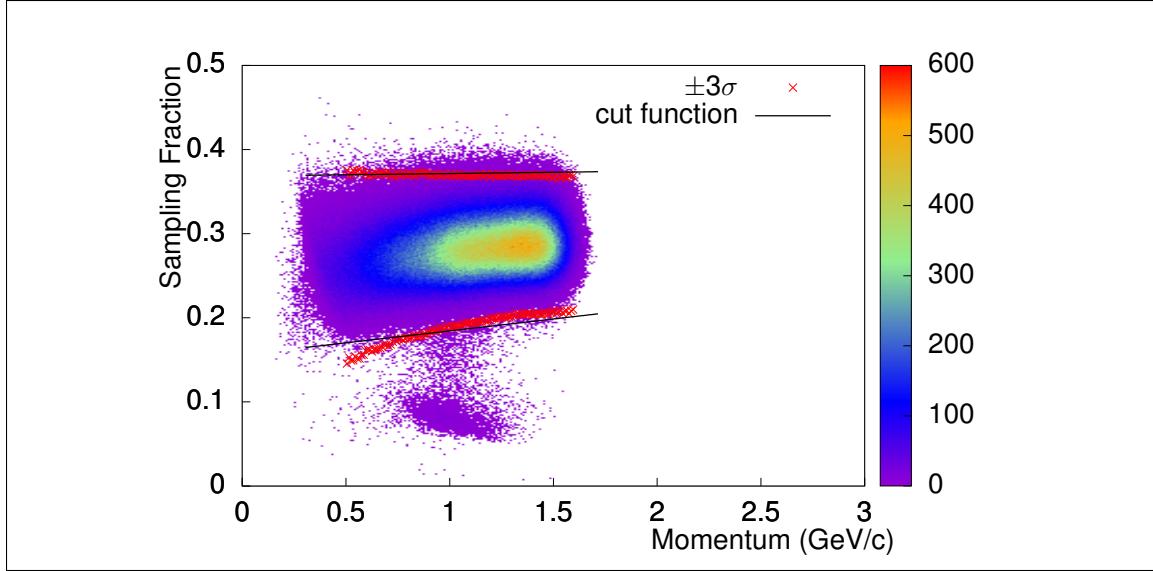


Figure 2.4: Sampling fraction f_s versus momentum distribution along with $3\text{-}\sigma$ boundaries and their linear fits.

in Figure 2.5. There is of course background noise in the PMT output, so that only potential electrons that produce more than a demanded minimum number of photo-electrons in the associated CC PMT are considered further given that only one PMT produced signal for that particle track. If both PMTs produced signal then the chance for background is negligible and thus those tracks are considered to have passed the CC photo-electron selection criterion. Ordinarily, identical selection criteria could be used to remove the noise events based on the photo-electron distributions for the experimentally measured yields and the Monte Carlo simulations, but the simulation software is not capable of simulating the Cherenkov detector response with sufficient accuracy. A better solution is to cut away background and fit the photo-electron signal distribution so that the amount of removed signal can be estimated, thus making it possible to reweight the data to take into account the missing signal. Figure 2.5 shows the number of photo-electrons N_γ distribution for a particular CC PMT with the low- N_γ background peak clearly visible in contrast with the higher- N_γ distribution for the electron signals. The signal fit function is a modified Poisson function, and the highlighted region under the fit indicates events that are removed by the N_γ cut.

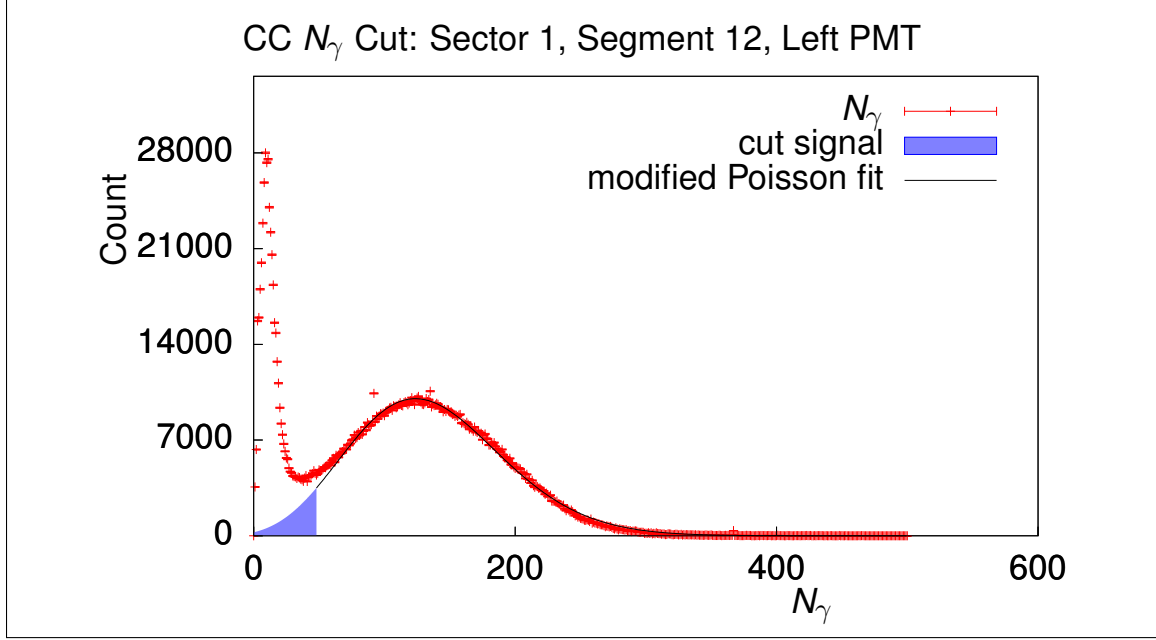


Figure 2.5: N_γ distribution for a selected PMT along with modified Poisson distribution fit to the signal region.

The cut is determined by using the signal fit to estimate the amount of background contribution included after applying a cut such that no more than 0.01% of the selected data is due to background events. The modified Poisson fit function is defined as

$$P_{\text{mod}}(x; A, \mu, \lambda) = A \frac{\mu^{x/\lambda}}{\Gamma(x/\lambda + 1)} e^{-\mu} \quad (2.3)$$

where A , μ , and λ are fit parameters and

$$\Gamma(z) = \int_0^\infty x^{z-1} e^{-x} dx \quad (2.4)$$

as per the standard definition of the Γ function. Using the integral of the distribution on both sides of the cut, the reweight factor is computed and applied for each event based on which PMT fired for the electron track of that event,

$$w_{\text{CC}} = \left(\int_{N_{\text{cut}}}^\infty S(N_\gamma) dN_\gamma \right)^{-1}, \quad (2.5)$$

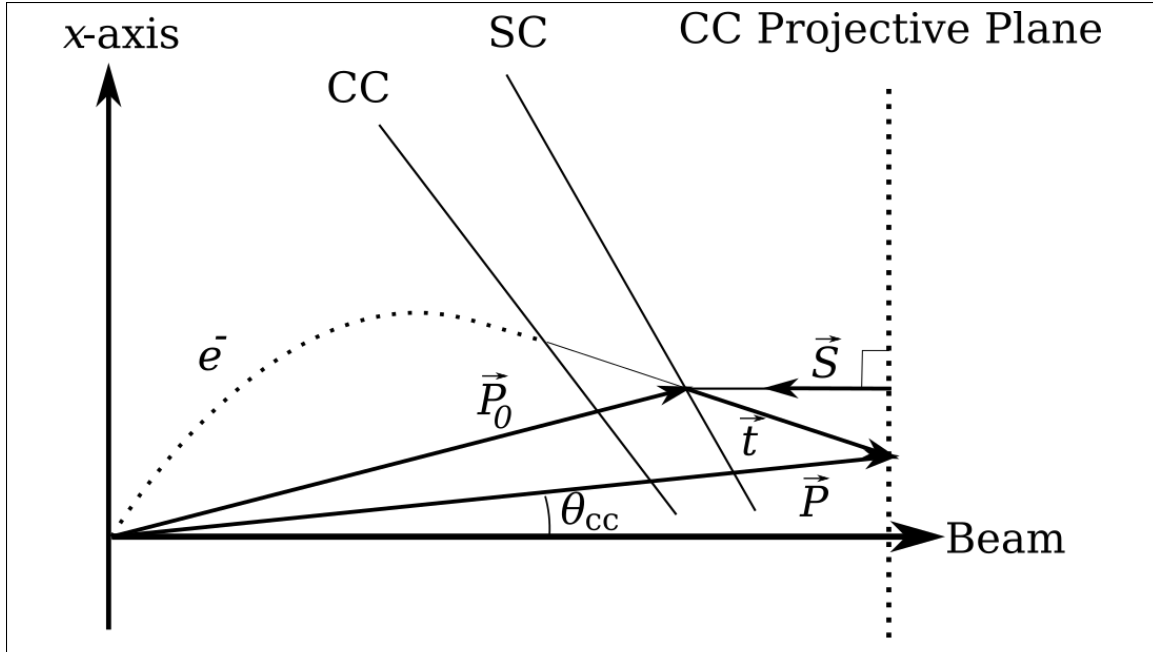


Figure 2.6: θ_{CC} angle, SC plane, CC plane, and CC projective plane diagram.

where $S(N_\gamma)$ is the normalized signal fit function such that $\int_0^\infty S(N_\gamma) dN_\gamma = 1$ and N_{cut} is the minimum N_γ cut criterion applied to the data for the a particular CC PMT.

A further constraint can be applied to the electron to ensure that the CC PMT that fired is consistent with the trajectory information gathered by DC: The CC angle-counter correlation [24]. Summarized briefly here, the drift chamber allows reconstruction of particle trajectories, which allows the point of intersection with the CC system to be determined. Electron identification can be improved by selecting only those trajectories that are consistent with the signaled CC counter. As the CC system involves reflecting light off curved mirrors, and therefore the geometrical considerations for dealing directly with the electron's intersection with the CC system is complex, a simpler approach as developed in [24] is to compare electron trajectories based on where they would have intersected an imaginary projective plane behind the CC system. Figure 2.6 shows an illustration of the SC, CC, and projective CC planes along with the angle θ_{CC} between the beam line and the line segment connecting

the vertex with the electron trajectory point of intersection on the projective CC plane. As illustrated in the diagram, the vector \vec{P}_0 represents the position of the track intersection with the SC plane taken from the DCPB bank x_{sc} , y_{sc} , and z_{sc} entries; \vec{S} is the perpendicular vector of the projective CC plane; and \vec{t} is the vector connecting \vec{P}_0 to the point of intersection of the unbent trajectory with the CC plane, \vec{P} . From [24], the CC projective plane's equation in lab coordinates for point \vec{p} is

$$\vec{S} \cdot \vec{p} + D = 0 \quad (2.6)$$

where $S_x = -0.000784 \text{ cm}^{-1}$, $S_y = 0 \text{ cm}^{-1}$, $S_z = -0.00168 \text{ cm}^{-1}$, and $D = 1$. Additionally, the direction of \vec{t} is known via the DCPB bank entries CX_SC , CY_SC , and CZ_SC such that

$$\vec{t} = t\hat{n} \quad (2.7)$$

where

$$\hat{n} = (CX_SC, CY_SC, CZ_SC). \quad (2.8)$$

Since

$$\vec{P} = \vec{P}_0 + \vec{t} = \vec{P}_0 + t\hat{n}, \quad (2.9)$$

determining \vec{P} , and therefore θ_{CC} , depends on solving the equation

$$\vec{S} \cdot \vec{P}(t) + D = 0 \quad (2.10)$$

for t . It follows that

$$t = -\frac{\vec{S} \cdot \vec{P}_0 + D}{\vec{S} \cdot \hat{n}}, \quad (2.11)$$

and therefore that

$$\vec{P} = \vec{P}_0 - \hat{n} \frac{\vec{S} \cdot \vec{P}_0 + D}{\vec{S} \cdot \hat{n}}, \quad (2.12)$$

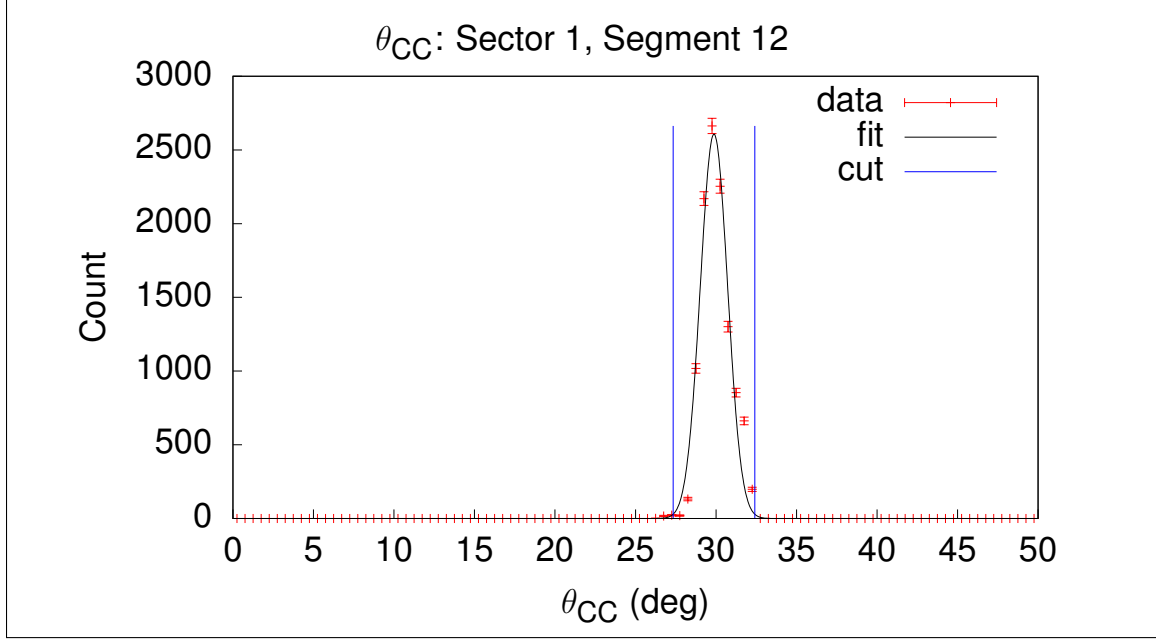


Figure 2.7: Single CC counter θ_{CC} distribution with Gaussian fit and asymmetrical cut lines.

so that

$$\cos \theta_{CC} = \frac{P_z}{|\vec{P}|} \quad (2.13)$$

where P_z is the component of \vec{P} along the beam line.

For each segment of the CC detector, there should be a distribution of these θ_{CC} angles around a central point, but noise events can potentially appear away from this central point relative to the distribution. Figure 2.7 shows such a distribution of θ_{CC} for a single counter from the CC system along with a Gaussian fit. To select only those events with a strong correlation between CC counter and θ_{CC} , a $3\text{-}\sigma$ cut is applied around the mean of the θ_{CC} Gaussian fit for each counter. Figure 2.8 shows a 2-D histogram of all counters from a single sector along with $3\text{-}\sigma$ cut boundaries computed from the Gaussian fits.

2.3 HADRON IDENTIFICATION

Identifying non-electron final state particles is primarily achieved through the momentum versus Δt cut which is to be defined here. Each kind of particle has a unique

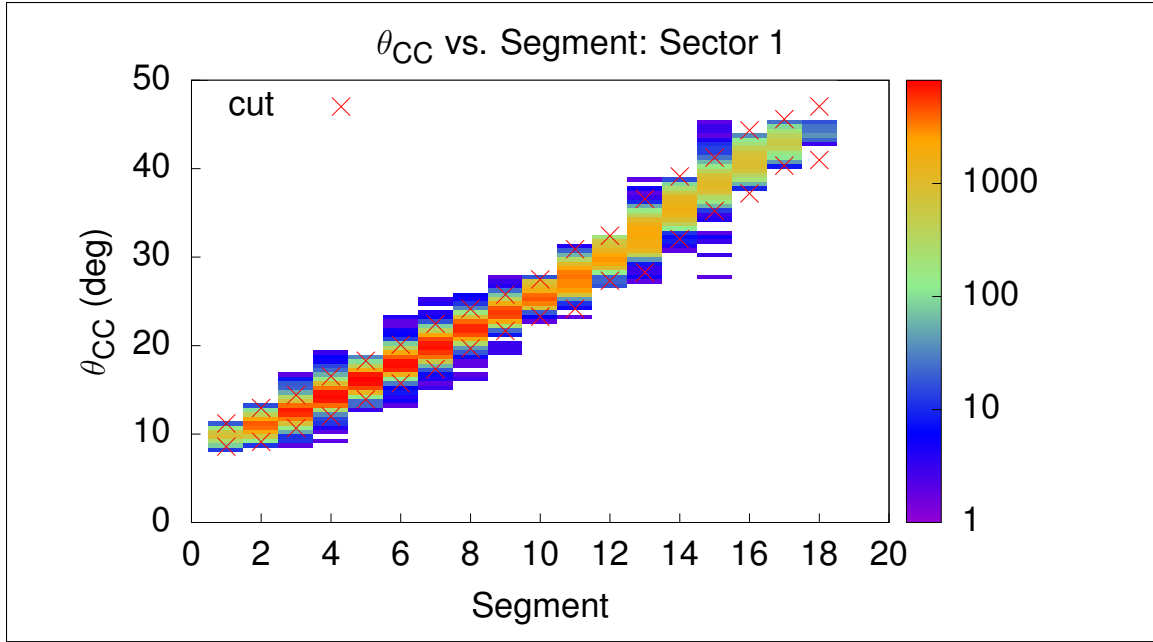


Figure 2.8: θ_{CC} distribution and cut boundaries for Sector 1 of the CC.

rest mass and electric charge, and this allows for two common methods of identifying particle types based on the same observable, their velocity. It is commonplace to assign a particle type to a reconstructed track either based on estimating the mass of the particle from its velocity measured by SC and momentum measured by DC (usually done by cutting around the ideal velocity-momentum curve for a given mass), or to compute a time difference which stays constant as a function of momentum whenever the rest mass is accurately assumed. Due to the ease of controlling selection strictness and visualization, the latter Δt method is used in this analysis.

Given that a particle is known to have traveled a distance l during a time T , the vertex time for this particle can be determined if the velocity is known. Since final state electrons have speeds indistinguishable from the speed of light c , the vertex time for the event can be readily known from the flight path length SC bank information for the principle electron. In the Δt particle identification method, the velocity for other particles is computed by assuming some value for the mass and calculating the difference between the electron's vertex time and the particle-in-question's vertex

time,

$$\Delta t = t_e - t, \quad (2.14)$$

where

$$t_e = T_e - l_e,$$

$$t = T - \frac{l}{\beta},$$

$$v = \frac{1}{\sqrt{1 + \left(\frac{m}{p}\right)^2}},$$

T_e and T are the recorded interaction times with the SC counters for the electron and particle in question, l_e and l are the path lengths for the electron and particle in question, p is the momentum for the particle in question as measured by the DC, β is the velocity of the particle, and m is the hypothetical mass of the particle, noting again for clarity that the units are chosen such that $c = 1$. Figure 2.9 shows Δt versus momentum histograms for positive and negative particles from E1E data. As the SC system is composed of many individual time of flight scintillators in bars with photo-multiplier tubes (PMTs) known as paddles [15], each of these paddles can potentially have an overall timing offset which can lead to the Δt distribution being shifted away from the ideal mean value of 0. In addition, there are some paddles which have nonsensical distributions due to various problems with calibration or the cooking process. There is still yet the fact that some paddles shared a single TDC. To address all of these effects, each paddle's Δt distribution can be assessed for quality and number of Gaussian distributions present, and in the presence of some number of Gaussian distributions, the Δt distribution can be fit by the sum of Gaussian distributions to allow regions of the Δt distribution to be shifted to have a mean of 0 prior to applying a selection cut. Figure 2.10 shows an example of a usable paddle Δt distribution along with a fit to the histogram made of a sum of Gaussian distributions,

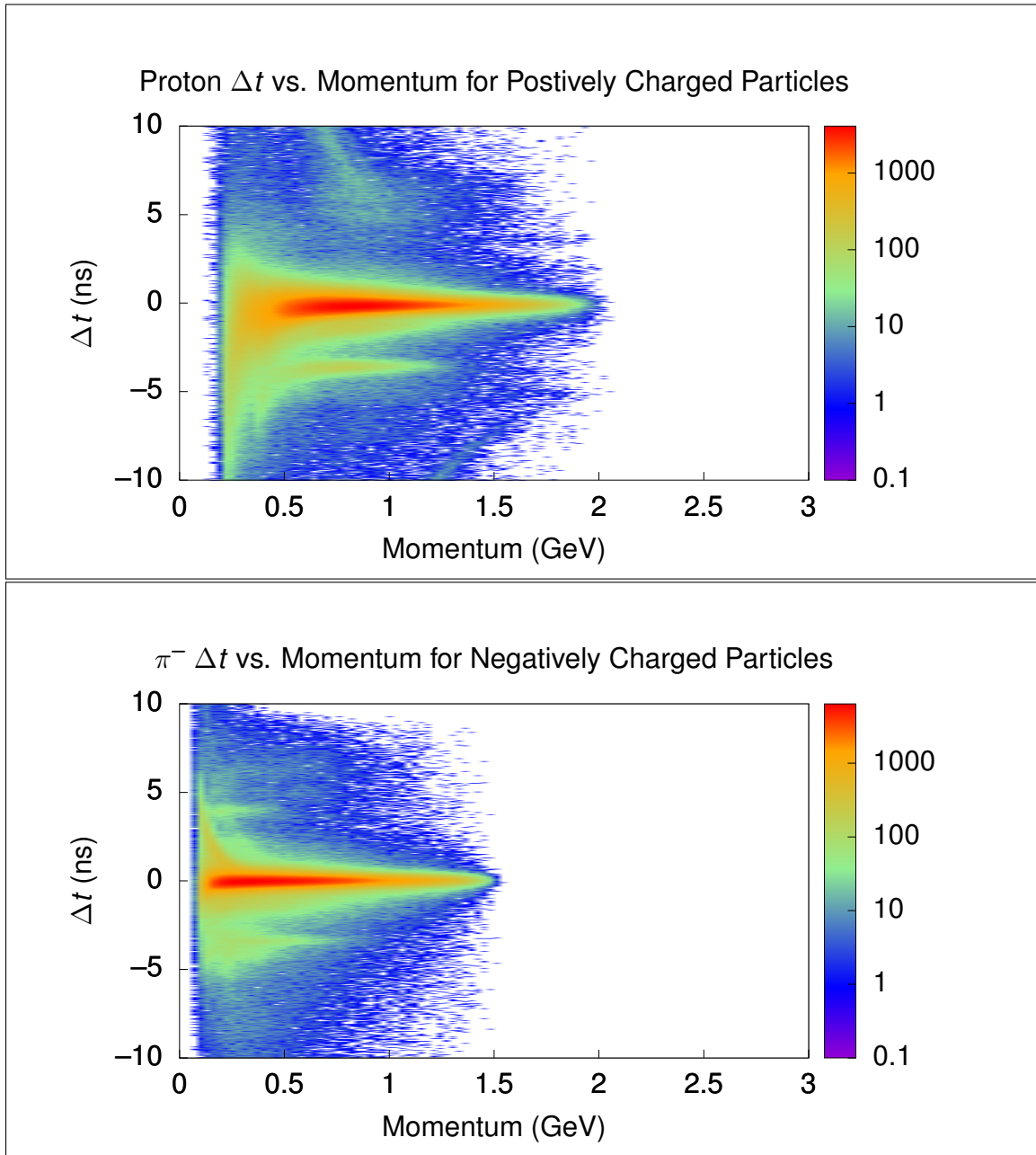


Figure 2.9: Δt versus momentum histograms for positive (top) and negative (bottom) particle tracks from E1E data with all selection criteria other than hadron identification applied in the final data set for the $\pi^- + p$ channel analysis.

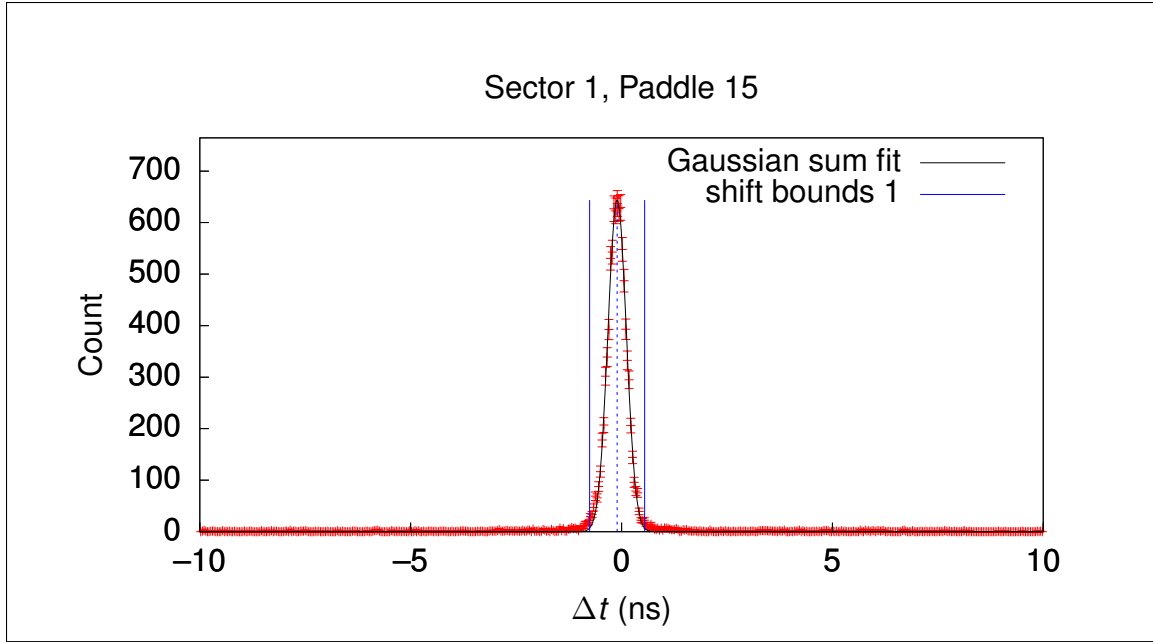


Figure 2.10: Example of a useful Δt distribution for a single SC paddle along with sum-of-Gaussian fit and $\pm 3\sigma$ boundaries.

and Figure 2.11 shows an example of an unusable Δt distribution. All paddles with unusable distributions are excluded from analysis.

Based on the location and width of the Gaussian regions of each Δt distribution, shifts can be defined which will move a particle's Δt mean to 0 to correct for these known errors in SC paddle time estimates. Figure 2.12 shows an example of the calculated shifts for a single sector. Once these shifts have been applied, the repaired Δt distribution appears as in Figure 2.13. Full tables of the shifts for all particle types and reaction channels are included in Appendix 7.

Once the Δt distributions have been repaired, each momentum slice can be fit with Gaussian distributions, and the $\pm 3\sigma$ limits of those distributions as functions of momentum can be fit with polynomial functions to provide clear selection criteria for particles that appear to match the hypothesized particle type used to compute Δt . Figure 2.14 shows π^- , π^+ , and proton Δt cuts along with histograms having all other cuts applied.

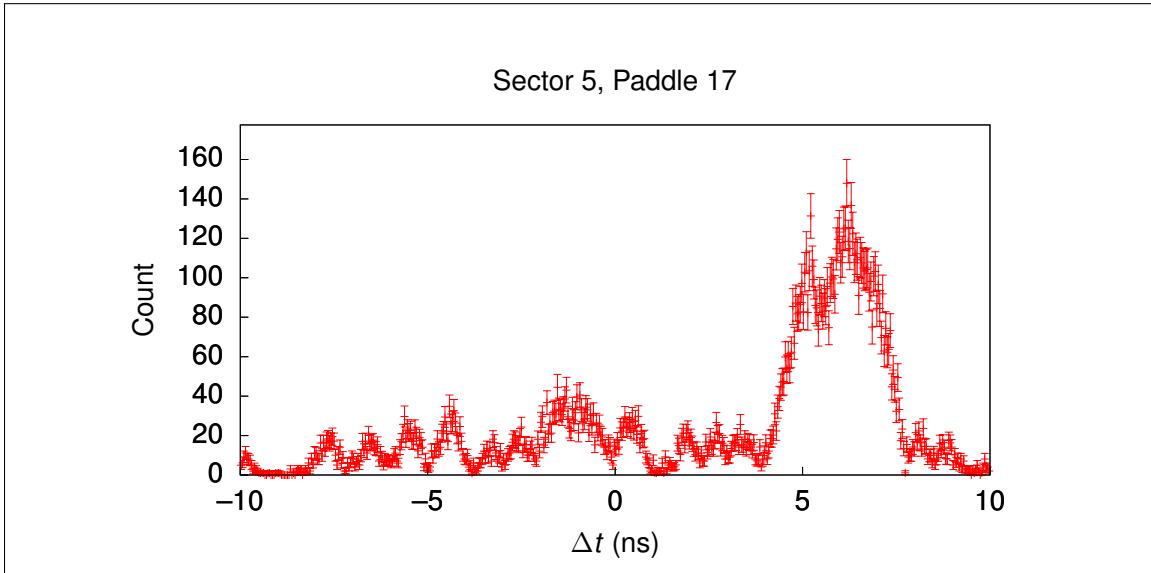


Figure 2.11: Example of a bad SC paddle Δt distribution.

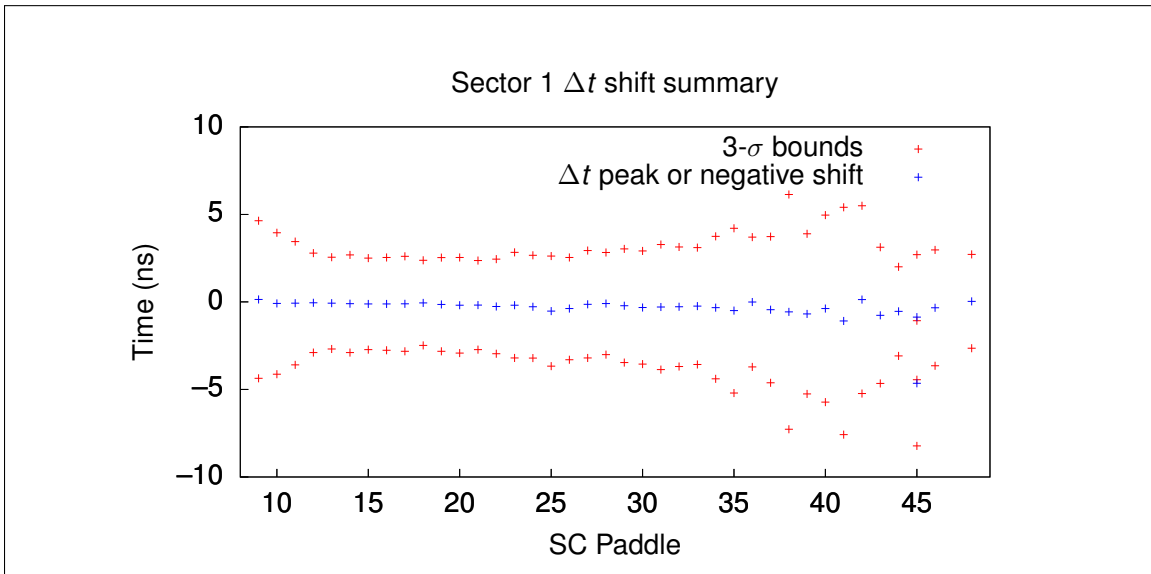


Figure 2.12: Example of calculated Δt shifts for protons in $\pi^- + p$ analysis. Here the arithmetic negative of the shifts are plotted as they are the peak positions detected in the Δt distributions, which is more convenient for visualizing and understanding the shifts in relation to the selection bounds. Note that not all paddles have sufficient data for determining shifts and are left as-is, such as paddles 1-8.

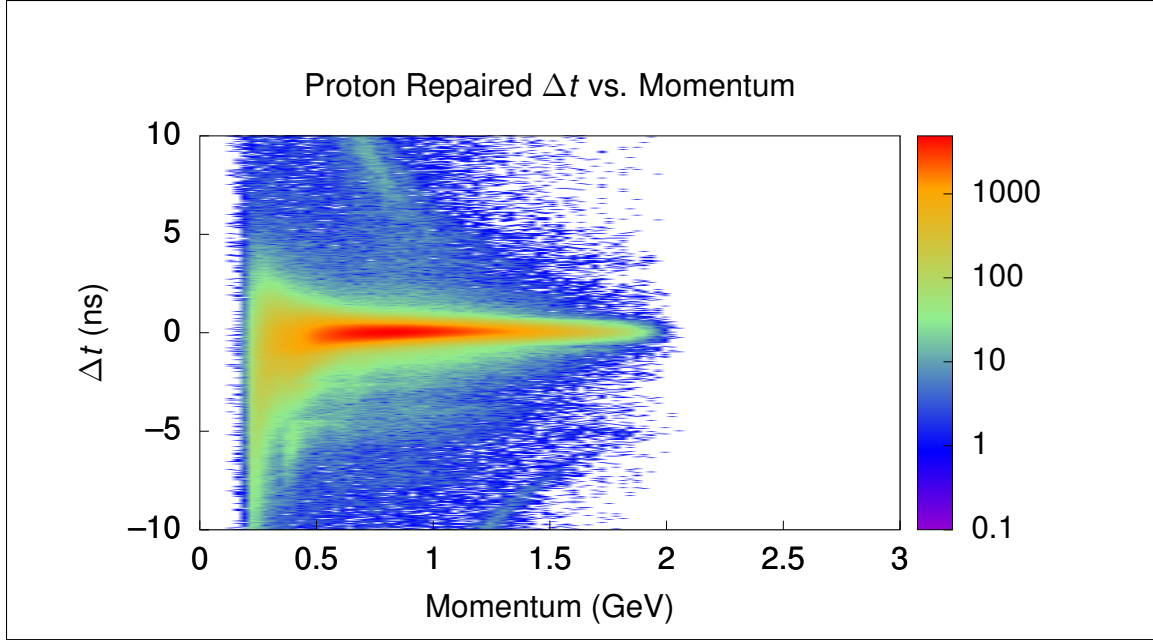


Figure 2.13: Example of repaired Δt .

2.4 FIDUCIAL CUTS

The CLAS detector, like all devices, has a domain of optimal performance, called the fiducial region. For each type of particle there is a different fiducial region for detecting that particle, and thus to ensure that the experimental data sets and Monte Carlo simulations match sufficiently well, fiducial cuts must be applied to both. Fiducial cuts are applied to the momenta three-vectors in magnitude, θ , and ϕ angles in the lab frame, implemented as ϕ cuts dependent on magnitude, θ , and sector. A minimum θ angle is also determined as a function of the momentum magnitude; for protons, this is a constant for all sectors, but pions and electrons exhibit variable minimum θ angles and need cuts which take this into account.

2.4.1 ELECTRON FIDUCIAL CUTS

There are two separate fiducial cuts for the electron: UVW coordinate cuts, and momentum- θ - ϕ cuts.

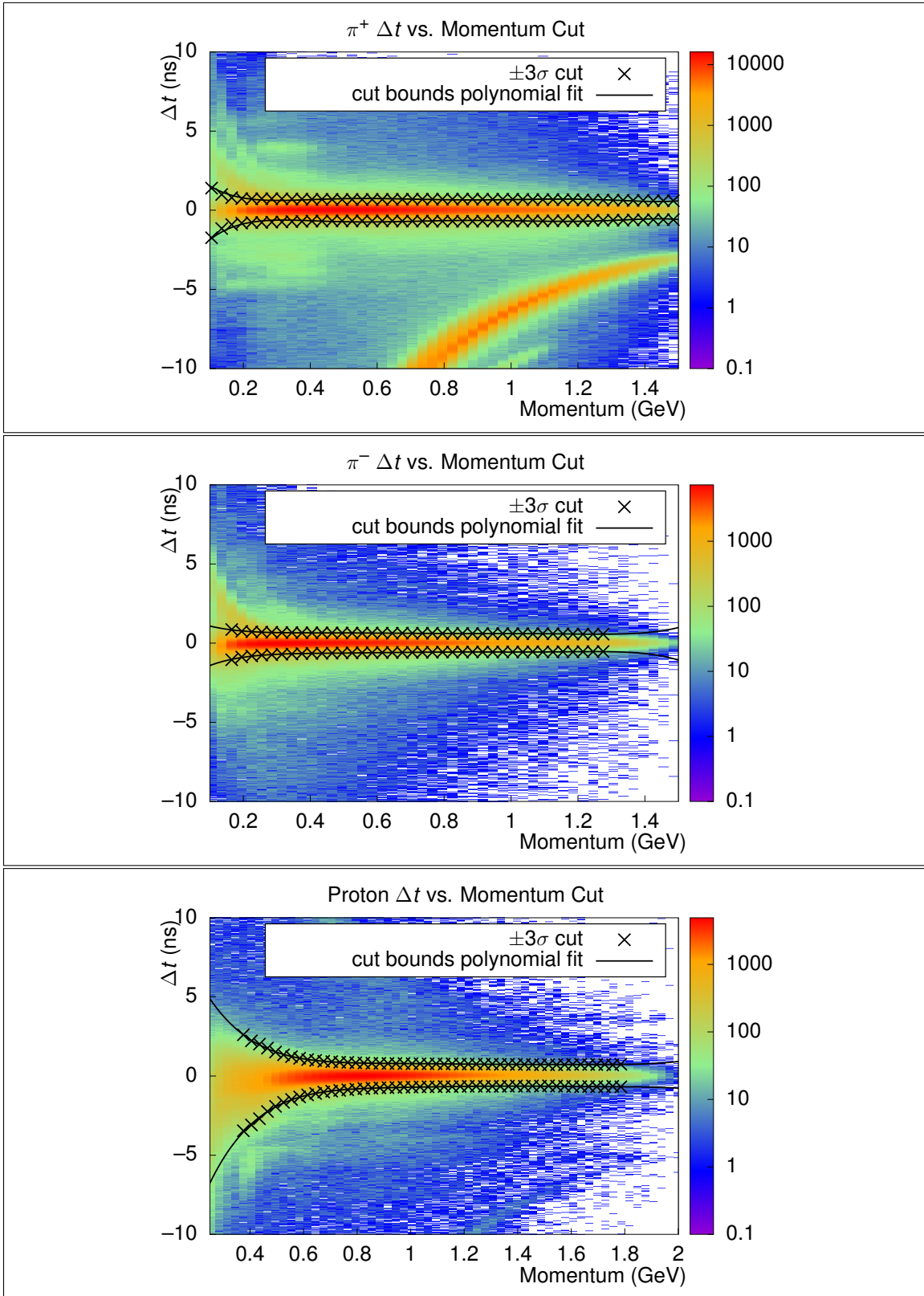


Figure 2.14: Particle ID cuts for π^- , π^+ , and proton candidate particles along with repaired Δt versus momentum histograms having all other cuts applied.

Table 2.1: EC UVW cuts.

Sector	U	V	W
All Sectors	$40 < U < 400$	$V < 370$	$W < 405$
Sector 3		$V < 305$ or $321 < V$	

EC UVW Fiducial Cuts

As described in [18], the EC system can provide UVW coordinates for electrons passing through the EC. These coordinates are appropriate for examining the EC's performance and potentially excluding events based on poor performance of a component. As shown in Figure 2.16, there is a single region of poor performance in the V coordinate for Sector 3, and so this is the only special cut applied to the UVW coordinates. There are general cuts applied to take data only in the nominal operating region of the EC in UVW space along with this special cut on the V coordinate. The applied cuts are summarized in Table 2.1, and Figures 2.15, 2.16, and 2.17 show these cuts applied to UVW histograms.

Momentum- θ - ϕ Fiducial Cuts

Figure 2.18 shows an example of a (θ, ϕ) histogram from experiment data for a given sector and momentum range with all other cuts applied. It is clear that if the shape of the simulated distribution in the same range does not exactly match this shape, then the acceptance will be inaccurate. For this reason, identical cuts are applied to experiment and simulation. The momentum- θ - ϕ cuts are determined in three stages.

1. Determine momentum and sector dependent θ_{\min} .
2. Determine fiducial boundaries for data binned in momentum, θ , and ϕ by examining individual ϕ slices.
3. Fit the determined fiducial boundaries of each ϕ slice with a function of momentum, θ and ϕ .

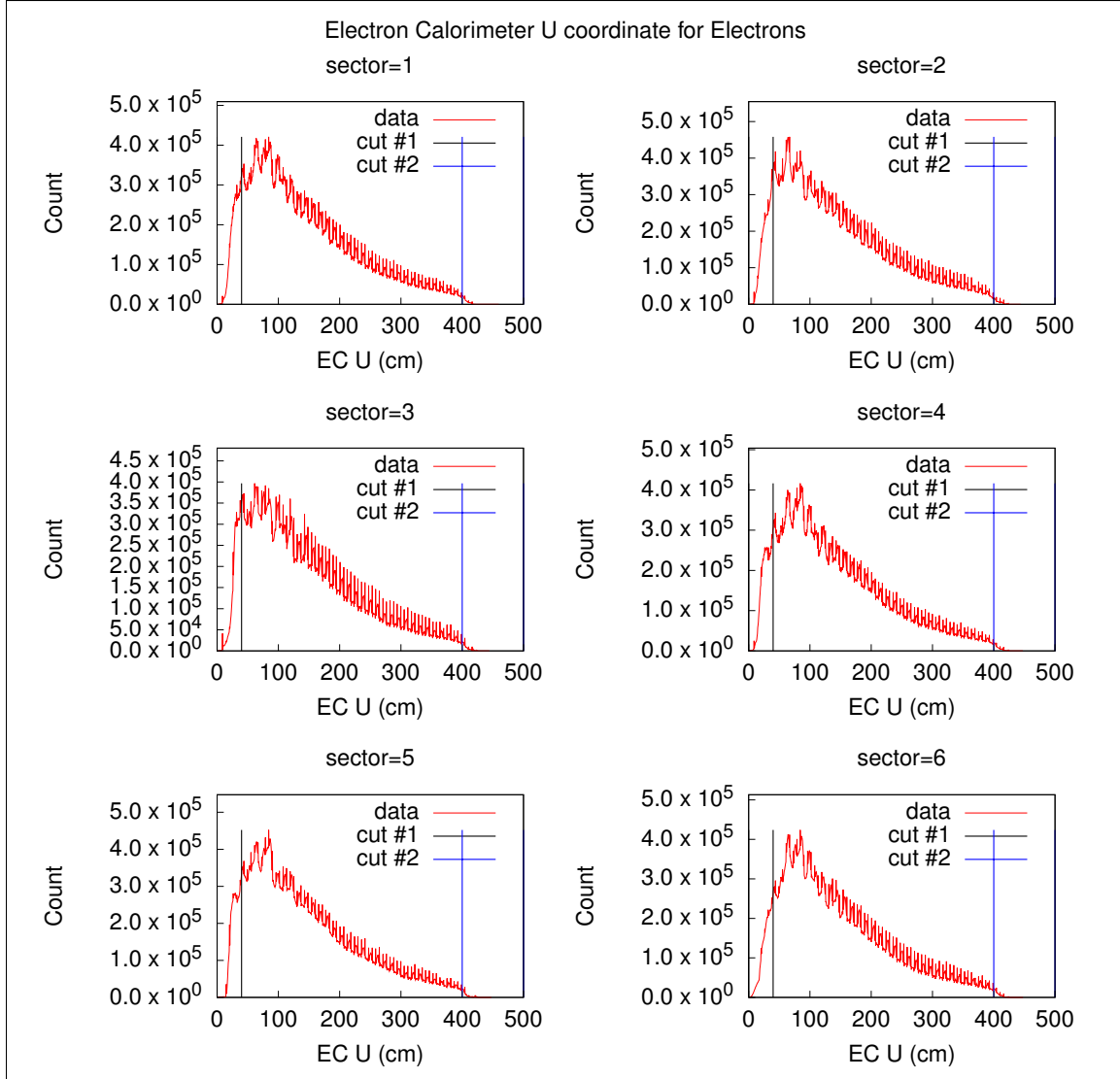


Figure 2.15: EC U cuts plotted along with U histograms for all sectors.

$\theta_{\min}(p)$, a function of momentum, is defined for each sector by fitting manually determined minimum θ angles from the shape of the θ - ϕ distributions within a given momentum slice; Figure 2.19 shows sample plots of the momentum- θ distribution along with θ_{\min} fits defined as

$$\theta_{\min}(p) = a + \frac{b}{p + c} \quad (2.15)$$

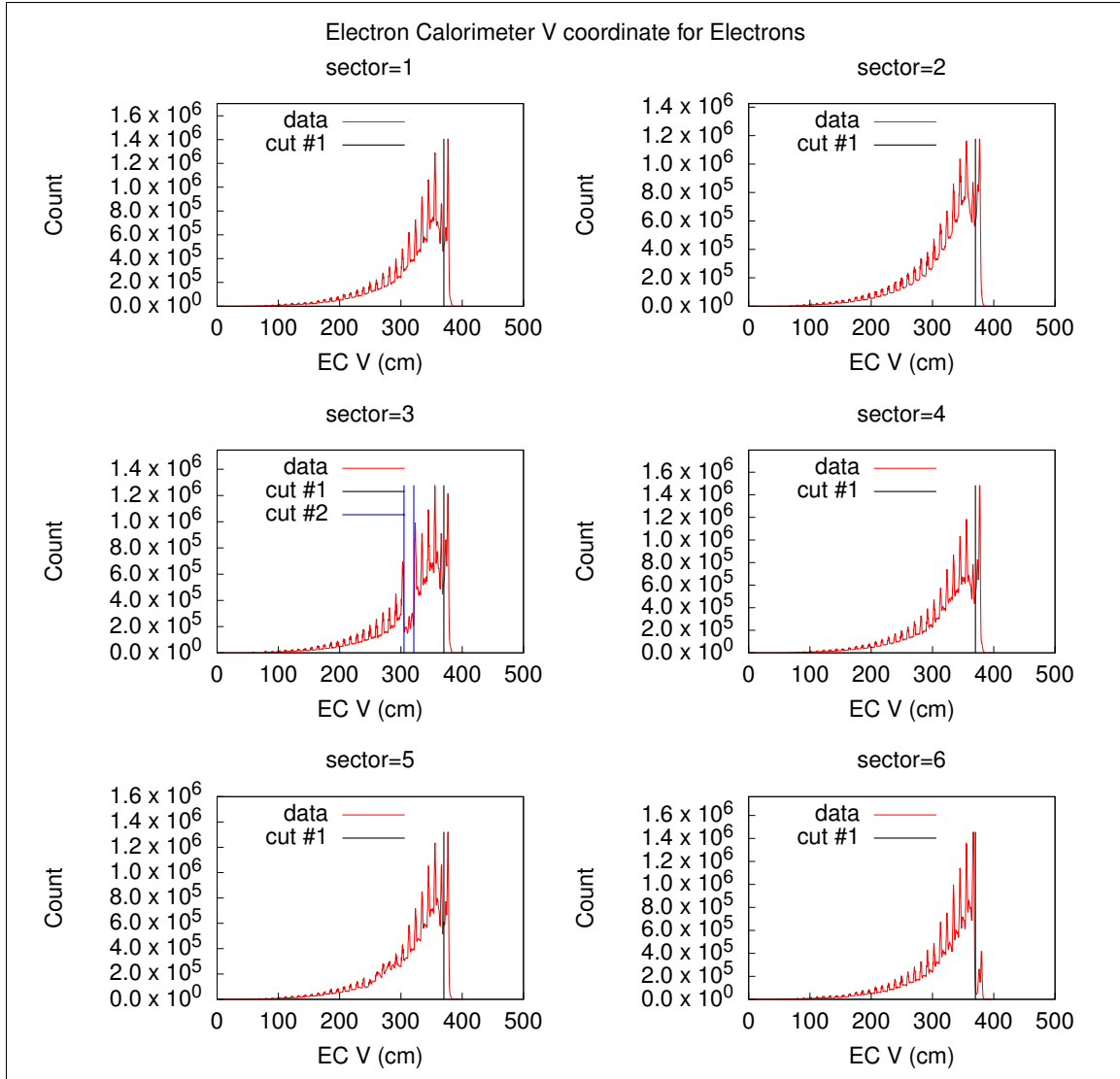


Figure 2.16: EC V cuts plotted along with V histograms for all sectors.

where a , b , and c are the fit parameters. As the distribution does not have a sharp edge, a threshold of 10% of the maximum histogram count for that particular θ slice was used to determine the minimum θ for a given momentum bin. In addition to the determined θ_{\min} cut, a fixed $\theta_{\max} = 50^\circ$ cut is also applied since measured yields decrease significantly for high- θ values.

Figure 2.20 shows a ϕ slice for a single momentum- θ bin in a given sector along with a trapezoid fit function. The trapezoid's peak is taken as the fiducial region of the detector for that ϕ slice, and the boundaries of these fiducial regions are fit with

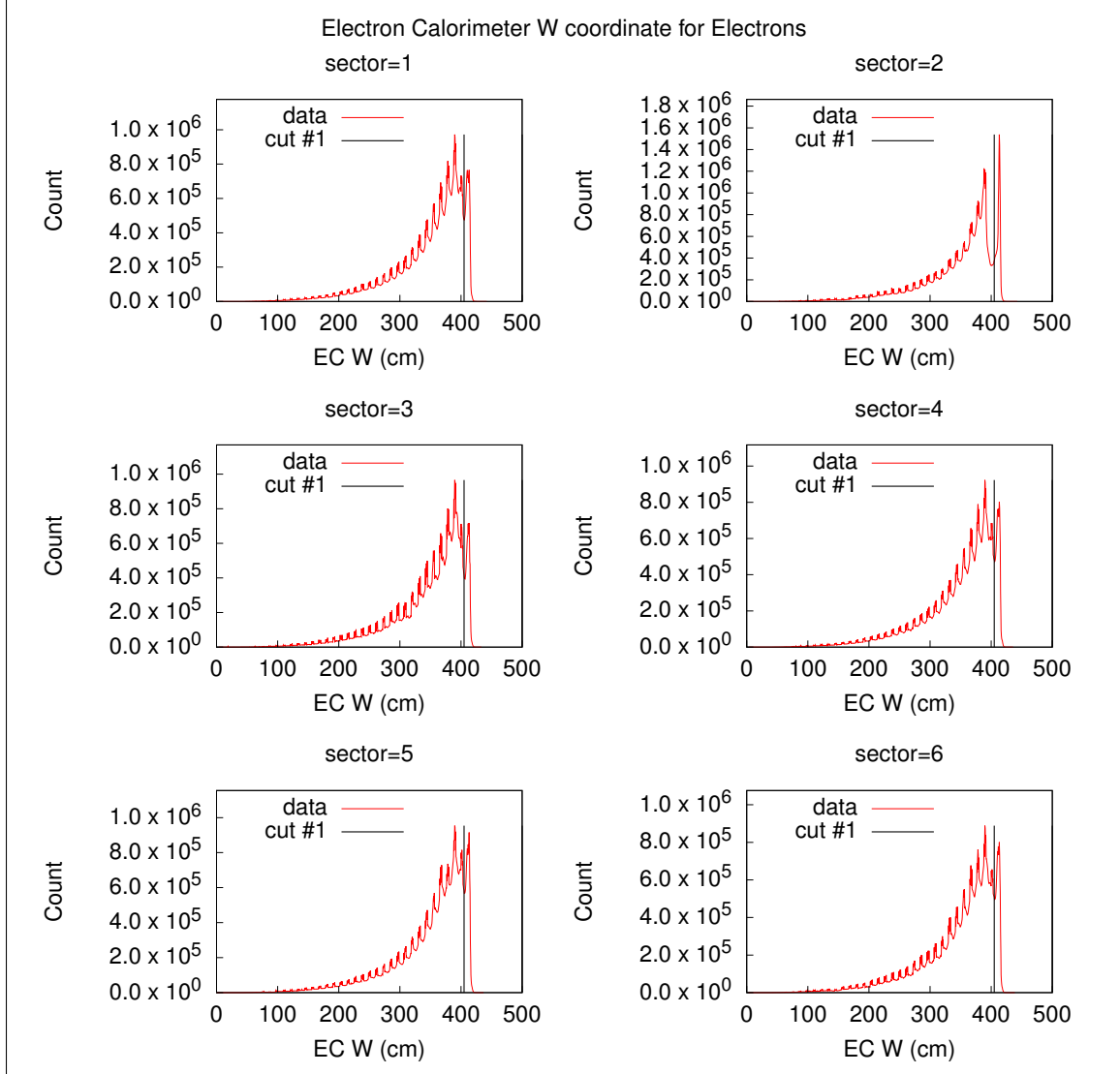


Figure 2.17: EC W cuts plotted along with W histograms for all sectors.

the electron fiducial cut function defined as

$$\phi_{\pm}^e(\theta, p) = A_{\pm} \text{pow}(\sin(\theta - \theta_{\min}(p)), k_0 + k_1 p + \frac{k_2 + k_3 p}{\theta} + \frac{B}{\theta^2}) \quad (2.16)$$

where p is the momentum, $\text{pow}(x, y) = x^y$, $A_{\pm} = \pm 37.14 \text{ deg}$, $B = 1500 \text{ deg}^2$, $\theta_{\min}(p)$ is the minimum θ fit function, and the k_j are fit parameters. Figure 2.21 shows a comparison between simulation and experiment against the fiducial cut functions

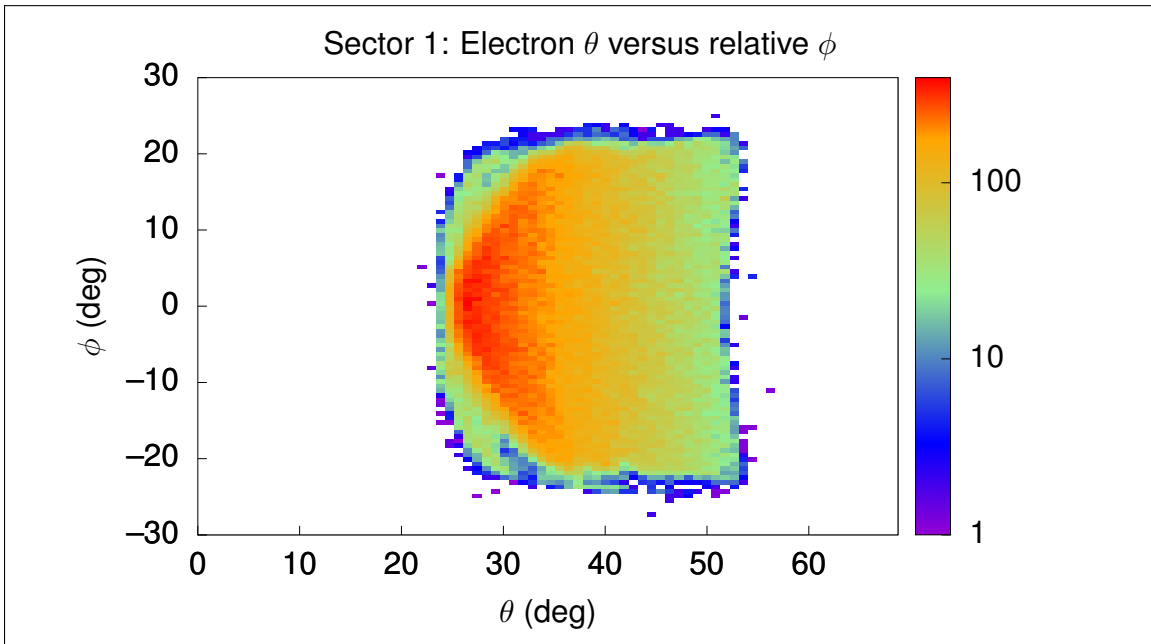


Figure 2.18: Electron (θ, ϕ) experiment data histogram for select sector and momentum in $(0.8, 1)$ GeV/c range. Note that a relative ϕ is used, so that each sector has a relative ϕ range of $(-30^\circ, 30^\circ)$.

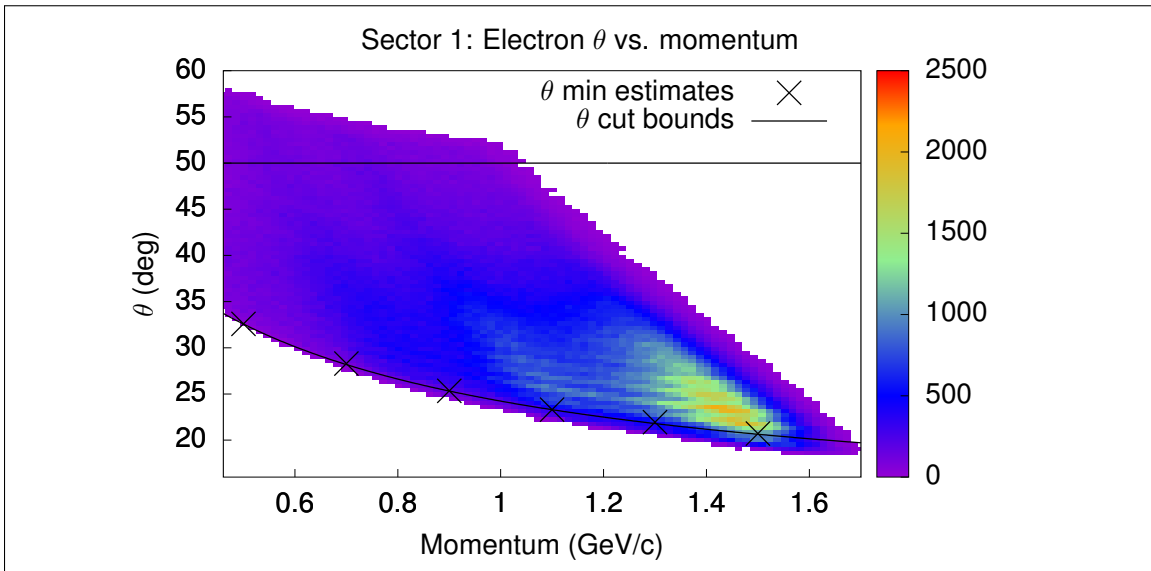


Figure 2.19: Electron momentum- θ experiment data histogram with θ_{\min} boundaries and fit function for a selected sector.

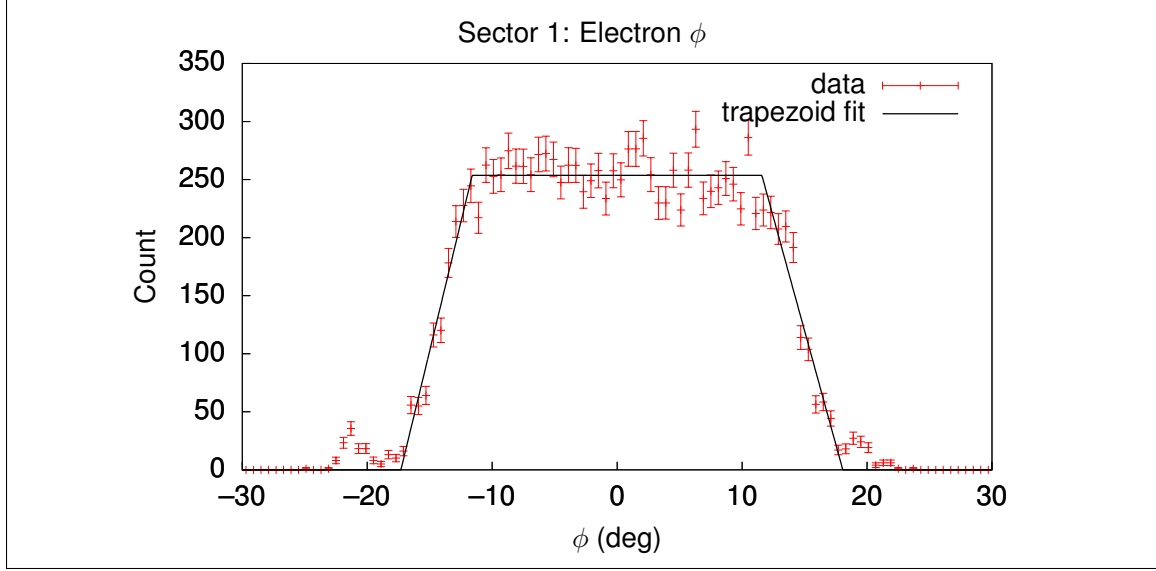


Figure 2.20: ϕ slice and trapezoid fit for momentum in (0.8, 1) GeV/c range and θ in (29.25°, 31.05°) range for Sector 1 experiment data.

applied to both in the $e^- + n \rightarrow e^- + \pi^- + p$ channel. All cut parameters are listed in Appendix B.4.

2.4.2 π^\pm FIDUCIAL CUTS

Because there are two reaction channels in this analysis, and they each have a different variety of charged pion in the final state, both π^+ and π^- fiducial cuts have been developed in this analysis. The same functional form is used for both, with only the parameters differing, and the same approach is taken as in the case of electron fiducial cuts, so that θ_{\min} functions are determined and ϕ slices are fit against trapezoid functions to determine fit fiducial regions for each ϕ slice. However, the 3-D momentum- θ - ϕ cut function form for the ϕ cut function is here defined as

$$\phi_{\text{cut}}^\pi(\theta, p) = u(p; c_0, c_1, c_2)(1 - \exp(-c_3(\theta + u(p; c_4, c_5, c_6)))), \quad (2.17)$$

where p is the momentum, the c_j are fit parameters, and $u(x; a, b, c) = a + bx + c/x$. Note that as there is no explicit θ_{\min} reference in this cut function, the minimum θ

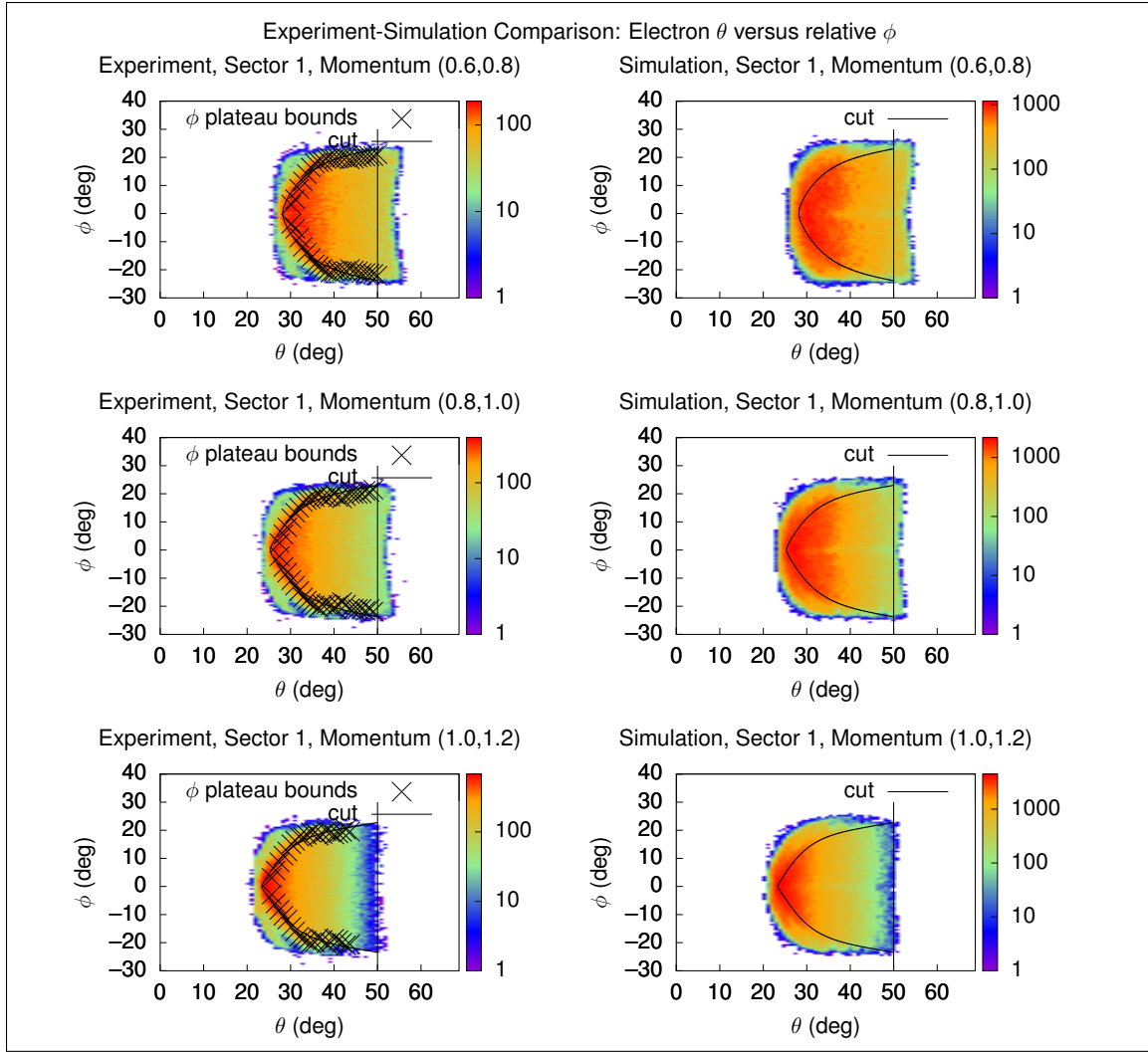


Figure 2.21: Comparison of electron fiducial cuts for experiment and simulation data for selected bins.

criterion is imposed as an additional constraint, and the θ_{\min} cut function is the same as in the electron fiducial cut from Equation 2.15.

Figure 2.23 shows example (θ, ϕ) distributions and fiducial cuts for a particular sector and momentum range for π^+ and π^- for experiment and simulation, and Figure 2.22 shows the θ_{\min} distributions and fit functions along with momentum and θ histograms for experiment and simulation. All cut parameters are listed in Appendix B.5 and Appendix B.6.

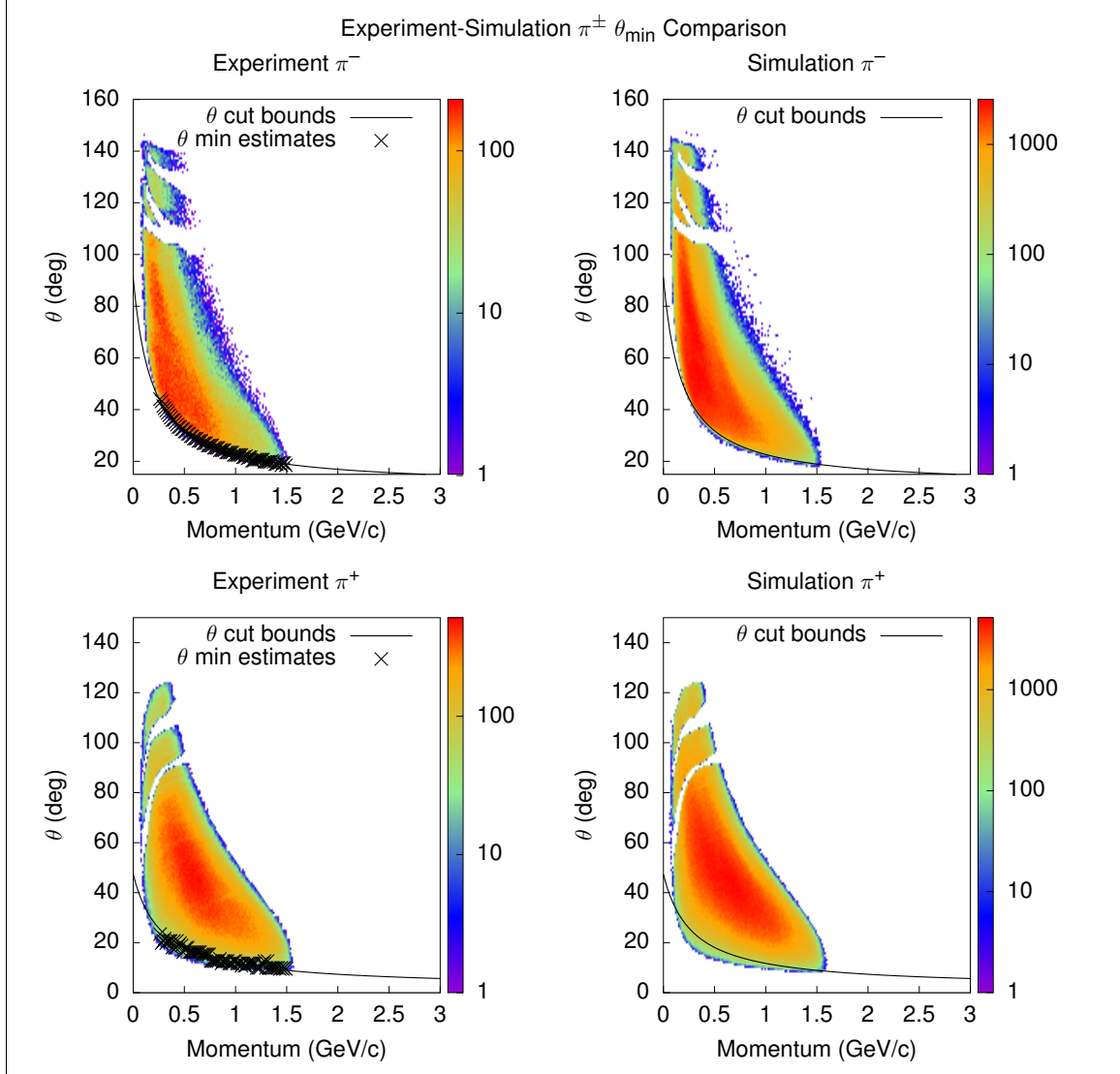


Figure 2.22: θ_{\min} determination for π^- and π^+ particles for experiment and simulation.

2.4.3 PROTON FIDUCIAL CUTS

Proton fiducial cuts are unique among the three kinds of fiducial cuts applied in this analysis due to the proton fiducial region having the simplest θ_{\min} cut, being just a constant within a given sector, as visible in the example of Figure 2.24. The functional form for proton ϕ fiducial cuts is given by

$$\phi_{\text{cut}}^p(\theta) = P_0(1 - \exp(-P_1(\theta + P_2))), \quad (2.18)$$

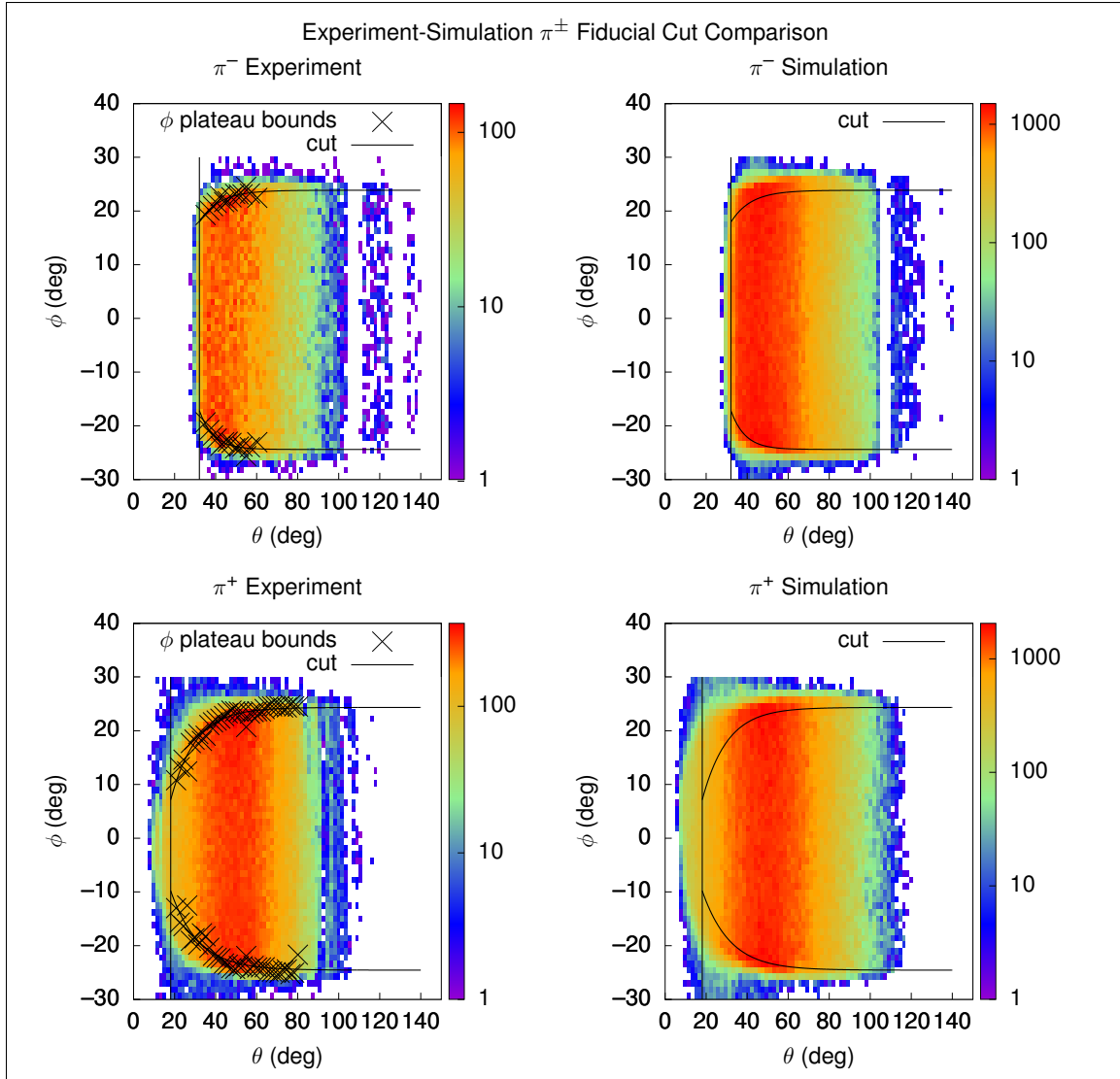


Figure 2.23: π^- and π^+ (θ, ϕ) histograms and fiducial cuts for experiment and simulation for Sector 1, momentum in (0.4, 0.6) GeV/c.

where ϕ_{cut}^p determines the upper or lower ϕ cut limit depending on the supplied parameters, and the P_k are the fit parameters. Figure 2.25 shows fiducial cuts applied to both experiment and simulation data. All cut parameters are listed in Appendix B.7.

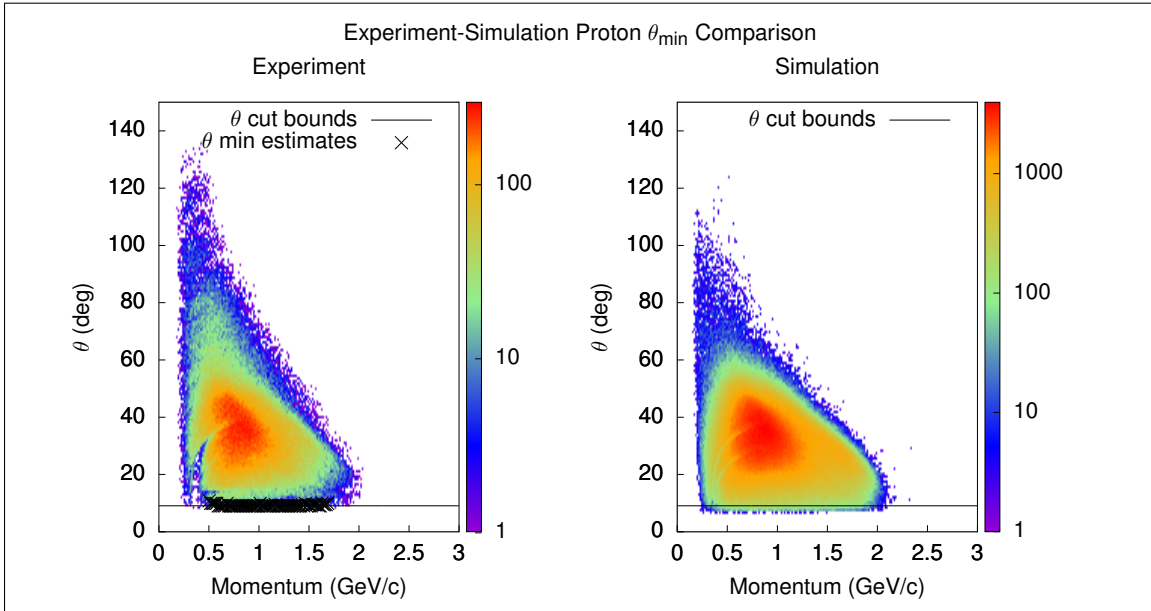


Figure 2.24: Proton θ versus momentum histograms for Sector 1 along with determined θ_{\min} cut for experiment and simulation.

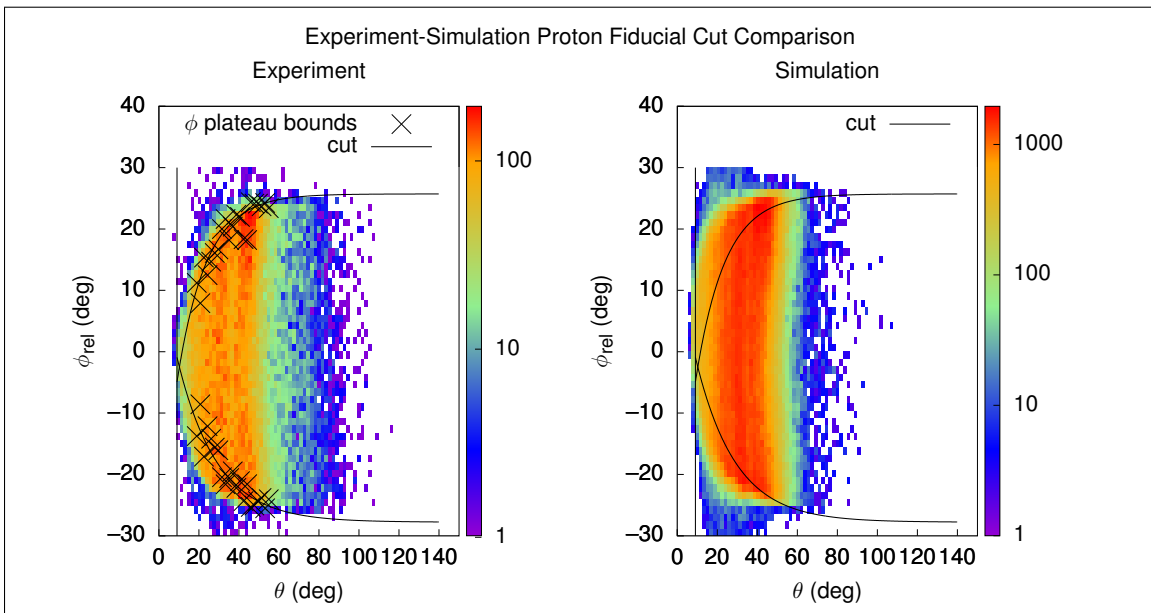


Figure 2.25: Example proton fiducial cuts for experiment and simulation, Sector 1, and momentum in $(0.47, 0.82)$ GeV/c. Note that in some bins the θ_{\min} cut is redundant, as in the case of this bin.

2.5 EXCLUSIVITY CUTS AND BACKGROUND SUBTRACTION

The most stringent selection criterion for all three analyses is the requirement that the missing mass from each event is consistent with the reaction channel of interest. For the $\pi^- + p$ analysis, the conservation of energy-momentum equation can be written as

$$q_\mu + d_\mu = \pi_\mu^- + p_\mu + p_{s\mu}, \quad (2.19)$$

where

$$d_\mu = (m_d, 0, 0, 0), \quad (2.20)$$

q_μ is defined as in Equation 1.9, m_d is the deuteron mass, and $p_{s\mu}$ is the Lorentz vector for the leftover proton from the nucleus, which for quasifree interactions is called the spectator proton. Since a cut on the leftover momentum will be made to select quasifree reactions for the $\pi^- + p$ analysis as per [1], the leftover baryon will be referred to as the spectator in the $\pi^- + p$ analysis. Therefore, the appropriate missing mass for this analysis would be that of the spectator,

$$M_{p_s}^2 = (q_\mu + d_\mu - \pi_\mu^- - p_\mu)^2. \quad (2.21)$$

For both the π^- and π^+ analyses, there is another missing baryon in addition to the missing leftover nucleon from the deuteron, so that there is no way to compute the missing Lorentz vectors from energy-momentum conservation alone. This is where the common practice of making the approximate but false assumption that the target nucleon is at rest, and therefore ignoring the other nucleon, can be used, which introduces Fermi-smearing into the resulting analysis. For the π^- analysis, the target nucleon is assumed to be a neutron at rest, so that the Fermi-smearred conservation

of energy-momentum equation would be written as

$$q_\mu + n_\mu^\circ = \pi_\mu^- + p_\mu, \quad (2.22)$$

and the appropriate missing mass would be

$$M_p^2 = (q_\mu + n_\mu^\circ - \pi_\mu^-)^2, \quad (2.23)$$

where $n_\mu^\circ = (m_n, 0, 0, 0)$ in the lab frame with m_n as the neutron mass. For the π^+ analysis, the target nucleon is assumed to be a proton at rest, so that the Fermi-smearing conservation of energy-momentum equation would be

$$q_\mu + p_\mu^\circ = \pi_\mu^+ + n_\mu, \quad (2.24)$$

and the corresponding missing mass would be

$$M_n^2 = (q_\mu + p_\mu^\circ - \pi_\mu^+)^2 \quad (2.25)$$

with $p_\mu^\circ = (m_p, 0, 0, 0)$ in the lab frame and m_p being the proton mass.

As already mentioned, in the context of the three analyses, the $\pi^- + p$ analysis is a special case as it is possible to directly select quasifree events. Additionally, as shown in [1], there is no significant double-pion background contamination given an appropriate missing mass cut, and the amount of visible final state interaction can be controlled by cutting on the missing spectator momentum. To summarize the findings from [1], by excluding leftover baryon momenta larger than 200 MeV/c, only quasifree events remain, and when a standard $\pm 3\sigma$ cut is applied to the squared missing mass distribution, no significant double-pion background remains. Figure 2.26 shows the missing mass distribution for the $\pi^- + p$ analysis along with a second

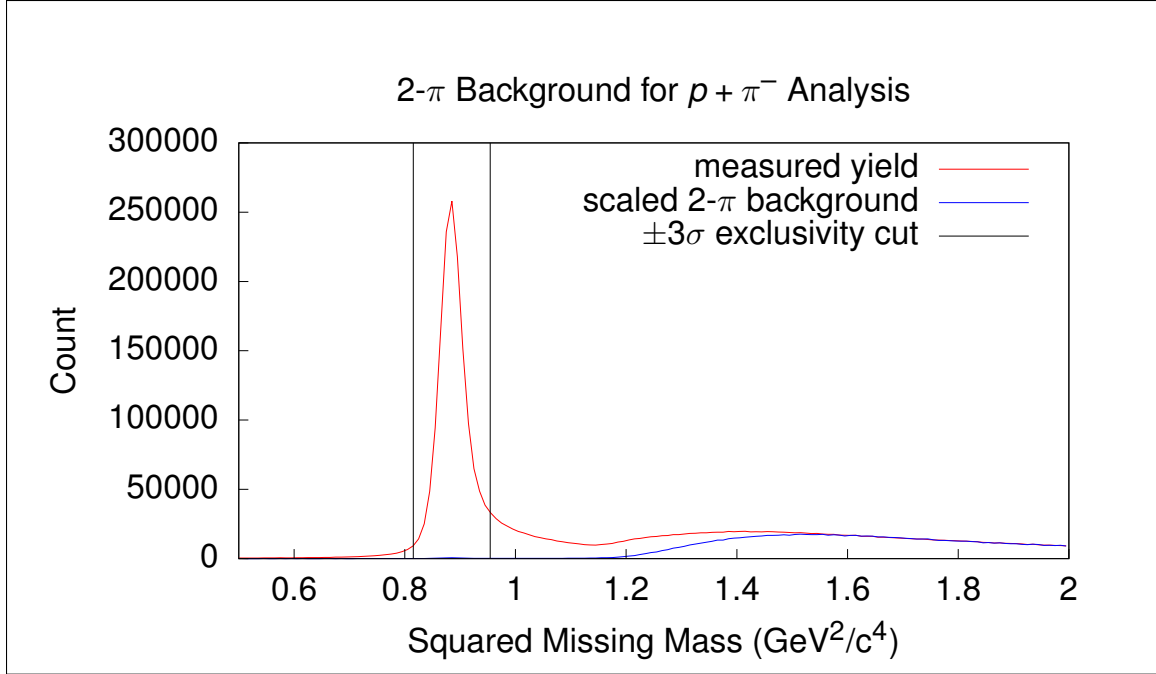


Figure 2.26: Squared missing mass distribution for the $\pi^- + p$ analysis integrated over full (W, Q^2) domain along with exclusivity cut and the same distribution for events with two pions reconstructed, showing no significant double-pion contamination within the cut range.

distribution from experiment data with an additional requirement that there was a π^+ reconstructed particle track in each event so as to conduct a basic test for the presence of double-pion contamination within the exclusivity cut range. As can be seen both here and in [1], there is no significant double-pion contamination within the exclusivity cut range.

The same cannot be said for the π^\pm analyses. Although Figures 2.27 and 2.28 show example squared missing mass distributions for selected $(W, Q^2, \cos(\theta^*))$ bins that reveal only small noticeable double-pion background contributions, the removal of the convoluted double-pion and final state interaction contributions is highly nontrivial. In an attempt to remove both of these contributions simultaneously, simulation is used to determine the shape of the signal missing mass distribution as a function of as few parameters as feasible, subtracting a scaled signal distribution from the total experiment yield distribution, and determining how much contamination remains

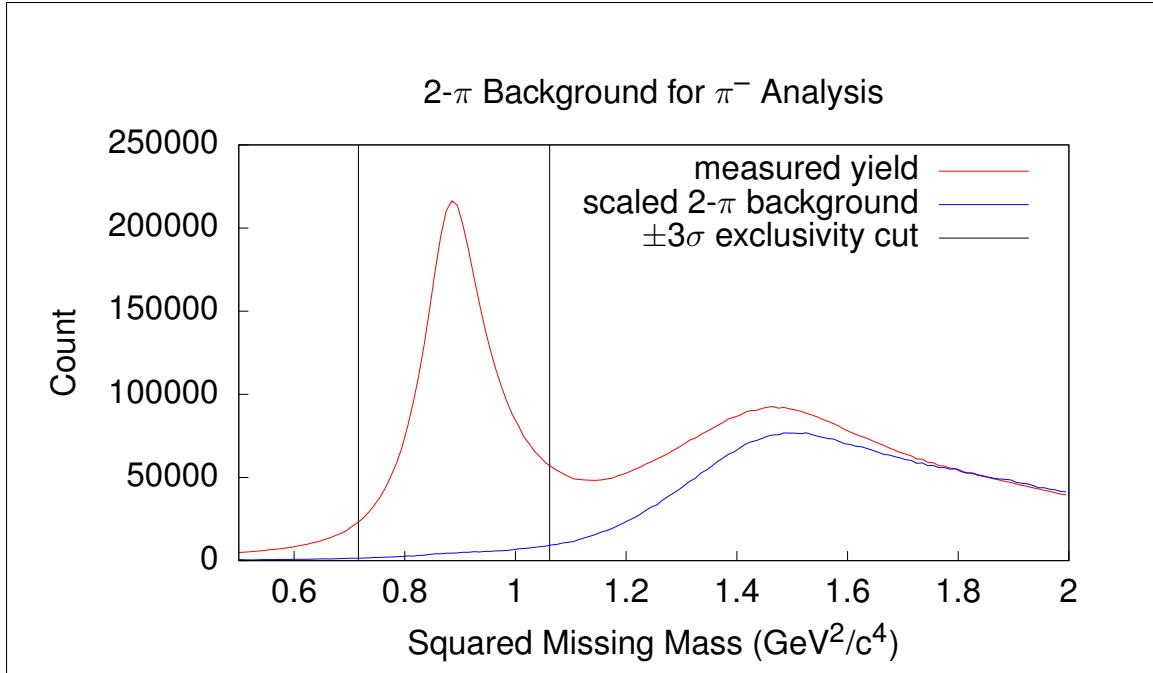


Figure 2.27: Squared missing mass distribution for the π^- analysis integrated over full (W, Q^2) domain along with the exclusivity cut showing noticeable double-pion contamination within the cut range.

within the exclusivity cut so that, at a minimum, the cross-section estimates can be reweighted to account for the amount of background and final state interaction contributions.

The ideal method for removing this contamination would be to know the true missing mass distribution shape for each $(W, Q^2, \cos(\theta^*), \phi^*)$ bin of the analysis and to have enough statistics in each bin so that the shape of both the signal and background missing mass distributions would be clearly visible in every 4-D bin, so that each cross-section point could be reweighted to perfectly remove the influence of background contamination. Unfortunately, there are not enough statistics to perform background estimates as a function all four parameters, but it is possible to perform background estimation as a function of $(W, Q^2, \cos(\theta^*))$ with nearest neighbor interpolation for bins where statistics are insufficient.

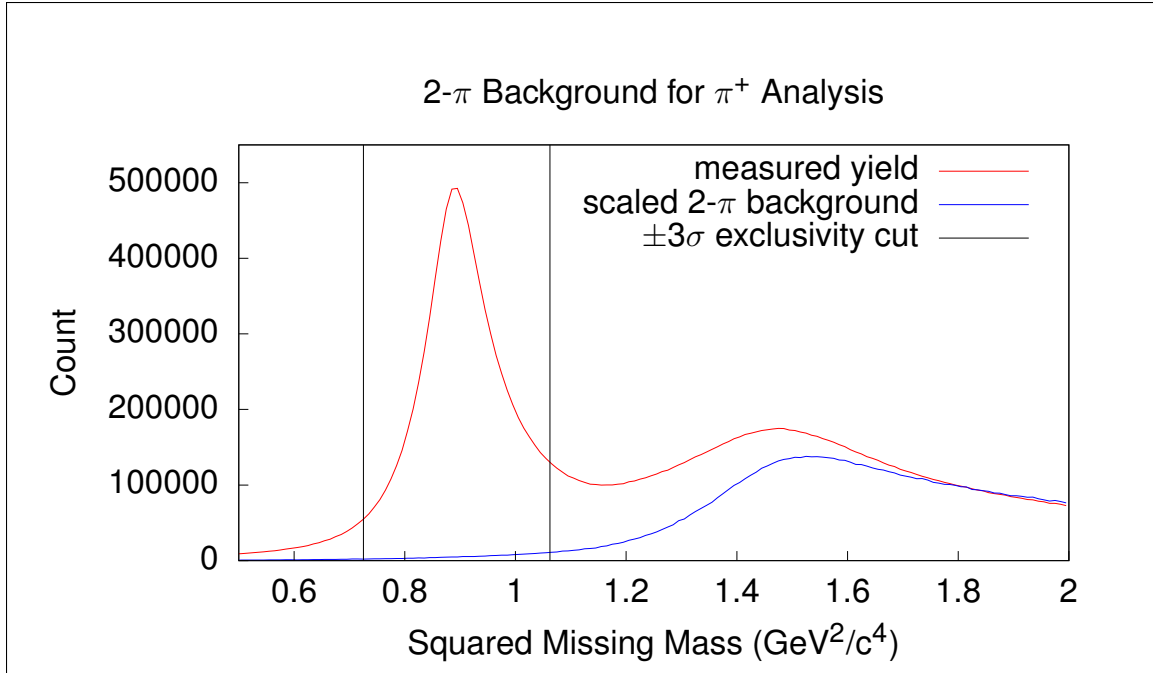


Figure 2.28: Squared missing mass distribution for the π^+ analysis integrated over full (W, Q^2) domain along with the exclusivity cut showing noticeable double-pion contamination within the cut range.

Due to imperfection in the Fermi-smearing effects added to simulation, there is a slight deviation in the missing mass distributions for simulated yields and measured yields. This defect does not appear in the absence of Fermi-smearing, and due to this defect it is not possible to apply the direct method of using simulation as a model of signal shape and subtracting this from measured yields to estimate background contributions. In response to this challenge, the background is modeled using a parametrization which attempts to describe a large family of possible background distributions, which is then fit against a background-dominated region of a given squared missing mass distribution, and then extrapolated and subtracted from the measured yields to estimate the signal distribution.

The model used for estimating and extrapolating background in the squared missing mass distributions is a sum of double-exponentially-convoluted Gaussian distri-

butions,

$$D(A, \mu, \sigma, \lambda_L, \lambda_R; x) = (E(\lambda_L, \lambda_R) \circ G(A, \mu, \sigma))(x), \quad (2.26)$$

where \circ denotes convolution, i.e. $(f \circ g)(x) = \int_{-\infty}^{\infty} f(t)g(x-t)dt$,

$$E(\lambda_L, \lambda_R; x) = \begin{cases} (\lambda_L^{-1} + \lambda_R^{-1})^{-1} \exp(\lambda_L x) & \text{for } x < 0 \\ (\lambda_L^{-1} + \lambda_R^{-1})^{-1} \exp(-\lambda_R x) & \text{for } x \geq 0 \end{cases}, \quad (2.27)$$

with λ_L, λ_R being positive parameters controlling the exponential tails of the model fit function and

$$G(A, \mu, \sigma; x) = \frac{A}{\sigma\sqrt{2\pi}} \exp\left(-\frac{(x-\mu)^2}{2\sigma^2}\right) \quad (2.28)$$

being the scaled Gaussian distribution. Due to the limitations of floating point arithmetic precision, it is recommended to use the following expression for the convoluted function D ,

$$D(A, \mu, \sigma, \lambda_L, \lambda_R; x) = \frac{A}{2}(\lambda_L^{-1} + \lambda_R^{-1})^{-1} \left(\exp\left(\frac{1}{2}(\sigma\lambda_L)^2 + \lambda_L(x-\mu) + \Psi\left(\frac{\sigma^2\lambda_L + x - \mu}{\sigma\sqrt{2}}\right)\right) + \exp\left(\frac{1}{2}(\sigma\lambda_R)^2 - \lambda_R(x-\mu) + \Psi\left(-\frac{\sigma^2(-\lambda_R) + x - \mu}{\sigma\sqrt{2}}\right)\right) \right), \quad (2.29)$$

where

$$\Psi(x) = \log(1 - \operatorname{erf}(x)),$$

and

$$\operatorname{erf}(x) = \frac{2}{\sqrt{\pi}} \int_0^x \exp(-t^2)dt$$

with $\Psi(x)$ available as a library function in some software libraries like the GNU Scientific Library's `gsl_sf_log_erfc` [25]. This exponential-convoluted Gaussian function D is able to describe some squared missing mass distributions directly, and others

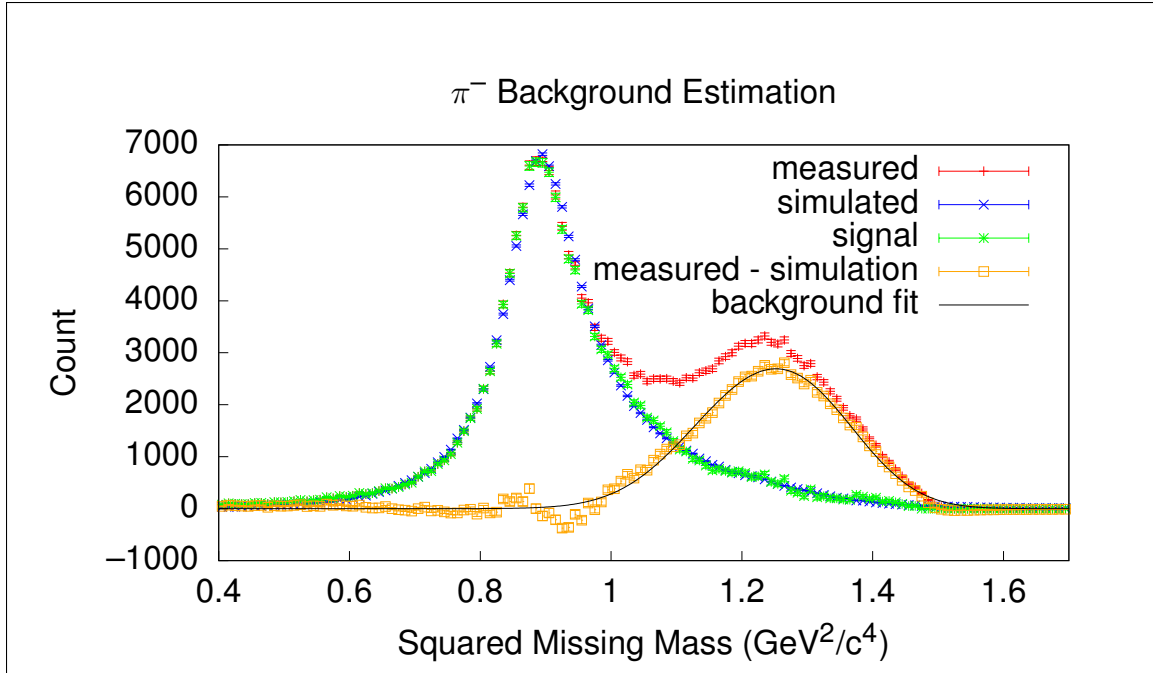


Figure 2.29: Example of background determination for the π^- analysis.

are described by a series of four or more with negligible error. Figures 2.29 and 2.30 show examples of fitting the difference between experiment yield and scaled simulation in the background-dominated high-missing mass region for the π^- and π^+ analyses, respectively. As can be seen, the modeled background function matches the yield distribution in the background-dominated region and then smoothens the region properly where the simulated distribution does not match the yield seamlessly because of a minimal shift of the simulated distribution relative to the measured distribution. Using this background function allows the signal-to-background ratio to be determined for a given squared missing mass cut, and vice versa, it allows the cut to be determined given a desired signal-to-background ratio. For simplicity, this latter method of determining cut boundaries given specific signal-to-background ratio is used to determine exclusivity cuts for the measured yields of all three analyses. As the simulation distributions for the π^- and π^+ analyses are slightly shifted and/or widened with respect to the measured yields, the squared missing mass cuts for simulation must be determined by another method. Cumulative distribution functions

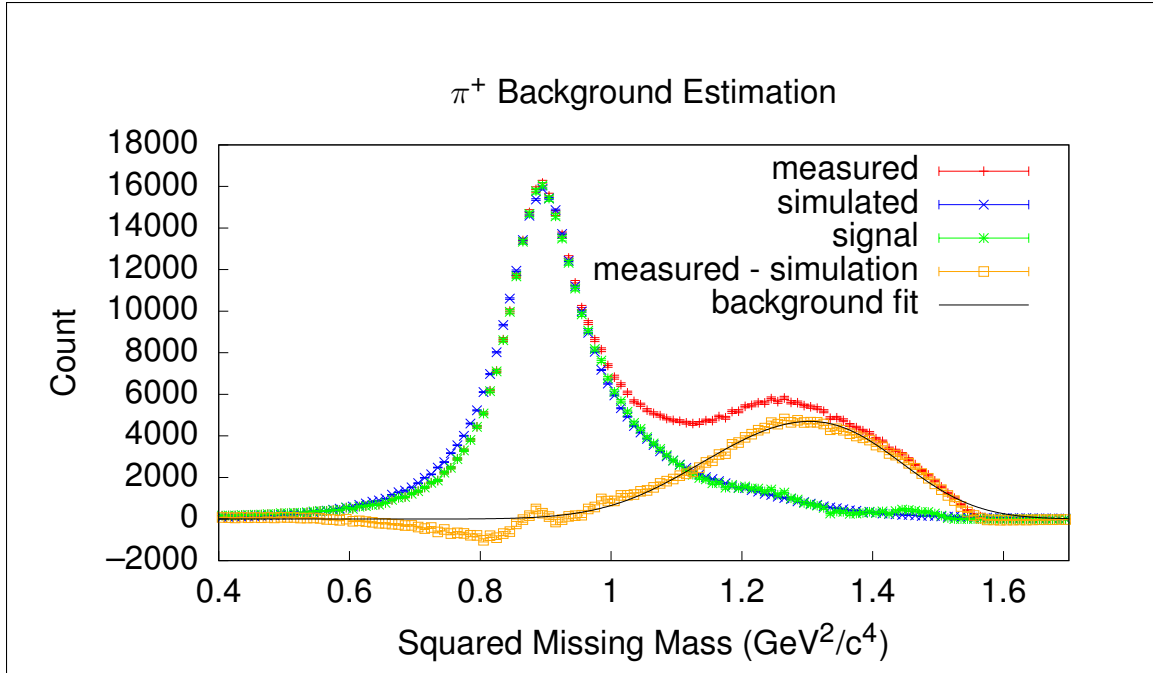


Figure 2.30: Example of background determination for the π^+ analysis.

(CDFs) for the estimated signal and background are then used to determine analogous cut boundaries such that the same amount of measured yield signal that was removed by the signal-to-background ratio determined cuts is removed from the corresponding simulation distribution. Figures 2.31 and 2.32 show examples of the final measured yield, background, signal, and simulation squared missing mass distributions along with the cuts applied to both measured yields and simulation for both analyses.

As noted earlier, this method controls the amount of background present due to cuts being determined in response to a demanded background ratio. Therefore, measured yields are corrected by multiplying by the signal-to-total ratio. The demanded background ratio used for final cross-section estimates in both analyses is 5% whenever there is significant background, and in the case of no noticeable background, there is no need for a multiplicative correction factor. Due to the fact that the choice of this ratio is arbitrary to some degree, systematic uncertainties associated with this method are included in Section 5.5.

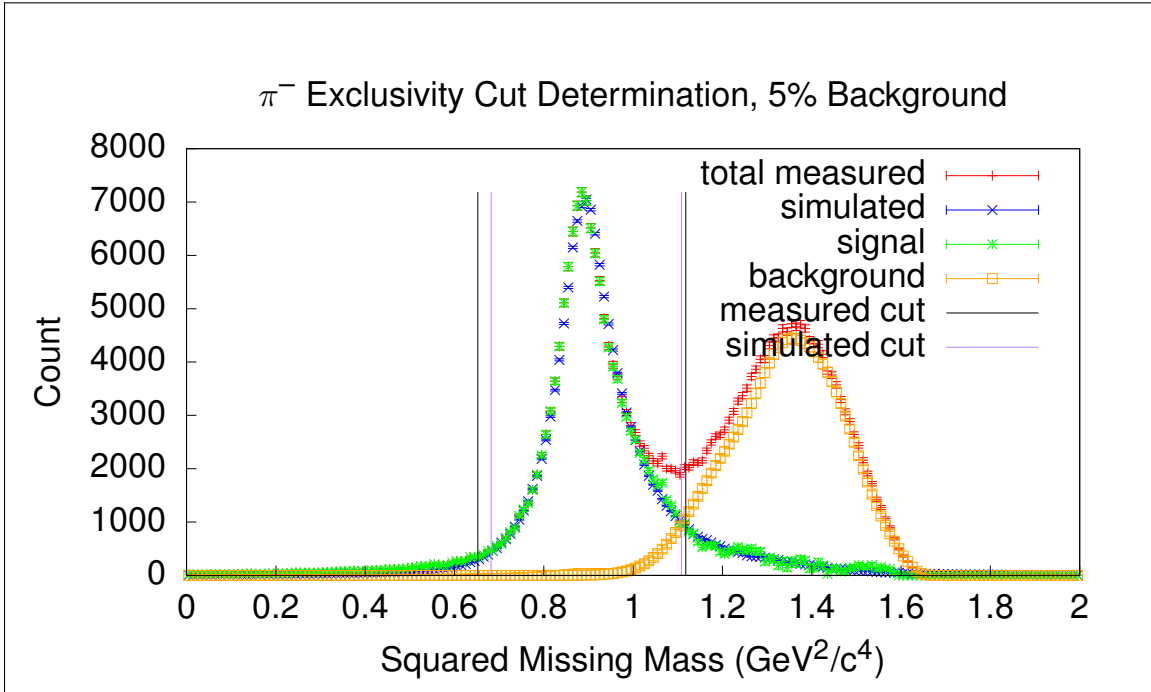


Figure 2.31: Example of squared missing mass cut determination for both experiment yields and simulation in the π^- analysis for a single $(W, Q^2, \cos(\theta^*))$ bin. Background ratio is set at 5%.

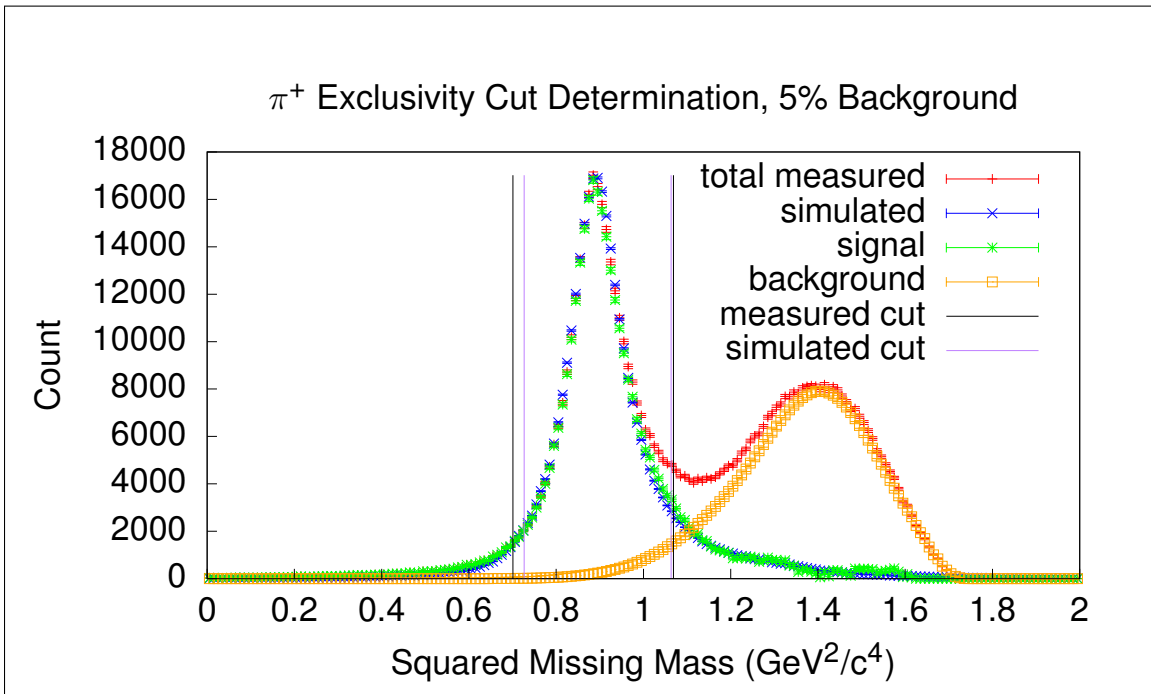


Figure 2.32: Example of squared missing mass cut determination for both experiment yields and simulation in the π^+ analysis for a single $(W, Q^2, \cos(\theta^*))$ bin. Background ratio is set at 5%.

2.5.1 FINAL STATE INTERACTIONS

As shown in [1], quasifree cross-sections can be extracted from the exclusive $\pi^- + p$ analysis by excluding events with missing spectator momenta above 200 MeV. In order to show that the background subtraction method used in this analysis removes final state interaction contributions, data from the exclusive $\pi^- + p$ analysis with this same 200 MeV missing spectator momentum cut applied is then treated as if the final state proton were not measured, resulting in Fermi-smearred quasifree yields. Comparing the squared missing mass distributions for the full yields and quasifree yields requires some careful treatment however, since cutting on the spectator momentum reduces the amount of Fermi-smearing in the yields by removing the high-momentum tail of the target nucleon momentum distribution. To address this, simulated yields are treated in the same way as the experiment yields, so that reconstructed events from the $\pi^- + p$ analysis are treated as if the proton were not reconstructed, both with and without the 200 MeV spectator momentum cut. The resulting simulated squared missing mass distributions are shown in Figure 2.33. To compare the signal squared missing mass distribution to the quasifree squared missing mass distribution from experiment, the signal is multiplied by a smearing-adjustment factor calculated as the ratio between the simulated full yield and simulated “quasifree” yield, i.e. simulated data with the 200 MeV spectator momentum cut applied.

$$S_{\text{qf}}(M_p^2) = \frac{N_{\text{qf}}(M_p^2)}{N(M_p^2)}, \quad (2.30)$$

where M_p^2 is the squared missing proton mass, N_{qf} is the ignored-proton yield with the 200 MeV spectator momentum cut applied, and N is the ignored-proton yield without the spectator momentum cut applied. This ratio is shown in Figure 2.34, and as shown in Figure 2.35, the smearing-adjusted signal shape acquired by the background subtraction method used in this analysis accurately reproduces the shape of Fermi-

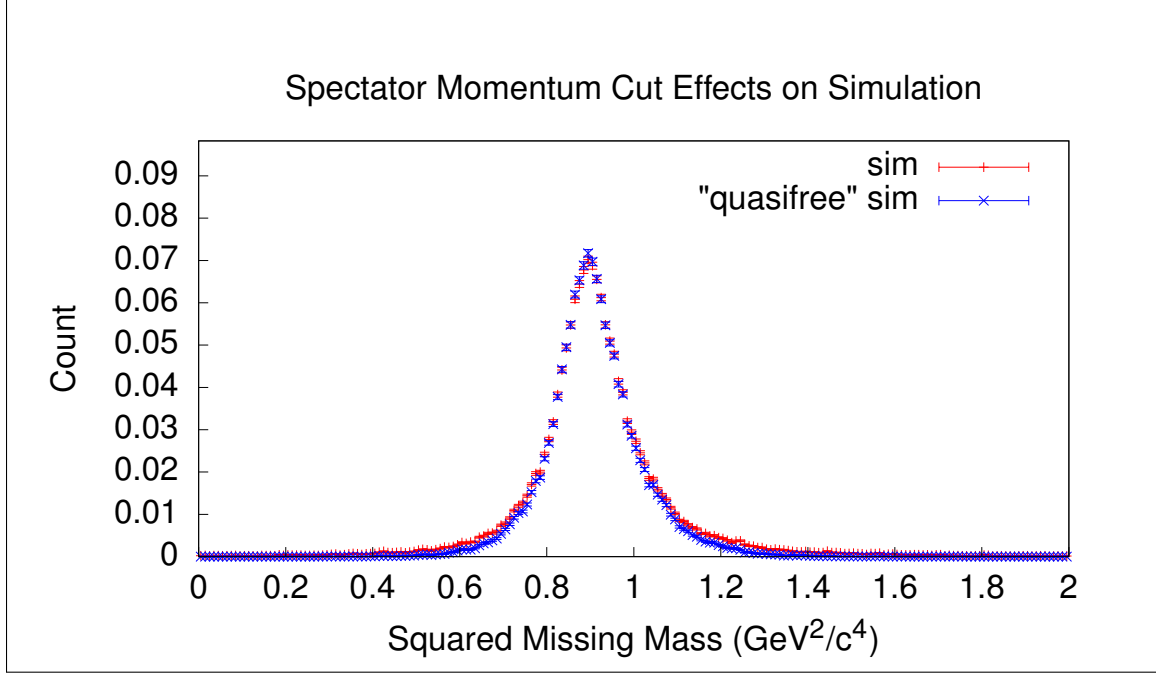


Figure 2.33: Comparison between simulated data with the 200 MeV spectator momentum cut and full simulation yields for the $\pi^- + p$ analysis.

smearred quasifree events except for the reduced width of the quasifree distribution, and therefore all noticeable final state interaction contributions have been removed by the background subtraction method.

2.6 BINNING

As the method for cross-section extraction in this work is to use binned data analysis, the binning must be specified. Following [1], three different binnings are used simultaneously for each of the three analyses, each being identical except for the number of bins along the ϕ^* axis as summarized in Table 2.2. Figures 2.36, 2.37, and 2.38 show the final selected (W, Q^2) yields for all three analyses with the (W, Q^2) binning superimposed.

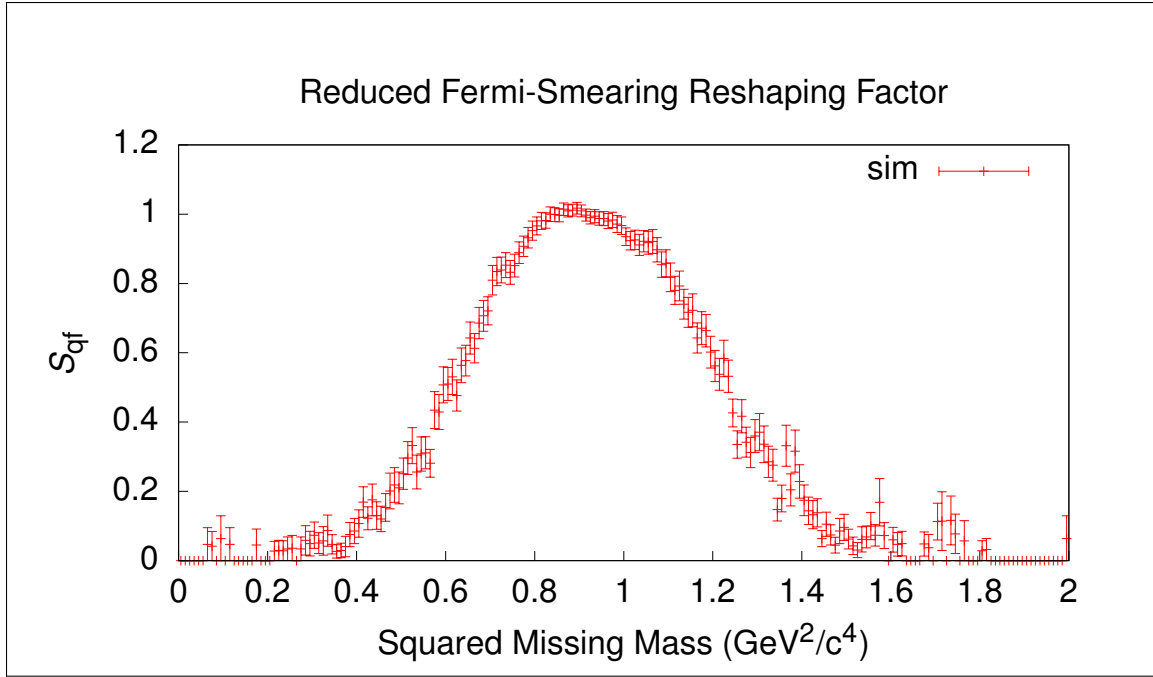


Figure 2.34: Factor by which the signal can be reshaped to account for missing Fermi-smearing after applying a 200 MeV missing spectator momentum cut.

Table 2.2: ($W, Q^2, \cos(\theta^*), \phi^*$) binnings.

Axis	Low	High	# Bins
W (GeV)	1.1	1.9	32
Q^2 (GeV^2/c^2)	0.4	1.0	3
$\cos(\theta^*)$	-1	1	10
ϕ^* #1 (deg)	0	360	6
ϕ^* #2 (deg)	0	360	8
ϕ^* #3 (deg)	0	360	9

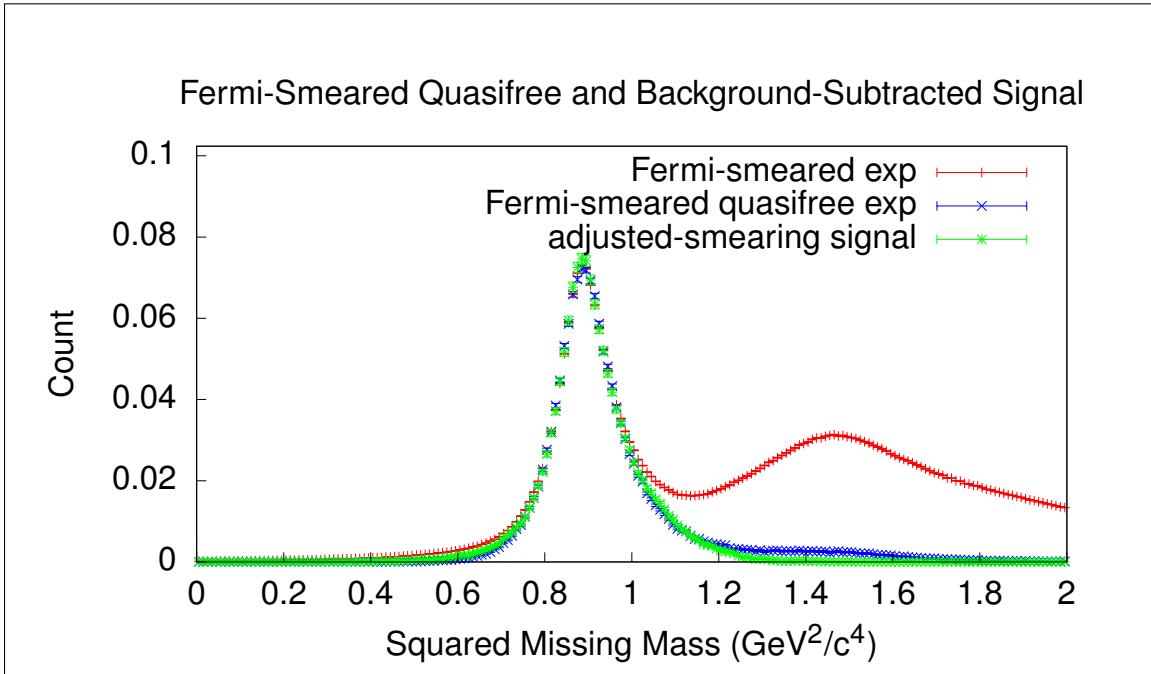


Figure 2.35: Comparison of squared missing mass distributions for Fermi-smeared yields, Fermi-smeared quasifree yields, and the adjusted-smearing signal distribution obtained from the background-subtracted π^- analysis. Since the signal shape matches the Fermi-smeared quasifree distribution after being adjusted for reduced Fermi-smearing due to the spectator momentum cut, all noticeable final state interactions have been removed via the background subtraction method.

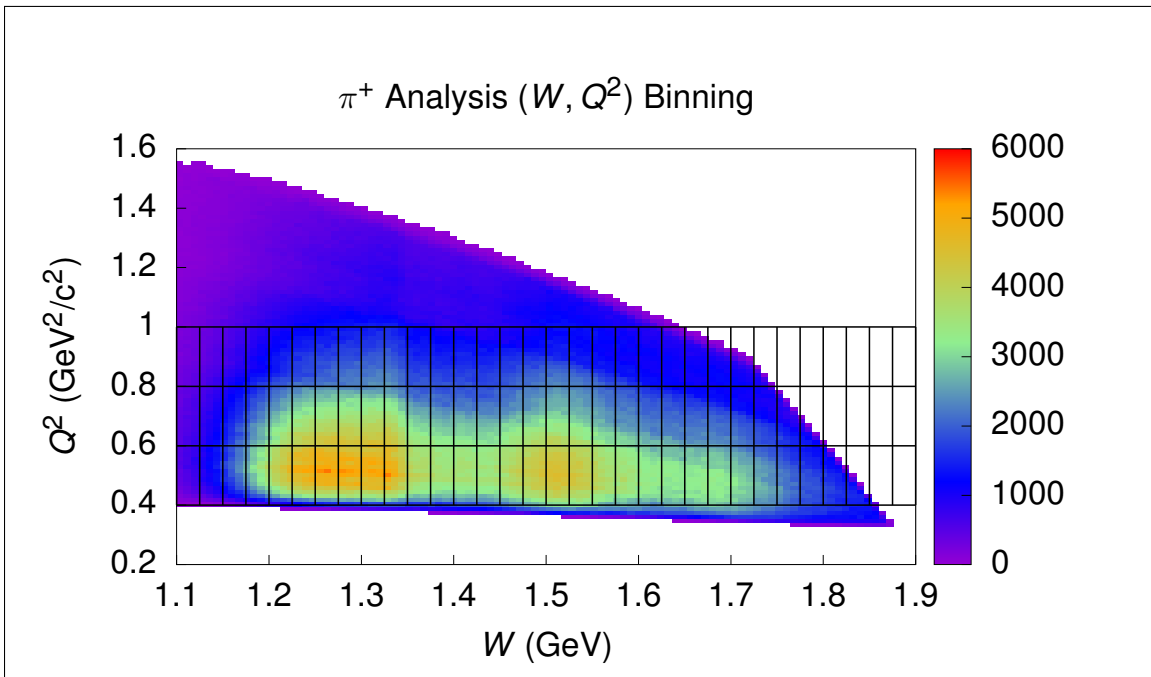


Figure 2.36: π^+ final (W, Q^2) yields with binning superimposed.

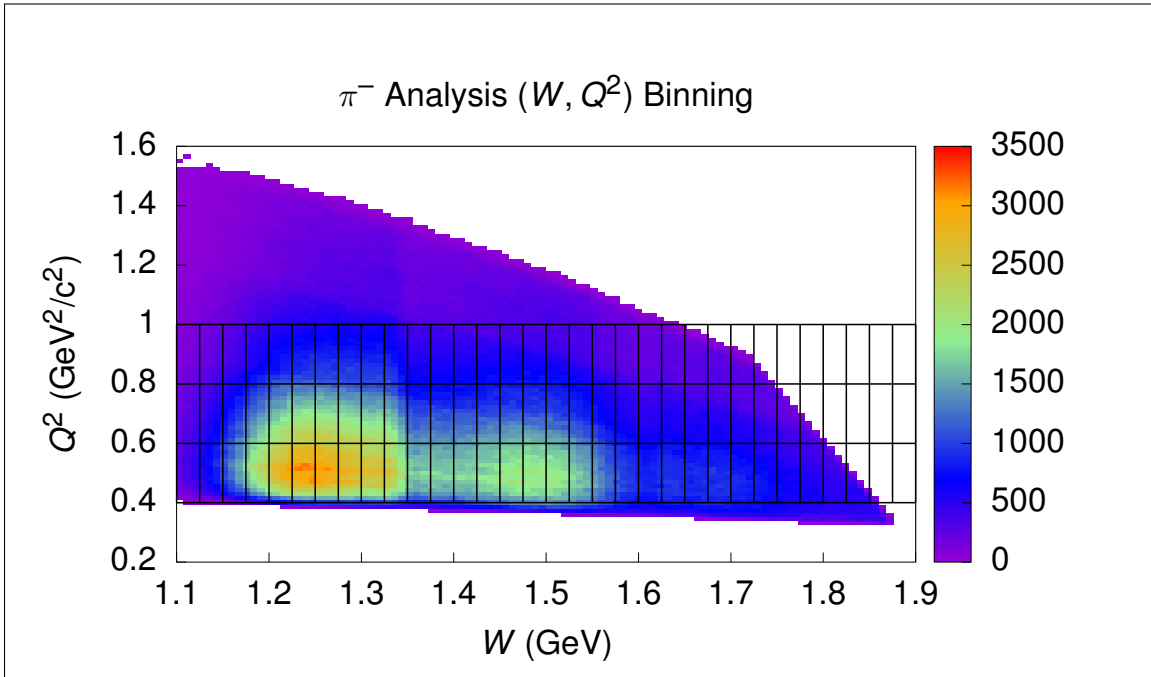


Figure 2.37: π^- final (W, Q^2) yields with binning superimposed.

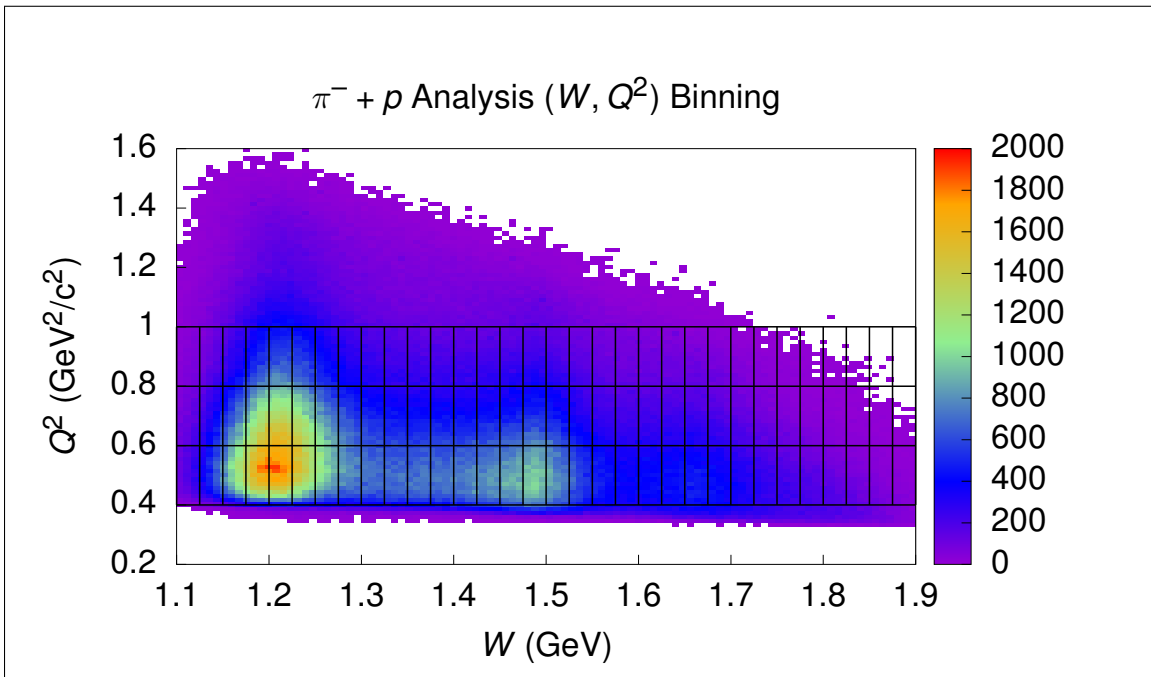


Figure 2.38: $\pi^- + p$ final (W, Q^2) yields with binning superimposed.

CHAPTER 3

DATA CORRECTIONS

Besides typical data corrections, like binning and acceptance corrections, there are a few known detrimental effects imposed on the data due to limitations of the CLAS detector, but they are well understood and can be removed systematically. In this analysis, this is achieved by kinematic and energy loss corrections applied to the electron and proton. There is also the effect described earlier in this work called Fermi-smearing, and as promised a method for Fermi-unsmearing affected data will then be presented in the next chapter.

3.1 BIN-CENTERING

When random variables are sampled from a probability density function and then binned, the centers of the bins cannot necessarily be used to naively recalculate an estimate of that probability density function (PDF) from the binned data. More precisely, for a random variable x governed by a PDF $\rho(x)$, the expected count in a bin B after N samples is

$$n(B) = N \int_B \rho(x) dx. \quad (3.1)$$

If the naive estimate taken directly from a histogram,

$$\rho(x) \approx \frac{n(B)}{V_B}, \quad (3.2)$$

with V_B being the volume of bin B , were used, then this estimate is the mean value of $\rho(x)$ over B , which is not necessarily the same as the value of $\rho(x)$ at the center of B . It is therefore necessary in cross-section extractions to attempt to correct for

this flaw when using binned yields to estimate differential cross-sections by using a model to estimate how different the cross-section would be at the center of each bin from the average cross-section value over each entire bin.

To this end, I wrote a program that uses the MAID model and ROOT's numerical integration routines to calculate the estimated average cross-section value for a given bin along with the cross-section value at the center of the bin so that the ratio between the center cross-section value $\bar{\sigma}(W, Q^2, \cos(\theta^*), \phi^*)$ and average cross-section value $\sigma(W, Q^2, \cos(\theta^*), \phi^*)$,

$$R_{BC} = \frac{\sigma(W, Q^2, \cos(\theta^*), \phi^*)}{\bar{\sigma}(W, Q^2, \cos(\theta^*), \phi^*)}, \quad (3.3)$$

can be computed and applied to cross-section estimates as the bin-centering correction. The necessary source code for this program can be found in [26], with a necessary utility library being found in [27]. Figures 3.1 and 3.2 show the bin-centering correction factor for some selected bins for both the $e^- + n \rightarrow e^- + p + \pi^-$ and $e^- + p \rightarrow e^- + n + \pi^+$ reaction channels.

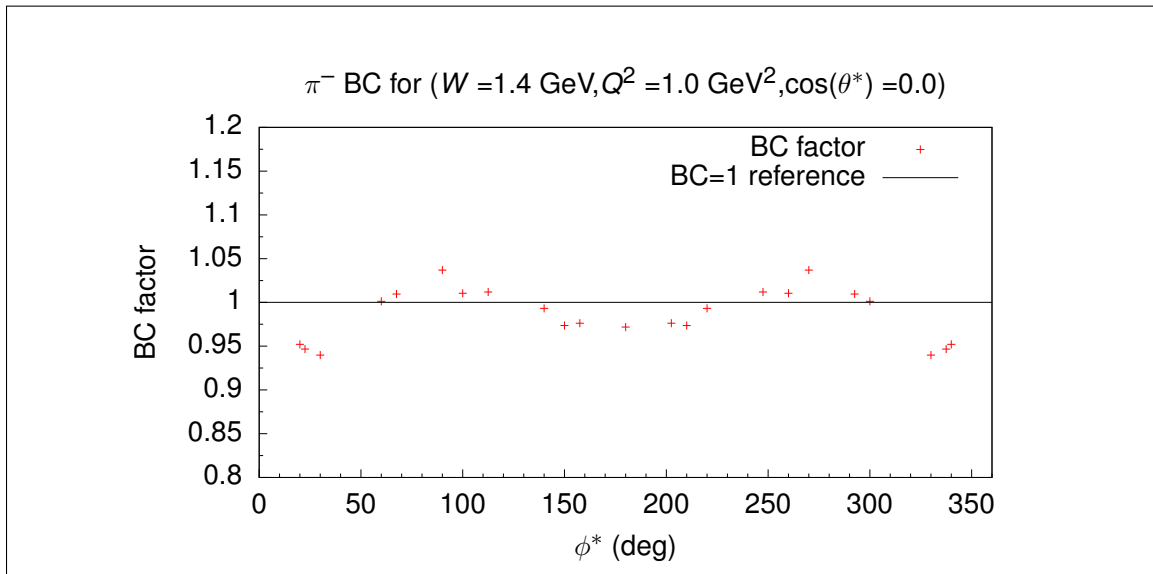


Figure 3.1: Bin-centering correction factor for selected bins for the $e^- + n \rightarrow e^- + p + \pi^-$ reaction channel.

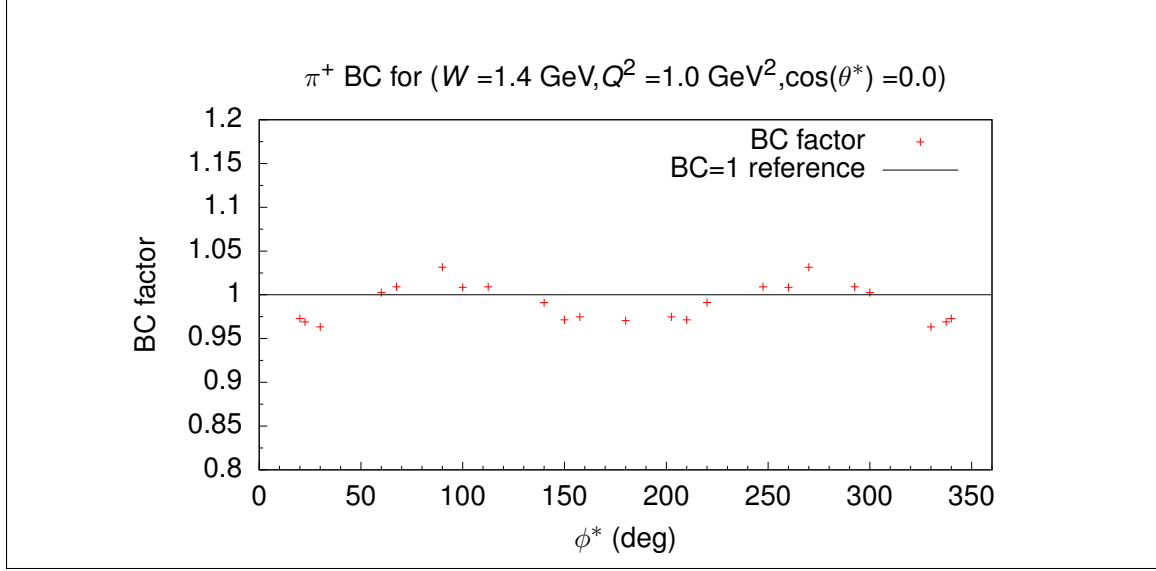


Figure 3.2: Bin-centering correction factor for selected bins for the $e^- + p \rightarrow e^- + n + \pi^+$ reaction channel.

3.2 KINEMATIC CORRECTIONS

In this analysis, there are two relevant kinematic corrections: Electron momentum corrections and proton energy loss corrections. The electron kinematic corrections need only be applied to experimental data, as the source of an erroneous momentum reconstruction is the lack of precise knowledge of the applied magnetic field. The proton energy loss corrections are applied to both experiment and simulation data as the erroneous proton energy reconstruction is an effect from the detector both in experiment data and the simulated detector.

3.2.1 ELECTRON MOMENTUM CORRECTIONS

Electron kinematic corrections are well-developed for CLAS data as described in [28], and the method will be briefly summarized here. The electron kinematic corrections method is based on using elastic scattering, and so the E1E proton target data is used rather than the deuterium target data since both were taken under identical

experiment conditions aside from the choice of target. The chief assumptions of the method are as follows.

1. Azimuthal angles are accurately measured.
2. Polar angle corrections do not depend on particle charge.
3. Polar angles greater than 35° (elastic scattering) are measured properly.

These assumptions allow for a detected proton polar angle θ_p , whenever greater than 35° , to be used to calculate the appropriate electron angle θ_e via the kinematic constraints of elastic scattering, namely

$$\theta_{\text{ecalc}} = 2 \tan^{-1} \left(\frac{m_p}{(E_b + m_p) \tan \theta_p} \right), \quad (3.4)$$

where m_p is the proton mass and E_b is the beam energy. Having both the initially measured θ_e and θ_{ecalc} , it is possible to parametrize the difference between measured and true electron angle as a polynomial function in (θ, ϕ) for each sector,

$$\delta\theta_e = \theta_{\text{ecalc}} - \theta_e = \sum_{j=0}^2 \sum_{k=0}^3 a_{jk} \theta_e^j \phi_e^k, \quad (3.5)$$

where a_{jk} are the parameters to be fit against the measured angle deviations.

Once θ corrections have been determined, the electron's corrected θ can be used to correct the electron momentum as a function of (θ, ϕ) as well,

$$p_{\text{ecalc}} = \frac{E_b}{1 + \frac{2E_b}{m_p} \sin^2\left(\frac{\theta_{\text{ecalc}}}{2}\right)}, \quad (3.6)$$

with the corrected momentum being modeled by

$$p_{\text{ecalc}} = p_e g(\theta_e, \phi_e, s), \quad (3.7)$$

where

$$g(\theta_e, \phi_e, s) = \sum_{j=0}^2 \sum_{k=0}^3 b_{jk}(s) \theta_e^j \phi_e^k, \quad (3.8)$$

θ_e is now the corrected polar angle of the electron, s is the sector of the scattered electron, and $b_{jk}(s)$ are the parameters to be fitted against the ratio p_{ecal}/p_e for each sector. Note here that ϕ_e is relative to each sector, so that ϕ_e always falls within the range $[-30^\circ, 30^\circ]$. Figure 3.3 shows an example $\delta\theta_e$ distribution along with the Gaussian fit, Figure 3.4 shows the fit results for $\delta\theta_e$ for a selected sector and various ϕ or θ values, and Figure 3.5 shows the fits for $g(\theta_e, \phi_e, s)$ in each sector.

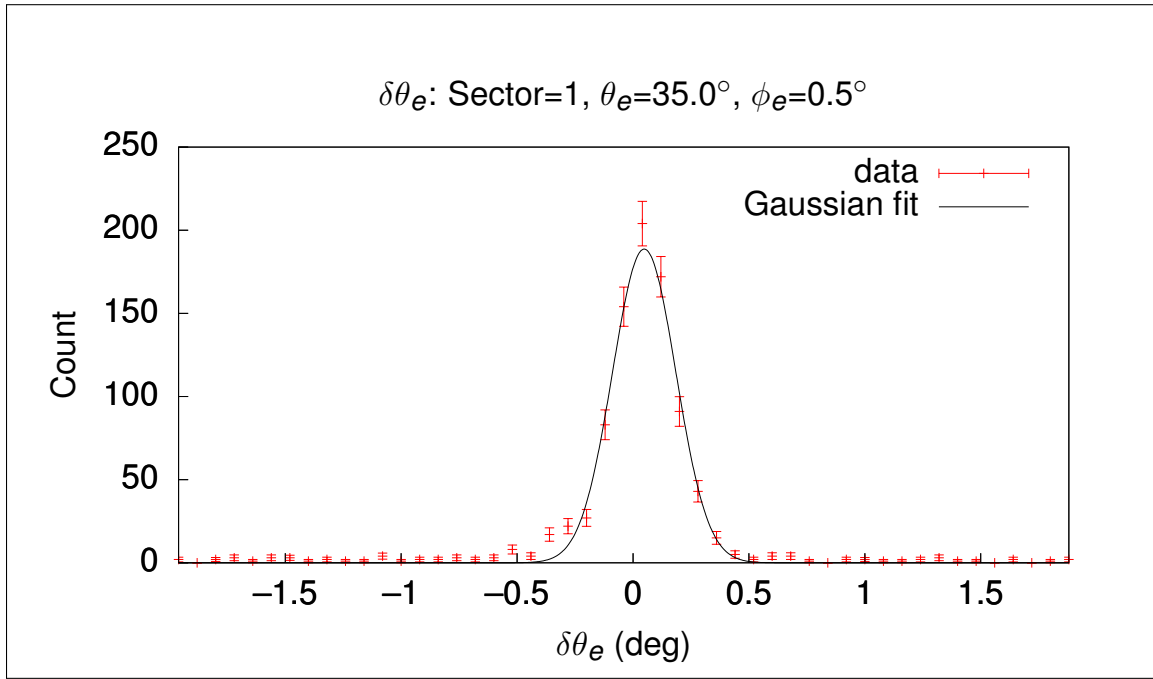


Figure 3.3: Example $\delta\theta_e$ distribution and fit for Sector 1, θ_e and ϕ_e .

The goal of kinematic corrections being to obtain accurate reconstruction of particle trajectories, a sure test for the efficacy of kinematic corrections is an improvement to the kinematically relevant features of the data. Figure 3.6 shows a comparison between the squared missing mass distributions for experiment data before and after kinematic corrections were applied to the electron momentum for the $\pi^- + p$ analysis.

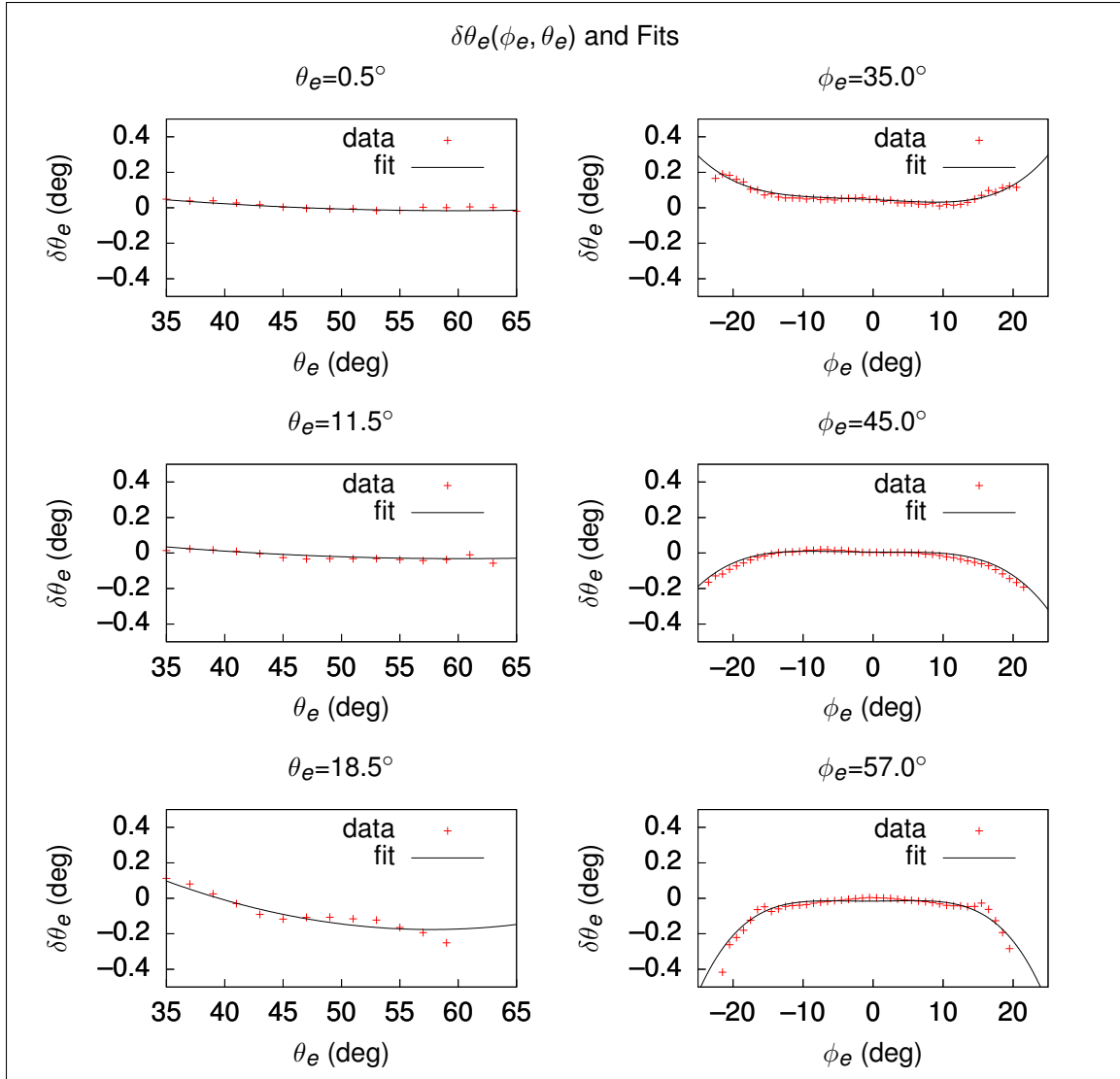


Figure 3.4: $\delta\theta_e$ versus. θ_e and ϕ_e with fits for Sector 1 and various θ_e or ϕ_e selections.

3.2.2 PROTON ENERGY LOSS CORRECTIONS

In both experiment and simulation, reconstructed protons are known to have inaccurate energies due to energy losses [1]. These energy losses can be corrected via Monte Carlo simulations of proton trajectories, so that the thrown proton energy is known as well as the reconstructed energy for each event. As this only affects the $\pi^- + p$ analysis as neither of the other two analyses rely on reconstructing proton tracks, and since the same data set is being analyzed, the proton energy loss correction is

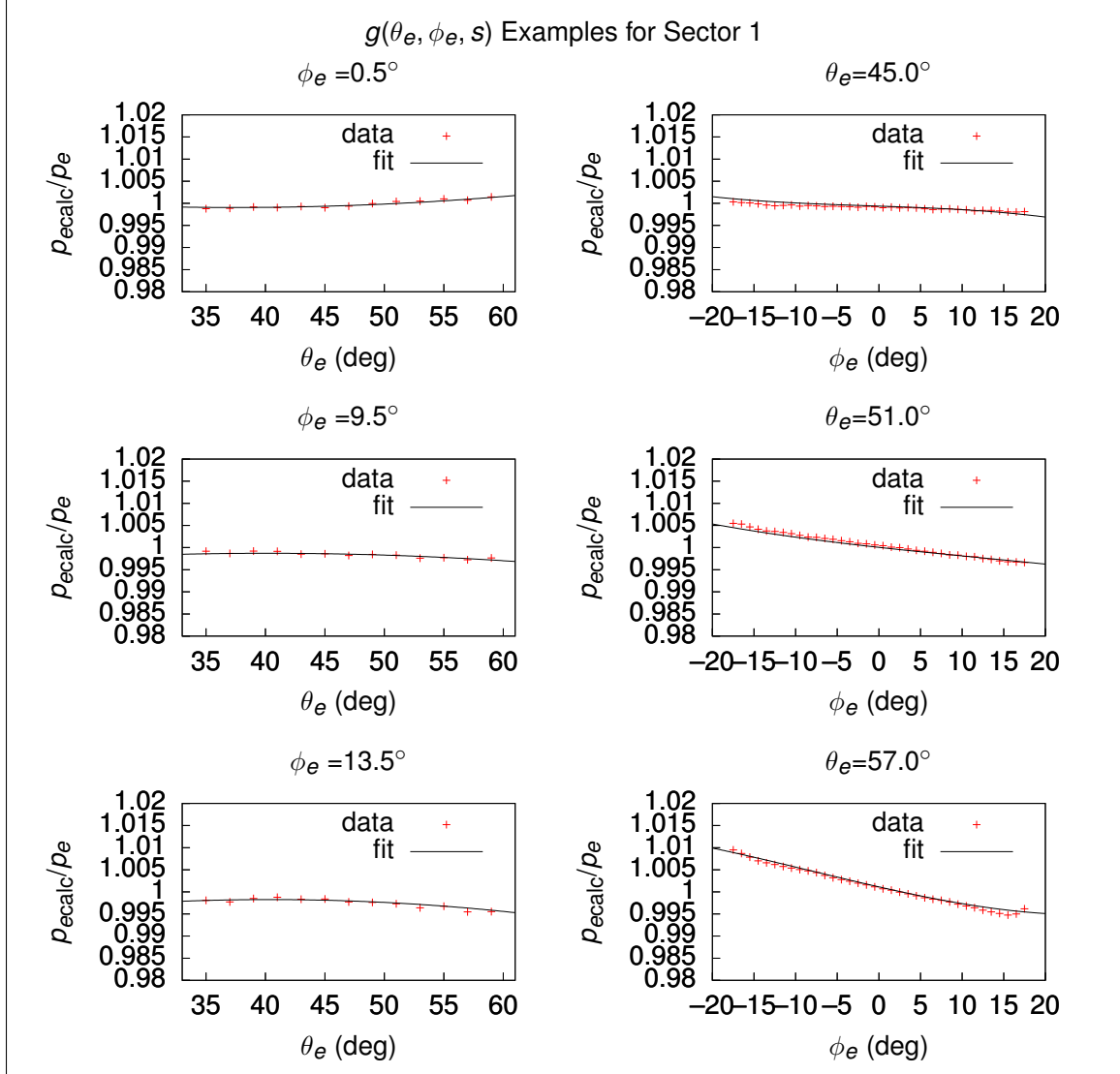


Figure 3.5: $g(\theta_e, \phi_e, s)$ fits versus θ and ϕ for Sector 1.

only summarized here, and the parameters from [1] are used directly for the $\pi^- + p$ analysis.

As described in [1], a custom proton Monte Carlo event generator is used in conjunction with GEANT, and the difference between thrown and reconstructed momenta is fit by a function of the proton's polar angle and momentum,

$$\delta p = \sum_{k=0}^2 a_k \theta_p^k + \sum_{k=0}^2 b_k \theta_p^k p + \sum_{k=0}^2 c_k \frac{\theta_p^k}{p}, \quad (3.9)$$

where p is the proton momentum, θ_p is the proton polar angle, and a_k, b_k, c_k are fit parameters. After fitting each of these δp histograms with Gaussian distributions for each θ_p and momentum bin, the fit-determined mean δp values, $\overline{\delta p}(p, \theta_p)$, for each bin can themselves be fit with the function defined in Equation 3.9. Figure 3.6 shows the effects of applying both electron kinematic corrections and proton energy loss corrections on the squared missing spectator mass distribution, resulting in a noticeable shift in the squared missing mass distribution.

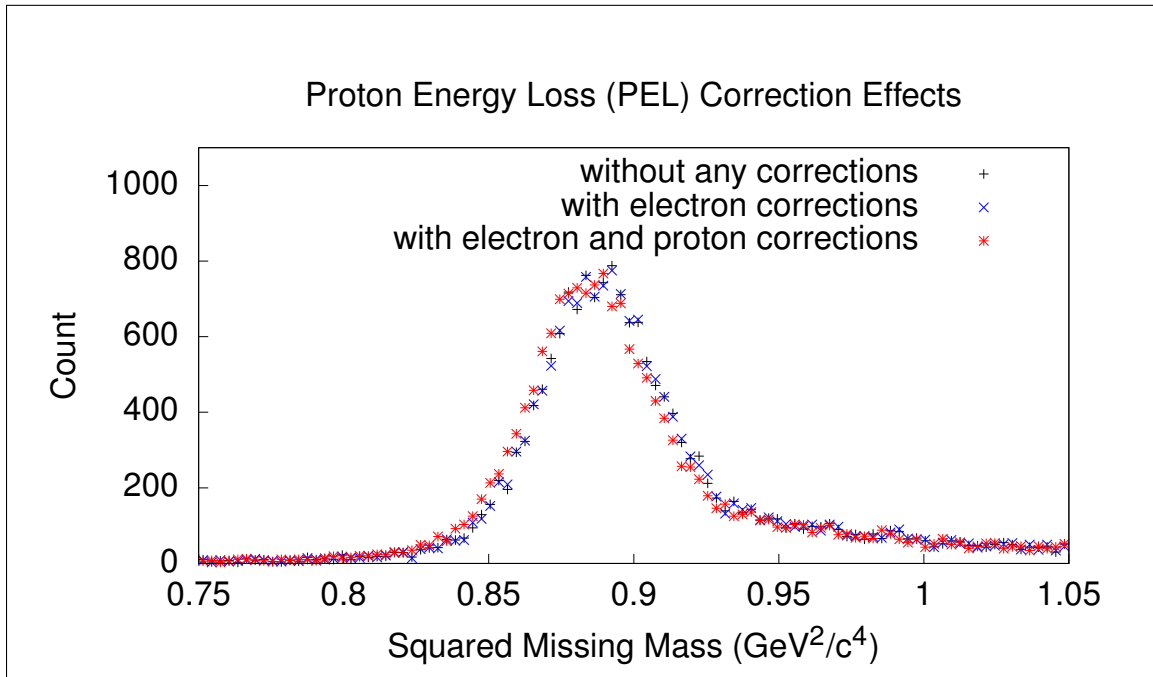


Figure 3.6: Comparison of the squared missing spectator mass with no kinematic corrections, just electron kinematic corrections, and both electron corrections and proton energy loss corrections applied for subset of $\pi^- + p$ analysis measured data.

3.3 ACCEPTANCE CORRECTIONS

Acceptance corrections are the single most important correction factor in cross-section extractions for this analysis. Acceptance is defined to be the ratio between the true number of events that have occurred and the measured number of events measured

by the CLAS detector,

$$A_{\text{ideal}} = \frac{N_{\text{measured}}}{N_{\text{true}}}. \quad (3.10)$$

This is not something that can be measured without some kind of perfect reference CLAS detector; therefore, simulations are used to estimate the acceptance in the confidence of understanding the fundamental physics and the design of the detector in sufficient detail. The practical definition of acceptance is

$$A = \frac{N_{\text{reconstructed}}}{N_{\text{thrown}}}, \quad (3.11)$$

where $N_{\text{reconstructed}}$ is the number of events that have been virtually measured by the simulated CLAS detector given some N_{thrown} simulated events as input to the simulated detector. All of these quantities can be parametrized or binned, so that the acceptance within a single bin is the ratio of reconstructed and thrown events within just that bin. As this analysis performs three separate cross-section extractions, there are three separate acceptance factors. The tables in Appendix B.7.2 provide a summary of the various cuts and correction factors that are applied to each of the three simulated yields and used to compute the acceptances. In all three analyses, the MAID2000 model [23] is used as it is the best MAID model for describing the $e^- + n \rightarrow e^- + p + \pi^-$ reaction channel as well as adequately describing the $e^- + p \rightarrow e^- + n + \pi^+$ reaction channel.

Figures 3.7, 3.8, and 3.9 show the acceptance for sample 4-D bins along with the acceptance values themselves gathered into a histogram to show the distribution of acceptance along the three ϕ^* binnings simultaneously for a given $(W, Q^2, \cos(\theta^*))$ bin. As the binned acceptance value plots show, there is a threshold value for acceptance below which a relatively large number of bins have very low acceptances. This leads to a variety of problems in extracting the cross-section estimates, and therefore a

selection criterion is imposed such that only bins with acceptances greater than 1% are used for cross-section extraction.

3.3.1 BEAM-OFFSET CORRECTION

During cooking, the beam is assumed to be at $x = 0$ cm, $y = 0$ cm in the detector coordinate system, and therefore an offset in the beam position will lead to inaccuracies in reconstructed particle trajectories. For E1E, the beam is known to be offset at approximately $x = 0.058$ cm, $y = -0.182$ cm. To address this, Monte Carlo data is reconstructed using a beam offset that matches the experiment data, so that reconstructed trajectories are affected by the offset in the same way that the experiment data is affected. Since the thrown data uses accurate trajectories, the acceptance correction factor includes the beam-offset correction. Figure 3.10 shows the electron vertex (x, y) distributions for experiment and simulation, which is a measure of the beam position, confirming agreement between the beam offsets in experiment and simulation.

3.4 RADIATIVE-EFFECTS CORRECTIONS

Radiative-effects in this analysis are corrected in two closely related but different ways due to the conditional use of the Fermi-unsmearing algorithm. It is mathematically equivalent to correct for radiative-effects and Fermi-smearing with either a single combined radiative-effects Fermi-unsmearing factor or separate radiative-effects and Fermi-unsmearing factors (described in detail in Chapter 4), provided that the Fermi-unsmearing factor has radiative-effects enabled. However, due to practical considerations, the combined radiative-effects Fermi-unsmearing method is used for the π^+ and π^- analyses, as doing so allows for only two Monte Carlo data sets to be maintained, one with neither radiative-effects nor Fermi-motion, and another with both. It is still possible to isolate the radiative-effects correction factors using this method, which is what is done in this section for all analyses, and as radiative-effects corrections

are a function of the reaction channel, not the analysis method, there are only two such factors. As mentioned in Section 1.5, `onepigen` is used to generate Monte Carlo simulations with and without radiative-effects or with and without Fermi-motion independently, so that radiative-only, Fermi-unsmearing-only, and combined radiative-Fermi-unsmearing corrections can be computed. As also stated before, the MAID2000 model is used for generating thrown events as it fits the $e^- + n \rightarrow e^- + p + \pi^-$ data best as described in [1].

Using the radiative-effects model from Mo and Tsai [29], correction factors can be defined in an analogous way as the acceptance correction factor was defined:

$$R = \frac{N_{\text{norad}}(W, Q^2, \cos(\theta^*), \phi^*)}{N_{\text{rad}}(W, Q^2, \cos(\theta^*), \phi^*)}, \quad (3.12)$$

where $N_{\text{rad}}(W, Q^2, \cos(\theta^*), \phi^*)$ and $N_{\text{norad}}(W, Q^2, \cos(\theta^*), \phi^*)$ are binned thrown data with radiative-effects from Mo and Tsai enabled or not enabled, respectively. As there is a factor for each reaction channel, R_- is used to denote this factor for the $e^- + n \rightarrow e^- + p + \pi^-$ channel and R_+ is used for the $e^- + p \rightarrow e^- + n + \pi^+$ channel. Cross-section estimates are simply multiplied by the appropriate R_{\pm} factor to remove radiative-effects from the estimate. Figures 3.11 and 3.12 show the radiative correction factor for selected bins for both reaction channels.

3.5 NORMALIZATION

Due to Ye Tian's analysis [1] already having verified and approved luminosity normalization for the E1E deuteron target data set, no normalization check is needed for this analysis. To summarize the findings, M. Osipenko's inclusive cross-section world data parametrization is compared with the inclusive cross-section extracted from E1E data, showing no significant difference between them, and therefore no additional corrections are needed to extract cross-sections from E1E deuteron target data sets.

3.6 EMPTY-TARGET SUBTRACTION

As the target is not the only material in the vicinity of the beam during scattering experiments, those additional materials will interact with the beam and add background noise to the desired reaction yields. To address this effect on the data, experiment runs are executed without the target cell being filled but otherwise identical experiment conditions. For E1E, these empty-target runs are 36597, 36617, 36618, and 36619. These runs are treated with identical selection criteria and kinematic corrections so that final binning histograms can be computed, scaled based on their luminosity, and subtracted from the filled-target runs in order to remove the effects of all additional materials beyond deuterium that are in the beam. In order to confirm that the scaling and subtraction are successful, the electron vertex z -coordinate distributions can be compared, as there is both the target housing and a thin film target placed separately in the beam line. To determine the scale factor between empty-target and filled-target runs, the Faraday cup charge is used to define the scale factor as

$$R_{\text{empty}} = \frac{Q_{\text{filled}}}{Q_{\text{empty}}}, \quad (3.13)$$

where $Q_{\text{filled}} = 4.323572 \text{ mC}$ is the total Faraday cup charge for the filled-target runs, and $Q_{\text{empty}} = 0.466258 \text{ mC}$ is the total Faraday cup charge for the empty-target runs. Figure 3.13 shows the electron vertex z -coordinate distributions of filled-target and scaled empty-target runs, in which the film location is visible in both. If the scaling factor is accurate, then the film region of the vertex z -coordinate distributions should match. Figure 3.14 shows a zoomed version of the same comparison plot so that the thin film region can be clearly compared. Note that there is also a need to shift the empty-target run vertex z -coordinate distributions by -1.5 mm as indicated in Figure 3.13 in order to have full coincidence of the film vertex z -coordinate distributions. As the scaling factor is accurate, this scaling factor is used to scale data from the empty-

target runs analyzed and binned in the same way as was the filled-target data, and this scaled empty-target data is then subtracted from the filled-target yields before applying other correction factors such as acceptance corrections or radiative-effects corrections.

As can be seen in Figures 3.13 and 3.14, the z-coordinate distributions for each sector do not match exactly. This is due to the beam offset in E1E. Correcting for the beam offset is accomplished via the acceptance correction factor as explained in Section 3.3.1.

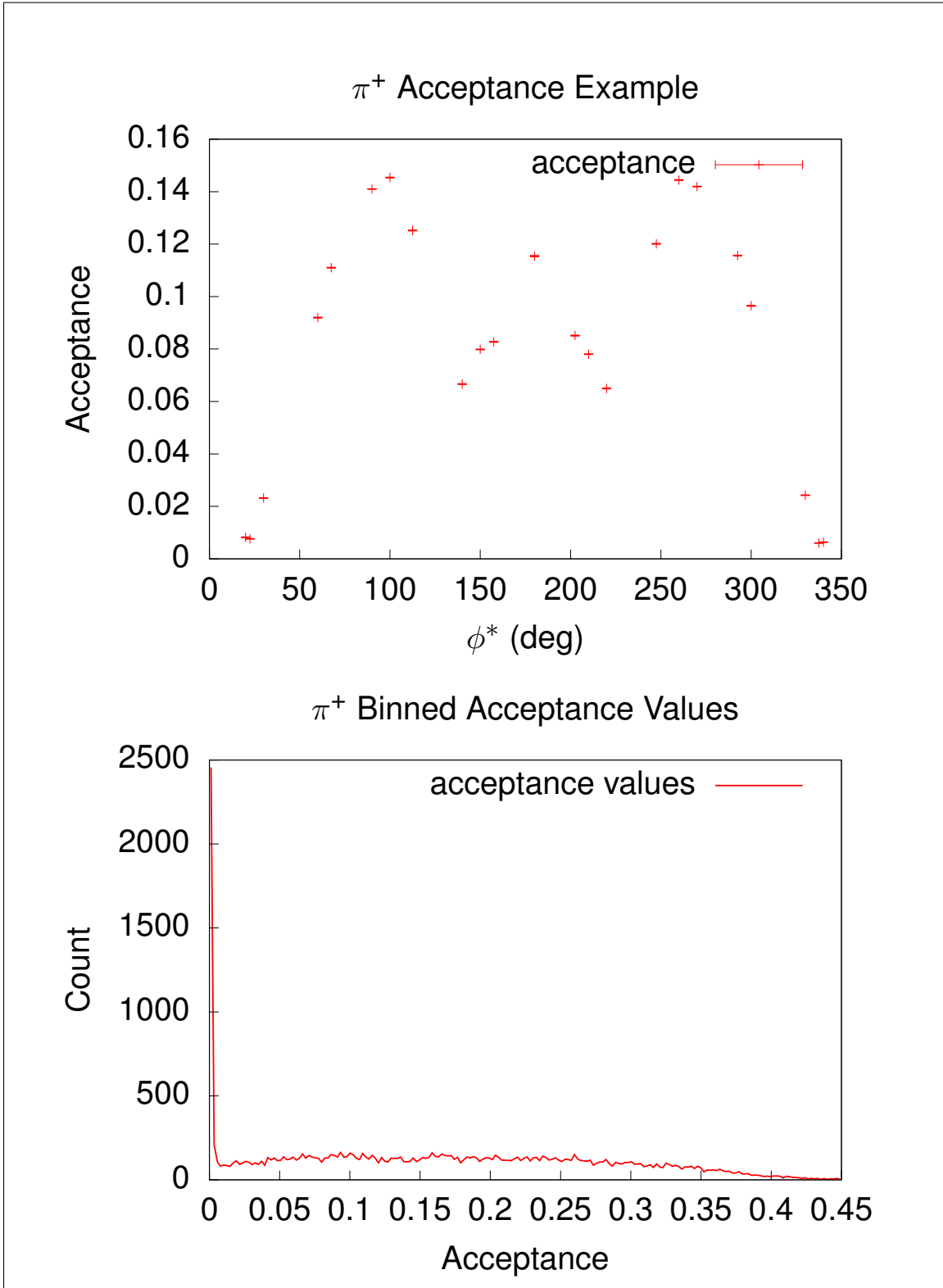


Figure 3.7: π^+ analysis acceptance for selected bins along with binned acceptance values. $W = 1.25$ GeV, $Q^2 = 0.5$ GeV²/c², $\cos(\theta^*) = 0.1$.

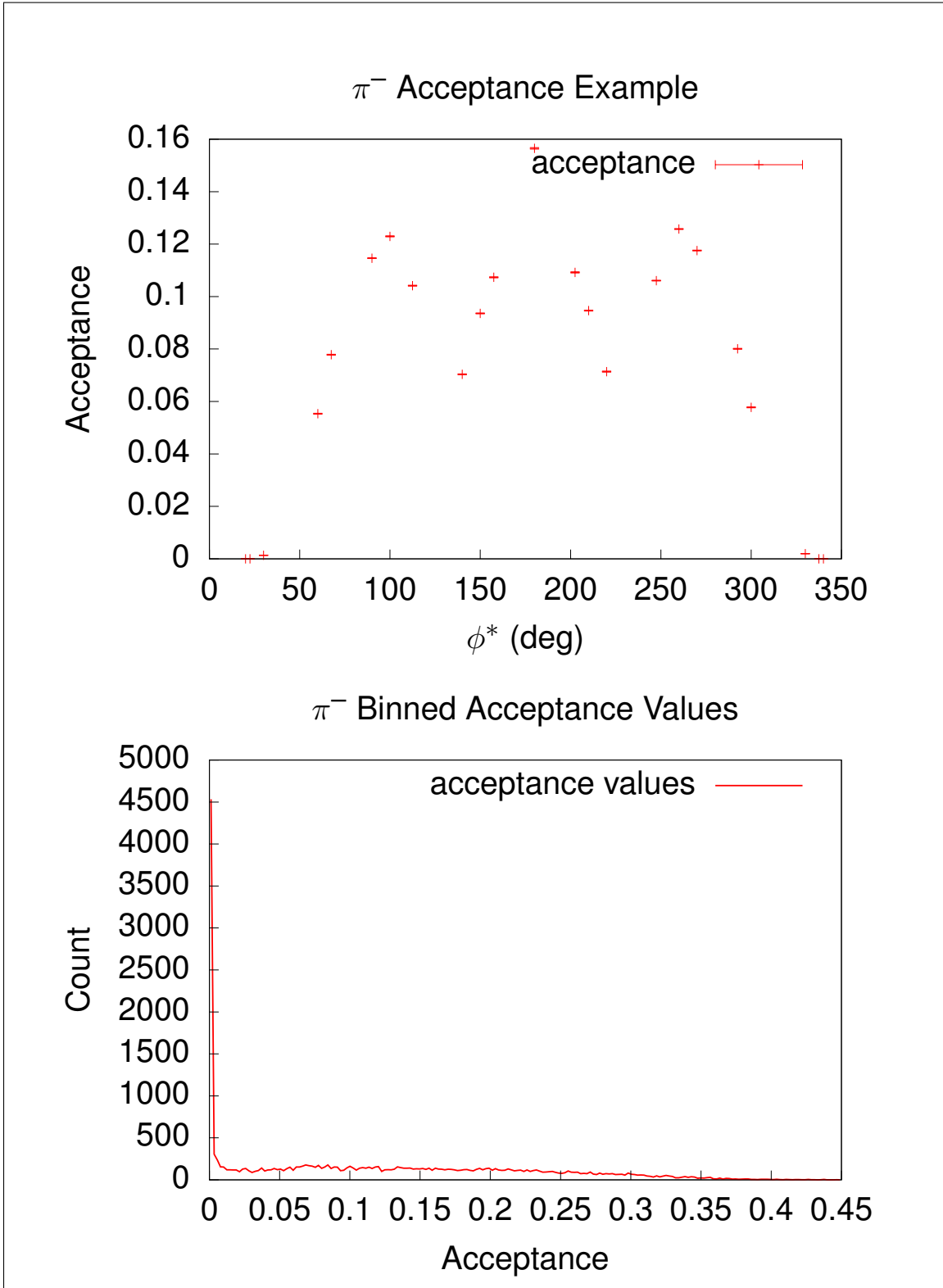


Figure 3.8: π^- analysis acceptance for selected bins along with binned acceptance values. $W = 1.25$ GeV, $Q^2 = 0.5$ GeV²/c², $\cos(\theta^*) = 0.1$.

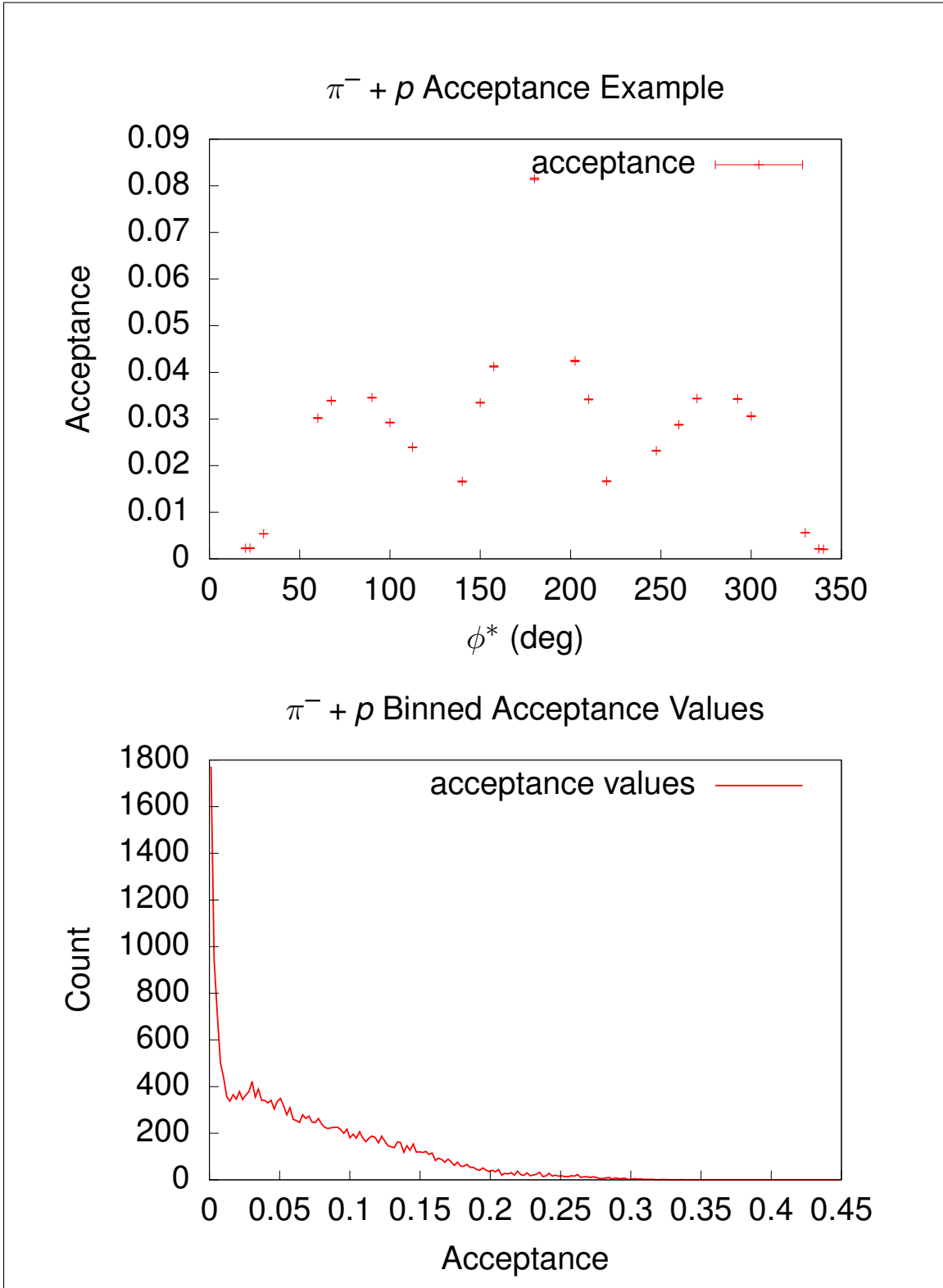


Figure 3.9: $\pi^- + p$ analysis acceptance for selected bins along with binned acceptance values. $W = 1.25$ GeV, $Q^2 = 0.5$ GeV²/c², $\cos(\theta^*) = 0.1$.

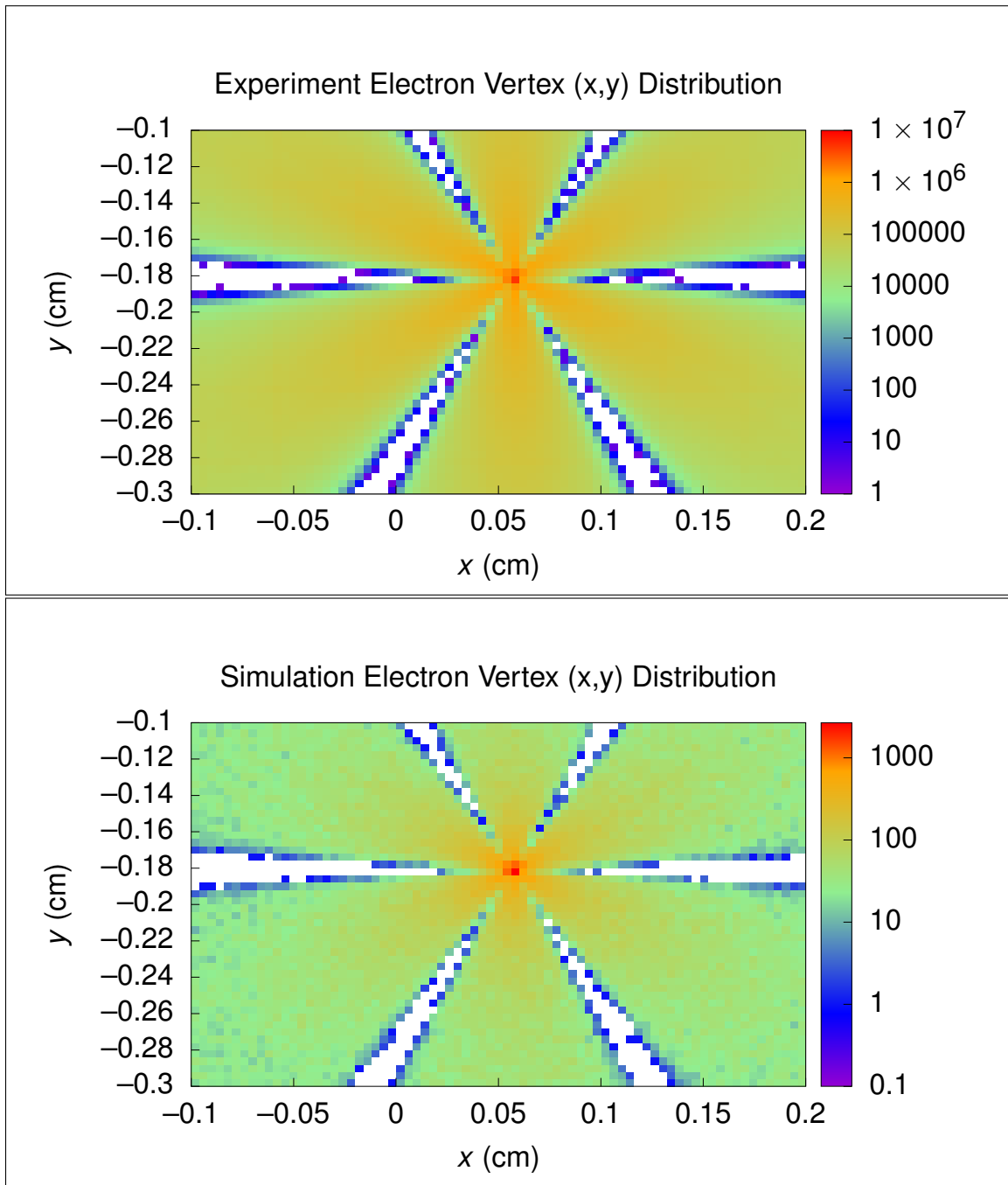


Figure 3.10: Comparison of electron vertex (x, y) distributions for experiment and simulation.

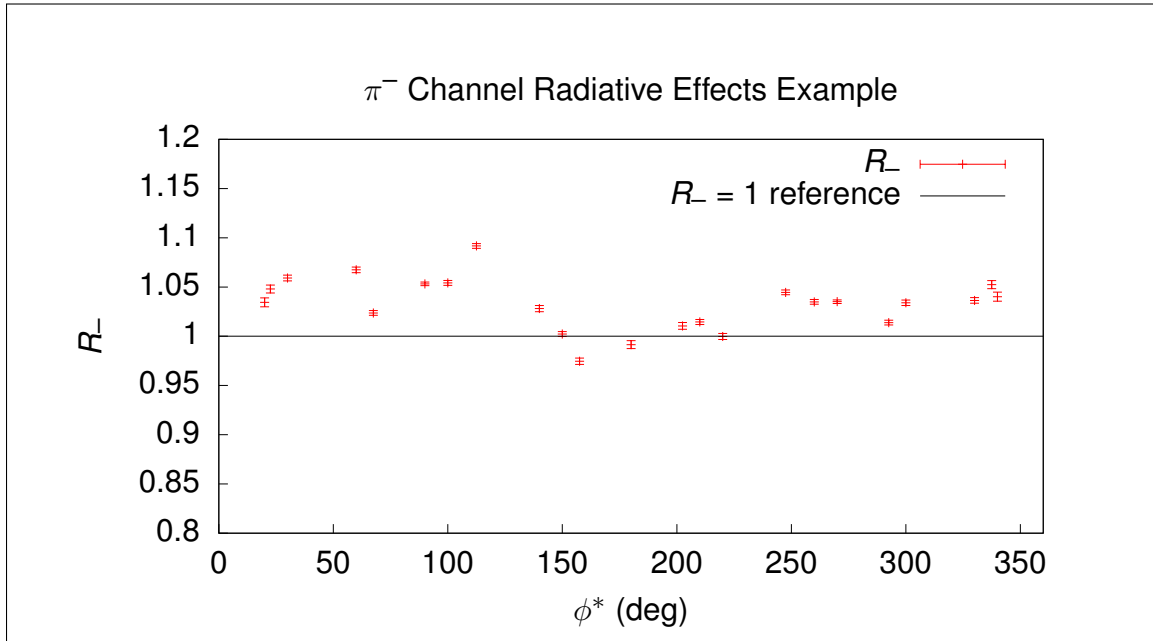


Figure 3.11: $e^- + n \rightarrow e^- + p + \pi^-$ channel radiative-effects correction for $W = 1.25 \text{ GeV}$, $Q^2 = 0.5 \text{ GeV}^2$, $\cos \theta^* = 0.1$ bin.

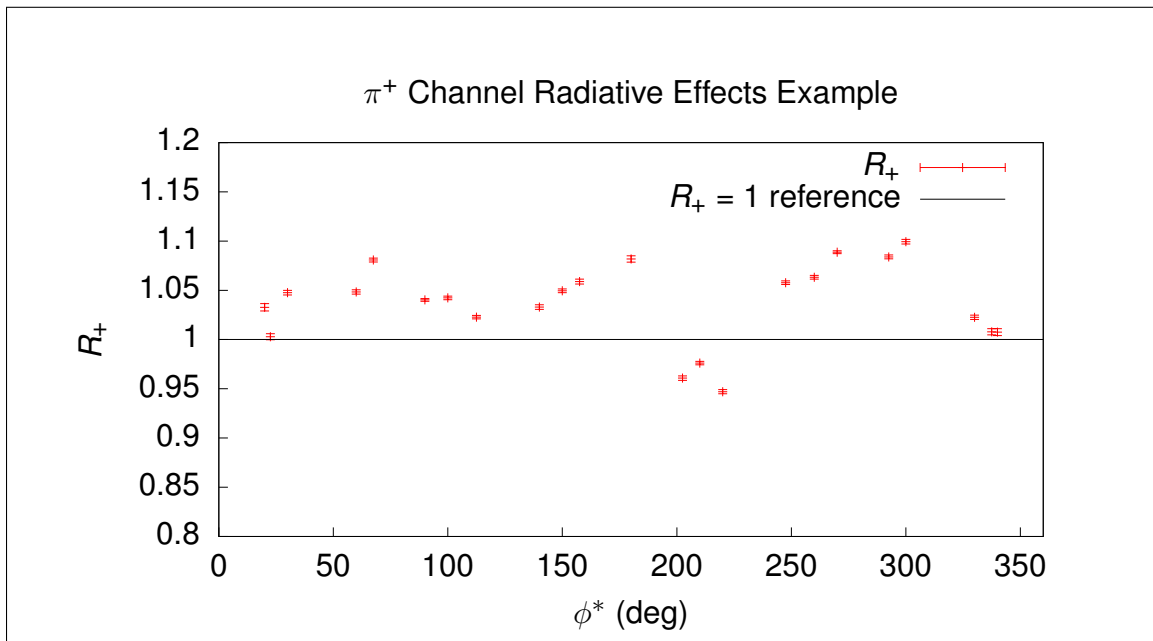


Figure 3.12: $e^- + p \rightarrow e^- + n + \pi^+$ channel radiative-effects correction for $W = 1.25 \text{ GeV}$, $Q^2 = 0.5 \text{ GeV}^2$, $\cos \theta^* = 0.1$ bin.

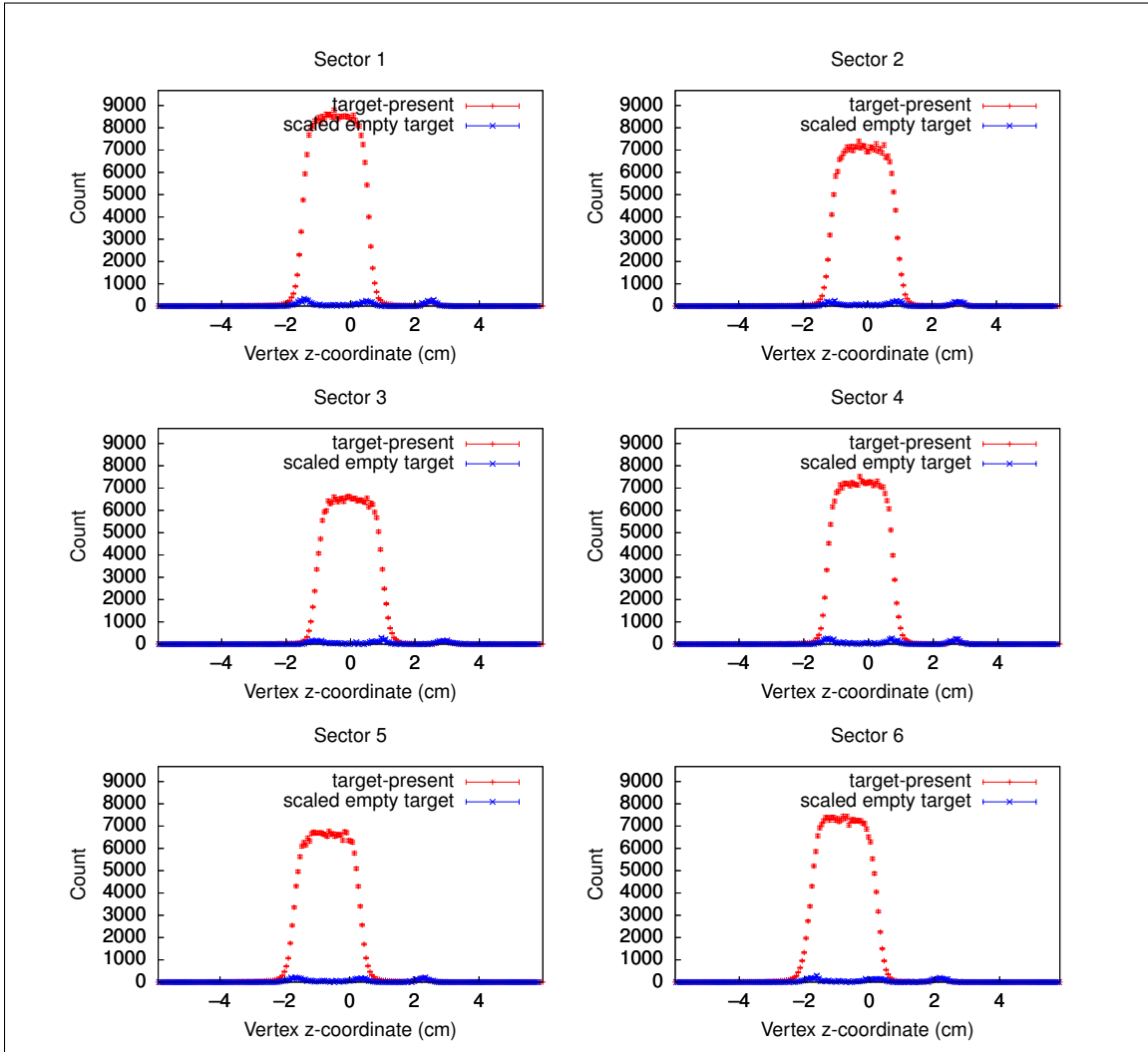


Figure 3.13: Comparison between filled-target and empty-target vertex z-coordinate distributions for the $\pi^- + p$ analysis. Note that the empty-target vertex data is shifted by -1.5 mm for full coincidence with filled-target data.

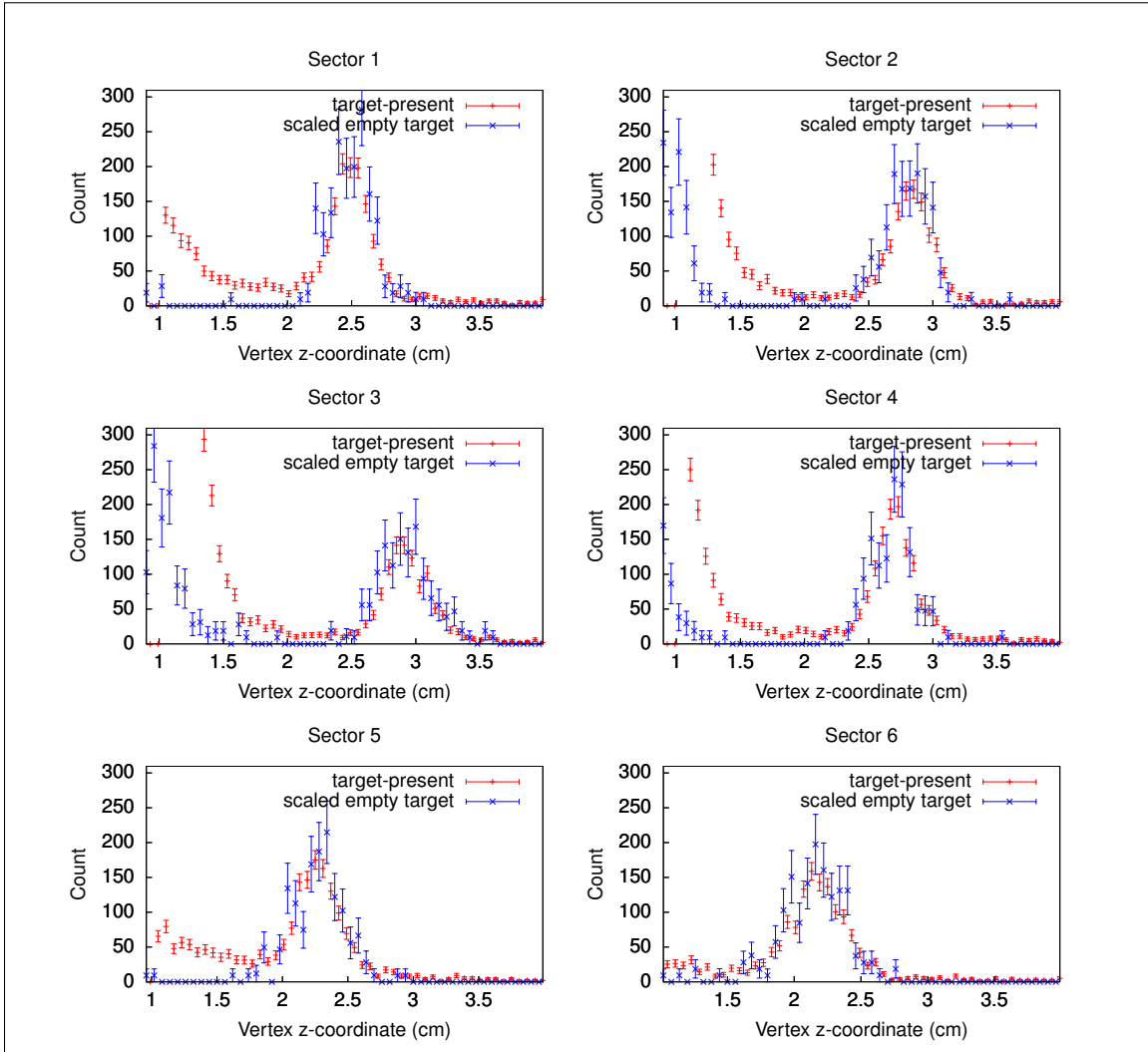


Figure 3.14: Comparison between filled-target and empty-target vertex z-coordinate distributions for the $\pi^- + p$ analysis, zoomed into the film target range. Note that the empty-target vertex data is shifted by -1.5 mm for full coincidence with filled-target data.

CHAPTER 4

FERMI-UNSMEARING

The method for removing Fermi-smearing is similar to calculating the acceptance or radiative-effects correction factors: Monte Carlo simulations are used to compute a correction factor, as illustrated by this informal general formula for such factors,

$$\text{correction} = \frac{\text{correct}}{\text{incorrect}}, \quad (4.1)$$

where some measured incorrect value is multiplied by this correction factor to yield an estimate of the measured correct value. For acceptance, “correct” is thrown data while “incorrect” is the reconstructed simulated data. For radiative corrections, “correct” is thrown data without radiative-effects and “incorrect” is thrown data with radiative-effects. For Fermi-unsmearing, “correct” is thrown data with a Fermi-moving target with known momentum, and “incorrect” is thrown data with a Fermi-moving target but with the false assumption that the target is at rest in the lab frame. As previously mentioned in Section 3.4, technically the Fermi-motion and radiative-effects factors are combined into a single factor,

$$F = \frac{\text{no rad, no smearing}}{\text{rad, smearing}}. \quad (4.2)$$

For the purposes of investigating the specific impact of the Fermi-unsmearing component of the combined radiative-effects and Fermi-unsmearing factor,

$$F_{\text{Fermi}} = \frac{\text{no smearing}}{\text{smearing}} \quad (4.3)$$

will be examined.

In the method presented here, a handful of modifications are needed for an existing Monte Carlo event generator to have Fermi-motion and therefore Fermi-unsmearing capabilities added to it. As a working model, the general structure of such a Monte Carlo event generator's main loop is constructed as follows.

1. Throw kinematic degrees of freedom based on cross-section. (W , Q^2 , center-of-momentum frame angles, masses, etc.)
2. Generate momentum Lorentz vectors for final state particles in the center-of-momentum frame.
3. Boost final state particles into lab frame.

Adding Fermi-motion to this event generator is accomplished as follows.

1. Ensure the beam energy is a programming variable in the context of the main loop, not a constant.
2. Throw Fermi-momentum three-vector and construct target nucleon momentum Lorentz vector in the lab frame (target-moving frame).
3. Boost the beam energy into the target-at-rest frame, and rotate the beam vector so that it aligns with the original beam axis.
4. Execute existing event generator algorithm given the modified beam energy.
5. Using the thrown Fermi-momentum three-vector and the rotation information used to align the boosted beam with the original beam axis, inverse rotate all final state Lorentz vectors and boost all final state Lorentz vectors into the lab

frame where the target is moving and the unboosted beam is aligned with the original beam axis.

- Optional: Use energy-momentum conservation to throw spectator particle(s) as additional final state particles.

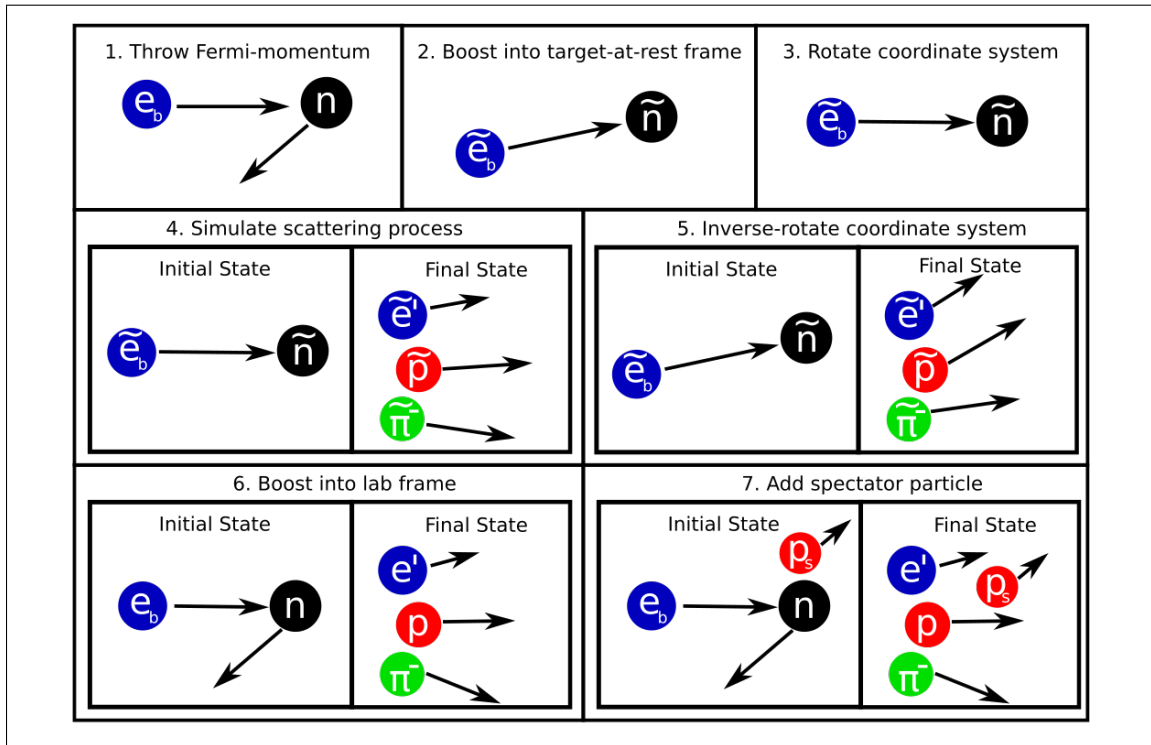


Figure 4.1: Flowchart of the needed Monte Carlo event generator modifications to include Fermi-motion of the target nucleon. Here a tilde denotes quantities being in the target-at-rest frame.

Figure 4.1 depicts this event generator process via a flowchart. Of course, this method is hiding complexity. In a real deuteron target made of bound nucleons, the deuteron itself has a real (not virtual) rest mass, i.e. it is on the mass shell. By energy-momentum conservation, the binding energy spoils the same trait for the nucleons bound in this deuteron. Real nucleons resolve this issue naturally, and due to this question not having an answer in the current state of science, the goal here is to develop a method of simulating moving nucleons which matches empirically measured data to as high a degree as feasible.

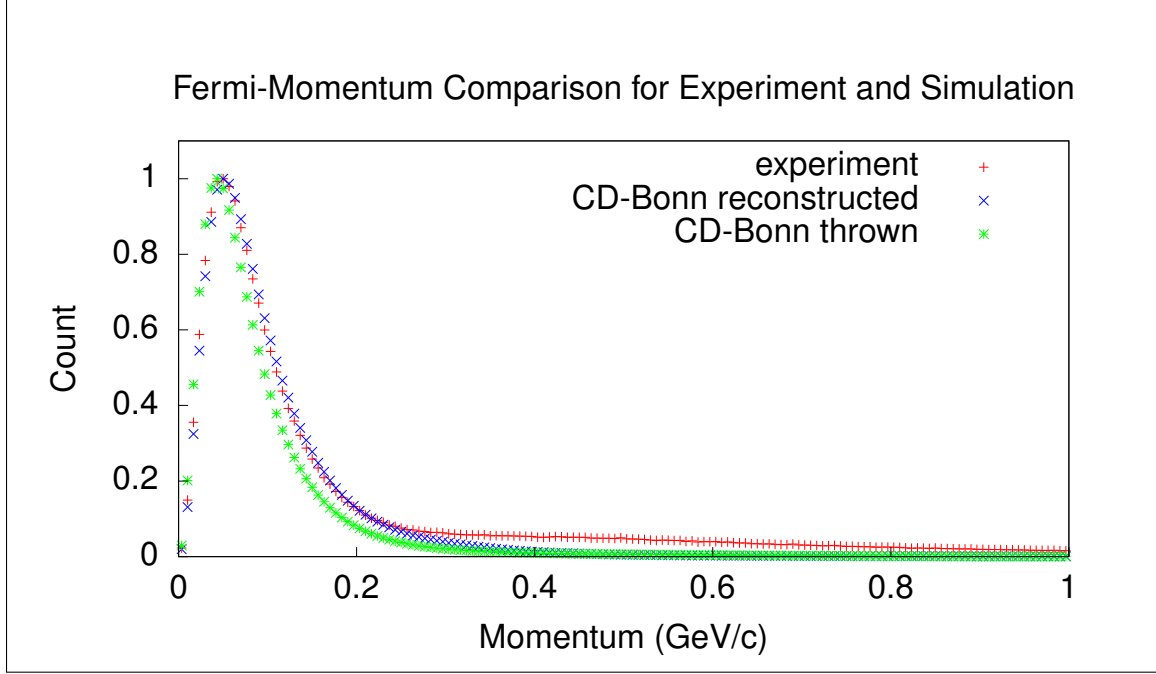


Figure 4.2: Comparison of missing spectator momentum between experiment and reconstructed simulation for the $\pi^- + p$ analysis using the CD-Bonn momentum distribution to generate Fermi-motion in the target. As can be seen, there is close agreement between experiment and reconstructed simulation below 200 MeV, at which point final state interactions become significant.

The Fermi-momentum distribution used in this work is from the CD-Bonn potential [30]. As demonstrated in [1] and again in Figure 4.2, the CD-Bonn potential after reconstruction results in a close approximation to the Fermi-momentum of the missing spectator nucleon below the 200 MeV cutoff where final state interactions become significant.

In order to conserve momentum-energy of the two bound nucleons in the deuteron, the three-momenta must have equal magnitudes and opposite directions, and to conserve energy their energies must add to be the deuteron mass scaled by c^2 . Therefore, from the previous considerations there is a question as to what the masses of the target and spectator particles should be, as energy conservation alone does not say how different each nucleon's mass should be from its rest mass at any given momentum. To clarify, let $d_\mu = (m_d, 0)$ be the deuteron target energy-momentum vector,

$t_\mu = (E_t, -\vec{f})$ be the target energy-momentum vector, and $s_\mu = (E_s, \vec{f})$ be the spectator energy-momentum, with \vec{f} being the Fermi-momentum three-vector and all in the lab frame. Then energy-momentum conservation demands that

$$d_\mu = t_\mu + s_\mu \implies m_d = E_t + E_s. \quad (4.4)$$

If the target nucleon were on-mass shell, then

$$E_t^{\text{on-shell}} = m_t + K(f, m_t), \quad (4.5)$$

where

$$K(f, m_t) = \sqrt{f^2 + m_t^2} - m_t \quad (4.6)$$

is the kinetic energy of the target nucleon as a function of mass and momentum (with $c = 1$ as stated in 1.3). As the actual nucleon is not on-mass shell, the target energy could be written as

$$E_t = m_t + K(f, m_t) + \Delta E. \quad (4.7)$$

The above question as to how to treat the moving nucleon's energy separates into two related questions.

1. What target mass should be used to look up cross-section values and throw a simulated reaction event?
2. How should the target mass be interpreted while analyzing simulated events?

The first question is fairly simple to answer through exploration by choosing values for the target mass in the target-at-rest frame which are different from the rest-mass, as this leads to very small differences in the thrown distributions. Figure 4.3 shows a comparison of W distributions for thrown events with various nucleon energy treatments, showing close agreement between them. Due to the simplicity of

treating the target in the same way for both reference frame boosting and energetic calculations,

$$E_t = m_t + K(f, m_t) \quad (4.8)$$

is used for the thrown target nucleon energy component.

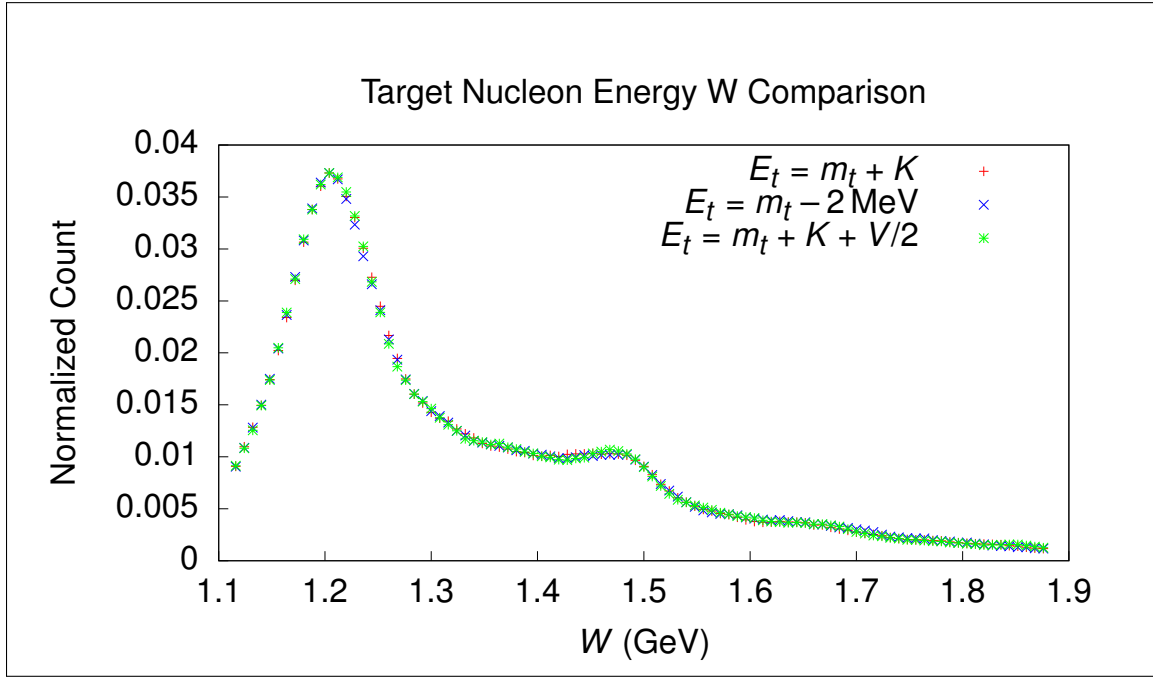


Figure 4.3: Comparison of target mass assumptions via resulting W distributions. The first treatment is the nucleon on-mass shell, the second is the nucleon rest mass plus the (negative) binding energy, and the third treatment is assigning exactly half of the virtuality $V = m_d - (m_t + K_t + m_s + K_s)$ to each nucleon, where m_s and K_s are the mass and kinetic energy of the spectator particle, respectively.

The second question branches into two cases: The Fermi-smeared analysis and the fully-exclusive analysis. For the fully-exclusive analysis, special consideration must be paid to analyzing simulated data if Fermi-motion is enabled in the simulation. Energy conservation from the perspective of the event generator's internal kinematics leads to the following expression for the target deuteron,

$$d_\mu^{\text{sim}} = (m_t + m_s + K_t + K_s, 0) \quad (4.9)$$

in the lab frame, where m_t , m_s are the target and spectator rest masses and K_t , K_s are the kinetic energies of the target and spectator, respectively. This expression follows the fact that the thrown particles obey the following conservation of energy-momentum relation in the target-at-rest frame,

$$t_\mu^\oplus + q_\mu^\oplus = \pi_\mu^\oplus + b_\mu^\oplus \text{ (simulated)}, \quad (4.10)$$

but in real scattering reactions, this conservation law,

$$d_\mu + q_\mu = \pi_\mu + b_\mu + s_\mu, \quad (4.11)$$

is obeyed. Therefore, if the missing spectator is to be defined in the simulation analysis as

$$s_\mu = d_\mu^{\text{sim}} + q_\mu - \pi_\mu - b_\mu, \quad (4.12)$$

then

$$d_\mu^{\text{sim}} = s_\mu - q_\mu + \pi_\mu + b_\mu = s_\mu + t_\mu = (m_s + m_t + K_s + K_t, 0) \quad (4.13)$$

since in the simulation $t_\mu = (m_t + K_t, -\vec{f})$ and $s_\mu = (m_s + K_s, \vec{f})$. Note that this requires thrown event data to be available at the event level in the reconstructed simulated data. As the final-state particle energy-momenta π_μ and b_μ are used to compute W and the center-of-momentum transformation and angles θ^* and ϕ^* , no additional special handling of the simulated data is needed beyond calculating the missing spectator.

For the Fermi-smear case, a way to extract a perfectly accurate simulated missing mass distribution was not discovered, as noted in Section 2.5. In order to accomplish accurate Fermi-smearing of W and the center-of-momentum transformation and angles θ^* and ϕ^* , the false target-at-rest assumption has to be used to simulate the Fermi-smearing effect, and simultaneously conservation of energy must also be

obeyed in order to accurately reproduce the W distribution as given by the reaction model. The treatment which yields an acceptable missing mass distribution while conserving energy is to set the simulated target nucleon's energy-momentum vector to

$$t_{\mu}^{\text{sim}} = (m_t + K_t, 0), \quad (4.14)$$

which is an intuitive compromise as the momentum component enables Fermi-smearing while the energy component conserves energy from the perspective of the event generator. In an attempt to discover alternative definitions, which might yield a better distribution shape, a simple model was used to explore the space of possible target treatments: Let the target nucleon energy-momentum vector be given by

$$\tilde{t}_{\mu}(a, b) = (m_t + aK_t, -b\vec{f}), \quad (4.15)$$

so that the Fermi-smearred missing baryon becomes

$$\tilde{b}_{\mu}(a, b) = q_{\mu} + \tilde{t}_{\mu}(a, b) - \pi_{\mu}, \quad (4.16)$$

and hence the squared missing baryon mass is a function of model parameters a and b . By comparing the distributions of squared missing masses for simulated data treated with this model and a subset of measured Fermi-smearred data with minimal background, a pair of parameters (a, b) might be found which yields optimally matching distributions. The specific metric used for this study is given by

$$\chi^2(a, b) = \int_{m_t^2 - \sigma_{m_t^2}}^{m_t^2 + \sigma_{m_t^2}} (S(a, b; m^2) - E(m^2))^2 dm^2, \quad (4.17)$$

where $S(a, b)$ and E are the model-treatment simulation and experiment distributions, respectively, and $\sigma_{m_t^2}$ is given by a Gaussian fit to the center of the experiment missing mass distribution. Figure 4.4 shows that there is a family of treatments which

locally minimize the $\chi^2(a, b)$ metric lying in a trough, and, conveniently, the intuitive compromise lies in the middle of this optimal trough. As the squared missing mass

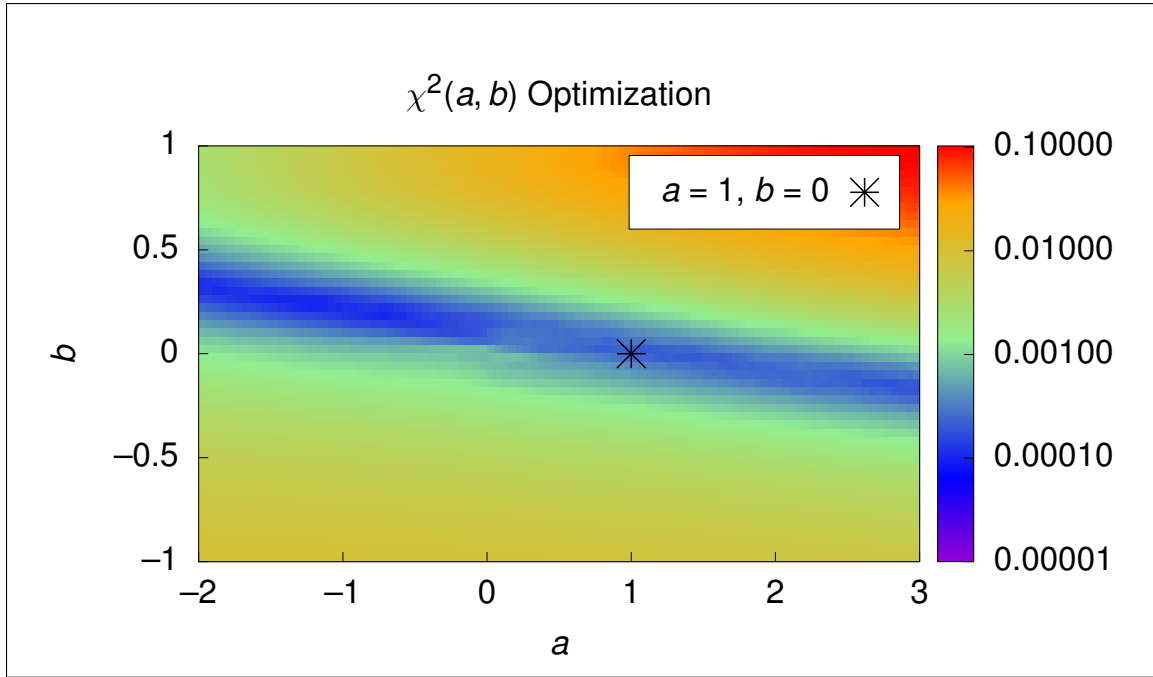


Figure 4.4: Plot of $\chi^2(a, b)$ along with the intuitive compromise, showing a trough of optimal treatments in the simple model and the compromise lying in the trough.

distributions for the Fermi-smearred analyses have already been presented in detail in Section 2.5, Figures 2.31 and 2.32 serve as examples of the resulting distributions.

Having describing the design and details of analyzing simulated data with Fermi-motion enabled, the Fermi-unsmearing correction factors can be examined. As there are two factors, one for each analysis, F_{Fermi}^- refers to the π^- factor and F_{Fermi}^+ to the π^+ factor. Figure 4.5 shows selected bins of the Fermi-unsmearing factor along with binned values of the Fermi-unsmearing factor for both the π^- and π^+ analyses.

The test of this method is to compare cross-sections extracted without any Fermi-smearing with those affected by and corrected for Fermi-smearing. The $\pi^- + p$ analysis, already conducted in [1], provides such a test. As mentioned previously, to produce the required Monte Carlo simulations the `aao_rad` and `aao` programs were combined and modified to create a single program which can enable or disable radiative-effects

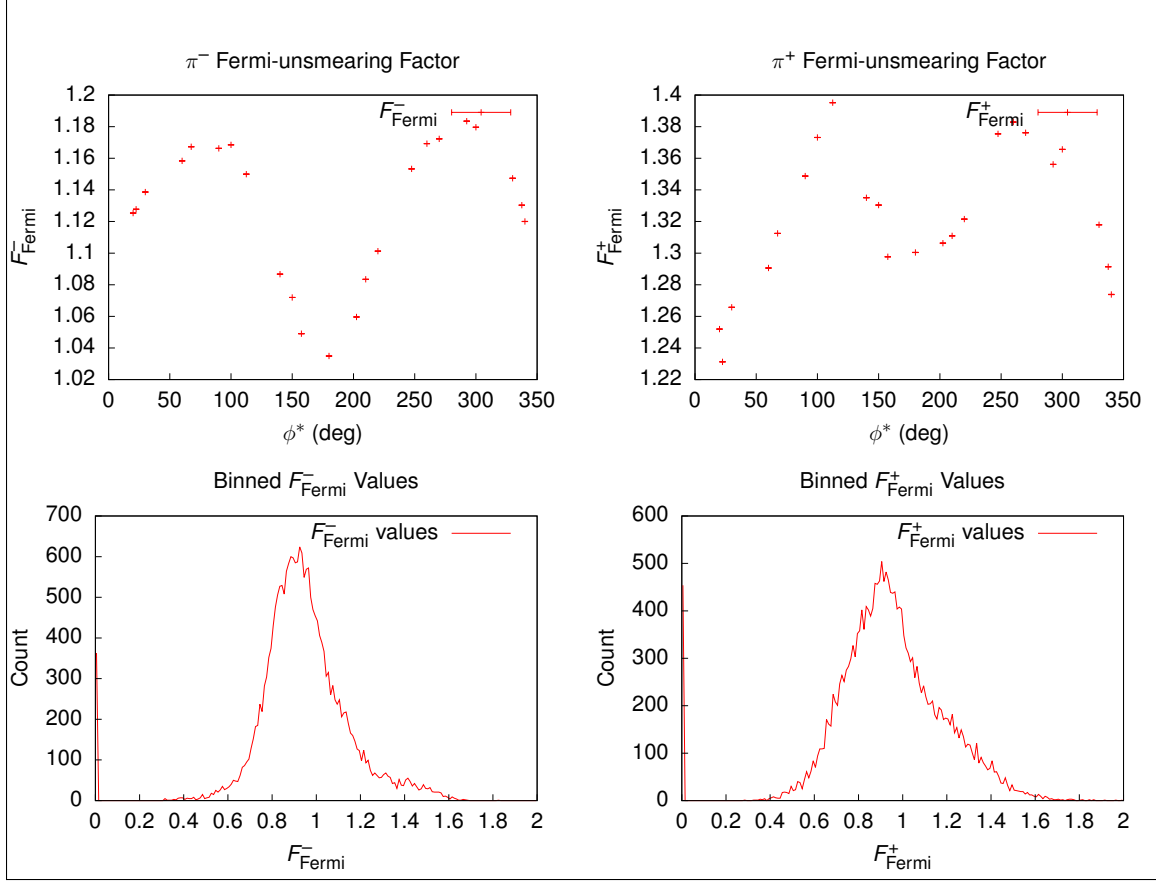


Figure 4.5: Fermi-unsmeared correction factor for π^- and π^+ analyses for $W = 1.25$ GeV, $Q^2 = 0.5$ GeV², $\cos \theta^* = 0.1$ bin along with binned values of the correction factor.

and Fermi-motion in the target independently; the program is called `onepigen` [22] and is available on the JLAB SVN system. Figure 4.6 shows a brief comparison between cross-sections extracted from the Fermi-unsmeared π^- and exclusive $\pi^- + p$ analyses.

4.1 Γ_ν AND ϵ VARIATION

As hinted to in Section 1.2, ϵ being a function of the target-at-rest frame beam energy varies event to event based on the Fermi-motion of the target nucleon. When the target is moving anti-parallel to the beam, the energy in the target-at-rest frame is higher than the lab frame beam energy, and when the target is moving parallel to the beam, the energy is lower. As ϵ is a monotonously increasing function of the

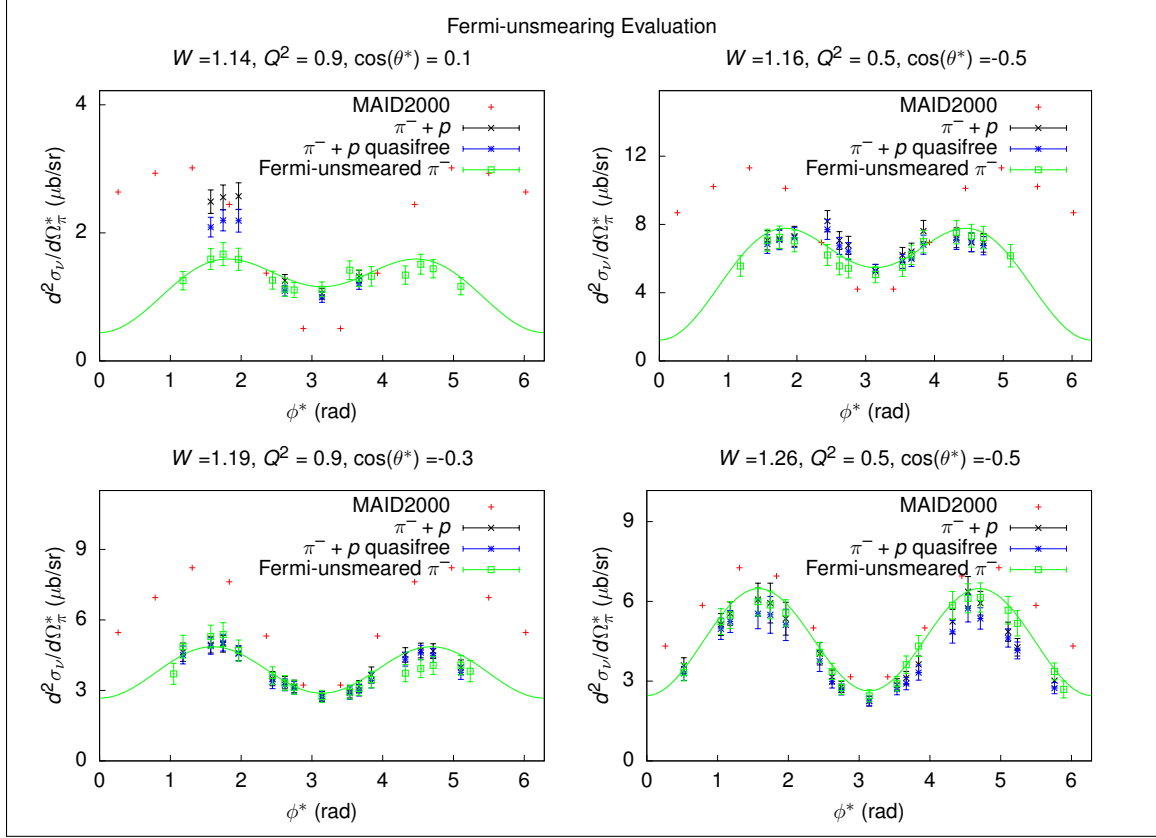


Figure 4.6: Comparison between π^- and $\pi^- + p$ cross-section estimates in select bins. $\pi^- + p$ results are taken from [1]. As illustrated here, the Fermi-unsmearing cross-sections are generally in agreement with the results from [1] with additional coverage of the cross-section. Note that the error bars are a combination of statistical and systematic uncertainties which are developed in Section 5.5.

beam energy for fixed W and Q^2 , an ϵ larger than the principle value for a given $(W, Q^2, \cos(\theta^*), \phi^*)$ bin occurs if and only if the target momentum is anti-parallel to the beam. As the mean observed ϵ values for all bins is larger than the principle ϵ value, there is therefore a systematic tendency to observe more events where the target and beam are anti-parallel than vice versa. In hindsight, this should have been expected simply because of there being more energy available to interact.

The only relevance these observations have to the scope of this work is accurately estimating the virtual photon flux Γ_ν as defined in Equation 1.13, since an event-by-event varying beam energy implies a varying ϵ , which implies a varying Γ_ν . To this end, the division of yields by Γ_ν is done by reweighting each event by a factor of $1/\Gamma_\nu$

rather than multiplying each bin of the yield histograms by a single $1/\Gamma_\nu$ factor. As the examples in Figures 4.7 and 4.8 illustrate, the mean values of Γ_ν and ϵ are slightly different from the principle values for most bins, but significantly different for others.

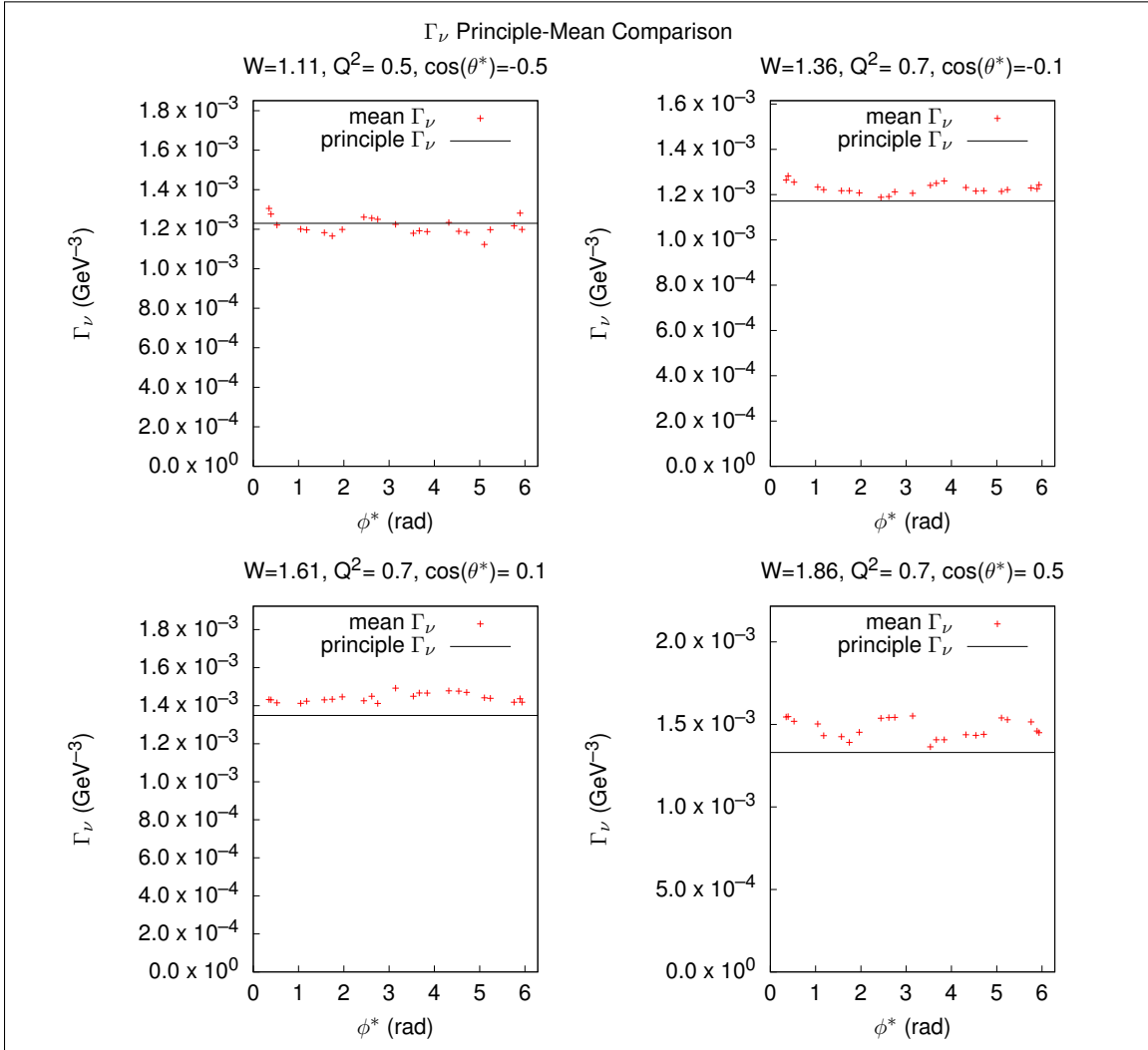


Figure 4.7: Examples of Γ_ν variation per event in comparison with the principle value from the kinematic bin.

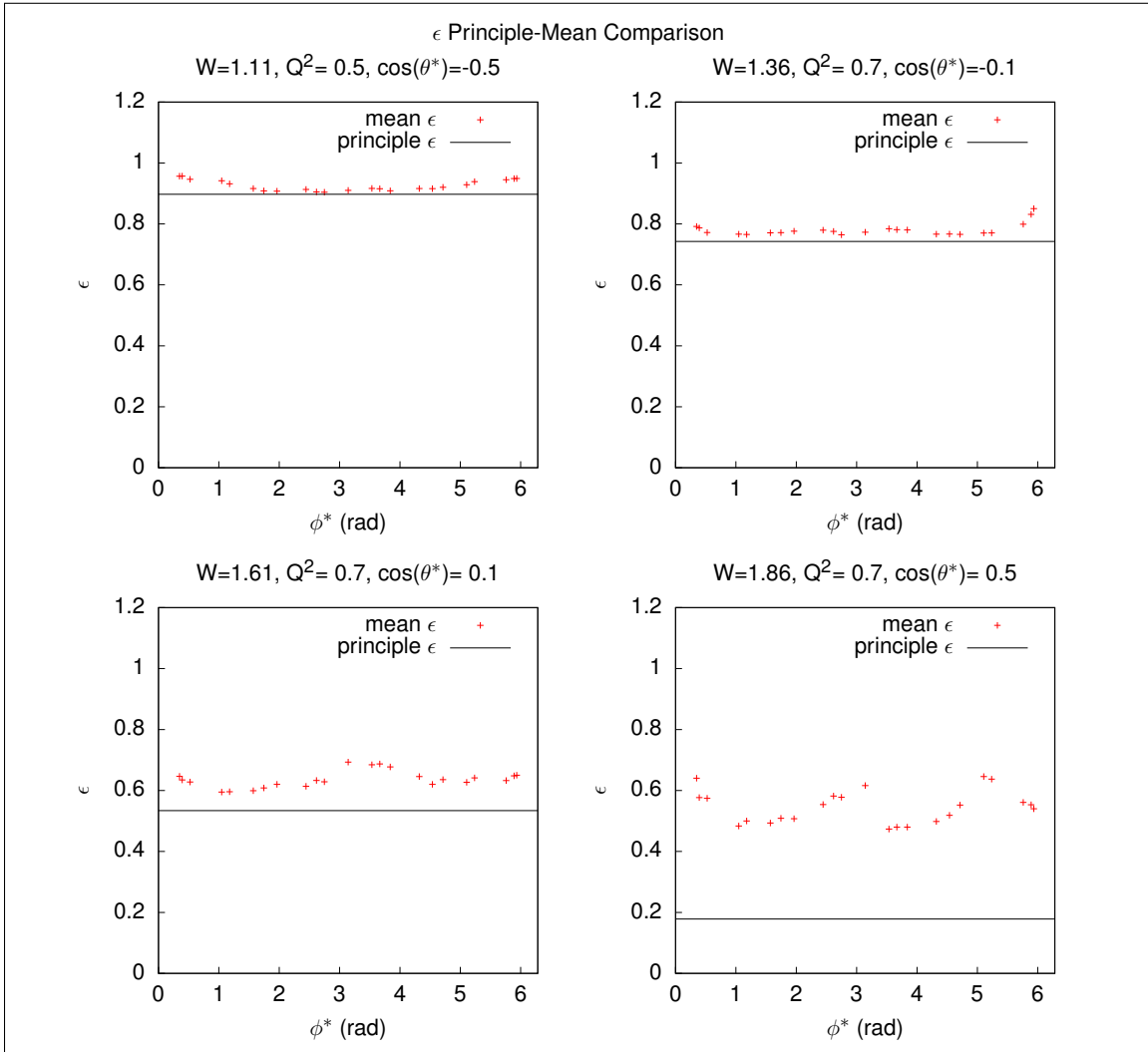


Figure 4.8: Examples of ϵ variation per event in comparison with the principle value from the kinematic bin.

CHAPTER 5

CROSS-SECTIONS

The π^- and π^+ analyses above can be used to both extract cross-sections and, in the case of the π^- analysis, confirm that the Fermi-unsmearing method has been successful by comparing with the $\pi^- + p$ analysis conducted by [1]. Figures 5.1 through 5.7 show comparisons between the π^- cross-section results from this work and the $\pi^- + p$ cross-sections from [1] for selected bins along comparisons between MAID2000, and Figures 5.8 through 5.14 compare results for the π^+ channel cross-section in comparison with MAID2000. Since the background subtraction method has been shown to produce cross-sections which agree with quasifree results in Section 2.5.1, the direct comparison between results from this work and those of [1] is between the cross-sections labeled “Fermi-unsmear π^- ” and “ $\pi^- + p$ quasifree”, with the fully exclusive but not quasifree results from [1] labeled as “ $\pi^- + p$ ”.

It should be noted that the (W, Q^2) domain for the π^- and π^+ cross-sections is partially new relative to MAID2000, and therefore there will naturally be differences between the MAID model and these cross-sections as the model has not yet seen cross-section data in this precise (W, Q^2) domain.

5.1 π^- CROSS-SECTIONS

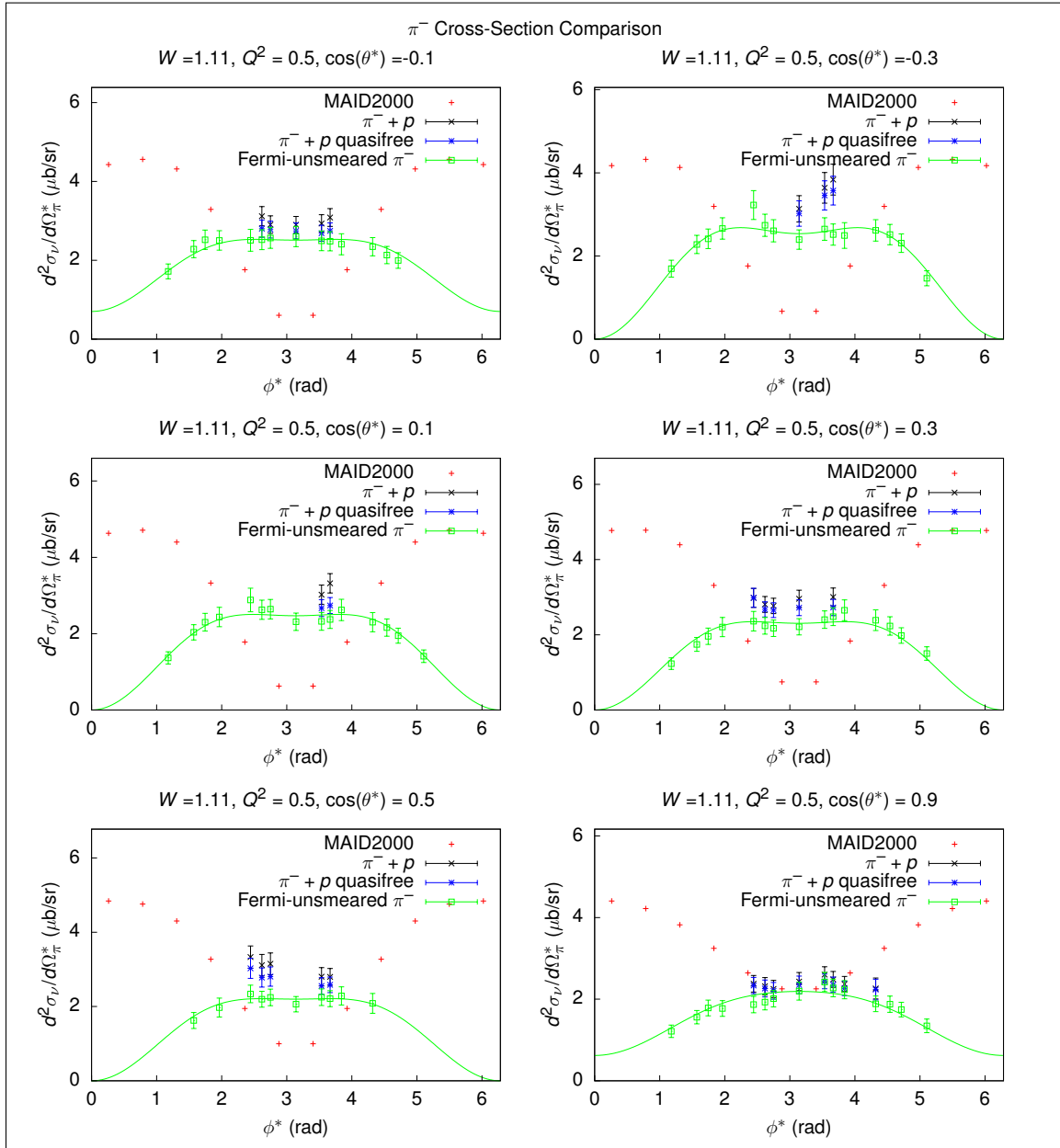


Figure 5.1: Comparison between MAID2000, π^- , and $\pi^- + p$ cross-sections for selected bins, with combined statistical and systematic uncertainties for each point.

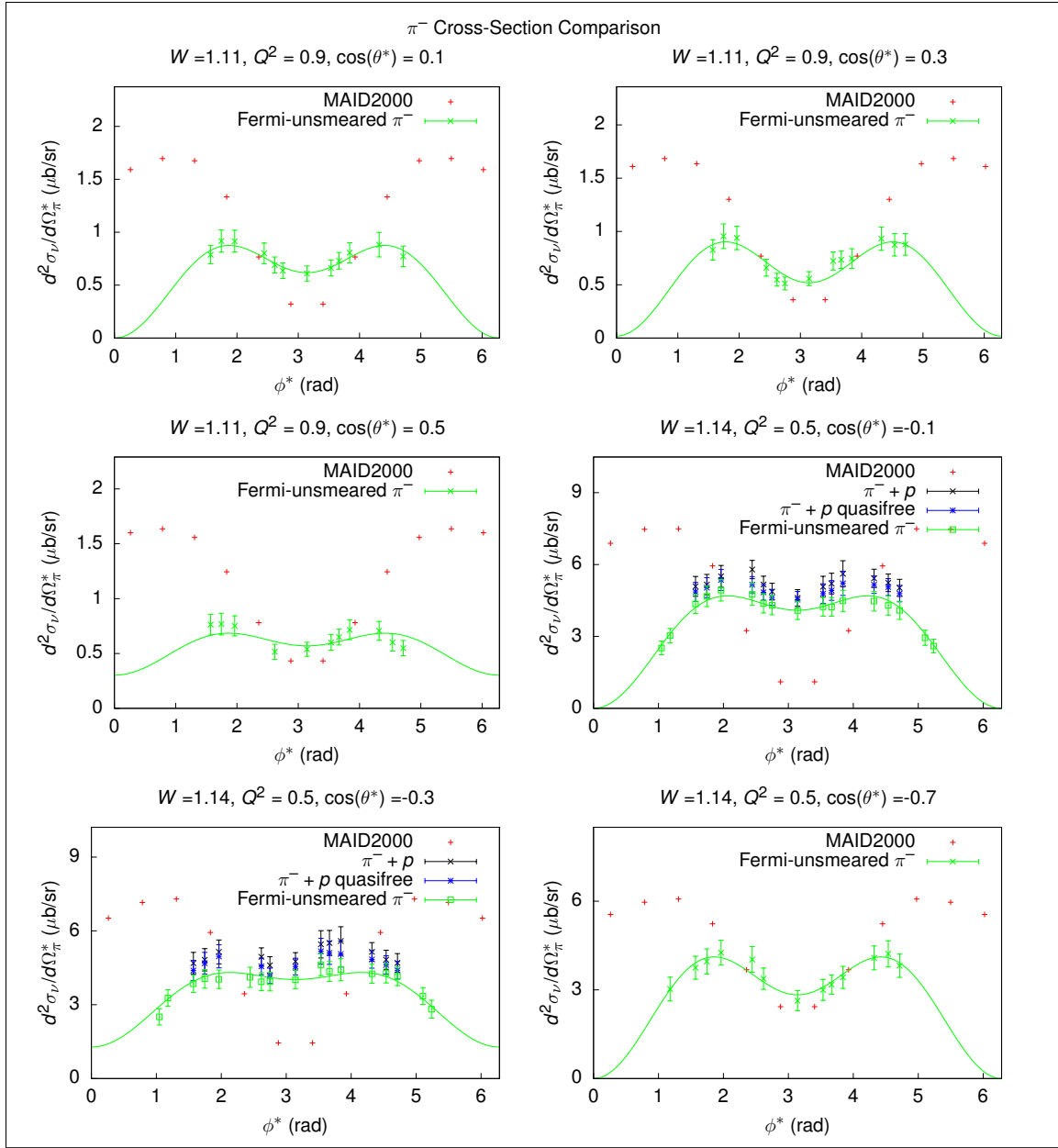


Figure 5.2: Comparison between MAID2000, π^- , and $\pi^- + p$ cross-sections for selected bins, with combined statistical and systematic uncertainties for each point.

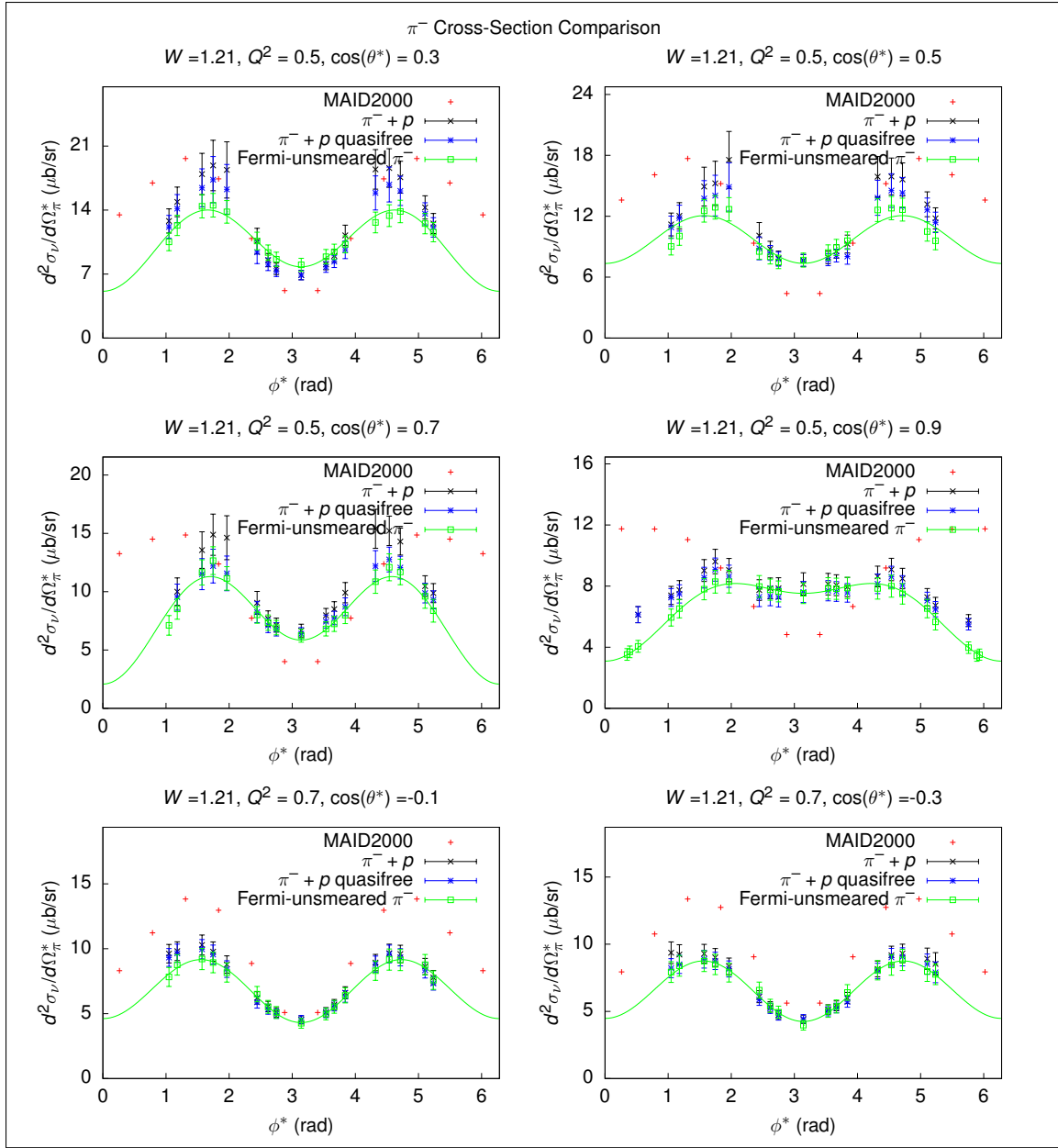


Figure 5.3: Comparison between MAID2000, π^- , and $\pi^- + p$ cross-sections for selected bins, with combined statistical and systematic uncertainties for each point.

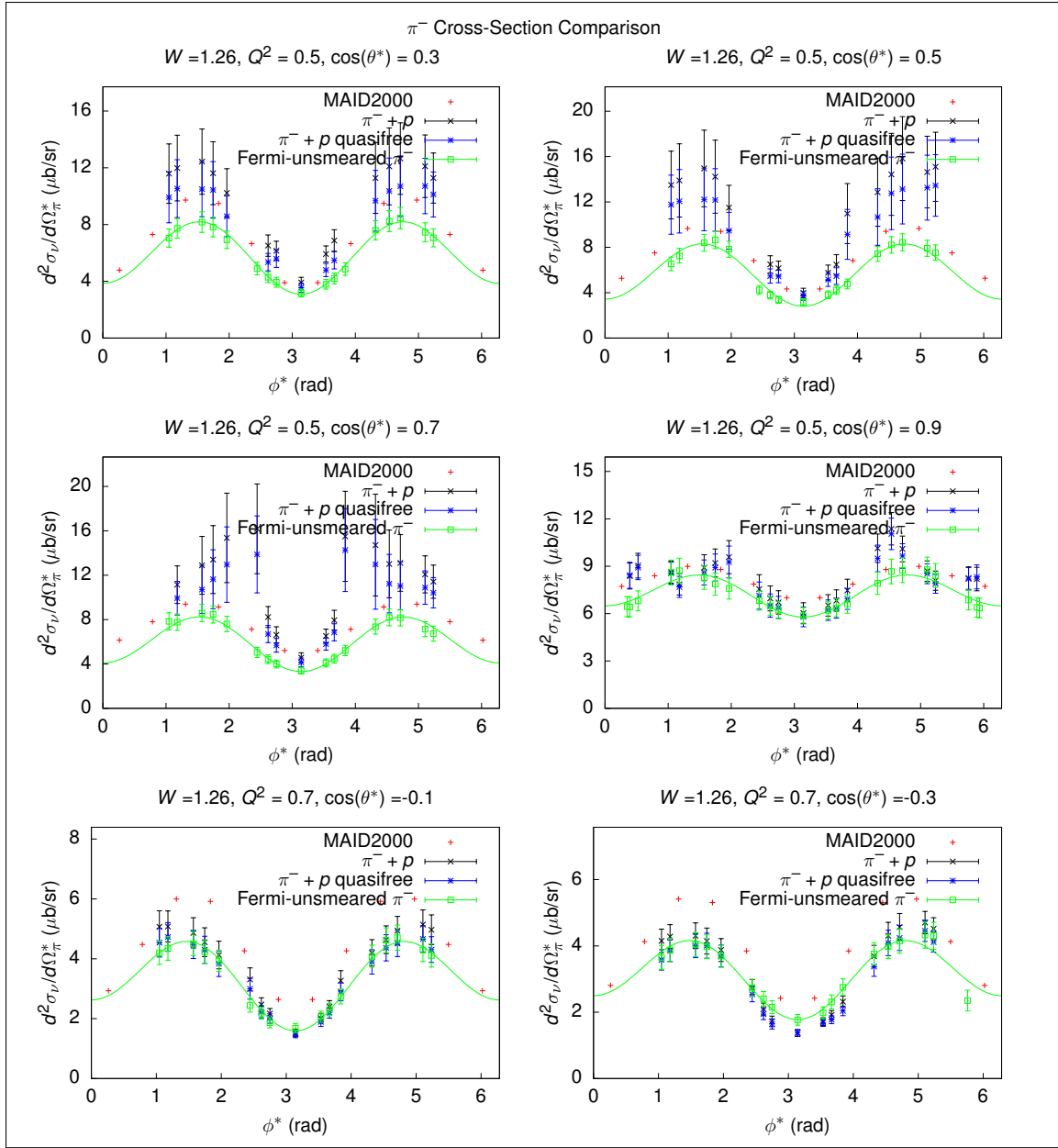


Figure 5.4: Comparison between MAID2000, π^- , and $\pi^- + p$ cross-sections for selected bins, with combined statistical and systematic uncertainties for each point.

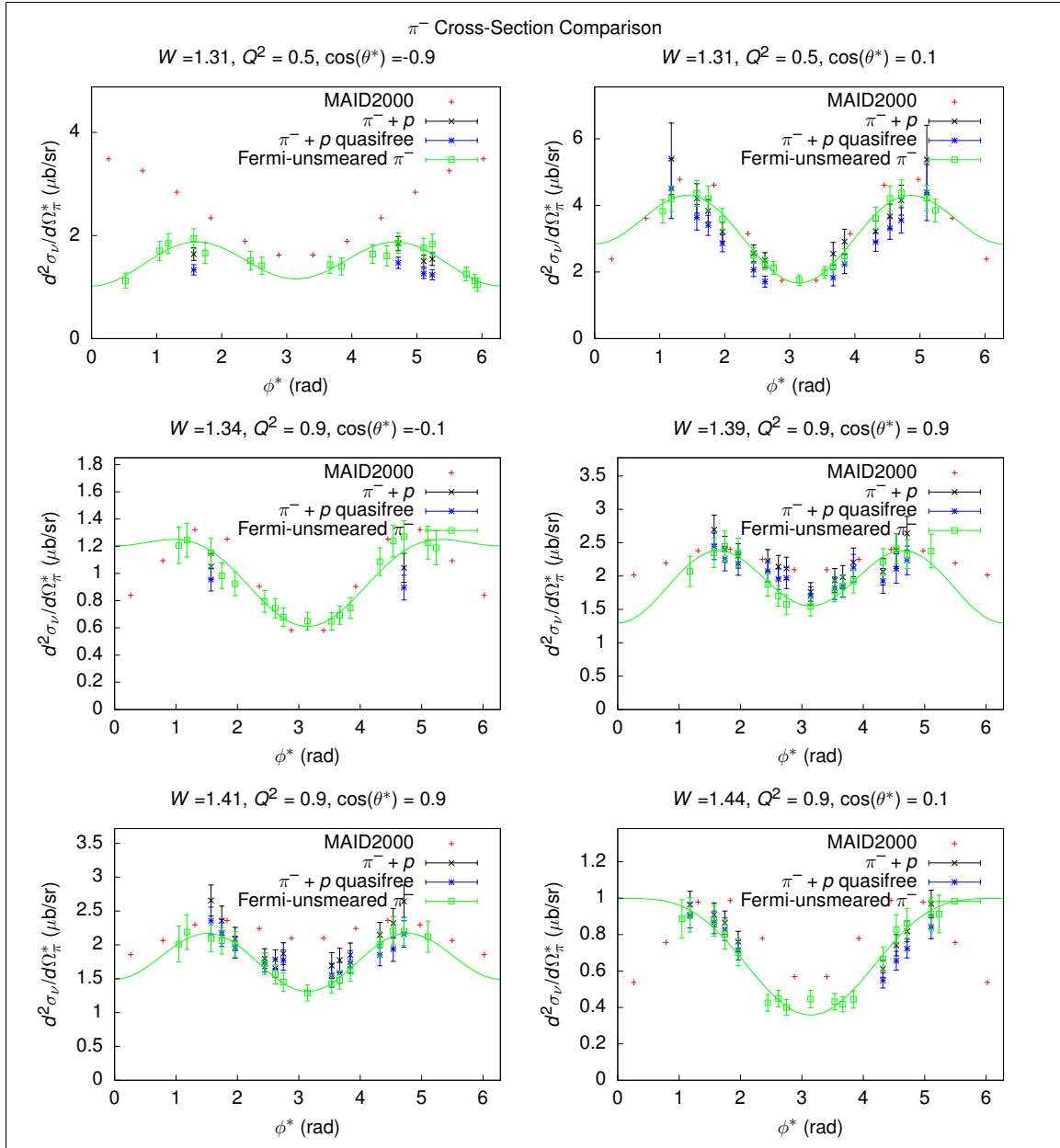


Figure 5.5: Comparison between MAID2000, π^- , and $\pi^- + p$ cross-sections for selected bins, with combined statistical and systematic uncertainties for each point.

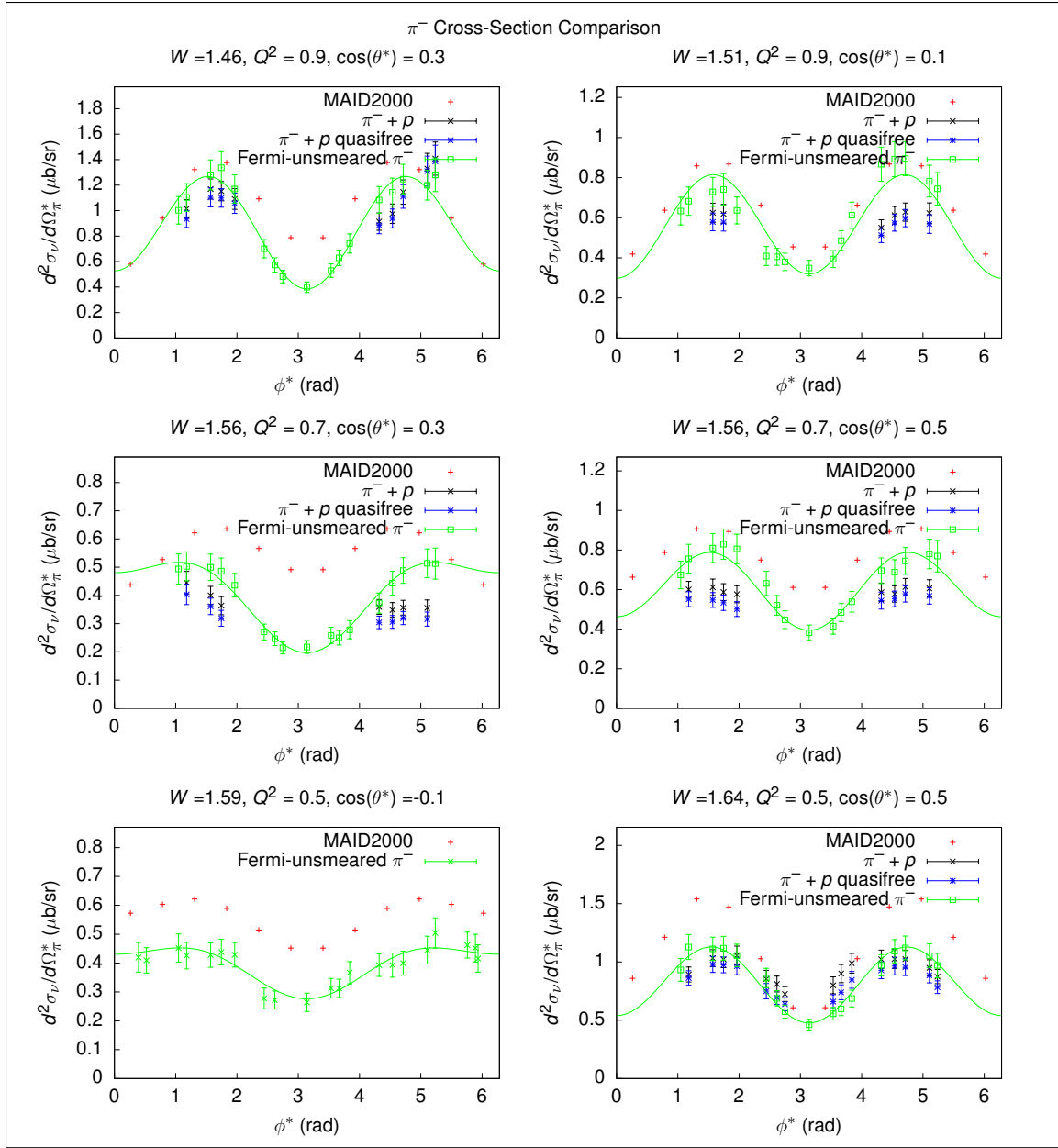


Figure 5.6: Comparison between MAID2000, π^- , and $\pi^- + p$ cross-sections for selected bins, with combined statistical and systematic uncertainties for each point.

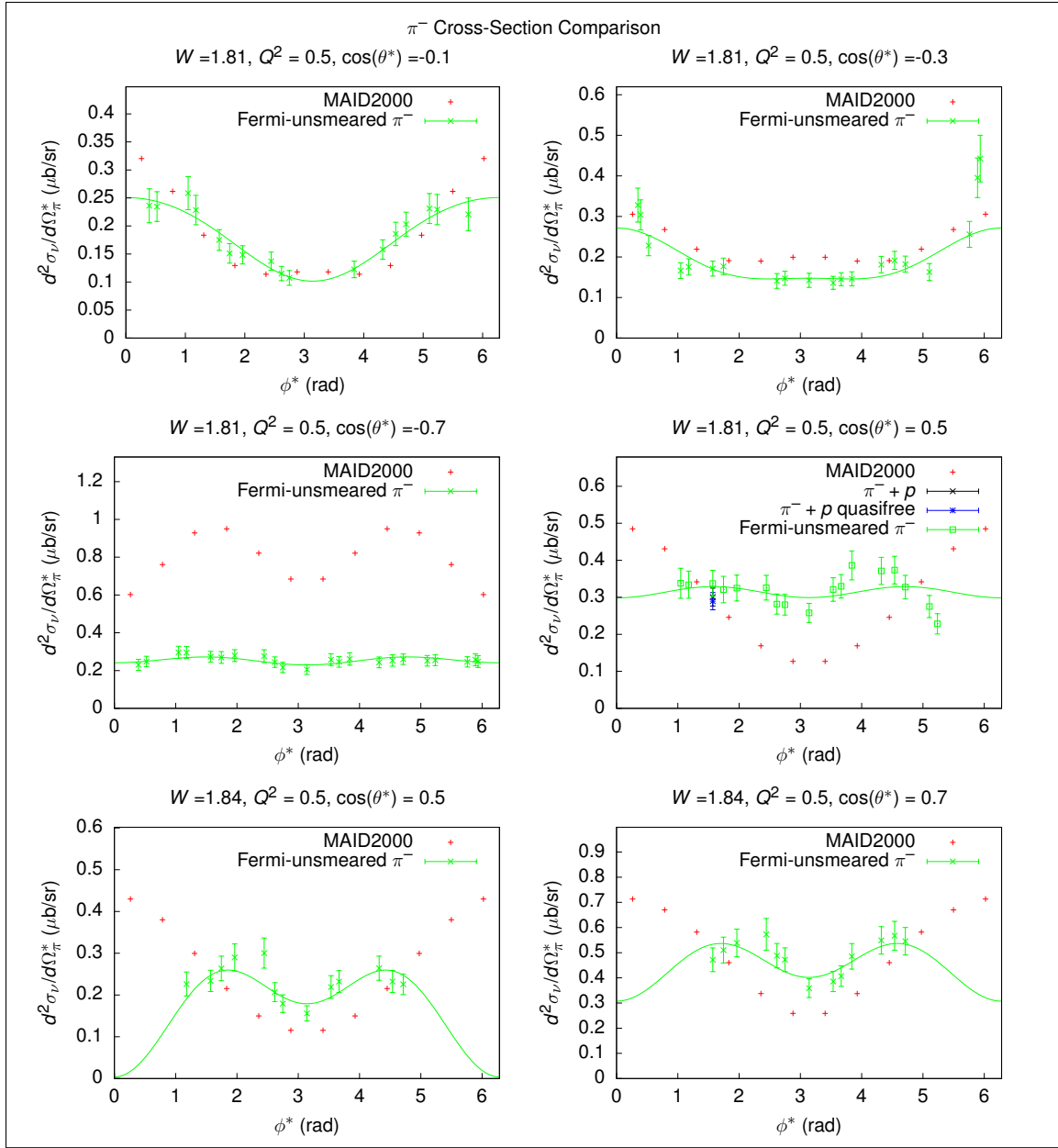


Figure 5.7: Comparison between MAID2000, π^- , and $\pi^- + p$ cross-sections for selected bins, with combined statistical and systematic uncertainties for each point.

5.2 π^+ CROSS-SECTIONS

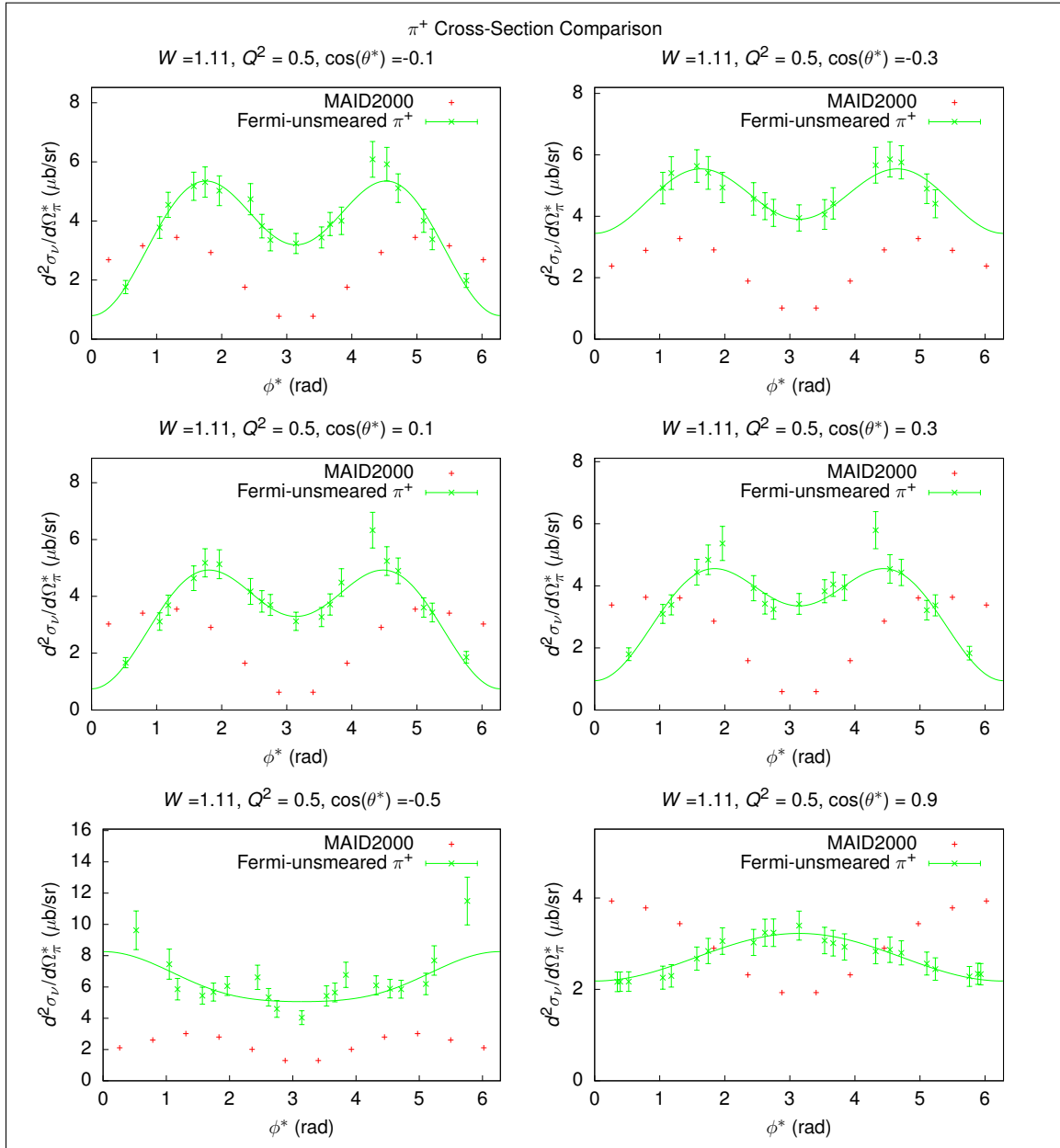


Figure 5.8: Comparison between π^+ cross-section and MAID2000 for selected bins, with combined statistical and systematic uncertainties for each point.

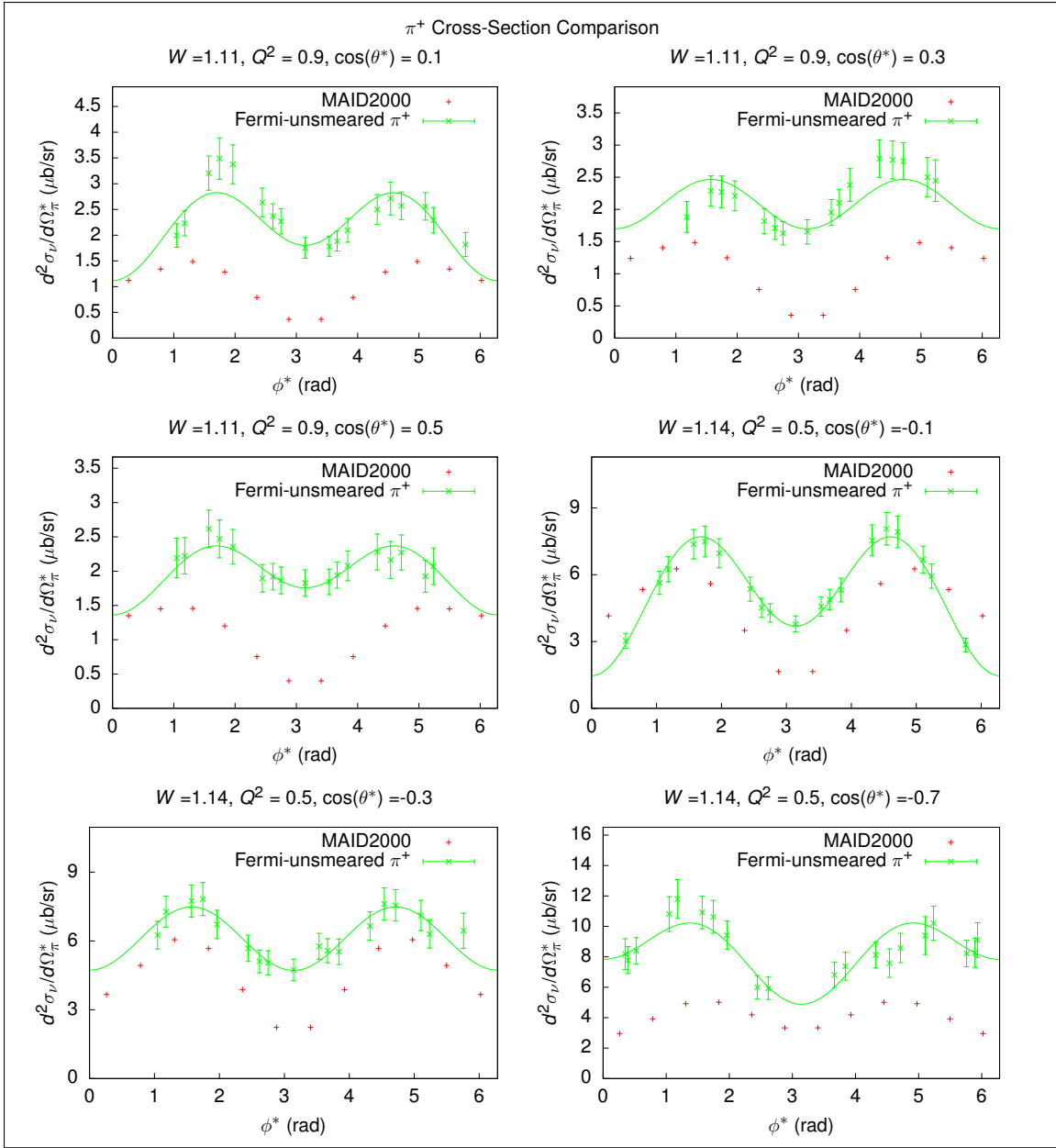


Figure 5.9: Comparison between π^+ cross-section and MAID2000 for selected bins, with combined statistical and systematic uncertainties for each point.

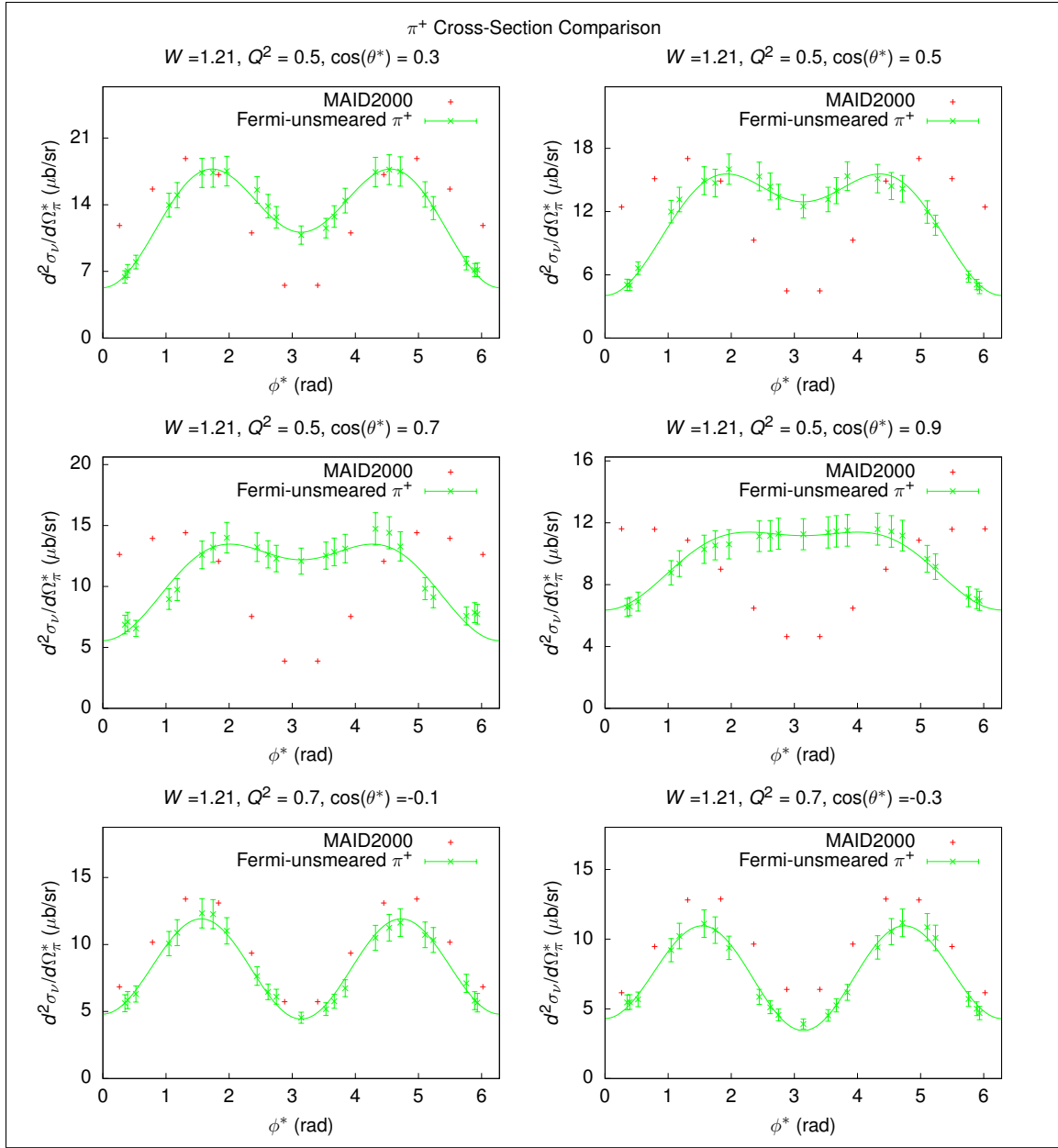


Figure 5.10: Comparison between π^+ cross-section and MAID2000 for selected bins, with combined statistical and systematic uncertainties for each point.

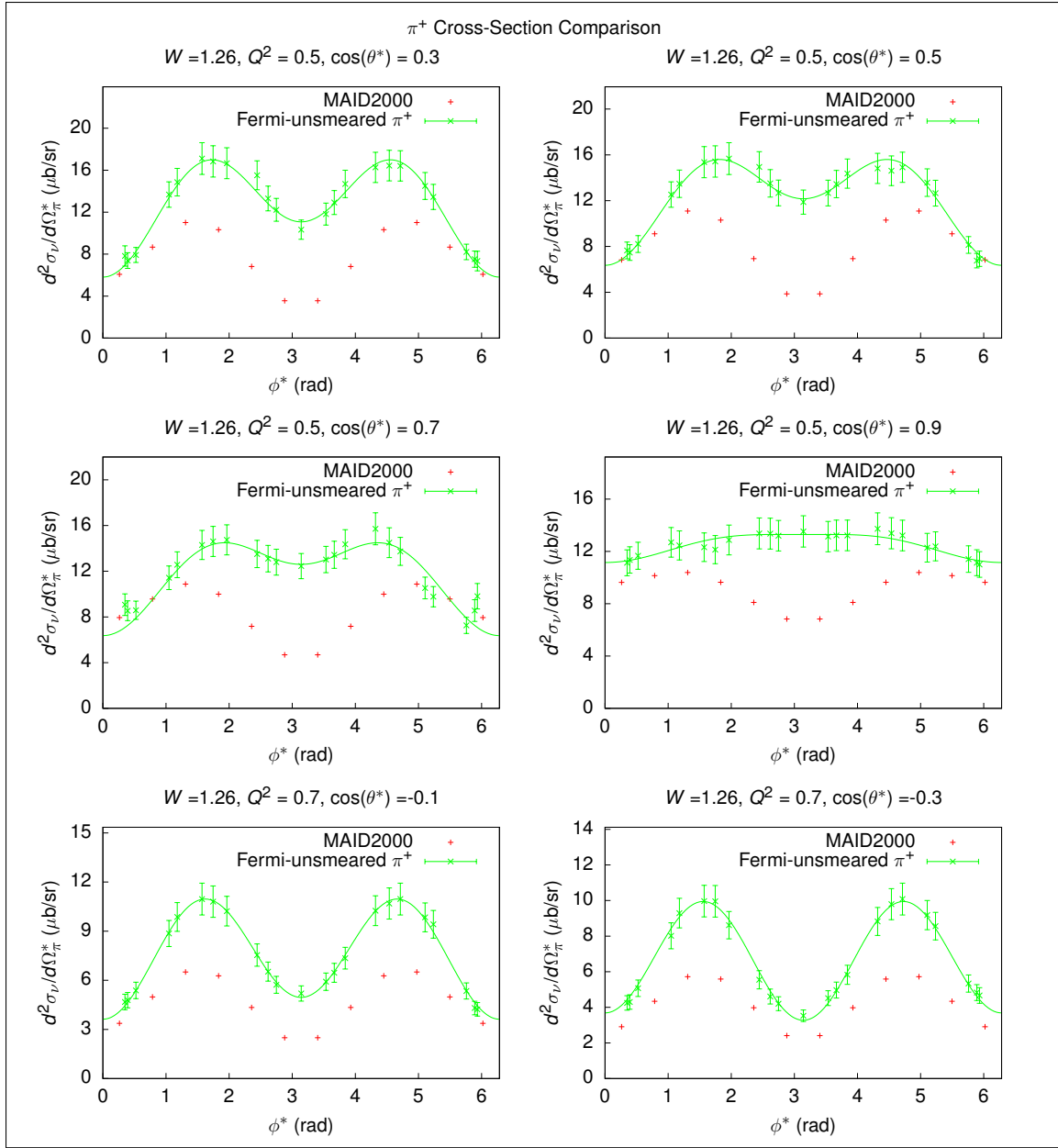


Figure 5.11: Comparison between π^+ cross-section and MAID2000 for selected bins, with combined statistical and systematic uncertainties for each point.

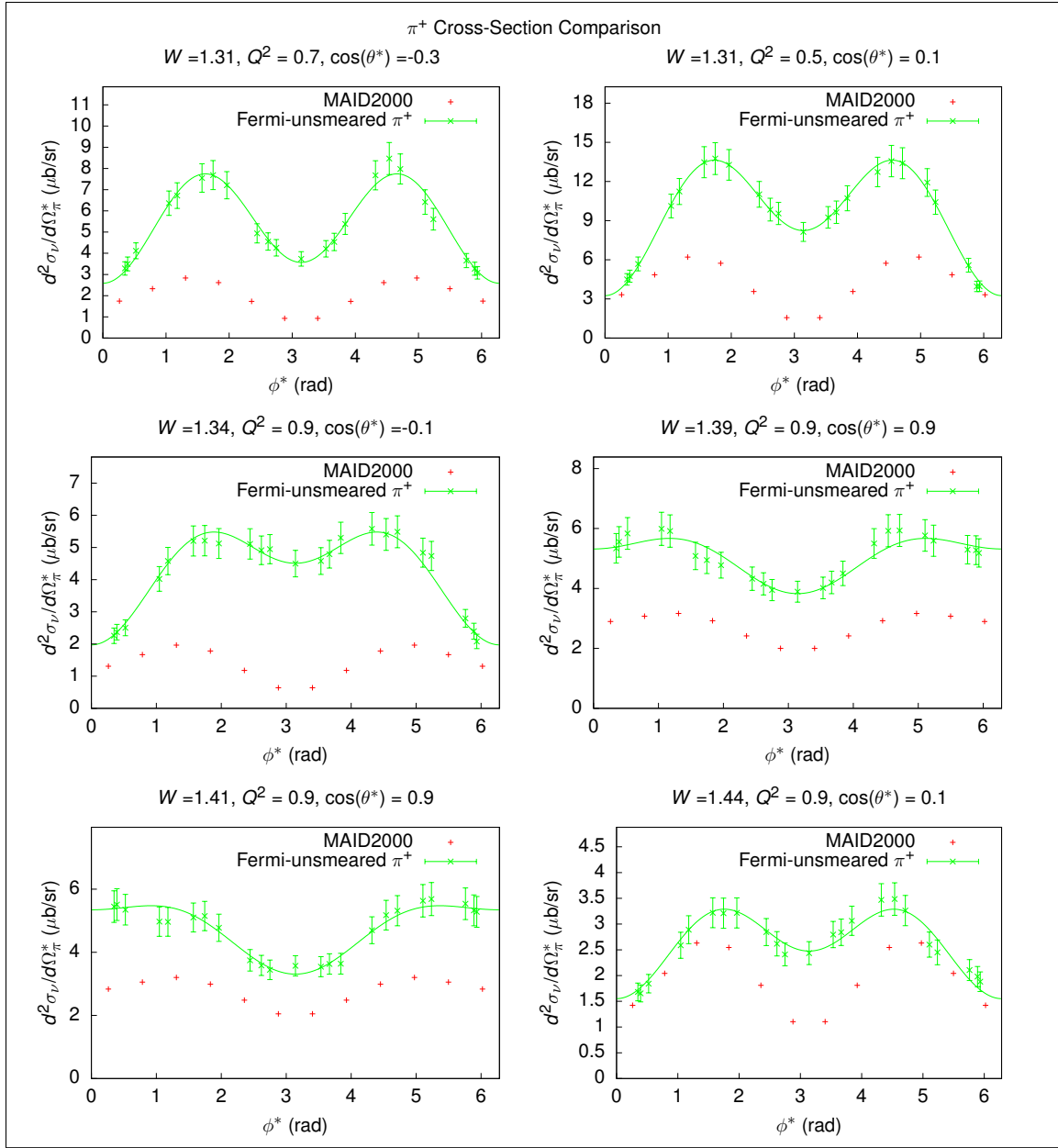


Figure 5.12: Comparison between π^+ cross-section and MAID2000 for selected bins, with combined statistical and systematic uncertainties for each point.

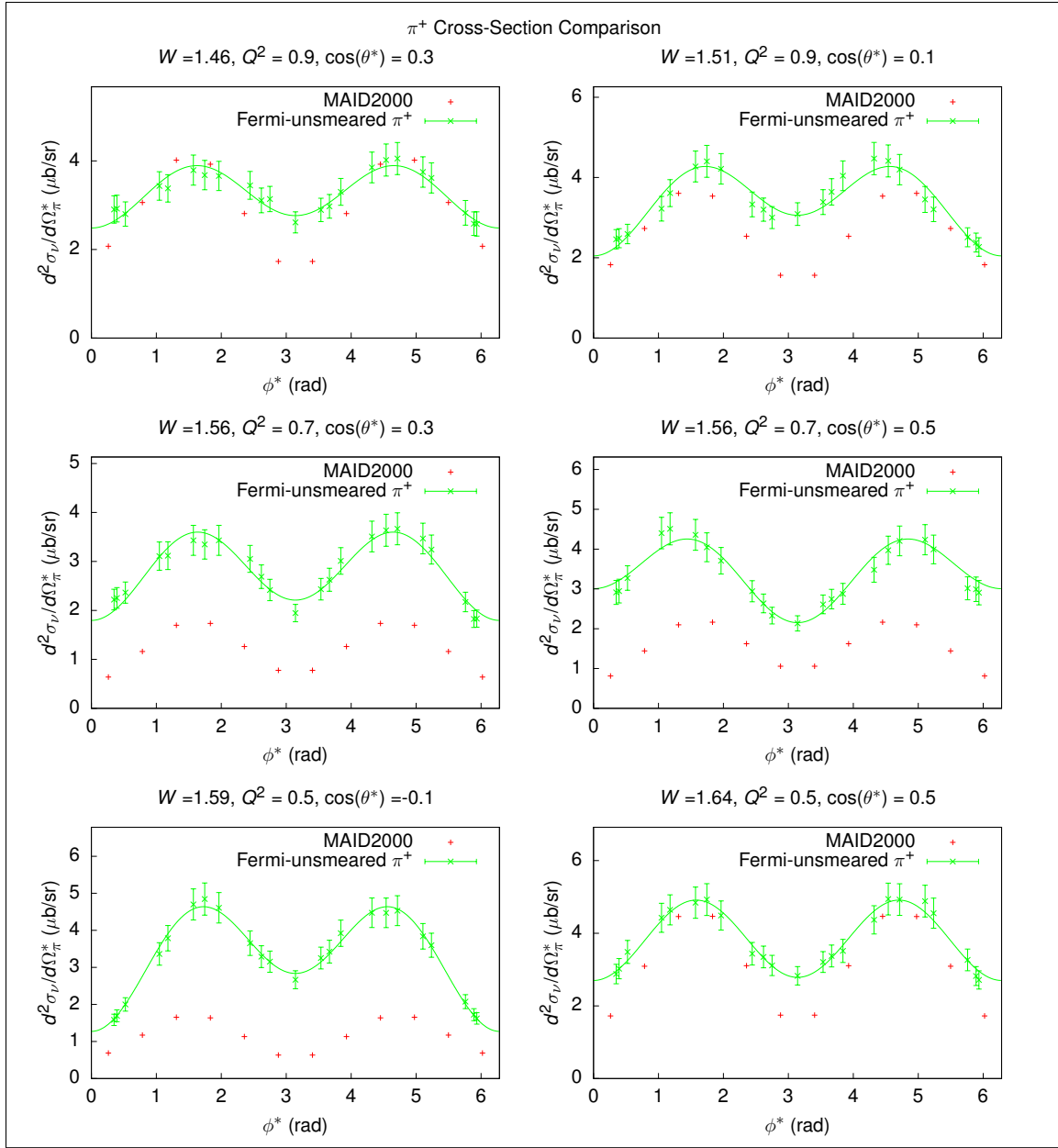


Figure 5.13: Comparison between π^+ cross-section and MAID2000 for selected bins, with combined statistical and systematic uncertainties for each point.

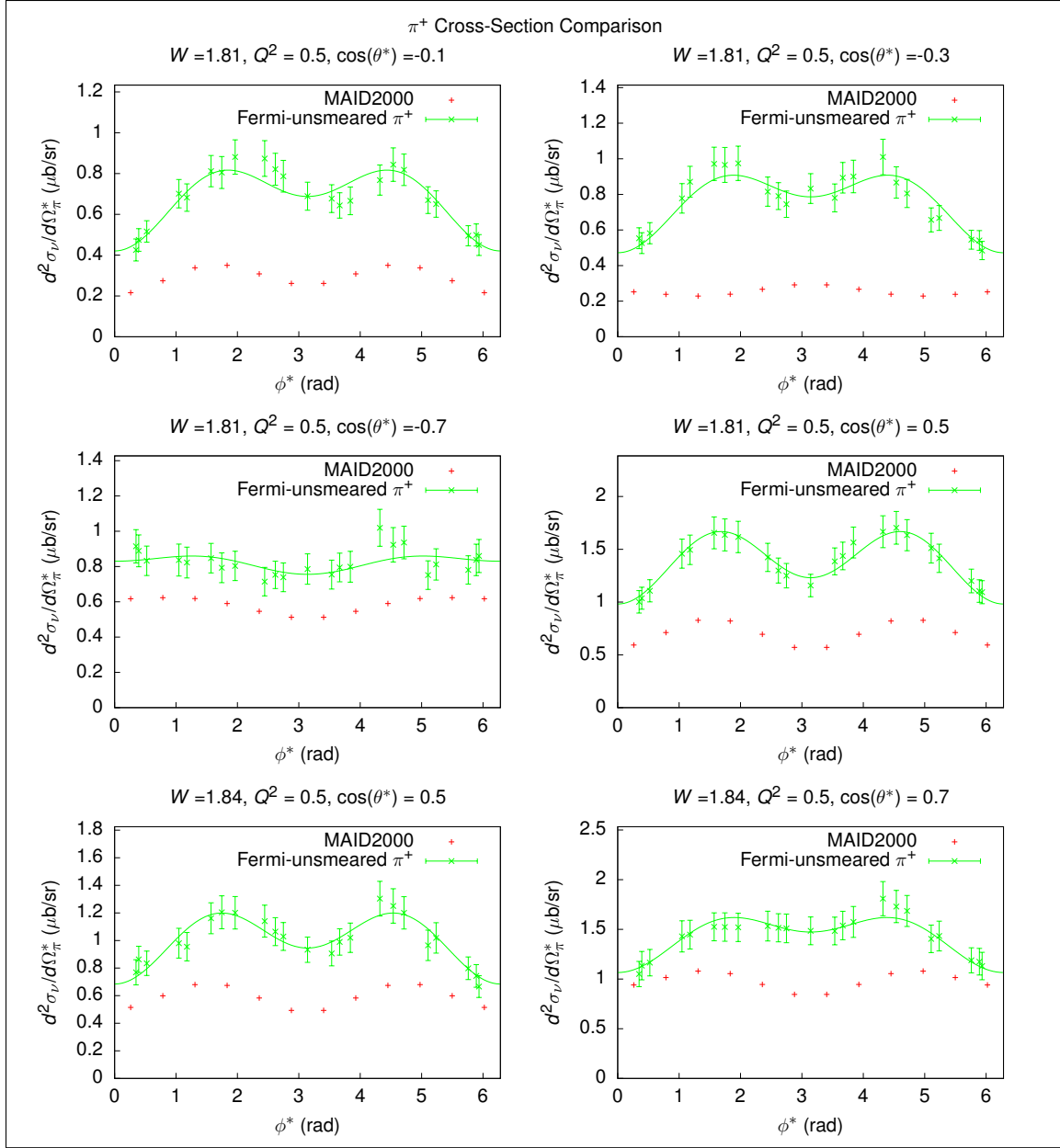


Figure 5.14: Comparison between π^+ cross-section and MAID2000 for selected bins, with combined statistical and systematic uncertainties for each point.

5.3 STRUCTURE FUNCTIONS

The plots in Figures 5.1 through 5.14 show cosine-series fits to the cross-section data of the form

$$f(\phi^*; A, B, C) = A + B \cos(\phi^*) + C \cos(2\phi^*), \quad (5.1)$$

so that A , B , and C are estimates of $\sigma_T + \epsilon\sigma_L$, $\sqrt{2\epsilon(1 + \epsilon)}\sigma_{LT}$, and $\epsilon\sigma_{TT}$, respectively. As described in more detail in Section 5.4, the fits are constrained so that the cross-section estimate cannot be negative, as negative cross-sections are unphysical. By constraining the fit to never be negative, the A , B , and C parameters are more realistic estimates.

Figures 5.15 through 5.20 show examples of the extracted $\sigma_T + \epsilon\sigma_L$, $\sqrt{2\epsilon(1 + \epsilon)}\sigma_{LT}$, and $\epsilon\sigma_{TT}$ structure functions for the π^- and π^+ analyses along with Legendre decomposition fits to each of them up to $l = 2$, so that

$$\sigma_T + \epsilon\sigma_L = \sum_{k=0}^4 A_k P_k(\cos(\theta^*)), \quad (5.2)$$

$$\sigma_{LT} = \sum_{k=0}^3 B_k P_k(\cos(\theta^*)), \quad (5.3)$$

and

$$\sigma_{TT} = \sum_{k=0}^2 C_k P_k(\cos(\theta^*)), \quad (5.4)$$

where P_k are the Legendre polynomials and A_k , B_k , and C_k are the Legendre coefficients of the cosine series fit parameters.

5.4 NON-NEGATIVE COSINE SERIES FITS

As cross-sections cannot be negative, ordinary least-squares fitting of ϕ -dependent cross-sections with a cosine series to match the form of Equation 1.16 can lead to unphysical fits. To clarify, let the cosine series ϕ^* -dependence model be

$$f(\phi; A, B, C) = A + B \cos(\phi^*) + C \cos(2\phi^*) \quad (5.5)$$

where A , B , and C are the fit parameters which will estimate the structure functions from 1.16, i.e.,

$$A = \sigma_T + \epsilon\sigma_L, \quad (5.6)$$

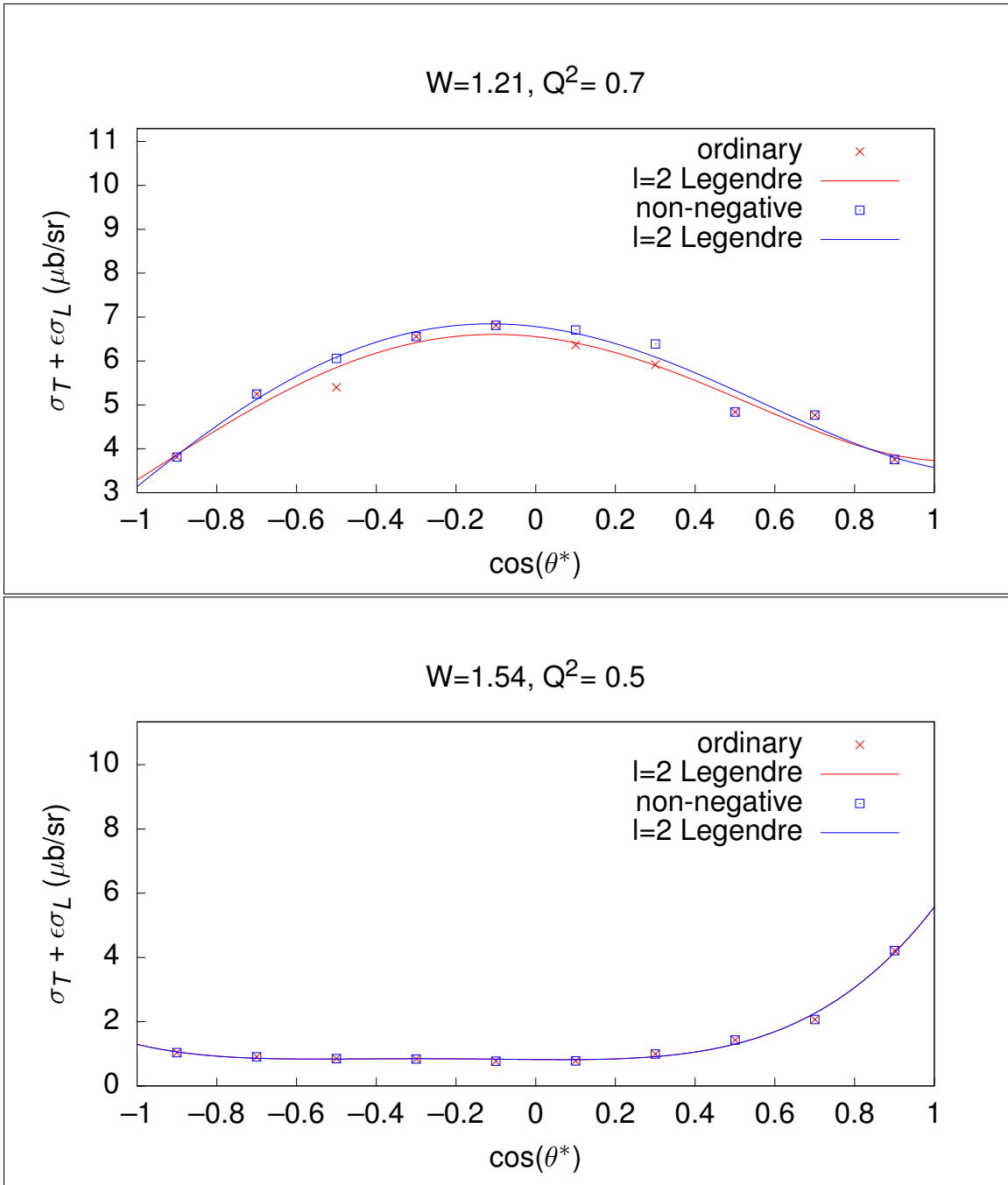


Figure 5.15: $\pi^- \sigma_T + \epsilon\sigma_L$ Legendre fits for selected (W, Q^2) bins for both ordinary and non-negative cosine fits. As can be seen, occasionally there is a difference between ordinary and constrained non-negative fit results.

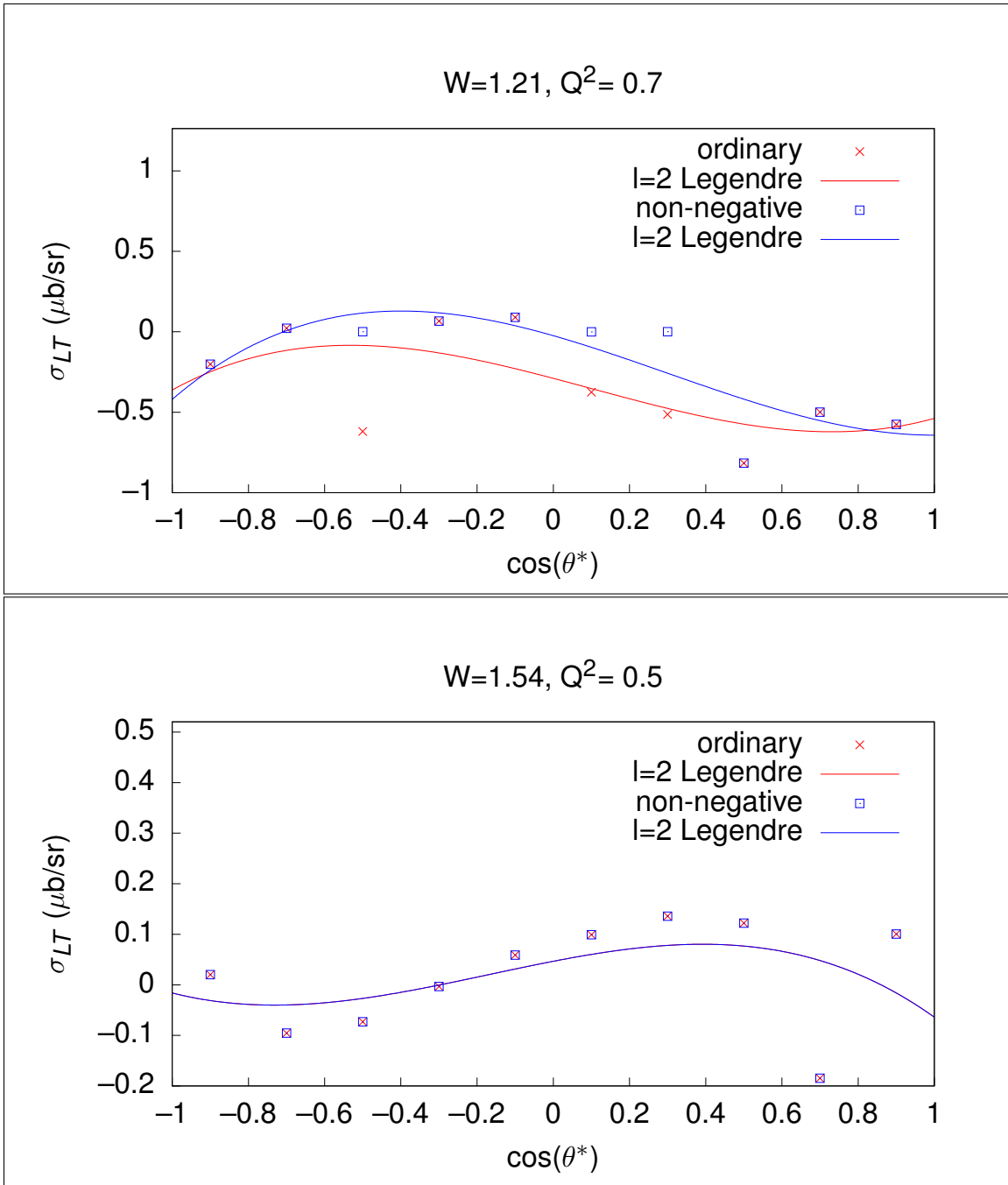


Figure 5.16: $\pi^- \sigma_{LT}$ Legendre fits for selected (W, Q^2) bins for both ordinary and non-negative cosine fits. As can be seen, occasionally there is a difference between ordinary and constrained non-negative fit results.

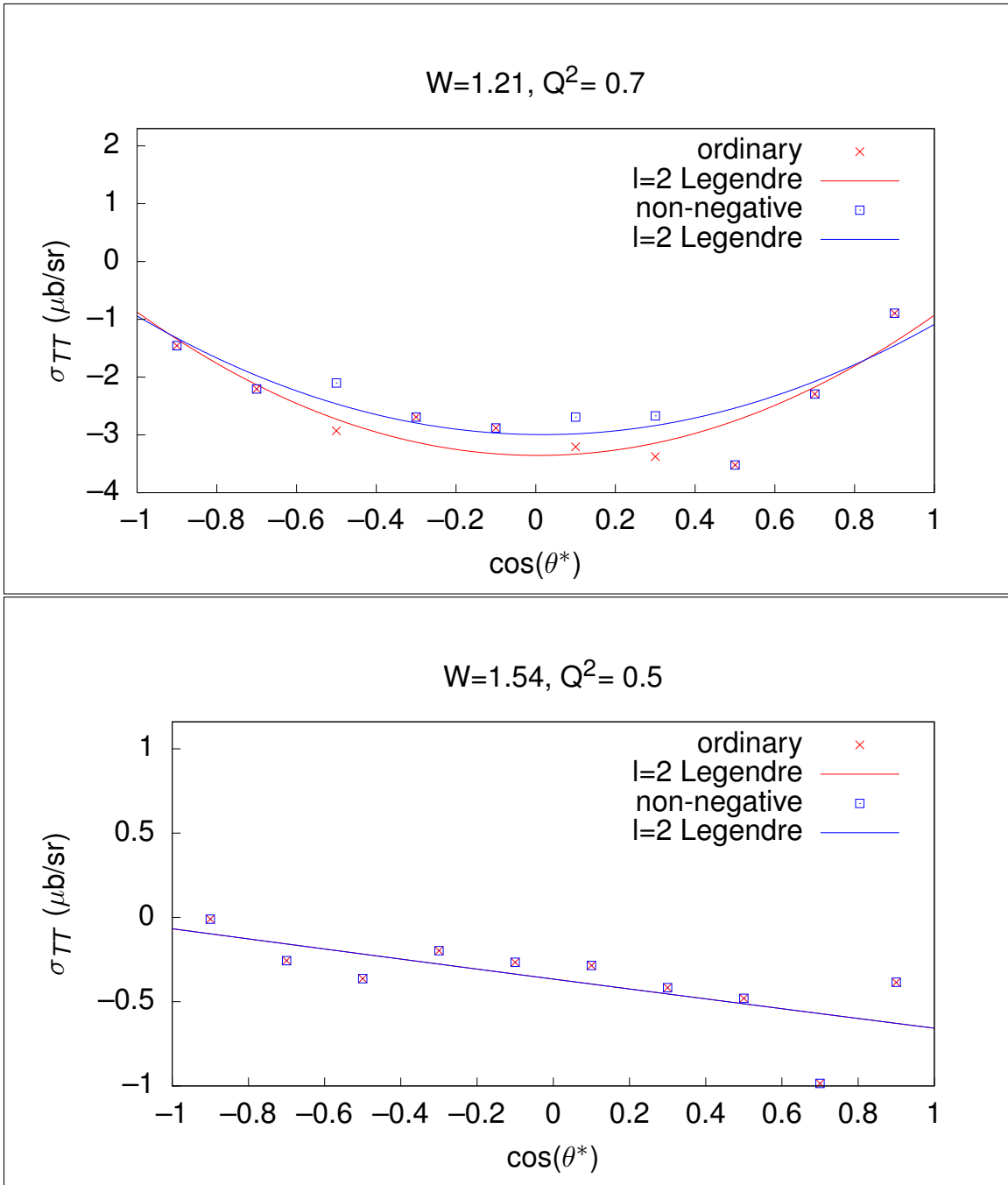


Figure 5.17: $\pi^- \sigma_{TT}$ Legendre fits for selected (W, Q^2) bins for both ordinary and non-negative cosine fits. As can be seen, occasionally there is a difference between ordinary and constrained non-negative fit results.

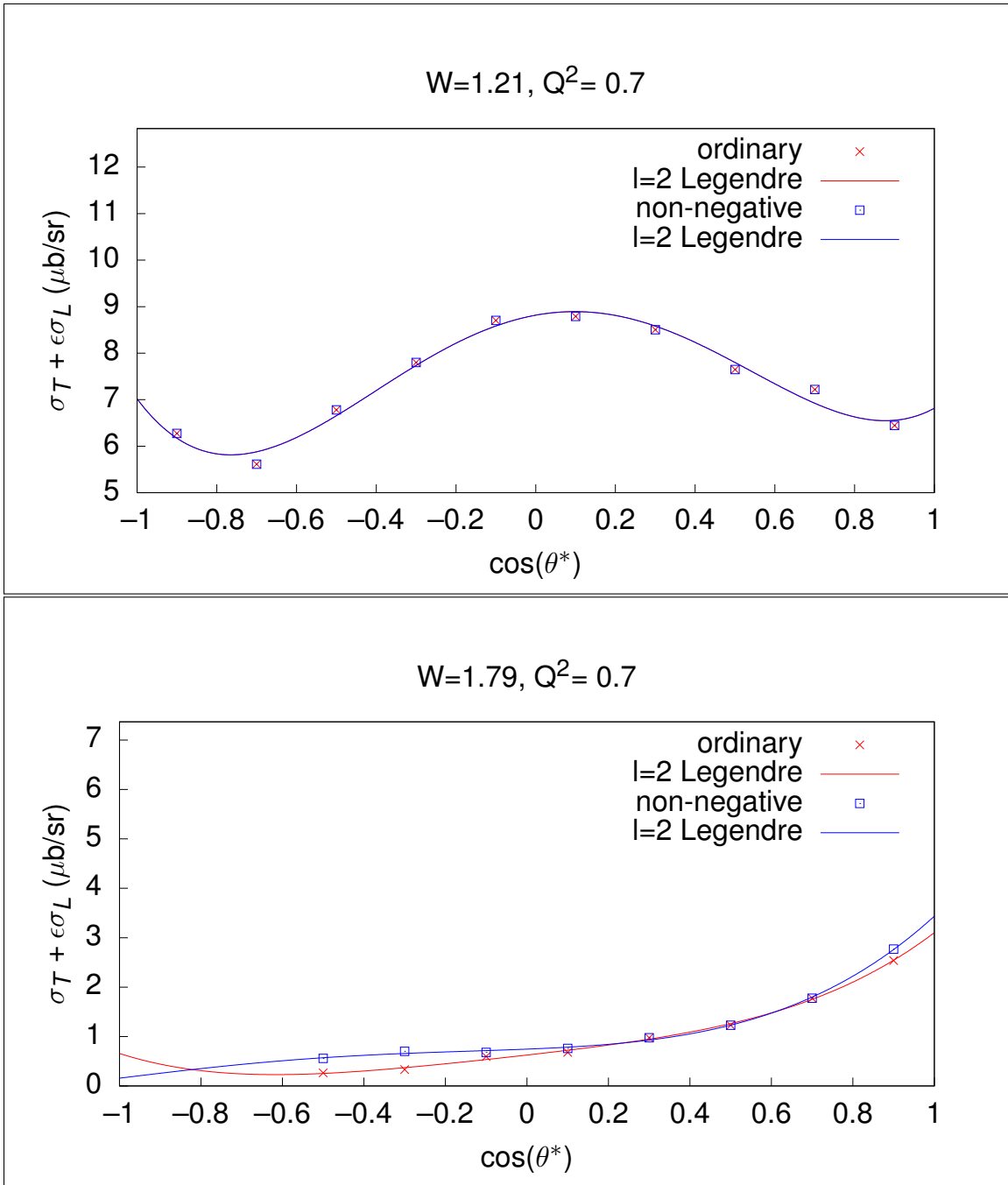


Figure 5.18: π^+ $\sigma_T + \epsilon\sigma_L$ Legendre fits for selected (W, Q^2) bins for both ordinary and non-negative cosine fits. As can be seen, occasionally there is a difference between ordinary and constrained non-negative fit results.

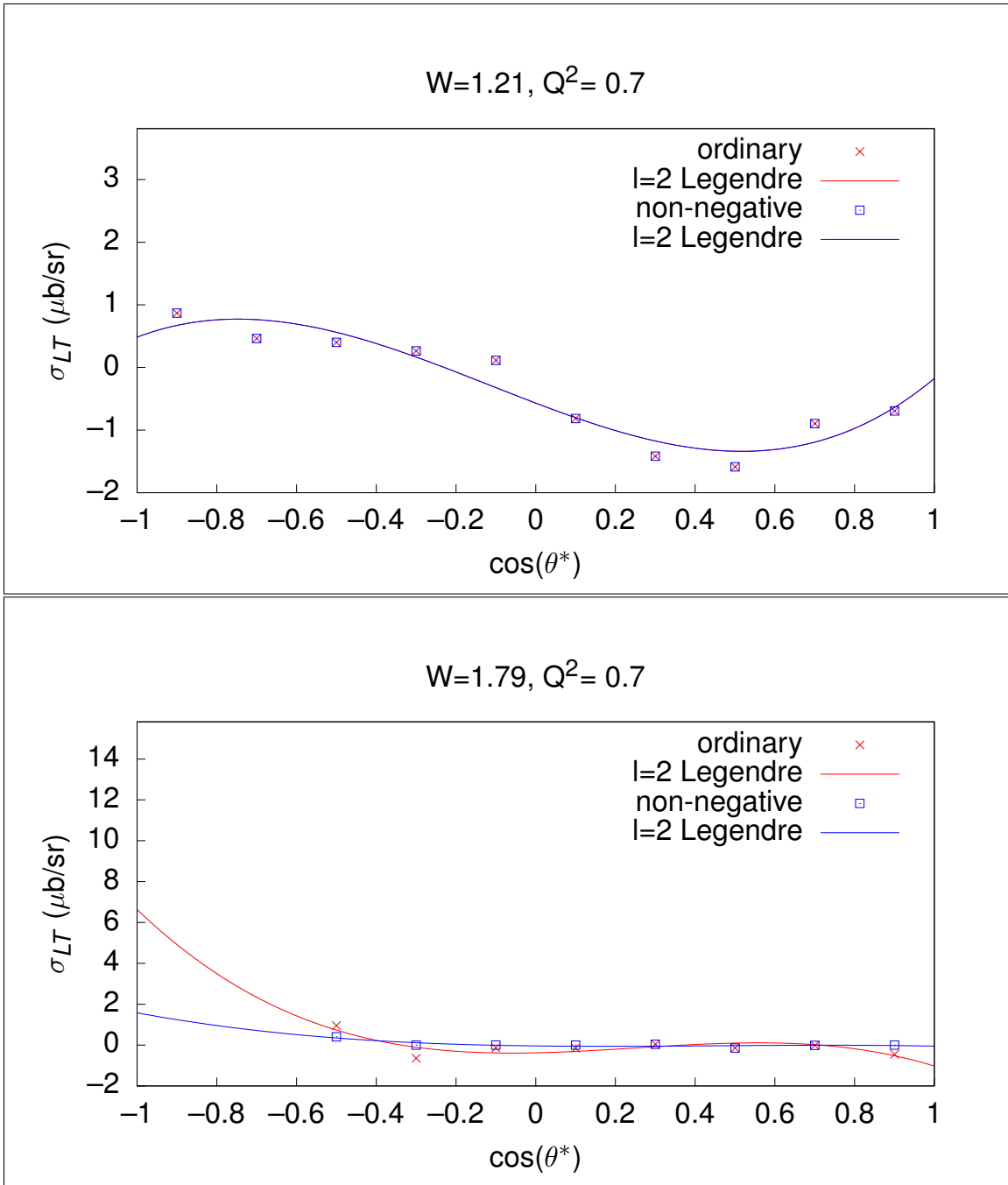


Figure 5.19: π^+ σ_{LT} Legendre fits for selected (W, Q^2) bins for both ordinary and non-negative cosine fits. As can be seen, occasionally there is a difference between ordinary and constrained non-negative fit results.

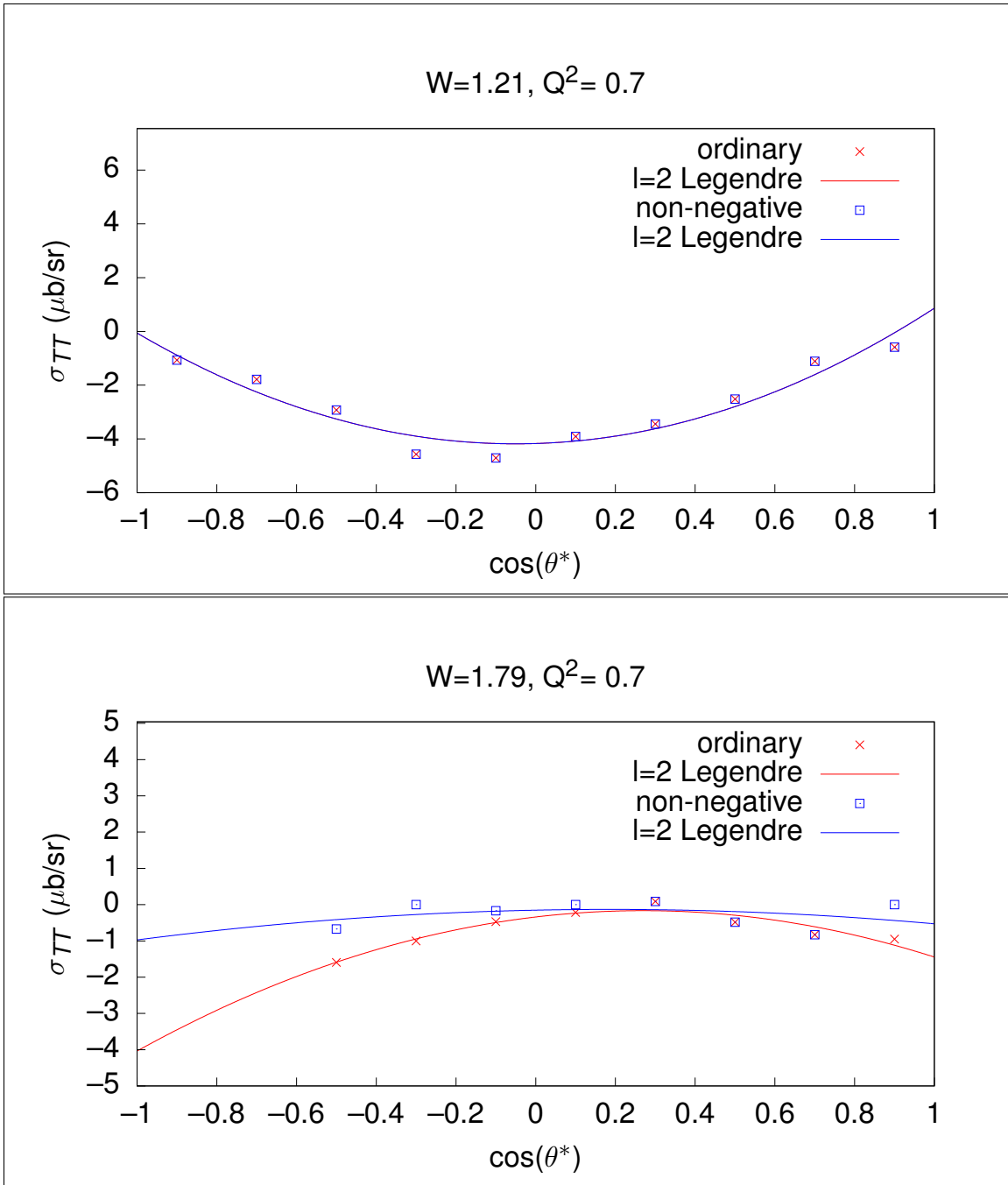


Figure 5.20: π^+ σ_{TT} Legendre fits for selected (W, Q^2) bins for both ordinary and non-negative cosine fits. As can be seen, occasionally there is a difference between ordinary and constrained non-negative fit results.

$$B = \sqrt{2\epsilon(1 + \epsilon)}\sigma_{LT}, \quad (5.7)$$

and

$$C = \epsilon\sigma_{TT}. \quad (5.8)$$

Figure 5.21 shows an example comparing an ordinary least-squares fit along with the result of the method developed here such that the overall cross-section is not allowed to be negative. The method used to generate the non-negative constrained fit is to

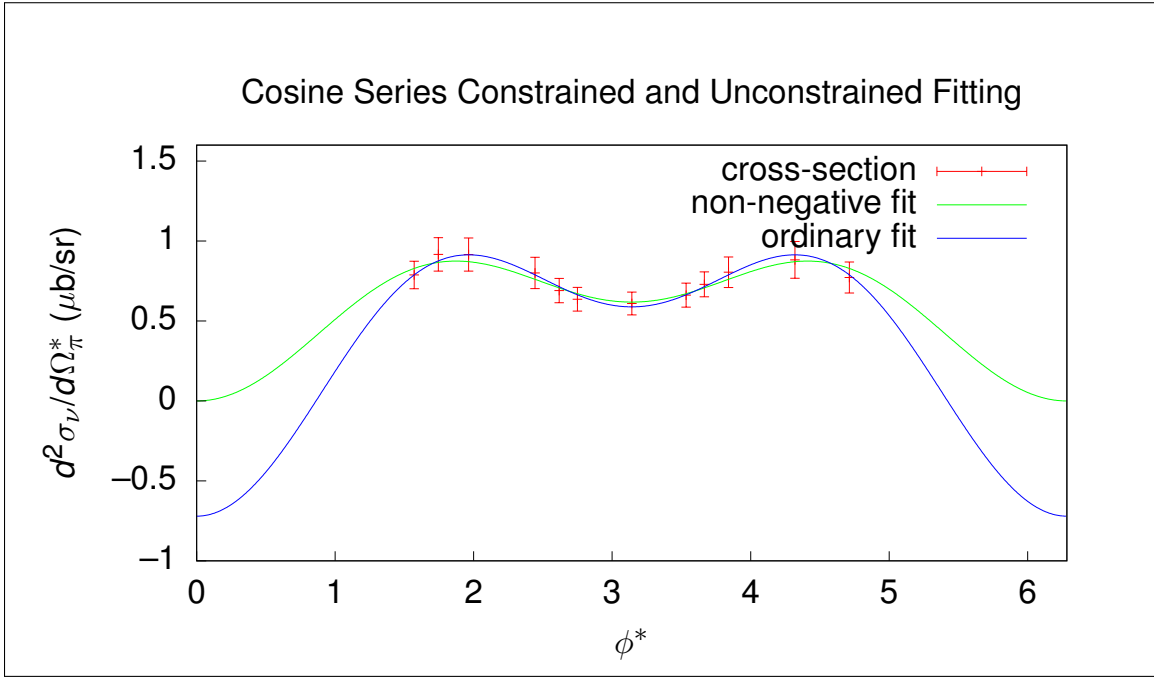


Figure 5.21: Example of ordinary least-squares fitting of cross-section data using a cosine series along with a non-negative constrained fit.

reparametrize the fit so that the parameters automatically forbid the overall fit from being negative anywhere along the ϕ^* domain.

To state the result before the derivation, the reparametrization is as follows. Let A be a function of a new parameter M and the other two parameters B and C ,

$$A(M, B, C) = \begin{cases} M^2 + B^2/(8C) + C & \text{for } C > 0 \text{ and } |B| \leq 4C \\ M^2 + |B| - C & \text{otherwise,} \end{cases} \quad (5.9)$$

so that the reparametrized fit function f is given by

$$f(\phi^*; M, B, C) = A(M, B, C) + B \cos(\phi^*) + C \cos(2\phi^*). \quad (5.10)$$

After fitting f against a cross-section ϕ^* -slice to yield the fit parameters (M, B, C) , the value for A can be found by directly evaluating $A(M, B, C)$.

To derive the method, the global minimum of the cosine series in Equation 5.5 must be determined. The global minimum g is given by

$$g = \min(\{f(m_k)\} \cup \{f(0), f(2\pi)\}), \quad (5.11)$$

where m_k are the arguments yielding the local minima of f such that

$$\frac{df}{d\phi^*}(m_k) = 0 \quad (5.12)$$

and

$$\frac{d^2 f}{d\phi^{*2}} > 0. \quad (5.13)$$

In the trivial case of $B = C = 0$, the global minimum is A . In the non-trivial case, since

$$\frac{df}{d\phi^*}(\phi^*) = -B \sin(\phi^*) - 2C \sin(2\phi^*) \quad (5.14)$$

and

$$\sin(2x) = 2 \sin(x) \cos(x), \quad (5.15)$$

it follows that

$$\frac{df}{d\phi^*}(m_k) = 0 \iff B \sin(m_k) = -4C \sin(m_k) \cos(m_k), \quad (5.16)$$

so that either

$$\sin(m_k) = 0 \quad (5.17)$$

or

$$\cos(m_k) = -\frac{B}{4C}. \quad (5.18)$$

$$\sin(m_k) = 0 \implies m_k = n\pi \text{ where } n \in \mathbb{Z}, \quad (5.19)$$

and therefore the boundaries $\phi^* = 0$ and $\phi^* = 2\pi$ are already included in the m_k , simplifying g so that

$$g = \min(\{f(m_k)\}). \quad (5.20)$$

Since $\cos(m_k) = \pm 1$ and $\cos(2m_k) = 1$ whenever $\sin(m_k) = 0$,

$$\sin(m_k) = 0 \implies f(m_k) = A \pm B + C, \quad (5.21)$$

so that the minimum value for these m_k is

$$\min_{\sin(m_k)=0} (\{f(m_k)\}) = A - |B| + C. \quad (5.22)$$

For $\sin(m_k) \neq 0$ and $C \neq 0$, the constraint on $\cos(m_k)$ combined with the fact that

$$\cos(2x) = 2\cos^2(x) - 1 \quad (5.23)$$

implies that

$$f(m_k) = A - B^2/(8C) - C. \quad (5.24)$$

To check these m_k for being minima or maxima, it follows that, for these specific m_k ,

$$\frac{d^2 f}{d\phi^{*2}}(m_k) = 4C, \quad (5.25)$$

so that these m_k are the ϕ^* values of local minima whenever $C > 0$. Note that there is an implied constraint from Equation 5.18 such that

$$|B| \leq 4|C|, \quad (5.26)$$

as the cosine function is always between -1 and 1 . In this case, since $C > 0$, this simplifies to

$$|B| \leq 4C. \quad (5.27)$$

Expressing the global minimum in the light of these new considerations, including that the trivial $g = A$ minimum is a special case of the $A - |B| + C$ local minimum, it follows that

$$g = \begin{cases} \min(\{A - |B| + C, A - B^2/(8C) - C\}) & \text{for } C > 0 \text{ and } |B| \leq 4C \\ A - |B| + C & \text{otherwise.} \end{cases} \quad (5.28)$$

The first case can be reduced further by noticing that at $|B| = 4C$, both local minima are equal, and whenever $|B| < 4C$, $-B^2/(8C) - C < C - |B|$, so that the $A - B^2/(8C) - C$ local minimum dominates, and therefore

$$g = \begin{cases} A - B^2/(8C) - C & \text{for } C > 0 \text{ and } |B| \leq 4C \\ A - |B| + C & \text{otherwise.} \end{cases} \quad (5.29)$$

Knowing the global minimum as a function, $g(A, B, C)$, allows a reparametrization based on the constraint that

$$g(A, B, C) \geq 0. \quad (5.30)$$

Inverting $g(A, B, C)$ to find $A(g, B, C)$ yields

$$A = \begin{cases} g + B^2/(8C) + C & \text{for } C > 0 \text{ and } |B| \leq 4C \\ g + |B| - C & \text{otherwise.} \end{cases} \quad (5.31)$$

Letting $g = M^2$ guarantees that g cannot be negative, leading to the reparametrization in Equation 5.9.

Note that this method can be further extended to allow an arbitrary minimum cross-section constraint by letting $g = M^2 + \sigma_{\min}$ in the reparametrization of $A(M, B, C)$, so that

$$A(M, B, C) = \begin{cases} M^2 + \sigma_{\min} + B^2/(8C) + C & \text{for } C > 0 \text{ and } |B| \leq 4C \\ M^2 + \sigma_{\min} + |B| - C & \text{otherwise.} \end{cases} \quad (5.32)$$

5.5 SYSTEMATIC UNCERTAINTY ESTIMATION

Systematic error here refers to those errors which are neither due to statistical fluctuations nor due to thoroughly understood flaws in the analysis methodology. If the flaws were perfectly understood then there would be a method to correct the analysis so that the results were no longer in error. As the majority of the sources of systematic error in this work have already been identified and their corresponding uncertainties estimated in [1], they will be used in this work along with additional systematic uncertainties incurred specifically in this analysis. Using the same quadrature sum of relative uncertainties approach as in [1], the systematic uncertainty estimate is given by

$$\sigma_{\text{sys}} = \sqrt{\sigma_{\text{cut}}^2 + \sigma_{\text{Fermi}}^2 + \sigma_{\text{BC}}^2 + \sigma_{\text{rad}}^2 + \sigma_{\text{norm}}^2}, \quad (5.33)$$

where

- σ_{cut} corresponds to data selection cuts,
- σ_{Fermi} corresponds to Fermi-unsmearing,
- σ_{BC} corresponds to bin-centering corrections,
- σ_{rad} corresponds to radiative-effects corrections, and
- σ_{norm} corresponds to normalization.

The terms in this analysis are identical to the terms from [1] with the exceptions of σ_{Fermi} and σ_{cut} , as Fermi-unsmearing was not needed in [1] and there are no proton related cuts applied in the π^- and π^+ analyses.

From [1] and with the exception of the proton related cuts, σ_{cut} is broken down into further quadrature components:

$$\sigma_{\text{cut}} = \sqrt{\sigma_{\text{eid}}^2 + \sigma_{\pi}^2 + \sigma_{\text{excl}}^2} \quad (5.34)$$

where

- σ_{eid} corresponds to electron identification,
- σ_{π} corresponds to pion identification, and
- σ_{excl} corresponds to exclusivity squared missing mass cuts.

As the electron identification and pion identification methods are identical in this work and [1], the systematic uncertainties should also be identical. The exclusivity cuts on the squared missing mass differ however, and therefore an analogous for evaluating the exclusivity cut systematic uncertainty is used. Rather than varying the cuts between specific ranges, the signal-to-background ratios are varied between 10% background and 2% background, with the result that the final cross-section estimates for the π^+ and π^- analyses varied on average by 2.4% and 2.35%, respectively, and

therefore the higher deviation of 2.4% is used to estimate the systematic uncertainty for both analyses. This combined with the values from [1] yields a selection cut relative systematic uncertainty of

$$\sigma_{\text{cut}} = 3.9\%. \quad (5.35)$$

Estimating the Fermi-unsmearing systematic uncertainty is accomplished by varying the MAID model used as well as through varying the Fermi-motion potential used to generate events using the same three models as referenced in [1], those being the CD-Bonn [30], Paris [31], and Hulthen [32] potentials. Using the momentum distribution from each potential, the Fermi-unsmearing correction factors had an average RMS deviation of 6%. Table 5.1 summarizes the systematic uncertainty components and the total systematic uncertainty of 8.81% for both the π^+ and π^- analyses.

Table 5.1: Systematic uncertainty components.

Component	Relative Uncertainty (%)
σ_{cut}	3.9
σ_{Fermi}	6.0
σ_{BC}	0.55
σ_{rad}	1.0
σ_{norm}	5.0
σ_{sys}	8.81

CHAPTER 6

DEPENDENCY ORIENTED PROGRAMMING

In an effort to explore advancements in software design, especially directed towards large scale data analysis such as the analysis presented in this work, I started an open source data analysis library and framework called cl-ana [20] and used it for this data analysis. As it stands, cl-ana provides a sufficient framework for analyzing large scale data in a paradigm which, lacking a better term, is called dependency oriented programming (DOP). This paradigm allows analysis software to scale better and allow for more modular and versatile software than other existing paradigms, as will be shown. DOP might best be first understood through comparison and contrast with other paradigms currently used for data analysis software development.

In physics data analysis, due to the scale of data sets and the need for efficient processing of that data, the selection of programming languages is severely limited when compared to other fields. Where many fields are well served by statistical computing languages like R or MATLAB, physicists conventionally choose between a pure performance-oriented language like C/C++ or FORTRAN with support from libraries such as ROOT [19] from CERN, or a hybrid approach where a higher-level script-like language such as Python is used to wrap together high-performance libraries written in the performance-oriented languages. These languages and libraries comprise mature, stable development platforms, but do lead to predictable software development trajectories with clear drawbacks which, with the appropriate choice of domain specific language (DSL), can be mitigated.

The typical first stage of software development in a particle physics data analysis project is exploration of the data set. This involves using relatively small sample

files to quickly view various visualizations of the data and conduct a preliminary investigation of data for the purpose of understanding and possibly discriminating the available data sources based on the kind of analysis being conducted; for example, one might desire to investigate a specific resonance and thus would investigate different experiment data sets to see which data set would be best suited for investigating that resonance. This stage is well-served by current software tools, which is to be expected due to the maturity of small scale data analysis tools, but is also a testament to the utility of large scale libraries like CERN's ROOT. However, the move from preliminary exploration to incrementally developed analysis software programs, which process the data and extract various features from it, moves the researcher far away from the simplicity and efficacy of the tools used initially and into the details of software engineering. For researchers who have little experience with software development, the learning curve is quite steep regardless of their physics and mathematics background. Nothing written here escapes the understanding of software developers already working in this field; indeed, there are already active efforts to address all of these concerns. There has already been a shift towards utilizing higher level languages such as Python to organize software and alleviate the burden of writing all software in languages better suited for efficient use of computing resources at the cost of difficulty in software development. There are also efforts to remove as much of burden of data processing as possible from researchers, an example being the new software libraries and data access structure being developed for CLAS12 data analysis. The second effort is related to the first: The less one needs to process the data, the less one needs to care about efficient use of computing resources. However, both efforts can be greatly improved by the development and use of more appropriate languages for their respective domains.

As all programming languages commonly used for large scale data analysis are strictly imperative languages, the overall structure of analysis software is a collection

of programs or scripts which either perform specific transformations or reductions of the data, e.g. effectively adding new fields to the data tables or computing summaries of the data like histograms. Often for both efficiency and the convenience of the user, these programs balloon into monoliths that are responsible for a wide variety of tasks controlled through a vast array of parameters. There might be a flag or parameter to enable or disable any number of cuts along with parameters to control how many reductions are computed from the data. This is a reasonable solution to the alternative problem of a vast array of small programs which must be designed to communicate seamlessly with each other and still maintain efficiency, which is all but impossible for large scale data analysis due to the challenge of efficiently managing hard drive access. A small number of programs each reading from and writing to disk simultaneously will be too inefficient on anything other than a machine specifically designed to support this with state of the art solid state drives or massive RAM capacity.

It should be clear that this design is closer to the needs of hardware than the needs of the researcher-programmer. What the researcher cares about is organizing the data and reducing it into various summaries that can be visualized or used for further simplified analysis such as modeling. This is the basis for dependency oriented programming. In DOP, analysis software is not written directly. Rather, computation targets are specified which designate subsets of data and reductions of that data. Whenever computation targets are set for calculation, a function or program is dynamically generated to compute just those targets. Other dependency oriented tools are GNU Make and ordinary spreadsheets, though when this approach is used to design a programming language, some novel and useful features emerge, as will be seen.

6.1 A SIMPLE EXAMPLE

A simple example can illustrate DOP in practice. As `cl-ana` is written in Common Lisp, a very brief primer on Lisp is in order. Lisp syntax is simply a universal prefix notation: Every call to a function or operator has the following form:

```
( f a b c ... )
```

where `f` is the function or operator and `a`, `b`, `c` etc. are the arguments supplied to `f`. This applies to arithmetic as well, so that `2 + 2` would be written as below.

```
(+ 2 2)
```

One aspect of Lisp syntax that might be confusing to those of other software backgrounds is the wide range of symbols available for naming variables and functions, such as hyphens and virtually all punctuation symbols other than parentheses. As a pathological example, `2+2=3` would be a perfectly valid name for a Lisp variable and would have nothing to do with the nonsensical mathematical meaning implied to the programmer by the variable name. The rest of what little complexity remains of Lisp syntax is not important for this example and will be left to the reader to investigate further in other sources if desired. The computing environment for Lisp is called a Lisp image and is an interactive compiler, linker, and execution program simultaneously. To run Lisp code, you instruct the image to load the software, which usually results in compilation when necessary and linking the compiled code to the running Lisp image, which enables the compiled binaries to be called directly from the running Lisp image. Using `cl-ana` consists of loading source code into the image and eventually making a function call to instruct the Lisp image to perform whatever work is necessary, such as the simple example below.

Suppose there is a structured data set A which has floating point fields (x, y) . As part of initial exploration, one might be interested in basic statistical measures for each field as well as measures of correlation, along with visualization for each of these.

With existing tools, this could be done in a variety of ways from single function calls to GUI assisted exploration of the data. In the DOP paradigm, it could take the form of a single operator that defines a collection of visualizations and reductions for this data set. The fundamental operation used by this exploration operator would be some way of defining result targets, which in `cl-ana` is called `defres` and might be used to define the source data set as follows.

```
(defres A
  (srctab (csv-opener “/path/to/dataset.csv”)))
```

This snippet of code says that there is a data set named `A` stored in a comma separated value (CSV) file located at “/path/to/dataset.csv” in the file system. One might then make a call to a statistical summary operator to initially investigate this data,

```
(statsummary (res A)
              :fields (x y)
              :stats (mean stddev hists1D hists2D))
```

which would result in averages, standard deviations, 1-D histograms, and 2-D histograms being defined for fields `x` and `y` from the data set `A`. Here the `res` operator is introduced; `res` references a specific result target that has been defined elsewhere. To avoid another possible point of confusion, Lisp operators can be defined to act directly on the code supplied to them rather than some values referred to by that code. So, in the `statsummary` example, you can notice that the `:stats` argument is a list that looks like it might indicate a call to a function called `mean` supplied with `stddev`, `hists1D`, and `hists2D` as arguments. However, `statsummary` treats the argument as a list of symbols that are read as instructions to enable various statistical measures.

So far, there’s nothing in this example that wouldn’t be possible with existing tools. However, taking a simplified peak under the hood of `statsummary` will help reveal the added potential of this approach. If this code is supplied to a Lisp im-

age, nothing substantial is actually done by the image. No statistical calculations are performed; no data is loaded from the CSV file into memory. These instructions are declarative, not imperative. The source data set is defined as something to be evaluated eventually, as are the statistical measures of interest. `statsummary` is an operator that *defines* quantities of interest rather than computing them. The various optional arguments supplied to `statsummary` control the specific definitions of those quantities and which quantities are defined at all. These definitions will be given regular names based on the source table name and their own meaning; the mean of field x might be called `(A mean x)` for example. This by itself is relatively useful for writing reusable software as it is possible to define libraries of definition operators that can define families of related calculations with regular naming schemes; to accomplish the same with other tools usually amounts to personal discipline in maintaining naming conventions, whereas this approach automates that effort. As will be made increasingly clear, this feature is orthogonal to a collection of orthogonal features that can combine to produce substantial ease of use and expressive power.

This is a good place to pause and point out a pair of noteworthy and simple orthogonal features: Result reference and data serialization/storage. As seen in the example above, the expression `(res A)` is taken to refer to the data set A . This is true for every result computed using `cl-ana`'s DOP system: The result of `(defres X ...)` can be referred to by other code as `(res X)`. Clearly, if all results are stored in memory then the size of an analysis project is severely limited. The second closely related feature addresses this: Automatic data serialization and storage to disk. Whenever possible and unless demanded otherwise by the user, `cl-ana` saves results to disk after computation. As specified by the caching algorithm chosen, these are loaded and unloaded from memory in response to requests for specific results via `(res ...)` expressions.

If the statistical quantities defined by `statsummary` were defined naively, one might expect that each quantity would amount to a loop over the data set, so that there would be as many passes over the data as there are quantities of interest. This is woefully inefficient, but mandates a solution. `cl-ana` addresses this problem with the *table transformation pipeline*. This is a pipeline of functions that are successively called on the definition table for the analysis project. These functions have access to all of the definitions and can transform them as seen fit. For this simple example, the useful transformation is called `tabletrans`, but the name is less important than the function. `tabletrans` determines the minimally necessary number of passes over all source tables and merges definitions so that targets can be defined as if they were independently looping over the source table, but will be executed simultaneously in a single loop. For this example, a single loop would be capable of computing all desired results.

Suppose that we are interested in a subset of data set A , say when $x < 2$ and $x + y < 5$. With existing tools, we are faced with a problem. If we decide to store this subset in their own file(s), then we could use existing programs or scripts without any issues aside from supplying them with new input file names. However, when the number of subsets is large, it can become prohibitively expensive to store every single subset to disk, as each new set of files is redundant. The other common solution is to store a list of row indices that defines the subset of data. The row index solution is typically reached for as the complexity of an analysis grows. This solution scales well but mandates that (outside of very sophisticated software design) separate passes over data sets are required for computing the index lists and quantities of interest. It also mandates that every reusable program or script must support list index arguments, which again means more complexity for code writing. As the subset criteria are often subject to refinement, the need for at least two passes over the data means frequent

doubling of delays as the time taken to iterate over data sets is significant. This is where another feature of `tabletrans` comes into play: Table subset definitions.

Suppose B is the desired subset of A .

```
(defres B
  (tab (res A) ()
    (csv-opener (work-path '“B.csv”’)
      :field-names (list ‘“X”’ ‘“Y”’)
      :read-from-string t)
    (when (and (< (field x) 2)
              (< (+ (field x)
                    (field y))
                  5))
      (push-fields))))
```

This introduces quite a few new terms, but suffice it to state only the necessary essentials. `tab` defines a data subset which will be stored in files, here defined to be another CSV file located wherever `(work-path ‘“B.csv”’)` happens to be. `work-path` is a utility function which returns paths under the project’s result directory. `push-fields` is an operator which has meaning in the context of data table subset definitions, designating a row of fields being inserted or “pushed” into the result table. Here, `push-fields` is in the context of a conditional statement via `when` such that it is evaluated only when the criteria of $x < 2$ and $x + y < 5$ are met. If we were also interested in the statistical summary of data set B , we could define it just like for A , only changing the source data ID argument.

```
(statsummary (res B)
  :fields (x y)
  :stats (mean stddev hists1D hists2D))
```

If all of the quantities defined so far were demanded to be calculated by `cl-ana`, then it would take a single pass over the data set, and the results would be all statistical summary quantities for A and B along with B being stored on the file system in a separate CSV file. If a change were made to the definition of B or if new quantities were desired at a future time, then only those quantities affected by the changes would be recomputed.

So far this does not obviously solve the problem posed earlier: How can code be written so that subsets of data can be analyzed without caring whether they are stored in separate files or accessed via index lists? This is solved by the introduction of a new concept and an operator to go with it: Logical data tables. A logical data table is a data table that only exists as an organizational construct. Logical tables are never stored on the file system, and when they are computed by `cl-ana`, their values are always the same: `NIL`, which is Lisp for nothing. However, during the transformation pipeline step, logical tables specify subsets of data, so that quantities can be defined as reductions of logical tables. The resulting computation will pass over the necessary data files, and quantities will be calculated only in the subsets for which they were defined. We might have defined B as a logical table from the start.

```
(defres B
  (ltab (res A) ()
    (when (and (< (field x) 2)
              (< (+ (field x)
                    (field y))
                  5))
      (push-fields))))
```

No change to the rest of the code would be necessary to switch from storing B in a separate CSV file to reading B from the original data files. (Unfortunately, this is one area of `cl-ana`'s implementation that I have not been able to completely finish in that

table index lists are not automatically generated and reused for logical tables; the computation passes over the entire source data set, and the contexts are evaluated every time a pass over the logical table is performed. This is an optimization I plan to finish implementing in the near future, but has not actually been necessary for this analysis.) Tools can be written to use tables regardless of where their source data originates; the only concern for operations using tables is the specific fields they contain.

6.2 HAVING AND EATING CAKE: DOP + ROOT + C++

The operators above have all strictly utilized Lisp, but as might be anticipated there can be efficiency concerns using Lisp for the most demanding computation tasks. In this analysis, Common Lisp turned out to be too slow either due to lack of optimization or due to lack of time to develop those optimizations. Here enters another benefit of this paradigm: It doesn't matter what language is used to actually calculate results. In response to the slowness of Lisp in looping over data sets and performing calculations directly, I have built analogous versions of `tabletrans` for local and remote C++ code execution. Although there are some necessary differences between operators and operations defined to run with C++ versus Lisp, the overall design is similar, and once results have been calculated it doesn't matter to the user where they came from.

As implemented, ROOT is used for the C++-side data analysis library, and data is assumed to be stored in ROOT's own data format. As an added bonus, I was able to build a version of this table transformation that would generate C++ code, upload and submit it to JLab's computing cluster, wait for the jobs to finish, check for errors or missing jobs and resubmit if needed, download, extract, and merge results into their finally usable forms. With a sufficient layer of convenience functions defined between

target definition code and user code, these three related table transformations enable location, format, and language agnostic code to be written by the user. To illustrate, here is a snippet of my own code used for this analysis that defines and plots electron identification histograms for the E1E deuteron target data set with minimal (called “sanity”) cuts applied.

```
(c++-eid-hists (res (jlab ele d san)))  
(draw-eid-hists (res (jlab ele d san)))
```

The first operator `c++-eid-hists` clearly refers to C++ due to needing to choose how to compute results, but the second operator `draw-eid-hists` does not care where the results come from. It expects that the necessary results have been defined and refers to them in the result targets it defines. The target IDs are derived from the name of the source table along with arguments given to the operators as part of the definition, which allows for suites of related operators to work together harmoniously. To show how far this development can lead, here is a snippet of code that defines the experiment data cross-section analysis chain for a particular reaction channel.

```
(recon-prechannel-chain  
  (jlab ele d)  
  :target :deuteron  
  ;; Custom Delta T cut arguments:  
  :san-cuts-deltat-cut-args *ele-san-deltat-cut-args*  
  ;; Fiducial Cut UYW:  
  :efid-cut-uvw-cut-plists *ele-efid-uvw-cut-plists*)
```

```
(recon-1pi-missing-hadron-chain  
  (jlab ele d)  
  :target :proton  
  ;; Custom Exclusivity Cut
```

```
:excl-cut-fit-range (cons 0.84d0 0.92d0)
:excl-cut-nsigma 1
:excl-cut-sigma-guess 0.005d0)
```

These two operators each define half of the analysis process for a complete analysis of experimental data from JLab's E1E deuteron target experiment, with data subsets, histograms, and automatic cut determination result targets being defined in response to whatever custom arguments are supplied, if any. This example is to show the scalability of writing code in this paradigm to the point where an entire analysis can be defined by a handful of functions. If this analysis were written entirely in C++ with conventional paradigms, there is no way to replicate the functionality of these example functions, as each operator would require multiple distinct programs or scripts to replicate their functionality. You could of course hide this complexity behind controller programs or scripts that would make calls to the lower-level programs or scripts, and you could even automate job submission, management, and download from a computing cluster. The point here is about the way software scales and its implications for designing data analysis software. There is no requirement for the user to think about the details of where code is to be executed and where the data is coming from aside from using operators with slightly different names to designate the broad class of the computation, such as local Lisp code or some kind of C++ code. Additionally, there is the bonus of having no need to worry about which specific scripts or programs need to be re-run when a change is made to parameters, as these will automatically be determined on demand in response to the user changing the definition of a target. An auxiliary benefit of dependency oriented programming is straightforward visualization of an analysis project. Figure 6.1 shows a graph of the targets defined in the simple example for our fictional data sets *A* and *B* above. Functions for generate these dependency graphs are included with `cl-ana`, and the types of targets included in the drawn graph can be filtered so that an analysis can

be seen from different perspectives and levels of detail, e.g. viewing only the data subsets or viewing only targets related to a specific cross-section calculation.

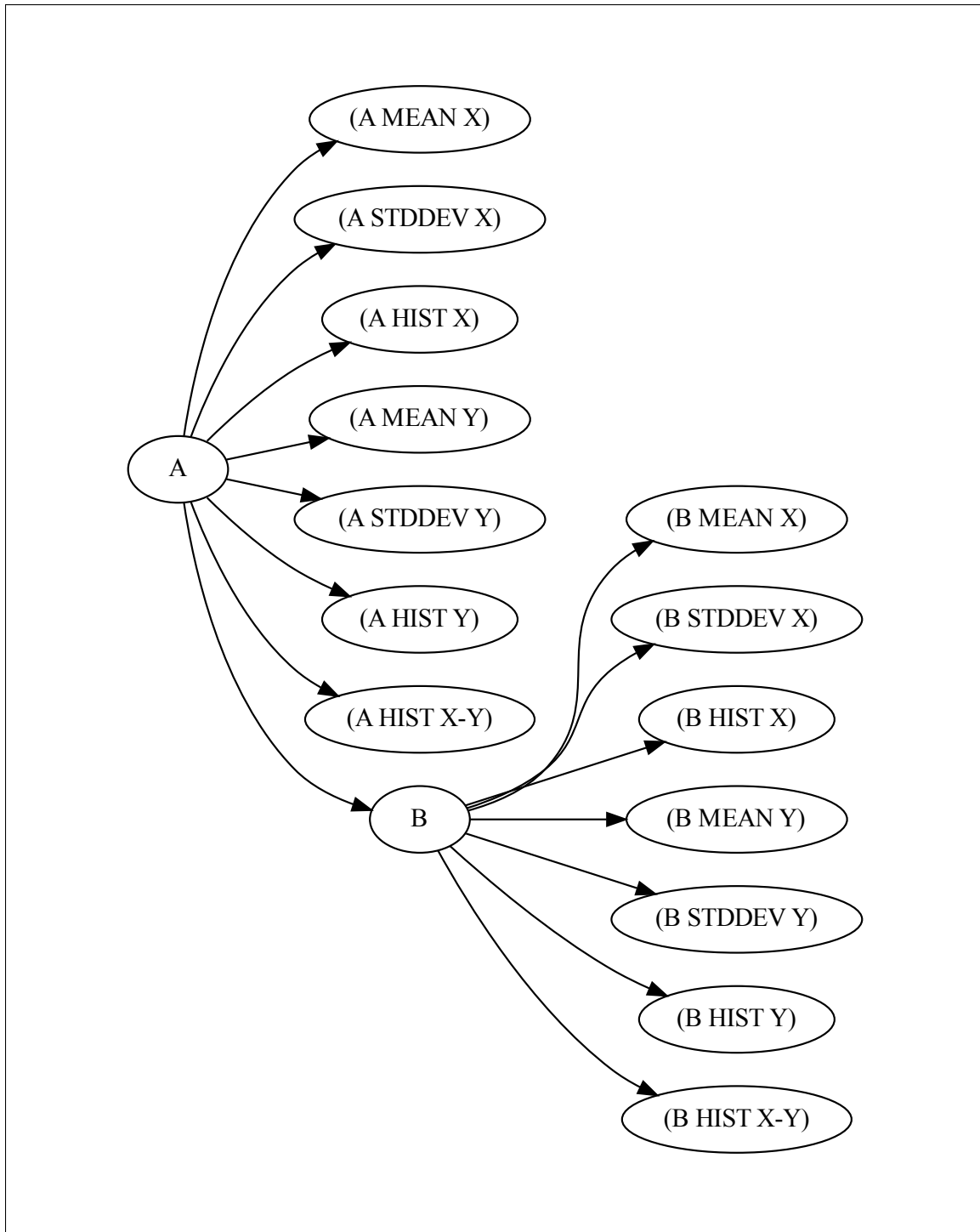


Figure 6.1: Target graph for simple example.

6.3 ADVANCED USAGE

The `tabletrans` transformation has been shown to be useful for allowing efficient analysis of structured data with result targets specified independently, but there are other more exotic transformations that have already been defined as built-in features of `cl-ana` as well as a few that I have added for this analysis but which have not been refined to the point of including in a general purpose data analysis library.

6.3.1 BRANCHTRANS

Often in an analysis project, it is desirable to experiment with many different possible settings or versions of a calculation. Maybe one is not sure precisely how wide to make a cut, or which specific set of parameters out of a collection of many possible sets is optimal for the analysis. `branchtrans` is designed precisely for this inevitability. `branchtrans` implements computation branching where the branches of the computation depend on some set of parameters which can be selected from a list of possibilities. `branchtrans` is orthogonal to `tabletrans` and the other transformations, which makes it convenient to define branching data subsets or reductions over those subsets. Nested branching is also supported, so that multiple sets of parameters can be tested as a Cartesian product of possible parameters. The one drawback to `branchtrans` as implemented is that the set of possible parameters must be known at the time the transformation is applied. This is true of all the transformations, as a transformation is applied to the entire target table before any calculations are performed. Implementing branching that depends on results would demand a more sophisticated approach where the transformations are performed in an indeterminate way, so that some parts of transformations can be known to be safe and thus immediately performed, while others must be delayed until more information is available. This breaks the current model of `cl-ana`'s dependency oriented system since there is a pipeline of transformations which feed directly into each other. There doesn't appear

to be any obvious obstacle to implementing the indeterminate transformation scheme aside from the time and complexity of the problem, however.

As a simple example of `branchtrans`, consider the original simple example of two data sets A and B . Suppose that the selection criteria for B is in question; suppose $x + y < P$ for some parameter P . To define B as a branching table as a function of some parameter P , we might do the following.

```
(defres P
  (branch (range 1 10)))

(defres B
  (branch (res P)
    (ltab (res A) ()
      (when (and (< (field x) 2)
                 (< (+ (field x)
                        (field y)))
                (branch))))
    (push-fields))))
```

Here P is defined to branch based on the integers 1 through 10, and B is copied into a variant for each value of P , which is stated through different uses of the same `branch` operator. When used to defined a branching calculation, `branch` is supplied with an expression which must evaluate to a list of options. When used to denote one of the calculations tethered to the original branching calculation, the first use of `branch` specifies the source of the branch or another co-branching target, and uses of `branch` inside this context needs no arguments and refers to the value of the branching parameter. For nested branching, the parameter `branch` calls should be supplied an argument to identify their source.

6.3.2 NOCUTTRANS

In data analysis where there is a large variety of cuts being applied simultaneously, it is often useful to understand the effects of a cut in the context of all other cuts being applied. The difference between the data subset with or without just this one cut can be seen as the effective strength of that cut. If one already has a complete analysis program implemented with the ability to manipulate all cut parameters from command line arguments or some other convenient interface, then it is trivially simple to disable or modify individual cuts to examine their impact. However, in the dependency oriented approach, it is not trivial in the same way without a new transformation. This is the purpose of `nocuttrans`, which can both disable and modify existing cuts and create separate chains of data subsets starting from a true source table and ending wherever the user decides to end it. This is one ability that the dependency oriented approach makes trivial which would not be trivial in the ordinary procedural approach: Generating new subsets which can have arbitrary subset definition substitutions. With `nocuttrans`, it is possible to insert entirely different selection criteria in place of existing criteria. This becomes very useful when it is unclear whether alternative cut strategies would perform better or worse than a given strategy. These distinct strategies can be compared easily by using `nocuttrans` to switch out one cut for another and maintain the cut structure otherwise. (At this point it should be clear that ‘‘`nocuttrans`’’ is not the most descriptive possible name for this transformation; it would probably be better called ‘‘`modcuttrans`’’ or something similar.)

As an example, one might be interested in comparing different ways of handling particle ID. One way of handling particle ID is to use every possible combination of reconstructed tracks passing all PID cuts, and another way might be to only take the combination of tracks that ranks the highest according to some scoring system, perhaps selecting the combination of tracks that minimizes the RMS Δt value for

all tracks or something similar. ‘‘nocuttrans’’ makes substituting either of these for the other as simple as defining a new table target as a subset of some existing final data set table, and then declaring which parent table needs to be swapped with the alternative definition. In response, cl-ana will generate a copied chain of table definitions with the PID table definition only changed for the new table.

6.4 DIRECTIONS FOR FUTURE DEVELOPMENT

As it stands, dependency oriented programming is useful for researchers willing to work with Common Lisp, but researchers working with Common Lisp are in the extreme minority. Although Lisp made the development of a dependency oriented data analysis framework feasible to develop and use within a single doctoral thesis along with an analysis using it, Lisp is not likely the optimal language for exporting the tool of dependency oriented programming to researchers in general. This creates obvious directions for future development in the form of building either dependency oriented frameworks in more commonly used languages, such as Python or C++, or possibly developing front-ends in those languages which depend on the existing cl-ana system.

There are many places in the existing cl-ana system which could be optimized, as well as improvements to the interface and operator names. As I have been the predominant user of the library, the interface may make sense to me personally and yet lack intuitive ease for the general user. This would be redundant in the case of designing interfaces or new systems for other languages, as it would be very unlikely for each new language to support the same kind of interface as the one designed for Lisp.

Further table transformations could also be developed. There are doubtless more useful concepts that could be implemented to assist in making research more efficient and easier to describe, but as with all creative exercises, more minds thinking about a subject leads to more creative output. So far there has only been one perspective

and one analysis, which has doubtless limited the tool set and interface to those features which I deemed useful and necessary for this analysis. Visualization and plotting could very well be areas for improvement; so far no transformations were added which were specifically aimed at improving visualization descriptions. The plotting model for `cl-ana` is functional with lean data types, so it was convenient to define plots and generate comparisons from existing functions, but it would have been much more convenient to have comparison plots automatically generated in a similar way as the previous transformations generated data subsets or branched calculations.

There is also the possibility of moving towards graphical user interfaces for complex data analysis. The power and impact of spreadsheet GUI programs cannot be missed, having come to dominate almost every domain of data analysis outside of science. Trying to use a common spreadsheet program to analyze particle accelerator data is futile, both due to limitations of the data-interface model as well as for efficiency of the software. However, common spreadsheet programs already support a form of dependency oriented design, and it is likely that the power gained from combining an intuitive graphical interface with a robust programming language under the hood would lead to a useful tool for data analysts in need of something more than a common spreadsheet program. What `cl-ana` already provides is something like an infinite spreadsheet with the possibility of programmatically generating cells and manipulating arbitrary collections of cells simultaneously through the use of utility operators like `statsummary` or the various transformations mentioned above, along with the ability to refer to data stored outside the hypothetical infinite spreadsheet as if it is an ordinary cell. If there were an interface that could take advantage of the natural graph structure created by expressing calculations in the dependency oriented paradigm, some questions which are currently tedious to answer would become much simpler and quicker to answer. For example, it often occurs in the beginning and middle of a project that one loses sight of the forest for the trees; the detailed

work on a single part of the project occupies so much mental space that the overall scope of the project fades out of attention. For this reason, it can be useful to have a convenient visualization for the entire project, and the utility is related to the reason that flowcharts are so commonly used to visually express processes, algorithms, or business models.

The examples of dependency oriented operators like `statsummary` or the cross-section analysis chain operators also reveal a potentially useful compression of information that would be amenable to visualization. The keyword arguments supplied to them do not usually change the fundamental role of the operator, but simply tweak their behavior to suit a specific situation. Visually, it would be possible to remove all or most of those control parameters and not hide the fundamental structure of the analysis project. One might wish to project the project into different modes of organization, perhaps one based on the data subsets being analyzed and another based on the types of analysis being conducted. Each could have a nested-compressed structure, so that clicking on a compressed version of a group of result targets would reveal the inner structure and allow traversal through the graph in a different way.

CHAPTER 7

SUMMARY AND CONCLUSIONS

This work was completed to improve understanding of the strong interaction through the use of the experiment data collected through JLab's CLAS detector. Using the newly developed and validated Fermi-unsmearing method, it was possible to extract more of the cross-section for the $e^- + n \rightarrow e^- + p + \pi^-$ reaction off the bound neutron in deuterium than was previously possible, and in addition the cross-section for the $e^- + p \rightarrow e^- + n + \pi^+$ reaction off the bound proton was extracted without Fermi-smearing thanks to the same Fermi-unsmearing method. These cross-sections can be used in the extraction of N-N* transition form factors, which provide distinct information beyond elastic form factors, and in turn can shed light on the way QCD transforms smoothly from the high- Q^2 current quark-dominated behavior, into the mid- Q^2 confined quark regime, and finally into the fully-dressed quark low- Q^2 regime. As the light quark masses differ, flavor separation is a relevant consideration, and therefore the cross-sections off both the bound neutron and the bound proton provide uniquely useful information for investigating QCD.

The method of Fermi-unsmearing provides an additional tool for extracting cross-sections from the bound proton and neutron in deuterium, as it is now possible to extract cross-sections in wider (W, Q^2) domains as well as having more dense coverage of the cross-section in the hadronic degrees of freedom. There is also the possibility to extract Fermi-unsmear cross-sections using existing data sets for reaction channels for which the Fermi-smearing effect had previously been unavoidable. For the purpose of this analysis, the `onepigen` Monte Carlo event generator program was developed as an adapted synthesis of the `aao` and `aao_rad` programs so that radiative-effects and

Fermi-motion can be independently enabled and disabled, allowing for the calculation of correction factors for any combination of radiative-effects and Fermi-smearing for cross-section extractions of proton-target or neutron-target single-pion electro-production reactions. Additionally, a method for addressing Fermi-motion-induced variations in the simulated missing-mass distributions was developed in combination with a method for performing background subtraction. This combined exclusivity cut and background subtraction method was then applied to extract cross-sections with both the double-pion background contribution and the kinematically visible component of the final state interaction background contribution subtracted.

As part of an exploration into alternative data analysis software development techniques, the software system cl-ana, as an implementation of what is here called dependency-oriented programming, was developed and used to perform this data analysis, and various lessons learned through this process as well as potentially fruitful directions for future development were presented in this work.

BIBLIOGRAPHY

- [1] Y. Tian, “Exclusive π^- Electroproduction off the Neutron in Deuterium in the Resonance Region.,” *University of South Carolina (Doctoral Dissertation)*, 2016.
- [2] Günther Dissertóri, Ian Knowles, and Michael Schmelling, *Quantum Chromodynamics: High Energy Experiments and Theory*. New York: Oxford University Press, 2003.
- [3] P. Skands, “Introduction to qcd,” 2017.
- [4] Chris Quigg, *Gauge Theories of the Strong, Weak, and Electromagnetic Interactions*. Princeton University Press, second ed., 2013.
- [5] M. Procura, B. U. Musch, T. Wollenweber, T. R. Hemmert, and W. Weise, “Nucleon mass: From lattice qcd to the chiral limit,” *Phys. Rev. D*, vol. 73, p. 114510, Jun 2006.
- [6] Rajan Gupta, “Introduction to Lattice QCD,”
- [7] Craig D. Roberts and Anthony G. Williams, “Dyson-Schwinger Equations and their Application to Hadronic Physics,” *Progress in Particle and Nuclear Physics*, vol. 3, pp. 477–575, 1995.
- [8] Simon Capstick and Nathan Isgur, “Baryons in a Relativized Quark Model with Chromodynamics,” *Physical Review D*, vol. 34, no. 9, p. 2809, 1986.
- [9] Stephan Hartmann, “Models and Stories in Hadron Physics,” *Models as Mediators: Perspectives on Natural and Social Science*, vol. 52, p. 326, 1999.

- [10] SP Klevansky, “The Nambu-Jona-Lasinio Model of Quantum Chromodynamics,” *Reviews of Modern Physics*, vol. 64, no. 3, p. 649, 1992.
- [11] Walter Heupel, Gernot Eichmann, and Christian S. Fischer, “Tetraquark Bound States in a Bethe-Salpeter Approach,” *Phys. Lett. B*, vol. B718, pp. 545–549, 2012.
- [12] Kubrak Stanislav, Richard Williams, and Christian S. Fischer, “Spectra of Heavy Mesons in the Bethe-Salpeter Approach,” *Eur. Phys. J.*, vol. A51, no. 10, 2015.
- [13] F. Foster and G. Hughes, “Electroproduction of nucleon resonances,” *Reports on Progress in Physics*, vol. 46, no. 12, p. 1445, 1983.
- [14] B. A. M. et al., “The CEBAF large acceptance spectrometer,” *Nucl. Instrum. Methods A*, vol. 503, pp. 513–553, 2003.
- [15] E. S. S. et al., “The Time-Of-Flight System for CLAS,” *Nucl. Instrum. Methods A*, vol. 432, pp. 265–298, 1999.
- [16] M. D. M. et al., “The CLAS Drift Chamber System,” *Nucl. Instrum. Methods A*, vol. 449, pp. 81–111, 2000.
- [17] G. A. et al., “The CLAS Cherenkov detector,” *Nucl. Instrum. Methods A*, vol. 465, pp. 414–427, 2001.
- [18] M. A. et al., “The CLAS forward electromagnetic calorimeter,” *Nucl. Instrum. Methods A*, vol. 460, pp. 239–265, 2001.
- [19] “ROOT Homepage.” <https://root.cern.ch/>. [Accessed: 2020-02-18].
- [20] “cl-ana Homepage.” <https://github.com/ghollisjr/cl-ana>. [Accessed: 2020-02-18].

- [21] “CERNLIB Homepage.” <http://cernlib.web.cern.ch/cernlib/>. [Accessed: 2020-11-11].
- [22] “onepigen Source.” <https://github.com/ghollisjr/onepigen>. [Accessed: 2020-03-18].
- [23] “MAID Homepage.” <http://portal.kph.uni-mainz.de/MAID//>. [Accessed: 2020-02-18].
- [24] A. V. M. Osipenko and M. Taiuti, “Matching between the electron candidate track and the Cherenkov counter hit,” *CLAS Note 2004-020*, 2004.
- [25] “GNU Scientific Library Special Functions.” <https://www.gnu.org/software/gsl/doc/html/specfunc.html>. [Accessed: 2020-10-08].
- [26] “bincentering Source.” <https://github.com/ghollisjr/bincentering>. [Accessed: 2020-03-18].
- [27] “maid_xsection Source.” https://github.com/ghollisjr/maid_xsection. [Accessed: 2020-03-18].
- [28] K. P. et al, “Kinematics Corrections for CLAS,” *CLAS Note 2003-012*, 2003.
- [29] L. W. Mo and Y. S. Tsai, “Radiative corrections to elastic and inelastic ep and up scattering,” *Rev. Mod. Phys.*, vol. 41, pp. 205–235, Jan 1969.
- [30] R. Machleidt, “The High precision, charge dependent Bonn nucleon-nucleon potential (CD-Bonn),” *Phys. Rev.*, vol. C63, p. 024001, 2001.
- [31] M. Lacombe, B. Loiseau, R. Mau, J. Côté, P. Pirés, and R. de Tournel, “Parametrization of the deuteron wave function of the paris nn potential,” *Physics Letters B*, vol. 101, no. 3, pp. 139 – 140, 1981.

- [32] J. B. Cladis, W. N. Hess, and B. J. Moyer, "Nucleon momentum distributions in deuterium and carbon inferred from proton scattering," *Phys. Rev.*, vol. 87, pp. 425–433, Aug 1952.

APPENDIX A: Δt SHIFTS

A.1 PROTON Δt SHIFTS

A.1.1 EXPERIMENT

Table A.1: Experiment Δt shifts for proton.

Sector	Paddle	Low (ns)	High (ns)	Shift (ns)
1	10	-0.5784	0.5121	0.0332
1	11	-0.6908	0.5722	0.0593
1	12	-0.6407	0.5545	0.0431
1	13	-0.6817	0.5459	0.0679
1	14	-0.7326	0.5529	0.0898
1	15	-0.7561	0.5481	0.1040
1	16	-0.8622	0.6532	0.1045
1	17	-0.8244	0.6334	0.0955
1	18	-0.7389	0.6479	0.0455
1	19	-0.8656	0.5941	0.1357
1	20	-0.9388	0.5916	0.1736
1	21	-0.9593	0.6390	0.1601
1	22	-1.1190	0.6891	0.2149
1	23	-1.2454	0.9789	0.1332
1	24	-1.2730	0.9305	0.1712
1	25	-1.3137	0.4658	0.4239

1	26	-1.2803	0.6427	0.3188
1	27	-1.2203	1.0554	0.0825
1	28	-1.2160	1.1518	0.0321
1	29	-1.5160	1.2363	0.1398
1	30	-1.5959	1.1307	0.2326
1	31	-1.7069	1.3402	0.1834
1	32	-1.6263	1.2459	0.1902
1	33	-1.8535	1.5278	0.1628
1	34	-1.9445	1.5385	0.2030
1	35	-2.3900	1.6751	0.3575
1	36	-2.0621	2.2401	-0.0890
1	37	-2.3602	1.7141	0.3231
1	38	-2.6877	1.9177	0.3850
1	39	-2.9052	1.7944	0.5554
1	40	-2.8030	2.3004	0.2513
1	41	-3.9890	2.2534	0.8678
1	42	-1.5934	0.1521	0.7206
1	42	-4.8545	4.7425	0.0560
1	42	0.3604	2.7636	-1.5620
1	43	-3.1049	1.8632	0.6208
1	44	-6.3419	3.0748	1.6335
2	9	-0.8323	0.5242	0.1541
2	10	-0.7260	0.4420	0.1420
2	11	-0.7679	0.4413	0.1633
2	12	-0.8106	0.5208	0.1449
2	13	-0.7915	0.4810	0.1553

2	14	-0.7980	0.4852	0.1564
2	15	-0.8086	0.4853	0.1617
2	16	-7.8267	-0.9319	4.3793
2	17	-0.8509	0.4984	0.1762
2	18	-0.9032	0.5294	0.1869
2	19	-0.9023	0.5762	0.1630
2	20	-0.9529	0.5750	0.1890
2	21	-0.9997	0.5916	0.2040
2	22	-1.1317	0.7102	0.2108
2	23	-1.2729	0.6787	0.2971
2	24	-2.5575	-0.3337	1.4456
2	25	-1.2272	0.6933	0.2670
2	26	-1.4929	0.8057	0.3436
2	27	-0.9062	1.4989	-0.2964
2	28	-1.6565	0.9353	0.3606
2	29	-1.2807	1.5415	-0.1304
2	30	-1.7904	1.1807	0.3049
2	31	-1.8731	1.2151	0.3290
2	32	-1.8176	1.2803	0.2686
2	33	-2.0819	1.4220	0.3299
2	34	-2.0929	1.3429	0.3750
2	35	-2.4081	1.6488	0.3797
2	36	-1.8541	2.1952	-0.1705
2	37	-2.4262	2.2385	0.0939
2	38	-2.7008	1.9433	0.3787
2	39	-2.5865	1.8576	0.3645

2	40	-3.0017	2.4159	0.2929
2	41	-7.0628	-0.8053	3.9341
2	42	-8.4914	-1.8328	5.1621
2	42	-5.5031	4.1365	0.6833
2	43	-11.5005	-5.4151	8.4578
2	43	-8.0012	-5.7164	6.8588
2	44	-13.4218	-1.3319	7.3769
2	44	-7.8828	-0.4913	4.1871
3	9	-0.7629	0.4940	0.1344
3	10	-0.7415	0.4699	0.1358
3	11	-1.7651	0.7884	0.4883
3	12	-0.7857	0.4852	0.1503
3	13	-0.8423	0.4760	0.1832
3	14	-0.8167	0.4769	0.1699
3	15	-0.8200	0.5019	0.1591
3	16	-1.1236	0.6792	0.2222
3	17	-0.9366	0.4995	0.2186
3	18	-0.7206	0.6320	0.0443
3	19	-0.9750	0.5541	0.2104
3	20	-1.1440	0.5769	0.2836
3	21	-1.1012	0.5645	0.2684
3	22	-1.2676	0.6406	0.3135
3	23	-1.1560	1.9947	-0.4194
3	24	-1.1379	1.4969	-0.1795
3	25	-4.4444	-2.7646	3.6045
3	26	-1.0042	0.9859	0.0092

3	27	-1.5742	0.8103	0.3820
3	28	-1.5717	1.0032	0.2842
3	29	-1.6852	1.0148	0.3352
3	30	-1.2412	2.0301	-0.3945
3	31	-1.4253	1.5810	-0.0778
3	32	-1.7403	1.4032	0.1686
3	33	-2.0602	1.4936	0.2833
3	34	-1.9153	1.4970	0.2092
3	35	-1.6486	1.9629	-0.1572
3	36	-1.9176	1.8281	0.0447
3	37	-2.4510	1.9417	0.2547
3	38	-1.9631	2.4786	-0.2577
3	39	-2.2983	1.8390	0.2297
3	40	-2.7366	2.6317	0.0525
3	40	1.0775	6.2139	-3.6457
3	41	-3.4712	3.4641	0.0036
3	42	-2.9940	5.0379	-1.0219
3	42	2.5147	4.9938	-3.7543
3	42	3.0608	7.1894	-5.1251
3	43	-4.1127	3.7705	0.1711
3	44	4.5531	11.8725	-8.2128
4	9	-0.6574	0.4532	0.1021
4	10	-0.7181	0.5012	0.1085
4	11	-0.6893	0.4818	0.1037
4	12	-0.7368	0.5176	0.1096
4	13	-0.7003	0.5176	0.0913

4	14	-0.6895	0.5250	0.0823
4	15	-0.8669	0.5706	0.1481
4	16	-0.8149	0.5423	0.1363
4	17	-0.7278	0.5507	0.0886
4	18	-0.9714	0.5455	0.2130
4	19	-0.9083	0.6279	0.1402
4	20	-0.8713	0.6596	0.1059
4	21	-0.9366	0.6615	0.1375
4	22	-1.0075	0.6943	0.1566
4	23	-0.8144	1.2304	-0.2080
4	24	-1.4752	0.8260	0.3246
4	25	-0.5329	1.1393	-0.3032
4	26	-0.6873	1.1406	-0.2267
4	27	-0.6136	1.6032	-0.4948
4	28	-1.3521	1.1136	0.1192
4	29	-1.5476	1.1659	0.1908
4	30	-1.6638	1.1901	0.2368
4	31	-1.6759	1.3806	0.1476
4	32	-1.5502	1.3442	0.1030
4	33	-2.1093	1.4966	0.3063
4	34	-1.8504	1.4274	0.2115
4	35	-2.3698	1.6223	0.3737
4	36	-2.1608	1.8235	0.1686
4	37	-1.7081	2.2188	-0.2554
4	38	-1.8273	2.5569	-0.3648
4	39	-6.7009	-2.1033	4.4021

4	40	-2.3816	2.5409	-0.0796
4	41	-3.3484	2.3214	0.5135
4	42	-6.8600	0.9387	2.9607
4	42	-2.1684	2.3084	-0.0700
4	43	-3.6378	3.5442	0.0468
4	44	-4.4976	3.7587	0.3694
4	45	-2.5887	2.3597	0.1145
5	10	-0.6754	0.4684	0.1035
5	11	-0.7013	0.4857	0.1078
5	12	-0.7460	0.5185	0.1137
5	13	-0.7187	0.4704	0.1242
5	14	-0.7771	0.4995	0.1388
5	15	-0.7597	0.5196	0.1201
5	16	-0.8320	0.5250	0.1535
5	17	3.6591	6.1322	-4.8956
5	17	3.8400	8.8002	-6.3201
5	18	-0.9204	0.5571	0.1817
5	19	-0.8828	0.6132	0.1348
5	20	-1.1082	0.8083	0.1499
5	21	-1.0372	0.7419	0.1477
5	22	-1.1610	0.8646	0.1482
5	23	-0.9956	0.8667	0.0645
5	24	-1.0979	0.8502	0.1239
5	25	-0.8290	0.9489	-0.0600
5	26	-1.2015	0.6520	0.2747
5	27	-1.2025	1.1299	0.0363

5	28	-1.4236	1.0803	0.1716
5	29	-1.4559	1.4016	0.0272
5	30	-1.4575	1.2116	0.1229
5	31	-1.5783	1.3010	0.1386
5	32	-1.8805	1.2546	0.3130
5	33	-1.8734	1.5479	0.1628
5	34	-1.7362	1.5848	0.0757
5	35	-1.9711	1.6758	0.1477
5	36	-2.0947	1.6767	0.2090
5	37	-2.4670	1.5657	0.4506
5	38	-2.4476	2.1024	0.1726
5	39	-2.3997	2.0287	0.1855
5	40	-7.7695	-2.2704	5.0199
5	40	-4.1872	0.4240	1.8816
5	41	-2.9876	3.0378	-0.0251
5	42	-2.5663	1.8589	0.3537
5	42	-0.0291	4.0442	-2.0076
5	43	-5.0503	2.7154	1.1674
5	43	-1.9349	2.4796	-0.2724
5	44	-3.1233	3.5583	-0.2175
5	44	1.0458	1.6396	-1.3427
5	45	-4.2569	3.5358	0.3605
6	11	-0.6374	0.5872	0.0251
6	12	-0.6064	0.5299	0.0383
6	13	-0.6281	0.5438	0.0421
6	14	-0.6758	0.5376	0.0691

6	15	-0.6769	0.5801	0.0484
6	16	-0.7250	0.5959	0.0646
6	17	-0.7593	0.5834	0.0879
6	18	-0.7395	0.5609	0.0893
6	19	-0.8792	0.5858	0.1467
6	20	-0.9161	0.6019	0.1571
6	21	-0.8928	0.6331	0.1299
6	22	-1.0638	0.7203	0.1717
6	23	-1.1644	0.8179	0.1732
6	24	-1.4193	0.8345	0.2924
6	25	-0.5765	1.5589	-0.4912
6	26	-1.0369	0.7998	0.1186
6	27	-1.2274	0.7701	0.2286
6	28	-1.2686	1.1297	0.0694
6	29	-1.4121	1.2805	0.0658
6	30	-1.9823	1.3799	0.3012
6	31	-3.2131	-0.2227	1.7179
6	32	-1.7969	1.1789	0.3090
6	33	-2.2876	1.3819	0.4528
6	34	-1.9467	1.5996	0.1736
6	35	-2.1246	1.7883	0.1682
6	36	-2.2694	1.5359	0.3668
6	37	-2.4244	1.7147	0.3549
6	38	-2.5032	2.0162	0.2435
6	39	-2.6334	2.0643	0.2846
6	40	-6.9366	-1.4196	4.1781

6	40	-3.0423	2.1563	0.4430
6	41	-3.3269	2.3051	0.5109
6	42	-3.5472	2.6656	0.4408
6	43	-4.3747	3.3957	0.4895

A.1.2 SIMULATION

Table A.2: Simulation Δt shifts for proton.

Sector	Paddle	Low (ns)	High (ns)	Shift (ns)
1	8	-0.6566	0.6782	-0.0108
1	9	-0.6447	0.6984	-0.0269
1	10	-0.6670	0.7175	-0.0253
1	11	-0.6754	0.7146	-0.0196
1	12	-0.6886	0.7237	-0.0176
1	13	-0.6960	0.7323	-0.0182
1	14	-0.6992	0.7407	-0.0208
1	15	-0.7138	0.7506	-0.0184
1	16	-0.7289	0.7669	-0.0190
1	17	-0.7512	0.7821	-0.0155
1	18	-0.7764	0.8005	-0.0121
1	19	-0.8291	0.8243	0.0024
1	20	-0.8674	0.8507	0.0083
1	21	-0.8921	0.8679	0.0121
1	22	-0.9308	0.8924	0.0192
1	23	-0.9895	0.9278	0.0308
1	24	-1.2340	0.9252	0.1544
1	25	-1.1816	0.9462	0.1177
1	26	-1.2337	1.0089	0.1124
1	27	-1.3121	1.0906	0.1107
1	28	-1.4108	1.1904	0.1102
1	29	-1.5445	1.3230	0.1108

1	30	-1.7397	1.4979	0.1209
1	31	-2.0768	1.7634	0.1567
1	32	-2.2327	1.9344	0.1491
1	33	-2.4263	2.0893	0.1685
1	34	-2.7758	2.4117	0.1820
1	35	-3.4460	2.6589	0.3935
1	36	-3.4445	2.8562	0.2941
1	37	-3.3759	2.6469	0.3645
1	38	-2.8541	2.4030	0.2256
1	39	-3.2889	2.6894	0.2997
1	40	-3.9118	3.2618	0.3250
1	41	-6.3694	5.3091	0.5301
2	7	-0.7567	0.6209	0.0679
2	8	-0.7339	0.6015	0.0662
2	9	-0.7396	0.6240	0.0578
2	10	-0.7354	0.6291	0.0531
2	11	-0.7476	0.6387	0.0545
2	12	-0.7536	0.6453	0.0541
2	13	-0.7699	0.6649	0.0525
2	14	-0.7767	0.6750	0.0508
2	15	-0.7872	0.6800	0.0536
2	16	-0.8042	0.6925	0.0558
2	17	-0.8258	0.7068	0.0595
2	18	-0.8542	0.7219	0.0662
2	19	-0.9044	0.7427	0.0809
2	20	-0.9443	0.7727	0.0858

2	21	-0.9691	0.7932	0.0879
2	22	-1.0120	0.8126	0.0997
2	23	-1.0709	0.8529	0.1090
2	24	-1.2207	0.8563	0.1822
2	25	-1.1888	0.8846	0.1521
2	26	-1.2460	0.9426	0.1517
2	27	-1.3321	1.0217	0.1552
2	28	-1.4400	1.1223	0.1588
2	29	-1.5505	1.2142	0.1681
2	30	-1.7334	1.3909	0.1713
2	31	-2.0449	1.6415	0.2017
2	32	-2.1537	1.7037	0.2250
2	33	-2.5103	1.9634	0.2735
2	34	-2.8255	2.2338	0.2959
2	35	-3.3315	2.5285	0.4015
2	36	-2.9098	2.2290	0.3404
2	37	-3.3124	2.6146	0.3489
2	38	-2.8889	2.2691	0.3099
2	39	-3.4616	2.8438	0.3089
2	40	-2.2298	1.6892	0.2703
2	41	-3.1531	2.5636	0.2948
2	42	-2.8456	0.9080	0.9688
2	42	-0.6015	0.6913	-0.0449
2	42	-0.9762	3.3262	-1.1750
3	7	-0.7837	0.5992	0.0923
3	8	-0.7684	0.6145	0.0769

3	9	-0.7551	0.6080	0.0736
3	10	-0.7529	0.6095	0.0717
3	11	-0.7516	0.6179	0.0668
3	12	-0.7667	0.6405	0.0631
3	13	-0.7716	0.6474	0.0621
3	14	-0.7819	0.6573	0.0623
3	15	-0.7992	0.6732	0.0630
3	16	-0.8132	0.6838	0.0647
3	17	-0.8372	0.6994	0.0689
3	18	-0.8659	0.7125	0.0767
3	19	-0.9188	0.7328	0.0930
3	20	-0.9637	0.7592	0.1023
3	21	-0.9886	0.7809	0.1039
3	22	-1.0311	0.8044	0.1133
3	23	-1.0894	0.8386	0.1254
3	24	-1.1318	0.8564	0.1377
3	25	-1.0979	0.8819	0.1080
3	26	-1.1695	0.9475	0.1110
3	27	-1.2673	1.0272	0.1201
3	28	-1.3908	1.1499	0.1204
3	29	-1.5318	1.2585	0.1367
3	30	-1.7637	1.4699	0.1469
3	31	-2.1059	1.7102	0.1979
3	32	-2.2056	1.8226	0.1915
3	33	-2.5072	2.0848	0.2112
3	34	-2.8261	2.3425	0.2418

3	35	-3.2732	2.4337	0.4197
3	36	-3.2580	2.6477	0.3051
3	37	-3.0244	2.4041	0.3101
3	38	-2.0605	1.3943	0.3331
3	39	-3.8284	3.2064	0.3110
3	40	-2.7995	2.3460	0.2268
3	41	-1.8417	1.3403	0.2507
3	42	-3.7581	3.6596	0.0492
4	7	-0.6756	0.6657	0.0049
4	8	-0.6832	0.7083	-0.0125
4	9	-0.6719	0.7106	-0.0193
4	10	-0.6815	0.7195	-0.0190
4	11	-0.6867	0.7355	-0.0244
4	12	-0.6877	0.7517	-0.0320
4	13	-0.6947	0.7710	-0.0381
4	14	-0.7046	0.8028	-0.0491
4	15	-0.7194	0.8309	-0.0558
4	16	-0.7391	0.8667	-0.0638
4	17	-0.7581	0.8994	-0.0707
4	18	-0.7915	0.9439	-0.0762
4	19	-0.8437	0.9912	-0.0738
4	20	-0.8889	1.0485	-0.0798
4	21	-0.9238	1.0972	-0.0867
4	22	-0.9604	1.1516	-0.0956
4	23	-1.0320	1.2308	-0.0994
4	24	-1.0000	1.1336	-0.0668

4	25	-0.9720	1.1912	-0.1096
4	26	-1.0388	1.2825	-0.1218
4	27	-1.1402	1.4023	-0.1311
4	28	-1.2559	1.5286	-0.1364
4	29	-1.3965	1.7113	-0.1574
4	30	-1.6180	1.9096	-0.1458
4	31	-2.0242	2.2776	-0.1267
4	32	-2.0617	2.3213	-0.1298
4	33	-2.3407	2.5823	-0.1208
4	34	-2.7816	2.9792	-0.0988
4	35	-2.7744	2.7842	-0.0049
4	36	-3.2162	3.3950	-0.0894
4	37	-2.8948	3.0983	-0.1017
4	38	-2.8705	3.0114	-0.0704
4	39	-4.0904	4.5198	-0.2147
4	40	-2.4330	2.8101	-0.1886
4	41	-5.1396	5.4334	-0.1469
5	7	-0.6099	0.7129	-0.0515
5	8	-0.6101	0.7394	-0.0646
5	9	-0.6127	0.7582	-0.0727
5	10	-0.6115	0.7479	-0.0682
5	11	-0.6301	0.7549	-0.0624
5	12	-0.6565	0.7720	-0.0578
5	13	-0.6583	0.7736	-0.0576
5	14	-0.6690	0.7786	-0.0548
5	15	-0.6791	0.7954	-0.0582

5	16	-0.6954	0.8062	-0.0554
5	17	-0.7111	0.8213	-0.0551
5	18	-0.7375	0.8386	-0.0505
5	19	-0.7850	0.8623	-0.0386
5	20	-0.8290	0.8955	-0.0332
5	21	-0.8477	0.9125	-0.0324
5	22	-0.8893	0.9413	-0.0260
5	23	-0.9485	0.9770	-0.0142
5	24	-0.9967	0.9406	0.0280
5	25	-0.9557	0.9673	-0.0058
5	26	-1.0183	1.0281	-0.0049
5	27	-1.0949	1.1013	-0.0032
5	28	-1.1887	1.1893	-0.0003
5	29	-1.3146	1.3079	0.0034
5	30	-1.5223	1.4916	0.0153
5	31	-1.8965	1.7961	0.0502
5	32	-1.9084	1.8424	0.0330
5	33	-2.3352	2.1306	0.1023
5	35	-3.1112	2.6621	0.2246
5	36	-2.5359	2.2506	0.1426
5	37	-3.2216	2.7507	0.2354
5	38	-2.6933	2.3982	0.1476
5	39	-4.4469	3.8911	0.2779
5	40	-3.9705	3.5568	0.2068
5	41	-5.3337	4.8242	0.2547
5	42	-3.4271	3.6526	-0.1127

6	9	-0.6124	0.8071	-0.0973
6	10	-0.6049	0.7733	-0.0842
6	11	-0.6266	0.7848	-0.0791
6	12	-0.6301	0.7814	-0.0757
6	13	-0.6272	0.7918	-0.0823
6	14	-0.6410	0.8035	-0.0813
6	15	-0.6546	0.8234	-0.0844
6	16	-0.6692	0.8387	-0.0847
6	17	-0.6765	0.8524	-0.0879
6	18	-0.7118	0.8823	-0.0853
6	19	-0.7537	0.9109	-0.0786
6	20	-0.7828	0.9330	-0.0751
6	21	-0.8114	0.9671	-0.0778
6	22	-0.8435	0.9958	-0.0761
6	23	-0.9071	1.0395	-0.0662
6	24	-1.0643	0.9434	0.0605
6	25	-1.0202	0.9840	0.0181
6	26	-1.0762	1.0496	0.0133
6	27	-1.1473	1.1281	0.0096
6	28	-1.2551	1.2317	0.0117
6	29	-1.3879	1.3765	0.0057
6	30	-1.6028	1.5599	0.0215
6	31	-1.9648	1.8662	0.0493
6	32	-2.0162	1.9129	0.0517
6	33	-2.4677	2.3229	0.0724
6	34	-2.6756	2.3805	0.1476

6	35	-2.9577	2.4038	0.2770
6	36	-2.8920	2.6339	0.1291
6	37	-2.7481	2.6378	0.0551
6	38	-8.0510	6.8390	0.6060
6	39	-5.3445	4.9403	0.2021
6	40	-3.6821	3.5095	0.0863
6	41	-7.8117	4.1648	1.8235
6	42	-1.4789	-0.5743	1.0266
6	42	-4.6623	4.3849	0.1387

A.2 π^- Δt SHIFTS

A.2.1 EXPERIMENT

Table A.3: Experiment Δt shifts for π^- .

Sector	Paddle	Low (ns)	High (ns)	Shift (ns)
1	1	-0.4785	0.6427	-0.0821
1	2	-0.5160	0.4674	0.0243
1	3	-0.5174	0.5200	-0.0013
1	4	-0.4987	0.5540	-0.0277
1	5	-0.4973	0.5476	-0.0252
1	6	-0.5120	0.5828	-0.0354
1	7	-0.5079	0.5650	-0.0285
1	8	-0.5375	0.5780	-0.0202
1	9	-0.5743	0.5953	-0.0105
1	10	-0.5744	0.5821	-0.0038
1	11	-0.6026	0.6183	-0.0079
1	12	-0.6138	0.6021	0.0059
1	13	-0.6280	0.5981	0.0149
1	14	-0.6685	0.6393	0.0146
1	15	-0.6744	0.6335	0.0204
1	16	-0.8527	0.7934	0.0297
1	17	-0.9041	0.7806	0.0617
1	18	-0.7625	0.6833	0.0396
1	19	-0.7723	0.6706	0.0508
1	20	-0.7748	0.6635	0.0557
1	21	-0.8342	0.6829	0.0757

1	22	-0.8871	0.7644	0.0613
1	23	-1.3741	1.2891	0.0425
1	24	-0.8172	0.9136	-0.0482
1	25	-0.9933	0.3550	0.3191
1	26	-0.8315	0.5094	0.1611
1	27	-0.7530	0.8529	-0.0500
1	28	-0.5947	0.7162	-0.0608
1	29	-0.7699	0.6880	0.0410
1	30	-0.7296	0.6488	0.0404
1	31	-0.7019	0.7396	-0.0188
1	32	-0.7279	0.6336	0.0471
1	33	-0.7236	0.6859	0.0188
1	34	-0.7459	0.5920	0.0769
1	35	-0.7177	0.7546	-0.0185
1	36	-0.3414	1.0891	-0.3739
1	37	-0.6778	0.6942	-0.0082
1	38	-0.7359	0.7602	-0.0121
1	39	-0.7633	0.5182	0.1226
1	40	-0.6588	0.6376	0.0106
1	41	-0.9380	0.6137	0.1622
1	42	-0.7765	0.9334	-0.0785
1	43	-0.8423	0.9933	-0.0755
1	44	-0.7633	0.8117	-0.0242
1	45	-1.8080	0.8886	0.4597
1	46	-0.5859	0.6706	-0.0424
2	1	-0.6189	0.4392	0.0898

2	2	-0.5714	0.4958	0.0378
2	3	-0.5455	0.4764	0.0345
2	4	-0.5128	0.5827	-0.0349
2	5	-0.6051	0.6504	-0.0227
2	6	-0.5404	0.5995	-0.0296
2	7	-0.6176	0.5859	0.0158
2	8	-0.8124	0.6447	0.0838
2	9	-0.7663	0.6367	0.0648
2	10	-0.6503	0.5734	0.0385
2	11	-0.6445	0.5649	0.0398
2	12	-0.7373	0.6414	0.0480
2	13	-0.6826	0.5802	0.0512
2	14	-0.6778	0.5677	0.0550
2	15	-0.6926	0.5961	0.0483
2	16	-7.6152	-1.4967	4.5559
2	17	-1.5412	0.9077	0.3167
2	18	-1.7400	1.3253	0.2074
2	19	-0.8396	0.7703	0.0347
2	20	-0.7868	0.6481	0.0693
2	21	-0.8615	0.7018	0.0799
2	22	-0.9119	0.7527	0.0796
2	23	-0.9066	0.7109	0.0979
2	24	-1.8893	-0.4445	1.1669
2	25	-0.7748	0.6561	0.0594
2	26	-0.7650	0.6069	0.0790
2	27	-0.2466	1.2004	-0.4769

2	28	-0.8637	0.5733	0.1452
2	29	-0.3332	1.0925	-0.3797
2	30	-0.7317	0.6698	0.0310
2	31	-0.7977	0.6249	0.0864
2	32	-0.7724	0.6074	0.0825
2	33	-0.7425	0.6478	0.0474
2	34	-0.8656	0.5875	0.1391
2	35	-0.7872	0.6929	0.0471
2	36	-0.2547	1.1639	-0.4546
2	37	-0.4625	0.9547	-0.2461
2	38	-0.7564	0.6537	0.0514
2	39	-0.7653	0.6319	0.0667
2	40	-1.1522	1.0671	0.0426
2	41	-3.7960	-2.2536	3.0248
2	42	-6.4277	-3.5375	4.9826
2	42	-1.6741	1.1757	0.2492
2	44	-4.6396	-3.1647	3.9021
2	45	-6.0936	-4.3350	5.2143
2	45	-0.6350	1.3107	-0.3379
2	46	-1.4141	-0.1700	0.7920
3	1	-0.5837	0.4903	0.0467
3	2	-0.5980	0.5522	0.0229
3	3	-0.4867	0.5359	-0.0246
3	4	-0.5085	0.4791	0.0147
3	5	-0.5328	0.5655	-0.0164
3	6	-0.5443	0.5648	-0.0103

3	7	-0.5502	0.5066	0.0218
3	8	-0.5573	0.5339	0.0117
3	9	-0.5752	0.5424	0.0164
3	10	-0.6022	0.5570	0.0226
3	11	-2.6842	1.8193	0.4324
3	12	-0.6279	0.5552	0.0363
3	13	-0.6508	0.5680	0.0414
3	14	-0.6577	0.5576	0.0501
3	15	-0.6894	0.5907	0.0494
3	16	-0.8645	0.7562	0.0541
3	17	-0.7531	0.6187	0.0672
3	18	-1.3384	0.9970	0.1707
3	19	-2.0860	1.4063	0.3398
3	20	-0.9695	0.7980	0.0857
3	21	-0.8611	0.6604	0.1003
3	22	-0.8990	0.7126	0.0932
3	23	-1.8775	1.3807	0.2484
3	24	-0.6002	1.2421	-0.3210
3	25	-4.0509	-2.7744	3.4127
3	26	-0.4996	0.7627	-0.1316
3	27	-0.9966	0.4919	0.2523
3	28	-0.7177	0.6171	0.0503
3	29	-0.7587	0.5702	0.0942
3	30	-1.2441	1.4798	-0.1178
3	31	-0.7053	0.8787	-0.0867
3	32	-1.2401	0.7072	0.2665

3	33	-0.8270	0.6819	0.0726
3	34	-0.6748	0.6772	-0.0012
3	35	-0.3866	1.1613	-0.3873
3	36	-0.5049	0.8522	-0.1737
3	37	-0.7945	0.7460	0.0242
3	38	-0.1730	1.2316	-0.5293
3	39	-0.7487	0.7539	-0.0026
3	40	3.2823	4.6470	-3.9646
3	41	-0.8013	0.6360	0.0826
3	42	0.3049	3.6021	-1.9535
3	43	-0.9169	1.1430	-0.1130
3	45	-1.1300	0.8425	0.1438
3	46	-0.0164	1.2549	-0.6193
3	46	2.6817	4.0542	-3.3679
4	1	-0.5010	0.5189	-0.0089
4	2	-0.5065	0.5390	-0.0163
4	3	-0.5201	0.4559	0.0321
4	4	-0.4994	0.5268	-0.0137
4	5	-0.5237	0.5284	-0.0024
4	6	-0.7388	0.7674	-0.0143
4	7	-0.5384	0.5319	0.0033
4	8	-0.5663	0.5315	0.0174
4	9	-0.5837	0.5322	0.0258
4	10	-0.6248	0.5735	0.0257
4	11	-0.6468	0.5483	0.0493
4	12	-0.6696	0.5842	0.0427

4	13	-0.6623	0.5636	0.0494
4	14	-0.6868	0.5773	0.0547
4	15	-0.7325	0.6363	0.0481
4	16	-0.7240	0.6003	0.0618
4	17	-0.7078	0.6097	0.0491
4	18	-0.7365	0.6505	0.0430
4	19	-0.8124	0.7101	0.0511
4	20	-0.8339	0.7239	0.0550
4	21	-0.8397	0.6844	0.0777
4	22	-0.8282	0.6908	0.0687
4	23	-0.5194	1.2463	-0.3634
4	24	-0.7280	0.6426	0.0427
4	25	-0.2743	1.0310	-0.3783
4	26	-0.3753	0.9462	-0.2854
4	27	-0.2318	1.1910	-0.4796
4	28	-0.7011	0.6064	0.0473
4	29	-0.7172	0.6600	0.0286
4	30	-0.8549	0.6827	0.0861
4	31	-0.6713	0.6263	0.0225
4	32	-0.6309	0.6598	-0.0144
4	33	-0.7969	0.6854	0.0557
4	34	-0.7398	0.6118	0.0640
4	35	-0.8184	0.7077	0.0554
4	36	-0.8204	0.8463	-0.0130
4	38	-0.1792	1.2454	-0.5331
4	39	-4.9298	-3.5467	4.2383

4	40	-0.5280	0.9469	-0.2094
4	41	-1.8536	0.8210	0.5163
4	42	-3.9567	-1.9298	2.9432
4	42	-0.8668	0.9140	-0.0236
4	43	0.3176	1.7108	-1.0142
4	44	-0.6568	0.8132	-0.0782
4	46	-1.9383	-0.4658	1.2021
4	46	-1.0683	0.6658	0.2013
5	1	-0.5336	0.4790	0.0273
5	2	-0.6437	0.6849	-0.0206
5	3	-0.5013	0.4858	0.0078
5	4	-0.5701	0.5385	0.0158
5	5	-0.5659	0.5634	0.0012
5	6	-0.5544	0.5292	0.0126
5	7	-0.5435	0.5396	0.0019
5	8	-0.5975	0.5720	0.0127
5	9	-1.0102	0.7841	0.1130
5	10	-0.6633	0.5745	0.0444
5	11	-0.6307	0.5135	0.0586
5	12	-0.6735	0.5842	0.0447
5	13	-0.6802	0.5401	0.0701
5	14	-0.7379	0.5942	0.0719
5	15	-0.7634	0.6333	0.0651
5	16	-0.7690	0.6125	0.0782
5	17	3.8917	5.9057	-4.8987
5	17	3.5985	9.0771	-6.3378

5	18	-0.7524	0.6419	0.0552
5	19	-0.8188	0.6504	0.0842
5	20	-1.1946	1.0722	0.0612
5	21	-0.8932	0.6786	0.1073
5	22	-1.0247	0.7498	0.1375
5	23	-0.9335	0.8092	0.0622
5	24	-0.5687	0.7474	-0.0893
5	25	-0.8583	0.6883	0.0850
5	26	-0.8680	0.4201	0.2239
5	27	-1.2368	1.0212	0.1078
5	28	-0.9855	0.6706	0.1575
5	29	-0.8751	0.7189	0.0781
5	30	-0.6080	0.6523	-0.0221
5	31	-0.6662	0.6412	0.0125
5	32	-0.7088	0.6937	0.0075
5	33	-0.7124	0.6953	0.0085
5	34	-0.6351	0.6966	-0.0307
5	35	-0.7260	0.7347	-0.0043
5	36	-0.7099	0.6812	0.0143
5	37	-1.1226	0.3252	0.3987
5	38	-0.7639	0.7143	0.0248
5	40	-5.4829	-3.8576	4.6702
5	40	-2.4253	-0.4856	1.4554
5	41	-1.2021	1.6271	-0.2125
5	42	-5.6364	5.2608	0.1878
5	43	-1.7118	0.7531	0.4794

5	44	-1.8422	0.3804	0.7309
5	44	-0.0969	1.6172	-0.7602
6	1	-0.7067	0.7151	-0.0042
6	2	-0.4677	0.4994	-0.0159
6	3	-0.4774	0.5215	-0.0221
6	4	-0.4728	0.5318	-0.0295
6	5	-0.5426	0.6085	-0.0330
6	6	-0.6262	0.6805	-0.0271
6	7	-0.5090	0.5564	-0.0237
6	8	-0.5141	0.5383	-0.0121
6	9	-0.5647	0.5745	-0.0049
6	10	-0.5970	0.5861	0.0054
6	11	-0.5757	0.5537	0.0110
6	12	-0.6132	0.5931	0.0100
6	13	-0.6147	0.5725	0.0211
6	14	-0.6364	0.5883	0.0241
6	15	-0.6865	0.6382	0.0241
6	16	-0.7494	0.6876	0.0309
6	17	-0.7211	0.6580	0.0315
6	18	-0.6850	0.6326	0.0262
6	19	-0.7361	0.6840	0.0260
6	20	-0.7976	0.6811	0.0583
6	21	-0.8059	0.6961	0.0549
6	22	-0.9226	0.7627	0.0799
6	23	-0.9156	0.8384	0.0386
6	24	-0.7408	0.7339	0.0034

6	25	-0.7232	1.5041	-0.3905
6	26	-0.6005	0.5644	0.0181
6	27	-0.8120	0.5179	0.1470
6	28	-1.4562	1.3387	0.0587
6	29	-0.5553	0.8690	-0.1569
6	30	-0.6928	0.7941	-0.0507
6	31	-2.2585	-0.8165	1.5375
6	32	-0.6334	0.6585	-0.0125
6	33	-0.6798	0.6948	-0.0075
6	34	-0.6807	0.6794	0.0006
6	35	-0.6142	0.9107	-0.1482
6	36	-0.7980	0.6058	0.0961
6	37	-0.7297	0.7065	0.0116
6	38	-1.1385	1.0520	0.0432
6	39	-0.7202	0.6854	0.0174
6	40	-4.6008	-3.2172	3.9090
6	40	-0.9369	0.8967	0.0201
6	41	-0.9915	0.9589	0.0163
6	42	-1.0272	1.0613	-0.0170
6	43	-0.7857	0.8046	-0.0094
6	44	-2.4592	-0.3004	1.3798
6	44	-1.1467	1.2718	-0.0625

A.2.2 SIMULATION

Table A.4: Simulation Δt shifts for π^- .

Sector	Paddle	Low (ns)	High (ns)	Shift (ns)
1	1	-0.5974	0.6419	-0.0223
1	2	-0.6179	0.6497	-0.0159
1	3	-0.6170	0.6471	-0.0150
1	4	-0.6231	0.6519	-0.0144
1	5	-0.6312	0.6593	-0.0140
1	6	-0.6393	0.6638	-0.0123
1	7	-0.6449	0.6684	-0.0118
1	8	-0.6493	0.6706	-0.0106
1	9	-0.6559	0.6739	-0.0090
1	10	-0.6664	0.6813	-0.0075
1	11	-0.6718	0.6850	-0.0066
1	12	-0.6756	0.6895	-0.0069
1	13	-0.6867	0.7004	-0.0069
1	14	-0.6977	0.7069	-0.0046
1	15	-0.7094	0.7229	-0.0067
1	16	-0.7186	0.7279	-0.0047
1	17	-0.7375	0.7444	-0.0034
1	18	-0.7525	0.7549	-0.0012
1	19	-0.7703	0.7748	-0.0022
1	20	-0.7802	0.7852	-0.0025
1	21	-0.7924	0.8005	-0.0041
1	22	-0.8036	0.8150	-0.0057

1	23	-0.8160	0.8237	-0.0038
1	24	-0.9493	0.7767	0.0863
1	25	-0.9355	0.7759	0.0798
1	26	-0.9256	0.7739	0.0758
1	27	-0.9199	0.7836	0.0682
1	28	-0.9109	0.7883	0.0613
1	29	-0.9103	0.7962	0.0571
1	30	-0.9043	0.8014	0.0515
1	31	-0.9060	0.8128	0.0466
1	32	-0.9014	0.8216	0.0399
1	33	-0.9018	0.8236	0.0391
1	34	-0.9122	0.8373	0.0375
1	35	-1.0032	0.8401	0.0815
1	36	-0.9031	0.8603	0.0214
1	37	-0.8822	0.8480	0.0171
1	38	-0.8678	0.8515	0.0082
1	39	-0.8492	0.8410	0.0041
1	40	-0.8420	0.8578	-0.0079
1	41	-0.8750	0.9232	-0.0241
1	42	-0.8209	0.8760	-0.0276
1	43	-1.0343	0.8153	0.1095
1	44	-0.8939	0.8117	0.0411
1	45	-0.9051	0.8588	0.0231
1	46	-0.8135	0.7876	0.0129
1	47	-0.7970	0.7722	0.0124
2	1	-0.6487	0.6022	0.0232

2	2	-0.6550	0.6013	0.0269
2	3	-0.6566	0.6032	0.0267
2	4	-0.6576	0.6046	0.0265
2	5	-0.6661	0.6077	0.0292
2	6	-0.6758	0.6130	0.0314
2	7	-0.7267	0.6463	0.0402
2	8	-0.7705	0.6804	0.0450
2	9	-0.7162	0.6524	0.0319
2	10	-0.7066	0.6494	0.0286
2	11	-0.7063	0.6518	0.0273
2	12	-0.7121	0.6567	0.0277
2	13	-0.7237	0.6669	0.0284
2	14	-0.7344	0.6742	0.0301
2	15	-0.7368	0.6767	0.0300
2	16	-0.7885	0.7064	0.0411
2	17	-1.1703	0.9009	0.1347
2	18	-1.0640	0.9221	0.0710
2	19	-0.8175	0.7454	0.0360
2	20	-0.8089	0.7501	0.0294
2	21	-0.8193	0.7657	0.0268
2	22	-0.8302	0.7830	0.0236
2	23	-0.8455	0.7910	0.0272
2	24	-0.9054	0.7363	0.0845
2	25	-0.9039	0.7441	0.0799
2	26	-0.9070	0.7517	0.0776
2	27	-0.9057	0.7611	0.0723

2	28	-0.9045	0.7637	0.0704
2	29	-0.9003	0.7701	0.0651
2	30	-0.9071	0.7837	0.0617
2	31	-0.9071	0.7872	0.0600
2	32	-0.9198	0.8052	0.0573
2	33	-0.9240	0.8162	0.0539
2	34	-0.9409	0.8282	0.0564
2	35	-1.0114	0.8650	0.0732
2	36	-0.9206	0.8942	0.0132
2	37	-0.8927	0.8766	0.0080
2	38	-0.8672	0.8664	0.0004
2	39	-0.8748	0.8728	0.0010
2	40	-0.8836	0.9101	-0.0132
2	41	-0.8704	0.8874	-0.0085
2	42	-0.8237	0.8777	-0.0270
2	43	-1.6145	1.3984	0.1080
2	44	-0.8421	0.7834	0.0294
2	45	-0.8532	0.7948	0.0292
2	46	-0.8141	0.7703	0.0219
3	1	-0.6652	0.5942	0.0355
3	2	-0.6692	0.5906	0.0393
3	3	-0.6716	0.5946	0.0385
3	4	-0.6731	0.5984	0.0374
3	5	-0.6785	0.6014	0.0386
3	6	-0.6856	0.6056	0.0400
3	7	-0.6918	0.6135	0.0391

3	8	-0.6977	0.6204	0.0387
3	9	-0.7000	0.6260	0.0370
3	10	-0.7077	0.6305	0.0386
3	11	-0.7160	0.6382	0.0389
3	12	-0.7204	0.6472	0.0366
3	13	-0.7316	0.6548	0.0384
3	14	-0.7446	0.6686	0.0380
3	15	-0.7491	0.6763	0.0364
3	16	-0.7521	0.6770	0.0375
3	17	-0.7799	0.6929	0.0435
3	18	-1.1800	0.9568	0.1116
3	19	-1.0852	0.9452	0.0700
3	20	-0.8558	0.7830	0.0364
3	21	-0.8303	0.7632	0.0336
3	22	-0.8434	0.7727	0.0354
3	23	-0.8451	0.7732	0.0360
3	24	-0.8354	0.7452	0.0451
3	25	-0.8373	0.7515	0.0429
3	26	-0.8499	0.7598	0.0450
3	27	-0.8502	0.7654	0.0424
3	28	-0.8535	0.7743	0.0396
3	29	-0.8654	0.7843	0.0406
3	30	-0.8734	0.7927	0.0403
3	31	-0.8857	0.8059	0.0399
3	32	-0.8991	0.8162	0.0415
3	33	-0.8990	0.8156	0.0417

3	34	-0.9218	0.8308	0.0455
3	35	-1.0061	0.8788	0.0636
3	36	-0.9136	0.9051	0.0043
3	37	-0.8929	0.8913	0.0008
3	38	-0.8590	0.8675	-0.0043
3	39	-0.8474	0.8834	-0.0180
3	40	-0.8521	0.8436	0.0043
3	41	-0.8540	0.8650	-0.0055
3	42	-0.8443	0.8440	0.0002
3	43	-0.9794	0.8321	0.0737
3	44	-0.9717	0.9196	0.0261
3	45	-0.8629	0.7904	0.0363
3	46	-0.8663	0.7602	0.0531
4	1	-0.6299	0.6266	0.0017
4	2	-0.6303	0.6238	0.0032
4	3	-0.6338	0.6228	0.0055
4	4	-0.6406	0.6302	0.0052
4	5	-0.6519	0.6388	0.0066
4	6	-0.6579	0.6430	0.0074
4	7	-0.6615	0.6461	0.0077
4	8	-0.6694	0.6519	0.0088
4	9	-0.6759	0.6561	0.0099
4	10	-0.6793	0.6590	0.0101
4	11	-0.6872	0.6653	0.0109
4	12	-0.6979	0.6752	0.0114
4	13	-0.7060	0.6853	0.0104

4	14	-0.7170	0.6904	0.0133
4	15	-0.7312	0.7021	0.0145
4	16	-0.7424	0.7163	0.0130
4	17	-0.7529	0.7238	0.0145
4	18	-0.7700	0.7379	0.0161
4	19	-0.7890	0.7539	0.0176
4	20	-0.7997	0.7691	0.0153
4	21	-0.8119	0.7860	0.0130
4	22	-0.8222	0.7977	0.0123
4	23	-0.8363	0.8060	0.0152
4	24	-0.8414	0.7669	0.0372
4	25	-0.8407	0.7662	0.0373
4	26	-0.8490	0.7747	0.0372
4	27	-0.8549	0.7780	0.0384
4	28	-0.8597	0.7845	0.0376
4	29	-0.8722	0.7895	0.0413
4	30	-0.8767	0.7988	0.0389
4	31	-0.8900	0.8074	0.0413
4	32	-0.8937	0.8114	0.0412
4	33	-0.9061	0.8210	0.0426
4	34	-0.9219	0.8277	0.0471
4	35	-0.9768	0.8400	0.0684
4	36	-0.9049	0.9225	-0.0088
4	37	-1.7240	1.6923	0.0159
4	38	-0.9537	0.8905	0.0316
4	39	-0.8959	0.8548	0.0206

4	40	-0.8866	0.8459	0.0204
4	41	-0.9041	0.8676	0.0182
4	42	-0.8570	0.8235	0.0167
4	43	-1.0484	0.8836	0.0824
4	44	-0.9229	0.8188	0.0520
4	45	-1.1118	0.9875	0.0622
4	46	-0.8890	0.7454	0.0718
5	1	-0.5833	0.6711	-0.0439
5	2	-0.5831	0.6675	-0.0422
5	3	-0.5957	0.6731	-0.0387
5	4	-0.5984	0.6718	-0.0367
5	5	-0.6013	0.6749	-0.0368
5	6	-0.6051	0.6820	-0.0385
5	7	-0.6231	0.6982	-0.0376
5	8	-0.6501	0.7156	-0.0328
5	9	-0.7891	0.7793	0.0049
5	10	-0.6543	0.7075	-0.0266
5	11	-0.6536	0.7071	-0.0268
5	12	-0.6558	0.7125	-0.0283
5	13	-0.6702	0.7223	-0.0260
5	14	-0.6813	0.7310	-0.0248
5	15	-0.6920	0.7397	-0.0239
5	16	-0.7000	0.7473	-0.0237
5	17	-0.7221	0.7648	-0.0214
5	18	-0.7338	0.7754	-0.0208
5	19	-0.7486	0.7907	-0.0211

5	20	-0.7610	0.8018	-0.0204
5	21	-0.7761	0.8217	-0.0228
5	22	-0.7885	0.8322	-0.0218
5	23	-0.8007	0.8390	-0.0191
5	24	-0.8091	0.7845	0.0123
5	25	-0.8179	0.7928	0.0126
5	26	-0.8283	0.8004	0.0139
5	27	-0.8219	0.8030	0.0095
5	28	-0.8296	0.8067	0.0115
5	29	-0.8409	0.8132	0.0139
5	30	-0.8541	0.8295	0.0123
5	31	-0.8572	0.8361	0.0105
5	32	-0.8626	0.8413	0.0106
5	33	-0.8785	0.8528	0.0128
5	34	-0.8883	0.8533	0.0175
5	35	-0.9853	0.8866	0.0493
5	36	-0.8881	0.8997	-0.0058
5	37	-0.8599	0.8833	-0.0117
5	38	-0.8992	0.9614	-0.0311
5	39	-1.3809	1.3930	-0.0061
5	40	-0.8374	0.8555	-0.0090
5	41	-0.8250	0.8448	-0.0099
5	42	-0.8775	0.8912	-0.0068
5	43	-0.9183	0.8949	0.0117
5	44	-0.8184	0.8602	-0.0209
5	45	-0.8137	0.8385	-0.0124

5	46	-0.7779	0.7833	-0.0027
6	1	-0.5684	0.6794	-0.0555
6	2	-0.5783	0.6732	-0.0475
6	3	-0.5812	0.6792	-0.0490
6	4	-0.5930	0.6891	-0.0481
6	5	-0.5953	0.6892	-0.0470
6	6	-0.6013	0.6950	-0.0469
6	7	-0.6115	0.6965	-0.0425
6	8	-0.6205	0.7042	-0.0419
6	9	-0.6257	0.7079	-0.0411
6	10	-0.6348	0.7138	-0.0395
6	11	-0.6414	0.7152	-0.0369
6	12	-0.6496	0.7247	-0.0375
6	13	-0.6602	0.7328	-0.0363
6	14	-0.6679	0.7401	-0.0361
6	15	-0.6774	0.7490	-0.0358
6	16	-0.6933	0.7613	-0.0340
6	17	-0.7061	0.7722	-0.0330
6	18	-0.7276	0.7895	-0.0309
6	19	-0.7408	0.8008	-0.0300
6	20	-0.7485	0.8086	-0.0301
6	21	-0.7668	0.8325	-0.0328
6	22	-0.7768	0.8473	-0.0352
6	23	-0.8018	0.8569	-0.0276
6	24	-0.9118	0.7879	0.0619
6	25	-0.9117	0.7961	0.0578

6	26	-0.8769	0.7808	0.0481
6	27	-0.9275	0.8405	0.0435
6	28	-1.5822	1.2870	0.1476
6	29	-0.9783	0.8472	0.0656
6	30	-0.9189	0.8182	0.0503
6	31	-0.9289	0.8353	0.0468
6	32	-0.9386	0.8438	0.0474
6	33	-0.9422	0.8449	0.0486
6	34	-0.9584	0.8458	0.0563
6	35	-1.0231	0.8619	0.0806
6	36	-0.9196	0.8750	0.0223
6	37	-0.9021	0.8657	0.0182
6	38	-1.0513	1.0569	-0.0028
6	39	-0.9606	0.9166	0.0220
6	40	-0.8681	0.8533	0.0074
6	41	-0.8618	0.8529	0.0044
6	42	-0.8359	0.8321	0.0019
6	43	-0.9723	0.8506	0.0608
6	44	-0.8420	0.8265	0.0077
6	45	-0.8387	0.8147	0.0120
6	46	-0.8276	0.8095	0.0090

A.3 π^+ Δt SHIFTS

A.3.1 EXPERIMENT

Table A.5: Experiment Δt shifts for π^+ .

Sector	Paddle	Low (ns)	High (ns)	Shift (ns)
1	9	-0.5402	0.5820	-0.0209
1	10	-0.5552	0.5999	-0.0224
1	11	-0.5791	0.6052	-0.0130
1	12	-0.5870	0.5954	-0.0042
1	13	-0.6018	0.5827	0.0096
1	14	-0.6387	0.6070	0.0159
1	15	-0.6399	0.6159	0.0120
1	16	-0.8155	0.7784	0.0186
1	17	-0.7898	0.7280	0.0309
1	18	-0.7055	0.6745	0.0155
1	19	-0.7005	0.6515	0.0245
1	20	-0.6834	0.6398	0.0218
1	21	-0.7064	0.6552	0.0256
1	22	-0.7635	0.7344	0.0146
1	23	-1.2244	1.2679	-0.0218
1	24	-0.8104	0.9137	-0.0517
1	25	-0.9745	0.3670	0.3038
1	26	-0.7661	0.4938	0.1361
1	27	-0.7074	0.8429	-0.0677
1	28	-0.5680	0.7278	-0.0799
1	29	-0.7184	0.6632	0.0276

1	30	-0.6611	0.6469	0.0071
1	31	-0.6351	0.7358	-0.0504
1	32	-0.6671	0.6238	0.0217
1	33	-0.6857	0.6965	-0.0054
1	34	-0.6964	0.6061	0.0451
1	35	-0.6540	0.7631	-0.0545
1	36	-0.2959	1.0543	-0.3792
1	37	-0.6395	0.7037	-0.0321
1	38	-0.6872	0.7371	-0.0250
1	39	-0.7550	0.5653	0.0949
1	40	-0.6579	0.6469	0.0055
1	41	-0.9200	0.6308	0.1446
1	42	-0.7293	0.9847	-0.1277
1	43	-0.7804	0.9294	-0.0745
1	44	-0.8200	0.7720	0.0240
1	45	-5.8035	-3.6706	4.7370
1	45	-1.6281	0.8344	0.3968
1	46	-0.6028	0.6843	-0.0408
1	47	-6.9005	-4.9731	5.9368
1	47	-0.9504	0.5494	0.2005
1	48	-0.7785	2.0051	-0.6133
2	9	-0.5992	0.5000	0.0496
2	10	-0.6219	0.4862	0.0679
2	11	-0.6303	0.4993	0.0655
2	12	-0.6858	0.5729	0.0565
2	13	-0.6455	0.5175	0.0640

2	14	-0.6640	0.5409	0.0616
2	15	-0.6784	0.5686	0.0549
2	17	-0.6737	0.5789	0.0474
2	18	-0.7123	0.6153	0.0485
2	19	-0.7092	0.6216	0.0438
2	20	-0.7174	0.6115	0.0530
2	21	-0.7316	0.6548	0.0384
2	22	-0.7727	0.7051	0.0338
2	23	-0.8626	0.6811	0.0907
2	24	-1.8137	-0.4482	1.1309
2	25	-0.6650	0.6430	0.0110
2	26	-0.6575	0.5980	0.0298
2	27	-0.1788	1.1780	-0.4996
2	28	-0.7883	0.5512	0.1185
2	29	-0.2646	1.0761	-0.4058
2	30	-0.6529	0.6324	0.0103
2	31	-0.7292	0.6064	0.0614
2	32	-0.6980	0.5868	0.0556
2	33	-0.6940	0.6588	0.0176
2	34	-0.7843	0.5611	0.1116
2	35	-0.7235	0.6849	0.0193
2	36	-0.2130	1.1690	-0.4780
2	37	-0.4089	0.9304	-0.2607
2	38	-0.6748	0.6153	0.0297
2	39	-0.7042	0.6157	0.0442
2	40	-1.0964	1.1790	-0.0413

2	41	-3.7652	-2.3016	3.0334
2	42	-5.8515	-3.7892	4.8204
2	44	-4.6366	-3.1813	3.9090
2	45	-5.9886	-4.5781	5.2833
2	45	-0.6430	1.1527	-0.2549
2	46	-8.6764	-7.4011	8.0388
2	46	-1.5680	-0.1258	0.8469
2	47	-1.1450	0.9072	0.1189
2	47	0.5516	2.7692	-1.6604
2	48	-1.3707	1.3713	-0.0003
3	9	-0.5999	0.4754	0.0622
3	10	-0.6099	0.4615	0.0742
3	11	-1.9383	0.8177	0.5603
3	12	-0.6312	0.5102	0.0605
3	13	-0.6464	0.5218	0.0623
3	14	-0.6564	0.5232	0.0666
3	15	-0.6549	0.5391	0.0579
3	16	-0.7935	0.7097	0.0419
3	17	-0.7253	0.6157	0.0548
3	18	-0.7815	0.6985	0.0415
3	19	-0.7087	0.5892	0.0597
3	20	-0.7501	0.5773	0.0864
3	21	-0.7342	0.6700	0.0321
3	22	-0.7786	0.6940	0.0423
3	23	-1.9764	1.5113	0.2326
3	24	-0.6343	1.1328	-0.2493

3	25	-3.9922	-2.7888	3.3905
3	26	-0.4746	0.7362	-0.1308
3	27	-0.9938	0.4807	0.2566
3	28	-0.6415	0.5746	0.0334
3	29	-0.7041	0.5402	0.0820
3	30	-1.3890	1.4889	-0.0499
3	31	-0.7600	0.8991	-0.0696
3	32	-1.3413	0.7647	0.2883
3	33	-0.7834	0.6468	0.0683
3	34	-0.6037	0.6616	-0.0289
3	35	-0.2805	1.0882	-0.4039
3	36	-0.4357	0.8053	-0.1848
3	37	-0.7326	0.6952	0.0187
3	38	-0.1611	1.2392	-0.5391
3	39	-0.6201	0.6582	-0.0191
3	40	-0.4991	0.7061	-0.1035
3	41	0.2153	1.5493	-0.8823
3	42	0.5492	3.5397	-2.0445
3	43	-0.9751	1.5856	-0.3052
3	44	7.3321	8.9815	-8.1568
3	45	-0.9667	0.7521	0.1073
3	46	-0.1060	1.3110	-0.6025
3	46	2.6734	4.0450	-3.3592
3	47	-3.1794	-0.8017	1.9905
3	47	-1.1282	0.9494	0.0894
3	48	-0.9071	0.7046	0.1012

4	9	-0.5891	0.4607	0.0642
4	10	-0.6509	0.5404	0.0553
4	11	-0.6426	0.4901	0.0762
4	12	-0.6794	0.5425	0.0684
4	13	-0.6516	0.5237	0.0639
4	14	-0.6490	0.5501	0.0495
4	15	-0.7110	0.6268	0.0421
4	16	-0.6966	0.5914	0.0526
4	17	-0.6647	0.5903	0.0372
4	18	-0.6832	0.6351	0.0241
4	19	-0.7416	0.6755	0.0331
4	20	-0.7263	0.6813	0.0225
4	21	-0.7374	0.6629	0.0372
4	22	-0.7307	0.6964	0.0171
4	23	-0.4530	1.2673	-0.4071
4	24	-0.6640	0.6521	0.0060
4	25	-0.2375	1.0155	-0.3890
4	26	-0.3477	0.9176	-0.2850
4	27	-0.2423	1.1671	-0.4624
4	28	-0.6601	0.5791	0.0405
4	29	-0.6772	0.6420	0.0176
4	30	-0.8407	0.6761	0.0823
4	31	-0.6276	0.6009	0.0133
4	32	-0.5743	0.6352	-0.0305
4	33	-0.7482	0.6914	0.0284
4	34	-0.6722	0.5903	0.0410

4	35	-0.7459	0.6795	0.0332
4	36	-0.7379	0.6620	0.0380
4	37	-0.2388	1.0880	-0.4246
4	38	-0.0568	1.1552	-0.5492
4	39	-5.4410	-3.1526	4.2968
4	40	-0.4906	0.8710	-0.1902
4	41	-2.0716	0.9122	0.5797
4	42	-0.6630	0.6628	0.0001
4	43	0.3012	1.6982	-0.9997
4	44	-0.7949	1.0577	-0.1314
4	45	-0.8792	0.7504	0.0644
4	46	-1.9863	-0.3675	1.1769
4	46	-0.8782	0.5790	0.1496
4	47	-0.9733	0.9363	0.0185
4	48	-2.4768	0.5939	0.9414
4	48	-0.2363	1.4335	-0.5986
5	9	-0.5402	0.4937	0.0233
5	10	-0.6115	0.5406	0.0354
5	11	-0.5856	0.4907	0.0475
5	12	-0.6433	0.5801	0.0316
5	13	-0.6366	0.4859	0.0754
5	14	-0.6859	0.5618	0.0621
5	15	-0.6982	0.5945	0.0519
5	16	-0.7279	0.5854	0.0713
5	17	-3.7700	2.1929	0.7885
5	17	1.3064	0.0810	-0.6937

5	17	-1.5311	5.9039	-2.1864
5	17	3.7174	6.1104	-4.9139
5	17	3.5875	9.1322	-6.3598
5	18	-0.6818	0.5814	0.0502
5	19	-0.7292	0.5913	0.0689
5	20	-1.0873	0.9749	0.0562
5	21	-0.7623	0.6079	0.0772
5	22	-0.9244	0.7414	0.0915
5	23	-0.8392	0.8297	0.0047
5	24	-0.5031	0.7327	-0.1148
5	25	-0.8657	0.6410	0.1123
5	26	-0.8342	0.4142	0.2100
5	27	-1.3306	1.0870	0.1218
5	28	-0.9742	0.6439	0.1651
5	29	-0.8591	0.6969	0.0811
5	30	-0.5669	0.6362	-0.0347
5	31	-0.6321	0.6461	-0.0070
5	32	-0.6424	0.6907	-0.0242
5	33	-0.6464	0.6625	-0.0081
5	34	-0.5829	0.6973	-0.0572
5	35	-0.6624	0.6882	-0.0129
5	36	-0.6635	0.6736	-0.0050
5	37	-1.1471	0.2791	0.4340
5	38	-0.6236	0.6474	-0.0119
5	39	-0.9228	0.6071	0.1578
5	40	-2.2858	-0.5345	1.4101

5	42	-6.1234	3.7048	1.2093
5	43	-1.9433	0.9479	0.4977
5	44	-2.1787	0.5076	0.8356
5	44	-0.0423	1.5141	-0.7359
5	45	-0.8359	0.6922	0.0718
5	46	-0.7557	0.7711	-0.0077
5	47	0.8462	3.4814	-2.1638
6	9	-0.5011	0.5584	-0.0286
6	10	-0.5333	0.5427	-0.0047
6	11	-0.5702	0.5366	0.0168
6	12	-0.5781	0.5572	0.0104
6	13	-0.5742	0.5427	0.0158
6	14	-0.6202	0.5640	0.0281
6	15	-0.6487	0.6164	0.0162
6	16	-0.6852	0.6540	0.0156
6	17	-0.6551	0.6230	0.0160
6	18	-0.6242	0.6007	0.0118
6	19	-0.6632	0.6346	0.0143
6	20	-0.7104	0.6625	0.0239
6	21	-0.6844	0.6393	0.0225
6	22	-0.8097	0.7276	0.0411
6	23	-0.8553	0.8339	0.0107
6	24	-0.6104	0.7147	-0.0522
6	25	-0.6786	1.4081	-0.3647
6	26	-0.5720	0.5825	-0.0053
6	27	-0.7195	0.4964	0.1116

6	28	-0.4406	0.7696	-0.1645
6	29	-0.4397	0.8290	-0.1946
6	30	-0.6136	0.7964	-0.0914
6	31	-2.2915	-0.7461	1.5188
6	32	-0.5530	0.6729	-0.0600
6	33	-0.5870	0.6931	-0.0530
6	34	-0.5820	0.6579	-0.0379
6	35	-0.5494	0.9187	-0.1847
6	36	-0.7503	0.6070	0.0716
6	37	-0.6270	0.6775	-0.0253
6	38	-0.5913	0.6421	-0.0254
6	39	-0.6414	0.6714	-0.0150
6	40	-0.7898	0.7156	0.0371
6	41	-0.9718	0.9696	0.0011
6	42	-0.8070	0.8394	-0.0162
6	43	-0.7165	0.7606	-0.0220
6	44	-4.7235	1.6710	1.5262
6	45	-1.0314	1.1042	-0.0364
6	46	-0.7159	0.6549	0.0305
6	47	-6.0701	-4.3003	5.1852
6	47	-1.6671	0.0056	0.8307
6	48	-1.1647	1.2142	-0.0248
6	48	-0.0709	5.3815	-2.6553

A.3.2 SIMULATION

Table A.6: Simulation Δt shifts for π^+ .

Sector	Paddle	Low (ns)	High (ns)	Shift (ns)
1	8	-0.6423	0.6919	-0.0248
1	9	-0.6554	0.6799	-0.0122
1	10	-0.6536	0.6840	-0.0152
1	11	-0.6692	0.6874	-0.0091
1	12	-0.6727	0.6873	-0.0073
1	13	-0.6761	0.6912	-0.0075
1	14	-0.6885	0.6969	-0.0042
1	15	-0.6930	0.7054	-0.0062
1	16	-0.7042	0.7097	-0.0027
1	17	-0.7200	0.7260	-0.0030
1	18	-0.7207	0.7300	-0.0046
1	19	-0.7382	0.7459	-0.0038
1	20	-0.7467	0.7536	-0.0035
1	21	-0.7565	0.7662	-0.0049
1	22	-0.7648	0.7758	-0.0055
1	23	-0.7807	0.7871	-0.0032
1	24	-0.9118	0.5701	0.1708
1	25	-0.9060	0.5851	0.1605
1	26	-0.8990	0.5955	0.1517
1	27	-0.8958	0.6130	0.1414
1	28	-0.8980	0.6335	0.1323
1	29	-0.8933	0.6482	0.1226

1	30	-0.8971	0.6655	0.1158
1	31	-0.8969	0.6819	0.1075
1	32	-0.8958	0.6952	0.1003
1	33	-0.8977	0.7167	0.0905
1	34	-0.8988	0.7318	0.0835
1	35	-0.9691	0.7302	0.1195
1	36	-0.8743	0.7681	0.0531
1	37	-0.8614	0.7741	0.0436
1	38	-0.8440	0.7750	0.0345
1	39	-0.8319	0.7782	0.0268
1	40	-0.8142	0.7873	0.0134
1	41	-0.7920	0.7976	-0.0028
1	42	-0.7584	0.8243	-0.0330
1	43	-1.0346	0.6409	0.1968
1	44	-0.9379	0.6721	0.1329
1	45	-0.8715	0.6742	0.0986
1	46	-0.8338	0.6967	0.0686
1	47	-0.8164	0.7165	0.0500
1	48	-0.8729	0.8540	0.0094
2	8	-0.7556	0.5995	0.0781
2	9	-0.7559	0.5922	0.0819
2	10	-0.7312	0.5960	0.0676
2	11	-0.7382	0.6055	0.0663
2	12	-0.7377	0.6162	0.0608
2	13	-0.7455	0.6334	0.0560
2	14	-0.7483	0.6376	0.0553

2	15	-0.7472	0.6430	0.0521
2	16	-0.7767	0.6809	0.0479
2	17	-0.7605	0.6696	0.0454
2	18	-0.7703	0.6763	0.0470
2	19	-0.7816	0.6904	0.0456
2	20	-0.7882	0.7018	0.0432
2	21	-0.8035	0.7158	0.0438
2	22	-0.8100	0.7210	0.0445
2	23	-0.8423	0.7311	0.0556
2	24	-0.9225	0.5930	0.1647
2	25	-0.8937	0.5948	0.1495
2	26	-0.8904	0.6038	0.1433
2	27	-0.8949	0.6225	0.1362
2	28	-0.8932	0.6321	0.1306
2	29	-0.8961	0.6448	0.1257
2	30	-0.8991	0.6597	0.1197
2	31	-0.9052	0.6735	0.1158
2	32	-0.9076	0.6830	0.1123
2	33	-0.9137	0.6948	0.1094
2	34	-0.9251	0.7133	0.1059
2	35	-0.9651	0.7572	0.1040
2	36	-0.8583	0.7857	0.0363
2	37	-0.8421	0.7777	0.0322
2	38	-0.8360	0.7775	0.0292
2	39	-0.8280	0.7788	0.0246
2	40	-0.8190	0.7809	0.0190

2	41	-0.8245	0.7958	0.0144
2	42	-0.8038	0.7964	0.0037
2	43	-1.7040	1.1636	0.2702
2	44	-0.8981	0.6600	0.1190
2	45	-0.8925	0.6494	0.1215
2	46	-0.8859	0.6466	0.1196
2	47	-0.8615	0.6412	0.1101
2	48	-0.8691	0.6592	0.1050
3	8	-0.7815	0.5567	0.1124
3	9	-0.7632	0.5783	0.0925
3	10	-0.7440	0.5837	0.0802
3	11	-0.7468	0.5904	0.0782
3	12	-0.7549	0.6089	0.0730
3	13	-0.7485	0.6201	0.0642
3	14	-0.7546	0.6310	0.0618
3	15	-0.7617	0.6420	0.0599
3	16	-0.7612	0.6494	0.0559
3	17	-0.7733	0.6596	0.0568
3	18	-0.7782	0.6688	0.0547
3	19	-0.7873	0.6796	0.0538
3	20	-0.8157	0.6934	0.0612
3	21	-0.8033	0.7036	0.0499
3	22	-0.8208	0.7216	0.0496
3	23	-0.8335	0.7357	0.0489
3	24	-0.8161	0.6550	0.0806
3	25	-0.8226	0.6588	0.0819

3	26	-0.8296	0.6710	0.0793
3	27	-0.8325	0.6745	0.0790
3	28	-0.8432	0.6839	0.0796
3	29	-0.8484	0.6893	0.0795
3	30	-0.8532	0.6959	0.0786
3	31	-0.8698	0.7086	0.0806
3	32	-0.8781	0.7187	0.0797
3	33	-0.8855	0.7256	0.0800
3	34	-0.8982	0.7341	0.0821
3	35	-0.9346	0.7722	0.0812
3	36	-0.8364	0.7931	0.0217
3	37	-0.8305	0.7880	0.0213
3	38	-0.8295	0.7801	0.0247
3	39	-0.8284	0.7792	0.0246
3	40	-0.8281	0.7781	0.0250
3	41	-0.8261	0.7696	0.0282
3	42	-0.8410	0.7921	0.0244
3	43	-0.9550	0.7064	0.1243
3	44	-0.8710	0.6974	0.0868
3	45	-0.8593	0.6711	0.0941
3	46	-0.8671	0.6645	0.1013
3	47	-0.8443	0.6478	0.0982
3	48	-0.8523	0.6605	0.0959
4	8	-0.6934	0.5860	0.0537
4	9	-0.6820	0.6489	0.0165
4	10	-0.6780	0.6537	0.0121

4	11	-0.6807	0.6677	0.0065
4	12	-0.6829	0.6757	0.0036
4	13	-0.6863	0.6846	0.0009
4	14	-0.6916	0.6942	-0.0013
4	15	-0.6933	0.7030	-0.0048
4	16	-0.7051	0.7170	-0.0060
4	17	-0.7091	0.7254	-0.0082
4	18	-0.7190	0.7388	-0.0099
4	19	-0.7249	0.7520	-0.0136
4	20	-0.7293	0.7626	-0.0167
4	21	-0.7391	0.7806	-0.0208
4	22	-0.7470	0.7961	-0.0245
4	23	-0.7530	0.8146	-0.0308
4	24	-0.7737	0.7003	0.0367
4	25	-0.7782	0.7119	0.0331
4	26	-0.7817	0.7185	0.0316
4	27	-0.7829	0.7302	0.0264
4	28	-0.7898	0.7438	0.0230
4	29	-0.7951	0.7551	0.0200
4	30	-0.7972	0.7656	0.0158
4	31	-0.8007	0.7805	0.0101
4	32	-0.8017	0.7885	0.0066
4	33	-0.8120	0.8057	0.0032
4	34	-0.8145	0.8173	-0.0014
4	35	-0.8527	0.8354	0.0086
4	36	-0.7786	0.8630	-0.0422

4	37	-0.7717	0.8606	-0.0445
4	38	-0.7636	0.8615	-0.0490
4	39	-0.9322	0.9735	-0.0207
4	40	-0.7447	0.8506	-0.0529
4	41	-0.7540	0.8651	-0.0555
4	42	-0.7278	0.8575	-0.0649
4	43	-0.8825	0.7826	0.0500
4	44	-0.8242	0.7907	0.0168
4	45	-0.7930	0.7302	0.0314
4	46	-0.7902	0.7013	0.0444
4	47	-0.7892	0.6868	0.0512
4	48	-0.8635	0.7410	0.0613
5	8	-0.5851	0.7235	-0.0692
5	9	-0.6024	0.7056	-0.0516
5	10	-0.6140	0.7220	-0.0540
5	11	-0.6174	0.7156	-0.0491
5	12	-0.6358	0.7291	-0.0466
5	13	-0.6399	0.7290	-0.0446
5	14	-0.6516	0.7377	-0.0430
5	15	-0.6559	0.7370	-0.0405
5	16	-0.6699	0.7470	-0.0386
5	17	-0.6975	0.7533	-0.0279
5	18	-0.6853	0.7639	-0.0393
5	19	-0.6979	0.7715	-0.0368
5	20	-0.7109	0.7838	-0.0365
5	21	-0.7214	0.7971	-0.0379

5	22	-0.7343	0.8065	-0.0361
5	23	-0.7458	0.8129	-0.0335
5	24	-0.7769	0.6983	0.0393
5	25	-0.7806	0.7012	0.0397
5	26	-0.7885	0.7091	0.0397
5	27	-0.7945	0.7142	0.0402
5	28	-0.7971	0.7206	0.0383
5	29	-0.8091	0.7310	0.0391
5	30	-0.8167	0.7395	0.0386
5	31	-0.8251	0.7473	0.0389
5	32	-0.8356	0.7558	0.0399
5	33	-0.8442	0.7630	0.0406
5	34	-0.8587	0.7750	0.0418
5	35	-0.9109	0.8080	0.0515
5	36	-0.8082	0.8255	-0.0086
5	37	-0.8066	0.8248	-0.0091
5	38	-0.7997	0.8169	-0.0086
5	39	-0.7923	0.8085	-0.0081
5	40	-0.8114	0.8228	-0.0057
5	41	-0.8054	0.8128	-0.0037
5	42	-0.7925	0.8027	-0.0051
5	43	-0.8552	0.8326	0.0113
5	44	-0.7760	0.7997	-0.0118
5	45	-0.7809	0.7667	0.0071
5	46	-0.7861	0.7360	0.0250
5	47	-0.9788	0.9133	0.0328

5	48	-1.7203	1.2160	0.2521
5	48	3.1184	4.7188	-3.9186
6	8	-0.5719	0.7762	-0.1021
6	9	-0.6027	0.7421	-0.0697
6	10	-0.5880	0.7402	-0.0761
6	11	-0.6024	0.7422	-0.0699
6	12	-0.6134	0.7379	-0.0622
6	13	-0.6234	0.7463	-0.0615
6	14	-0.6383	0.7510	-0.0564
6	15	-0.6456	0.7579	-0.0561
6	16	-0.6533	0.7578	-0.0522
6	17	-0.6608	0.7688	-0.0540
6	18	-0.6775	0.7818	-0.0521
6	19	-0.6841	0.7892	-0.0526
6	20	-0.6969	0.7995	-0.0513
6	21	-0.7050	0.8135	-0.0542
6	22	-0.7128	0.8235	-0.0554
6	23	-0.7322	0.8370	-0.0524
6	24	-0.8648	0.6119	0.1265
6	25	-0.8635	0.6219	0.1208
6	26	-0.8639	0.6339	0.1150
6	27	-0.8649	0.6416	0.1116
6	28	-0.8682	0.6570	0.1056
6	29	-0.8708	0.6710	0.0999
6	30	-0.8689	0.6772	0.0958
6	31	-0.8903	0.7100	0.0901

6	32	-0.8862	0.7044	0.0909
6	33	-0.8943	0.7208	0.0867
6	34	-0.8992	0.7266	0.0863
6	35	-0.9431	0.7829	0.0801
6	36	-0.8379	0.8094	0.0142
6	37	-0.8344	0.8146	0.0099
6	38	-0.8192	0.8102	0.0045
6	39	-0.8124	0.8160	-0.0018
6	40	-0.7978	0.8091	-0.0056
6	41	-0.7911	0.8288	-0.0189
6	42	-0.7773	0.8429	-0.0328
6	43	-0.8892	0.8149	0.0371
6	44	-0.8721	0.9120	-0.0200
6	45	-0.7422	0.7645	-0.0112
6	46	-0.7276	0.7676	-0.0200
6	47	-0.7451	0.7971	-0.0260
6	48	-0.8522	0.9165	-0.0321

APPENDIX B: FIDUCIAL CUTS

B.4 ELECTRON

B.4.1 θ_{\min} CUTS

Table B.1: $\theta_{\min}(p) = a + \frac{b}{p+c}$ minimum electron θ cut parameters.

a (deg)	b (deg GeV)	c (GeV)
11.6237	15.8224	0.2554

B.4.2 θ - ϕ CUTS

Table B.2: Electron θ - ϕ low fiducial cut parameters.

Sector	k_0	k_1 (GeV ⁻¹)	k_2 (deg)	k_3 (deg/GeV)
1	0.8087	0.8356	-59.4590	-25.5813
2	0.8685	0.8236	-61.1648	-25.2146
3	0.9018	0.9455	-63.3772	-27.1266
4	0.9560	0.7946	-63.7957	-23.9796
5	0.7077	1.1051	-55.6010	-33.9754
6	0.8845	0.8412	-62.6912	-25.5130

Table B.3: Electron θ - ϕ high fiducial cut parameters.

Sector	k_0	k_1 (GeV $^{-1}$)	k_2 (deg)	k_3 (deg/GeV)
1	0.9158	0.8250	-63.0621	-24.9560
2	0.9581	0.9177	-64.6222	-27.2322
3	0.6160	1.2775	-55.3141	-36.7551
4	0.9217	0.8338	-63.1094	-25.2192
5	0.8018	1.0996	-60.4296	-32.4621
6	0.9982	0.8118	-66.0243	-24.0002

B.5 π^- FIDUCIAL CUTS

B.5.1 θ_{\min} CUTS

Table B.4: π^- $\theta_{\min}(p) = a + \frac{b}{p+c}$ cut parameters.

a (deg)	b (deg GeV)	c (GeV)
10.4542	15.1398	0.1999

B.5.2 θ - ϕ CUTS

Table B.5: π^- θ - ϕ low cut parameters.

Sector	c_0 ($^\circ$)	c_1 ($^\circ$ /GeV)	c_2 ($^\circ$ GeV)	c_3 (1/ $^\circ$)	c_4 ($^\circ$)	c_5 ($^\circ$ /GeV)	c_6 ($^\circ$ GeV)
1	-31.6889	6.0945	2.1178	0.1447	-18.6255	4.2630	-3.5897
2	-29.7099	2.6414	1.8451	0.1046	10.2950	-26.2690	-8.3826
3	-33.5338	1.1697	3.0734	0.0608	-19.0786	4.0659	2.4515
4	-28.4197	0.7806	1.1789	0.0769	4.4186	-12.2408	-7.1786
5	-13.7459	-16.9838	-1.7311	0.0778	39.3141	-49.7432	-15.5317

6	-35.3421	8.4289	3.3309	0.1233	-30.7445	12.4321	1.2738
---	----------	--------	--------	--------	----------	---------	--------

Table B.6: π^- θ - ϕ high cut parameters.

Sector	c_0 ($^\circ$)	c_1 ($^\circ/\text{GeV}$)	c_2 ($^\circ \text{ GeV}$)	c_3 ($1/^\circ$)	c_4 ($^\circ$)	c_5 ($^\circ/\text{GeV}$)	c_6 ($^\circ \text{ GeV}$)
1	25.5039	0.7592	-1.0139	0.1021	-1.1303	-11.9699	-5.6658
2	15.9844	10.6392	0.8221	0.1102	52.7916	-70.6092	-16.9160
3	28.0521	-0.5263	-1.6895	0.0819	-3.5992	-7.1638	-2.9619
4	30.7100	-2.8202	-1.9925	0.0792	-13.4520	1.4032	-2.2367
5	28.2793	-3.5039	-1.2867	0.5213	0.5458	-15.4765	-12.1215
6	30.5180	-4.4174	-2.4740	0.1125	-10.5967	-6.8003	-3.4282

B.6 π^+ FIDUCIAL CUTS

B.6.1 θ_{\min} CUTS

Table B.7: π^+ $\theta_{\min}(p) = a + \frac{b}{p+c}$ cut parameters.

a (deg)	b (deg GeV)	c (GeV)
1.7751	12.6914	0.2780

B.6.2 θ - ϕ CUTS

Table B.8: π^+ θ - ϕ low cut parameters.

Sector	c_0 ($^\circ$)	c_1 ($^\circ/\text{GeV}$)	c_2 ($^\circ \text{ GeV}$)	c_3 ($1/^\circ$)	c_4 ($^\circ$)	c_5 ($^\circ/\text{GeV}$)	c_6 ($^\circ \text{ GeV}$)
1	-25.2664	-0.3005	0.4263	0.0744	-2.5340	-0.7207	-4.1834
2	-28.6158	3.6255	1.2574	0.0799	3.5339	-5.3241	-5.8873

3	-27.8608	4.3531	0.8709	0.1097	1.3172	-3.2516	-6.0324
4	-27.3160	1.7698	1.0151	0.1053	-1.2548	-3.4716	-5.2822
5	-25.8269	-1.3092	0.2898	0.0658	-11.2181	2.3782	-2.0057
6	-25.3716	-0.5274	0.3834	0.0647	-10.9040	3.5412	-1.7657

Table B.9: π^+ θ - ϕ high cut parameters.

Sector	c_0 ($^\circ$)	c_1 ($^\circ/\text{GeV}$)	c_2 ($^\circ \text{ GeV}$)	c_3 ($1/^\circ$)	c_4 ($^\circ$)	c_5 ($^\circ/\text{GeV}$)	c_6 ($^\circ \text{ GeV}$)
1	26.0438	-0.5684	-0.7111	0.0825	-10.3114	1.0991	-2.0606
2	28.1192	-4.8452	-1.2048	0.0848	-3.5254	-2.1585	-4.1861
3	26.4562	-3.2009	-0.6648	0.1033	-6.2371	0.5618	-3.8332
4	27.0902	-1.6887	-0.8294	0.0929	-4.9766	-0.4628	-3.8468
5	30.1941	-2.4007	-1.1963	0.0571	-20.7239	12.4395	1.7994
6	25.6838	-0.5001	-0.6588	0.0713	-15.2238	4.5313	-0.6251

B.7 PROTON FIDUCIAL CUTS

B.7.1 θ_{\min} CUTS

Table B.10: Proton θ_{\min} value.

θ_{\min} (deg)
9.0628

B.7.2 θ - ϕ CUTS

Table B.11: Proton θ - ϕ low cut.

Sector	P_0 (deg)	P_1 (deg ⁻¹)	P_2 (deg)
1	-27.7857	0.0507	-8.3884
2	-26.5884	0.0533	-7.6951
3	-22.6190	0.1020	-8.3135
4	-25.2390	0.0761	-8.1048
5	-30.3440	0.0432	-9.8088
6	-29.4843	0.0457	-12.1145

Table B.12: Proton θ - ϕ high cut.

Sector	P_0 (deg)	P_1 (deg ⁻¹)	P_2 (deg)
1	25.7151	0.0687	-11.6032
2	24.7569	0.0567	-8.4825
3	22.7075	0.0885	-8.9374
4	25.0113	0.0688	-6.9646
5	34.1731	0.0290	-4.8307
6	27.0907	0.0516	-12.2439

APPENDIX C: ANALYSIS CUT AND CORRECTION SUMMARY

Table C.1: Analysis cuts.

Cut	π^+ Exp	π^+ Sim	π^- Exp	π^- Sim	$\pi^- + p$ Exp	$\pi^- + p$ Sim
e^- ID	✓	✓	✓	✓	✓	✓
e^- Fiducial	✓	✓	✓	✓	✓	✓
π^- ID	×	×	✓	✓	✓	✓
π^- Fiducial	×	×	✓	✓	✓	✓
π^+ ID	✓	✓	×	×	×	×
π^+ Fiducial	✓	✓	×	×	×	×
Proton ID	×	×	×	×	✓	✓
Proton Fiducial	×	×	×	×	✓	✓

Table C.2: Analysis corrections.

Correction	π^+ Exp	π^+ Sim	π^- Exp	π^- Sim	$\pi^- + p$ Exp	$\pi^- + p$ Sim
Acceptance	✓	N/A	✓	N/A	✓	N/A
Bin- Centering	✓	N/A	✓	N/A	✓	N/A
Radiative- Effects	✓	N/A	✓	N/A	✓	N/A
Background & FSI	✓	N/A	✓	N/A	×	N/A
e^- Momentum	✓	×	✓	×	✓	×
Proton Energy	×	×	×	×	✓	✓
Fermi- Unsmearing	✓	N/A	✓	N/A	×	N/A